HAL
open science

Low frequency modes from small nanoparticles (metal nanocrystals) to large nanospheres (viruses) : an inelastic light scattering study

Sergey Sirotkin

To cite this version:

Sergey Sirotkin. Low frequency modes from small nanoparticles (metal nanocrystals) to large nanospheres (viruses) : an inelastic light scattering study. Other. Université Claude Bernard - Lyon I, 2010. English. NNT : 2010LYO10260 . tel-00847063

HAL Id: tel-00847063

https://theses.hal.science/tel-00847063v1

Submitted on 22 Jul 2013

HAL is a multi-disciplinary open access archive for the deposit and dissemination of scientific research documents, whether they are published or not. The documents may come from teaching and research institutions in France or abroad, or from public or private research centers.

L'archive ouverte pluridisciplinaire **HAL**, est destinée au dépôt et à la diffusion de documents scientifiques de niveau recherche, publiés ou non, émanant des établissements d'enseignement et de recherche français ou étrangers, des laboratoires publics ou privés.

N°d'ordre 260-2010 Année 2010

THESE DE L'UNIVERSITE DE LYON

Délivrée par

L'UNIVERSITE CLAUDE BERNARD-LYON 1

ECOLE DOCTORALE : PHAST

DIPLOME DE DOCTORAT

(arrété du 16 novembre 2010)

soutenue publiquement le 10 décembre 2010

par

M. Sergey Sirotkin

Low frequency modes from small nanoparticles (metal nanocrystals) to large nanospheres (viruses): an inelastic light scattering study

Jury

M. Alexei Sokolov	Professeur	Rapporteur
M. Lucien Saviot	Directeur de Recherche	Rapporteur
M. Vladimir Lorman	Professeur	
M. Emmanuel Cottancin	Maître de conférences	
M. Alain Mermet	Professeur	Directeur de thèse
M. Bernard Champagnon	Professeur	

UNIVERSITE CLAUDE BERNARD - LYON 1

Président de l'Université	**M. le Professeur L. Collet**
Vice-président du Conseil Scientifique	M. le Professeur J-F. Mornex
Vice-président du Conseil d'Administration	M. le Professeur G. Annat
Vice-président du Conseil des Etudes et de la Vie Universitaire	M. le Professeur D. Simon
Secrétaire Général	M. G. Gay

COMPOSANTES SANTE

Faculté de Médecine Lyon Est - Claude Bernard	Directeur : M. le Professeur J. Etienne
Faculté de Médecine Lyon Sud - Charles Mérieux	Directeur : M. le Professeur F-N. Gilly
UFR d'Odontologie	Directeur : M. le Professeur D. Bourgeois
Institut des Sciences Pharmaceutiques et Biologiques	Directeur : M. le Professeur F. Locher
Institut des Sciences et Techniques de Réadaptation	Directeur : M. le Professeur Y. Matillon
Département de Biologie Humaine	Directeur : M. le Professeur P. Farge

COMPOSANTES ET DEPARTEMENTS DE SCIENCES ET TECHNOLOGIE

Faculté des Sciences et Technologies	Directeur : M. le Professeur F. Gieres
Département Biologie	Directeur : M. le Professeur C. Gautier
Département Chimie Biochimie	Directeur : Mme le Professeur H. Parrot
Département GEP	Directeur : M. N. Siauve
Département Informatique	Directeur : M. le Professeur S. Akkouche
Département Mathématiques	Directeur : M. le Professeur A. Goldman
Département Mécanique	Directeur : M. le Professeur H. Ben Hadid
Département Physique	Directeur : Mme S. Fleck
Département Sciences de la Terre	Directeur : M. le Professeur P. Hantzpergue
UFR Sciences et Techniques des Activités Physiques et Sportives	Directeur : M. C. Collignon
Observatoire de Lyon	Directeur : M. B. Guiderdoni
Ecole Polytechnique Universitaire de Lyon 1	Directeur : M. le Professeur J. Lieto
Institut Universitaire de Technologie de Lyon 1	Directeur : M. le Professeur C. Coulet
Institut de Science Financière et d'Assurance	Directeur : M. le Professeur J-C. Augros
Institut Universitaire de Formation des Maîtres	Directeur : M R. Bernard

Remerciement

Ce travail a été effectué au Laboratoire de Physico-Chimie des Matériaux Luminescents de l'Université Claude Bernard Lyon 1. Tout d'abord, je voudrais remercier Marie-France Joubert, la directrice du laboratoire pour m'avoir mis à disposition une place dans le laboratoire.

Je remercie cordialement Bernard Champagnon pour son accueil au sein de l'équipe Verres, Nanostructures et Géomatériaux, pour sa disponibilité, ses bons conseils et son soutien. Je lui suis également reconnaissant pour sa participation au jury de thèse.

Ce travail ne se serait jamais écrit sans la participation de mon directeur de thèse, Alain Mermet. Toutes ses qualités et particulièrement son haut niveau professionnel, son approche scrupuleuse au travail, son expérience de la vie et son honnêteté personnelle, font de lui un coordinateur "magnifique". Merci infiniment pour son éducation et apprentissage pendant toutes ces années. Ce fût un grand honneur de travailler sous sa direction.

Je voudrais aussi exprimer ma reconnaissance à Max Bergoin (LCP, Montpellier II). Sans lui, mes travaux de recherche sur les virus auraient eu grande peine à se réaliser. Je le remercie pour les échantillons qu'il a mis à ma disposition et son soutien moral tout au long de ma thèse. Merci aussi pour avoir pris le temps de m'apprendre à produire et purifier des virus.

Merci beaucoup à Alexei Sokolov (Université de Tennessee, Knoxville) et Lucien Saviot (Université de Bourgogne, Dijon), qui ont aimablement accepté d'être rapporteurs. Leurs commentaires et leurs propositions ont été utiles et intéressés. Je remercie chaleureusement Lucien Saviot car il nous a gentiment permis d'utiliser ses programmes pour le calcul des fréquences de vibrations des nanoparticules et ses animations, qui sont de bons exemples de vibrations et facilitent de manière significative la compréhension de l'objet de nos recherches.

Je voudrais remercier Vladimir Lorman (Université Montpellier II) et Emmanuel Cottancin (LASIM) pour leur participation au jury de thèse, leurs bons conseils et remarques,

et aussi leur aide dans les calculs et des discussions utiles pendant l'écriture de la thèse.

Je voudrais dire merci aux personnes qui m'ont aidé dans mes travaux, notamment ceux impliquant des techniques qui m'étaient peu familières: Franois Morlé (FST) qui m'a donné la possibilité de travailler dans son équipe et qui m'a aidé avec les techniques de centrifugation, Armel Descamps (CLAMS, INSA Lyon) pour de nombreuses mesures sur AFM, Anne Pillonet (LPCML) pour la détermination de l'indice de réfraction du verre et son aide dans la préparation des échantillons, Estella Bernstein (LPMCN) pour le travail en TEM, Guillaume Bachelier (LASIM) pour son énorme contribution aux recherches théoriques, devenues essentielles pour notre travail et pour nos bonnes et intéressantes discussions, Hervé Portales (LM2N, Paris VI), dont les projets communs constituent une partie importante de ma thèse, James Van Etten (Université de Nebraska, Lincoln) qui nous a fournis des échantillons du virus PBCV-1.

Je tiens à remercier certaines personnes avec lesquelles j'ai directement travaillé. Merci beaucoup à Sergei Adishchev, qui est devenu mon camarade et ami, et qui m'a transféré ses connaissances de la spectroscopie Raman/Brillouin et ce faisant m'a beaucoup appris. Grâce à lui, j'ai pu rapidement m'intégrer dans mon travail. Merci, Serega!

Merci à Eugène Duval dont la riche expérience, les riches connaissances et la recherche constante d'idées, m'inspiraient pour de nouvelles recherches et études.

Merci à Bruno Stephanidis qui avait soutenu sa thàse deux ans avant moi dans le même groupe et avec qui j'ai eu l'honneur de travailler pendant une année.

Je voudrais remercier tous les membres du laboratoire et en particulier ceux de mon équipe Verres, Nanostructures et Géomatériaux, qui m'ont bien entouré dans une ambiance amicale. Je n'oublierai jamais ces personnes, ils m'ont laissé de bons souvenirs. En particulier je remercie Eric Nardou: sans lui je ne parlerais jamais franais et je ne me serais pas aussi bien intégré au mode de vie en France.

Merci beaucoup à la France et à Lyon! Je suis tombé amoureux de ce pays magnifique et de cette ville formidable, où j'ai passé trois brillantes, intéressantes et inoubliables années.

Je remercie infiniment mes parents et amis qui ont cru en moi, m'ont soutenu et m'ont aidé. Je vous aime!

Merci!

Contents

Contents **i**

List of figures **iii**

List of tables **xvi**

Introduction **1**

1 Vibrational dynamics of nano-spherical objects **7**

1.1 Basics of the theory of elasticity 7

1.2 Free sphere model 10

1.3 Vibration modes of free spheres 13

1.3.1 Nomenclature of the eigenmodes 13

1.3.2 Eigenfrequencies 15

1.4 Sphere embedded in a matrix 17

1.5 Degeneracy of the modes 18

2 Inelastic light scattering: Raman and Brillouin scattering **21**

2.1 Physics of inelastic light scattering 21

2.1.1 Short historical recall 21

2.1.2 Nature of the phenomenon 22

2.1.3 Raman and Brillouin scattering 29

2.2 Inelastic scattering from modes of spherical NPs 34

2.2.1 Selection rules for nanoparticle modes 35

2.2.2 Raman scattering from metal nanoparticles 38

2.2.3 Recent extension to nanoparticle modes from large viruses 47

2.3 Experimental Raman and Brillouin techniques 48

3 Low frequency Raman scattering from the metal nanoparticles 61

3.1 Bimetallic silver-gold nanoparticles embedded in a glass matrix 62

3.1.1 Sample presentation 62

3.1.2 Optical characterization.
Discussion about the type of NPs 64

3.1.3 Low frequency Raman scattering experiments 65

3.1.4 Summary 78

3.2 Gold nanocrystals deposited on the surface 80

3.2.1 Investigated samples. Optical characterization 80

3.2.2 Low frequency Raman scattering experiments
of gold nanocrystals 82

3.2.3 Summary 87

3.3 Copper nanoparticles embedded in a glass matrix 88

3.3.1 Sample presentation 90

3.3.2 Absorption: results and discussion 93

3.3.3 Low frequency Raman scattering studies 100

3.3.4 Discussion 117

3.4 Conclusion 119

4 Raman and Brillouin Scattering from Large Viruses 121

4.1 Biological description of the studied viruses 124

4.1.1 PBCV-1 125

4.1.2 Iridescent viruses 127

4.2 Physical characterization of the samples 130

4.2.1 Virus solution 131

4.2.2 Virus pellets 132

4.2.3 Polystyrene spheres 132

4.3 Morphological characterization 134

4.3.1 Techniques 135

4.3.2 USAXS and AFM sample characterization 138

4.4 Low frequency inelastic light scattering
from large viruses 147

4.4.1 Experimental details 147

4.4.2 Results and discussion 148

Conclusions and perspectives **165**

References 169

List of Figures

1 The diagrams on the left display the model of the modes illustrated for lumazine synthase (a protein enzyme which is capable to create an icosahedral assemblies). The arrows indicate the directions of collective motions on/above the surface. The middle and right columns display the equivalent mode shapes generated by the theory for a hollow sphere with comparable dimensions and packing density. The diagrams on the right column are also colored by the mobilities of the nodes [10]. 5

1.1 Fundamental spheroidal vibrational modes of a spherical object. **Up:** a spherical (breathing) mode $\ell = 0$; **down:** a quadrupolar mode $\ell = 2$. . . . 14

1.2 Fundamental torsional vibrational modes of a spherical object: **left:** a mode $\ell = 1$; **right:** a mode $\ell = 2$. 14

1.3 The scheme of the splitting of the quadrupolar mode occurring when the anisotropy appeases in the inner structure of NPs. 19

2.1 An example of a Raman spectrum at low energy. The elastic line (ν_0) is cut. The Stokes side is a Raman response to the vibrational energy transfer from a photon to the substance, the anti-Stokes side corresponds to the transfer of vibrational energy from the substance to the photon. . . 24

2.2 The modulation of the linear induced dipole produced by an electromagnetic field of frequency ω and scattering molecule vibrating with frequency ω_i. As an output we have three frequencies: ω, $\omega - \omega_i$ and $\omega + \omega_i$ (see Eq.(2.16)). 27

2.3 A scheme of Brillouin scattering from the quantum point of view: the Stokes process is a transfer of a quantum of acoustic phonon energy to the lattice from the photon and the anti-Stokes process is a reverse symmetrical process. Vibration levels are labeled with the index n. 30

2.4 The ω-q dependence for acoustic vibrations in a crystal lattice (a is the typical atomic separation). The linear behavior depicts the Debye approximation. 31
2.5 The backscattering geometry of the scattered light detection. 32
2.6 The 90N geometry of the scattered light detection. 32
2.7 The 90R geometry of the scattered light detection. 33
2.8 The 90A geometry of the scattered light detection. 34
2.9 The ω-q dependence for the optical branch of lattice vibrations. 35
2.10 Real and imaginary parts ϵ_1 and ϵ_2 of the dielectric function of silver (left) and gold (right). Comparison between the Drude model (solid lines) and the experimental measurements (squares). The influence of d-core electrons is patent in the imaginary part of ϵ where an increase of ϵ_2 appears around 1.9 eV for gold and 4 eV for silver corresponding to the interband transition threshold. Retrieved from [46]. 40
2.11 A scheme of the dipolar charge redistribution in the metal nanosphere under influence of electric field with $\lambda \gg D$. 41
2.12 Theoretical absorption spectra of silver (**a**), gold (**b**) and copper (**c**) NPs of size of 10 nm embedded in a glass matrix with refractive index $n = 1.5$. These spectra were calculated by P. Yang and H. Portales (LM2N, University Paris 6, Paris, France) with the DDA method. 43
2.13 The manyfold reflection of a light beam in a Fabry-Perot resonator with air space between mirrors. 49
2.14 The distribution of the relative intensities I/I_{max} in the interference of a FP resonator as a function of δ for different values of the reflection coefficient r. 50
2.15 Brillouin scattering spectrum of a glass made by one FP spectrometer [71]. The free spectral range is 22.43 GHz. R designates the Rayleigh line and B_l and B_t the longitudinal and transverse Brillouin components, respectively. The second-order lines are indicated by a prime and one line of a third order is indicated by a double prime (B_l''). The Rayleigh peaks scaled down by a factor of 100 are also shown. 52
2.16 Transmitted intensity of a tandem made of two sequential resonators FP: $I = I_{FP_1} I_{FP_2}$. The intensities of the single FP are in linear scales, the intensity of the tandem is in logarithmic scale. 53
2.17 The scheme of the Tandem FP. 54

2.18 The five-grating monochromator Z40 [72]. 59

2.19 The comparison of spectrum quality between the Z40 (**blue**) and the Tandem FP (**red**). Both spectra are the scattered signal from copper nanoparticles of size of $\sim$ 21 nm. The Z40 spectrum was recorded with exciting wavelength 514.5 nm whereas the Tandem's spectrum was made using the YAG line 532 nm. It is clear that the Tandem's spectrum contains two peaks which are not resolved in the Z40 spectrum. 60

3.1 AuAg samples annealed during 8, 16, 32 and 64 hours at the temperature of 490°C. 63

3.2 Absorption spectra of the AuAg samples annealed during 8, 16, 32 and 64 hours at 490°C. Red arrows mark the positions of the SPR peaks of pure gold and pure silver NPs of the same sizes. **Inset:** the dependence of the SPR peak position on the values of x (atomic ratio of Ag in the NPs) . . . 64

3.3 LFRS VV spectra of the AuAg samples annealed during 8, 16, 32 and 64 hours at the temperature of 490°C. Spectra are normalized on maximum and shifted along vertical log-scaled axes for clarity. **Inset:** the zoom of the the lowest frequency line demonstrates a splitting of the quadrupolar mode. 66

3.4 LFRS high-resolution spectrum of Au NPs embedded in St.Louis matrix [59]. 67

3.5 Comparison of the VV and VH spectra of the richest Au sample (64H annealing). The intensities were scaled with respect to the most intense line. **Inset A:** Enlargement of the Stokes side; the arrows point the modified regions. **Inset B:** The difference spectrum (VV-VH) unveils the contributions from the spherical mode. 69

3.6 Five Lorentzian fit of the VH spectrum of the sample annealed for 64 hours ($Ag_{0.66}Au_{0.34}$). The non-labeled arrows point the detected high order harmonics. 70

3.7 Comparison of the experimental (symbols) and the CFM calculated (lines) values of the harmonic-to-fundamental frequency ratios of the Raman active harmonics of the $\ell = 2$ mode, for the four different samples ($x = 0.66, 0.7, 0.77$ and 0.82). The top scale indicates the corresponding diameters, as deduced from the T_{2g} component. 72

3.8 Normalized Raman spectra of silver NPs calculated with $R = 2.5$ nm, excitating wavelength is 496.5 nm. **A:** A spectrum corresponding to the volume coupling mechanism; **B:** A spectrum corresponding to the surface coupling mechanism, the frequency range 16–80 cm^{-1} is zoomed in 10 times. The figure was taken from [49]. 74

3.9 LFRS VH spectrum of the AuAg sample annealed during 64 hours at the temperature of 490°C. The size of the corresponding NPs is approximatelly 23.5 nm. Red solid curve is the RSI prediction of the Raman spectrum for NPs embedded in the matrix; red solid bars are the RSI prediction for the quadrupolar mode and its harmonics of free NPs; black arrows are the CFM predictions. **Inset:** Zoom of the the higher frequency part of the spectrum. 75

3.10 **Left:** The RSI calculated (red) and experimental (black) VV (solid line) and VH (dashed line) Raman spectra of the $Ag_{0.66}Au_{0.34}$ NPs. The spectra are normalized with respect to the quadrupolar mode. **Right:** The RSI calculated (red) and experimental (black) Raman difference spectra ($I_{VV} - kI_{VH}$). Black arrows are the CFM prediction of the positions of the spherical mode and its harmonics. 77

3.11 Relative change of the transmission of the 64H sample, as measured through pump probe spectroscopy. The pseudoperiod derived from a single vibration component ($T = 6.8$ ps) agrees well with that derived in the frequency domain from the Raman spectrum (inset B of the Fig.3.5). 78

3.12 Spherical mode frequency values (fundamental and second harmonic), as derived from Raman experiments (circles), pump probe experiments (triangles) and CFM calculations (crosses), for three different samples ($x = 0.66, 0.77$ and 0.82). The top scale indicates the corresponding diameters, as deduced from the ($\ell = 2, n = 1$) mode. 79

3.13 3D scheme of the Au NCs deposited on HOPG. 81

3.14 **A:** Bright field scan TEM image of Au NCs of 5.3 nm; **B:** Dark field scan of the same NCs; **C:** Several zoomed areas of the TEM image presented different types of the NC shapes: 1. decahedron, 2. icosahedron, 3. undefined polycrystal, 4. single-twinned particle; **D:** Zoomed zone of the TEM image presented the monocrystal NPs: of cuboctahedral shape and of truncated octahedron shape. Retrieved from [74]. 82

3.15 Experimental UV-vis extinction spectrum (filled black curve) of the colloidal Au solution plotted along with those calculated by using the DDA method for nanoparticles of different shapes: cuboctahedron (blue curve), icosahedron (violet curve), truncated octahedron (green curve), decahedron (red curve) and sphere (orange curve). The vertical dotted lines indicate the wavelengths of the various laser lines used as excitation sources for the LFRS experiments. Retrieved from [74]. 83

3.16 LFRS spectra of Au NCs measured from three samples of Au NCs: 4.3 nm (green curve), 5.1 nm (red curve) and 5.3 nm (blue curve). The excitation wavelength is 532 nm. All spectra are shifted along vertical axis for clarity. Black arrows at the anti-Stokes side point the middle band. Retrieved from [74]. 84

3.17 LFRS spectra of 5.3 nm Au NCs. The wavelengths of the different laser lines used as the excitation sources are 514.5, 647.1, and 676.4 nm, from the bottom to the top. Spectra have been vertically shifted and amplitudes normalized to the maximum of the lowest frequency band for clarity. Retrieved from [74]. 85

3.18 High-resolution Stokes LFRS spectrum of 5.3 nm Au NPs recorded for an excitation at 532 nm. Retrieved from [74]. 85

3.19 Temperature/time conditions of the differently prepared samples preparation. The red line marks T_g temperature of the glass. 90

3.20 Determination of the T_g temperature of the St.Just glass by the DSC method. The green vertical line is a middle of the transition zone; the blue dashed lines are the temperatures used to anneal the samples. 92

3.21 **a:** Absorption spectra of Cu NPs grown through annealing below T_g over times ranging from 1 to 40 hours (batch S_1). **b:** The same spectra in comparison with theoretically calculated spectra (red curves). The volume fraction q of the Cu involved in the formation of the NPs in the glass is found to increase from 0.001% to 0.012%, while the annealing time increases from 1 to 40 hours. The green line at the position of 532 nm is the excitation line used in the LFRS investigations. 94

3.22 **a:** Absorption spectra of Cu NPs grown at 580°C for annealing times ranging from 0.5 to 90 hours (batch S_3). **b:** Same spectra in comparison with theoretically calculated spectra (red curves) with different values of the volume fraction q of the Cu involved in the formation of Cu NPs in the glass in the range of 0.0032% to 0.01%. Vertical lines at the positions of 532 and 561 nm are the excitation lines used in the LFRS investigations of these samples. **c:** Comparison between two samples annealed during 16 hours at temperature below T_g (blue curve) and slightly above T_g (red curve). 95

3.23 Evolution of the volume fraction of copper engaged in Cu NPs, as a function of annealing for the samples annealed at 525°C (red curve) and 580°C (blue curve). 96

3.24 Absorption spectra of the NPs grown at 700°C for annealing times ranging from 0.5 to 8 hours. The red curve is the theoretically calculated spectrum for Cu_2O NPs and the blue curve is the theoretically calculated spectrum for CuO NPs. 97

3.25 Absorption spectra from the NPs annealed at fixed time (2 hours) over a temperature range between 525°C to 700°C. Vertical bars are the positions of the exciting lines used for the LFRS investigations. 98

3.26 Absorption spectrum of the Cu NPs grown at 525°C during 40 hours (black curve). Red and green curves are theoretically calculated spectra assuming Cu NPs only and coexisting {Cu + Cu_2O NPs} respectively. 99

3.27 X-ray diffraction spectrum of Cu NPs grown at 700°C during 8 hours. This curve does not contain any Bragg peak attributed to copper crystals. The large peak around 30° is the first sharp diffraction peak attributed to the scattering from Si–O bonds. 101

3.28 **a:** LFRS VV spectra from samples annealed below T_g (batch S_1). The spectra are normalized on the maximum and shifted along the vertical axis for clarity. **Left inset:** Evolution of the NP average radius with annealing time: two stages of growing may be distinguished (see text). **Right inset:** Dependence of the ratio $\Delta\nu/\nu$ on the annealing time. **b:** Recall of the absorption spectra of the same samples (see section 3.3.2). 102

3.29 **a:** Recall of the absorption spectra from the samples annealed well above T_g (700°C) over time ranging between 0.5 and 8 hours. **b:** LFRS VV spectra from the same samples. The spectra are normalized on the maximum and shifted along the vertical axis for clarity. **c:** Evolution of the average radius as a function of annealing time assuming Cu NPs for the two series of the samples: "$T_a < T_g$" (blue stars) and "$T_a \gg T_g$" (red circles) as derived from the P_1 peak. **d:** The dependence of the ratio $\Delta\nu/\nu$ for the P_1 peak on the annealing time for the same series of the samples. 105

3.30 Polarized/depolarized low frequency Raman spectra from the sample annealed at 700°C during 8 hours (batch S_2). The spectra are normalized on the maximum intensity. Red bars are the theoretical CFM predictions of the spherical mode ($\ell = 0$); blue bars are those for the quadrupolar mode ($\ell = 2$). The heights of the bars are irrelevant to intensities. **a:** Cu_2O and Cu NPs assumptions are respectively indicated on the Stokes and anti-Stokes sides. **b:** Same spectra recorded over a broader frequency range, using the Z40 quintuple monochromator (anti-Stokes side only). Vertical bars correspond to the Cu assumption. The double peak structure (black arrows) between 800 – 910 GHz and the peak near 620 GHz are due to Raman scattering from air contained in microbubbles. 106

3.31 TEM image of the NPs embedded in St.Just glass and prepared through annealing at 700°C during 2 hours. One Cu NP is spotted by the red arrow. The white arrow points to large ring like structure of unidentified nature. . 107

3.32 **a:** Recall of the absorption spectra from the samples annealed slightly above T_g (580°C) over time ranging from 2 to 90 hours (batch S_3). **b:** LFRS spectra from the same samples. The spectra are normalized on the maximum and shifted along the vertical axis for clarity. 110

3.33 Polarized/depolarized LFRS spectra from the sample annealed slightly above T_g (580°C) during 16 hours (batch S_3). Red bars are the CFM predictions of the spherical mode ($\ell = 0$); blue bars are those for the quadrupolar mode ($\ell = 2$). **a:** The CFM hypothesis of the NPs of isotropic Cu NPs (Stokes side) and of anisotropic Cu NPs (anti-Stokes side). 111

3.34 Depolarized LFRS spectra from the NPs annealed at 580°C during 16 hours. Spectra were recorded with exciting lines: 532 nm (**green**) and 561 nm (**orange**). **Inset:** Absorption spectrum of the same sample with marked positions of the exciting wavelengths. 112

3.35 LFRS spectra (exciting line is 532 nm) from the NPs prepared through annealing between 525°C to 700°C during 2 hours (batch S_4). The lower panel was recorded with a lower FSR in order to resolve the inelastic signal for higher temperature of annealing. 114

3.36 TEM image of the sample annealed at 605°C during 2 hours (batch S_4). . . 115

3.37 LFRS VV and VH spectra (exciting line is 532 nm) from the NPs annealed at the temperature 605°C during 2 hours and the theoretical CFM prediction of the frequency positions of the vibrational modes and their harmonics for Cu NPs with average size 13.8 nm with the assumption that the NPs are crystals. **Inset:** The difference spectrum $I_{VV} - kI_{VH}$, where k is a normalizing coefficient. 115

3.38 LFRS spectra of the sample annealed at 630°C and after cooled down with the rate of 100°C/h (**up**) or rapidly quenched (**down**). 116

3.39 Evolution of the average radius as a function of annealing time assuming Cu NPs for the three series of the samples: "$T_a < T_g$" (blue), "$T_a \gg T_g$" (red) and "$T_a > T_g$" (green) — and corresponding schematic profiles of the lowest frequency modes. 117

4.1 Inelastic intensity of the fundamental ($n = 1$) vibrational eigenmodes with $\ell = 0$ and $2 \leq \ell \leq 7$ for a free vibrating polystyrene latex sphere as a function of the product of scattering wavevector q and radius R [114]. . . . 124

4.2 Schematic inner structure of a spherical virus. 125

4.3 **a:** Shaded surface view of PBCV-1 3D reconstruction at 15Å resolution, viewed along a 2-fold axis [122]. **b:** Central cross-section of the cryo-EM density (scale bar: 500 Å) [119]; the red arrow points to the spike-structure, the white arrow indicates the inner lipid layer. 126

4.4 **a:** Shaded surface view of CIV 3D reconstruction at 13Å resolution, viewed along a 2-fold axis [125]. **b:** Insect infected by CIV demonstrates the opalescent shade due to CIV self organization. **c:** Micrograph of vitrified CIV virions suspended over a hole in a carbon support film [129]. 128

4.5 TEM image of a CIV pellet. The white bar corresponds to the scale of 460 nm. 129
4.6 **a:** Insect infected by WIV (**left**) and uninfected one (**right**). TEM image (**inset**) showes closed-packed arrays of viruses within the cell cytoplasm [132]. **b:** Cryo-TEM of dispersed WIV particles. The image shows six particles viewed along a threefold symmetry axis. The higher magnification inset shows features corresponding to the fibrillar structure, emanating from the proteinaceous capsid [132]. 130
4.7 Absorption spectra of CIV suspensions with different virion concentrations. 131
4.8 CIV pellets obtained through centrifugation of the virus suspensions. **a:** View in reflected light. **b:** View in absorbed light. 133
4.9 USAXS from a suspension of PLA NPs and from a PBCV-1 solution. These curves show that PBCV-1 viruses are monodisperse spheres whereas PLA NPs possess a high polydispersity and therefore they cannot serve as proper references for our low frequency inelastic scattering experiments. 134
4.10 Schematic of an atomic force microscope [139]. 136
4.11 USAXS intensity from a dilute suspension of PMMA NPs with $R = 40.9$ nm (volume fraction $\phi_S = 0.3\%$). The dotted line is a fit of the spectrum by monodisperse model. The continuous line is a fit to polydisperse sphere function given by equation (4.3) for Gaussian size distribution with deviation 2.8 nm [140]. 137
4.12 USAXS spectra of CIV (blue curve) and PBCV-1 (red curve) virus solutions of the concentrations of 15 and 8 mg/ml respectively. Both axes are log-scaled. 139
4.13 USAXS experimental data (blue curves) and the best fits (red curves) for PBCV-1 (**a**) and CIV (**b**) solutions. In order to fit the PBCV-1 data a hard sphere model was used, for CIV data — core-shell sphere model. . . . 140
4.14 **a:** Comparison of the USAXS 1D azimthal averaged profiles from the diluted suspensions of CIV (red curve) and pellets of CIV (blue curve). Black arrows mark the Bragg peaks which were used for Table 4.1, the orange arrow is the theoretical position of the third order Bragg peak. Vertical axis is log-scaled. **b:** Characteristic two-dimensional pattern of the higly concentrated CIV. **c,d:** Same as (a,b) for PBCV-1. 143
4.15 AFM image of a pellet (probably dried) of CIV: **a:** 2D; **b:** 3D. 144

4.16 AFM height-contrast image of the PBCV pellet. 144

4.17 USAXS spectra of PS NPs solutions: PS-187 (green curve) and PS-297 (blue curve). Vertical axis is log-scaled. 145

4.18 **Left:** Experimental (blue) and fitted (red) USAXS spectra of PS-187 NPs in water solution. **Right:** Structure factor of PS-187 NPs diluted in water obtained as a result of the fitting. 146

4.19 AFM images, two-dimensional (**a**) and three-dimensional (**b**) from a drop of PS-187 NP solution dried on a glass substrate. The distortion of the spheres can be explained by the mechanical motion of the scanning tip of the AFM which sometimes may push NPs. 146

4.20 **a:** Azimuthally averaged USAXS spectra of PS-187 NPs in solution (red curve) and in pellets (blue curve). Vertical axis is log-scaled. **b:** Associated 2D pattern of the pellets. 147

4.21 "Sandwich" with PS pellet in reflected light. 148

4.22 Low frequency inelastic scattering spectra, VV (red) and VH (blue) of PBCV-1, CIV, WIV and PS-187. All spectra are normalized on maximum intensity and shifted along vertical axis for clarity. **a:** Low frequency inelastic scattering spectra of CIV, WIV and PS-187 diluted in water and PBCV-1 virus diluted in Tris buffer of pH 7.8 in backscattering geometry of experiment. **b:** Low frequency inelastic scattering spectra of WIV virus water solution in backscattering, 90A and 90R geometries of experiment. **c:** Low frequency inelastic scattering spectra of CIV, WIV, PBCV-1 and PS-187 pellets. Viruses' spectra are recorded in backscattering geometry of experiment whereas PS-187 spectrum is represented in 90A geometry. **d:** Low frequency inelastic scattering spectra of CIV pellets in backscattering, 90A and 90R geometries of experiment. 150

4.23 Inelastic scattering VH spectra recorded in backscattering scheme of: **a:** CIV, WIV and PBCV-1 solutions; **b:** CIV, WIV and PBCV-1 pellets; **c:** CIV, PS-187 and PS-297 solution; **d:** CIV, PS-187 and PS-297 pellets. . . 151

4.24 **a:** Inelastic scattering spectra of PS-287 PBCV-1 solutions recorded at different wavelength excitations. **b:** The same but for PS-187, CIV and WIV pellets. 153

4.25 Depolarized (**a**) and polarized (**b**) low frequency inelastic scattering spectra of PS-187 solutions of different concentrations. All spectra are normalized on the amount of scans. 153

4.26 Inelastic light scattering VH spectra of PS-187 of different volume fractions. 155

4.27 Low frequency inelastic scattering spectra of PS-187 and PS-297 colloid suspensions of high concentration (the PS volume fraction is around 75%). The P_1 band is hardly seen on the anti-Stokes side because of an asymetry of the elastic laser line. 156

4.28 Evolution of the low frequency inelastic scattering spectra of placed in "sandwich" PS-187 (**a**) and PS-297 (**b**) caused by the extinction of the PS pellets. 157

4.29 Scattered intensity of the fundamental ($n = 1$) vibrational eigenmodes with $\ell = 0$ and $2 \leq \ell \leq 7$ for a free vibrating polystyrene latex sphere as a function of the product of scattering wavevector q and radius R. Vertical lines correspond to $q_{max}R$ values for PS-187 and PS-297 for excitations of 476.5 nm (blue) and 532 nm (green). Vertical shaded rectangles are supposed to mark the $q_{max}R$ value for viruses; their width corresponds to estimated range of virus refractive index. 158

4.30 Comparison between experimental (black solid line) and calculated (blue) spectra of silica and PS spheres using the sound velocities (c_L, c_T) and diameter d given in the plots. The sharp (red) lines denote the contributions of the individual modes (n, l) labeled above the spectrum. The blue line is the sum of all modes broadened with a Gaussian line shape and corrected for a linear background (dashed line). For clarity, only the anti-Stokes side is shown [114]. 159

4.31 Anti-Stokes sides of the inelastic spectra of PS-187 (**a**) and PS-297 (**b**) "dry" NPs for exciting wavelength 532 nm ($q_{max}R = 3.51$ and 5.58 respectively). Red bars are the theoretically predicted SPH modes made by the FSM calculations with intensities (bar heights) predicted by M. Montagna with help of its method [114]. According to the FSM calculations the real size of PS-297 is about 319 nm. 160

4.32 Low frequency Raman spectra of the PS-187 and PS-297 NPs for two exciting wavelengths: 532 and 476.5 nm. 161

4.33 Anti-Stokes sides of the inelastic spectra of PS-187 (**a**) and PS-297 (**b**) "dry" and wet colloids for exciting wavelength 532 nm ($q_{max}R = 3.51$ and 5.58 respectively). Red bars are the theoretically predicted SPH modes made by the FSM calculations. The heights of the bars do not correspond to intensities of the modes. According to the FSM calculations the real size of PS-297 is about 319 nm. 162

List of Tables

1.1 Important elastic parameters for materials of interest in the present work. . 10

1.2 Nature of the displacement $\vec{u}$ involved in SPH and TOR modes. 15

1.3 The values of the parameter S from equation (1.30), calculated for different substances for Free Sphere/Embedded Sphere (see section 1.4) models. The embedding medium is a so-called St.Just glass (see Chapter 3) which was used in the case of Cu NPs samples. 16

2.1 Main characteristics of the Tandem FP built by J.R. Sandercock, together with those of the exciting sources used at the LPCML. 56

2.2 Some important characteristics of Z40 60

3.1 Composition of the St.Louis glass. 63

3.2 Several important characteristics of the St.Louis glass. 63

3.3 Comparison of experimental (Exp) and calculated (Calc) harmonic frequency positions and harmonic-to-fundamental frequency ratios for the quadrupolar mode of a $Ag_{0.66}Au_{0.34}$ nanoparticle with 20.5 nm diameter in the embedded (Emb) case (CFM) and 17.2 nm diameter in the case of a *free* sphere. The bold values emphasize the correspondance between experimental and calculated values. 68

3.4 Comparison of the vibrational frequencies of 5.3 nm Au NCs measured by LFRS with those calculated by using the RUS approach for objects with different elastic properties and shapes. 86

3.5 Composition of the St.Just glass. 91

3.6 Several important elastic parameters of the St.Just glass. 91

3.7 Cu-glass sample description. 92

4.1 Theoretical values of the ratios of the Bragg peak positions for different types of crystal structure [140] and those derived from USAXS experiments of CIV and PS-187 pellets. 141

Introduction

The investigations of the nanoworld have already stopped to be something exotic for either scientific medium or whole society. Hundreds of laboratories and thousands of scientists are working in this area augmenting our knowledge and understanding of it every day. In spite of their efforts there are still a lot of unanswered questions across the many fields of science where the nanoworld has stepped in. One central issue in nanoscience is the physical characterization of nano-objects, either in the aim of addressing fundamental questions like confinement effects (on electronic properties for instance) or in order to reveal new properties that may be harnessed in technological applications. Over the past two decades, vibration modes of nanosystems have emerged as valuable and readily seizable informations, which in a first stage were essentially used to understand rather fundamental aspects of vibrational confinement. Progressively, the study of vibrational dynamics in confining systems has become an original means of characterization that thanks to significant parallel theoretical developments now enables to cover essential features of nanoparticle and nanoparticle assemblies like size, shape, interaction with an embedding medium, crystallinity, etc.

This thesis is dedicated to the investigations of the vibrational dynamics from two different types of nanoparticles (NP), that differ from each other in terms of nature and size: "small" solid NPs and "large" biological NPs[1]. Although the parallel study of these two types of nanoobjects may appear at first glance rather strange, it meets the scientific aims described above: while the study of small solid NPs essentially aims at better understanding the physics of NP vibrations, the investigation of biological NPs is performed in order to explore the relevance of confined vibrational dynamics in such systems. For both types of objects, the main tool we used for our experimental investigations is inelastic light scattering, as it has established as very efficient in the detection of NP vibration

[1] As developed later, the terms "small" and "large" are defined with respect to visible light wavelengths, i.e. several hundreds of nanometers

modes [1, 2]. The solid NPs of interest were chosen as *metallic*; the main reason for it is that within an inelastic light scattering study, the interplay between electronic and vibrational properties leads to a strong enhancement of the scattering efficiency; this is most appreciated when working with *minute* quantities of particles of *nanometric* dimensions. Furthermore, the metallic NPs we have studied were specifically termed as "nano*crystal*s" since a significant part of our works deal with the effect of nano-crystallinity on NP vibration modes. As for biological NPs, our choice has set on *viruses*, as we justify it in more details below.

Known from the very ancient times (Roman empire), metal NPs, like Au, Ag and Cu (but also semiconductor NPs like CdS) are used as common colorants for commercial glasses. This extensive use, initiated in arts, roots in unique electronic properties that essentially derive from the smallness of the NPs with respect to visible light wavelengths. Today, the use of optical properties from metal NPs goes much beyond artitistic considerations; it spans applications ranging from biology, biotechnology, telecommunication, electronics, optics, etc. As mentioned above, the exceptional electronic properties of metal NPs considerably eases the experimental detection of their vibrational modes, at least when using inelastic light scattering; it may also make the interpretation of the related data more specific, as opposed to non-metallic nanostructures. Based on the study of metal NP vibrations (but definitely not only) a lot has been learned on how acoustic vibration modes redistribute as the size of a solid is reduced from bulk to nanometric dimensions. The experimental detection and the theoretical description of so-called Lamb modes (named after the mathematician H. Lamb [4] who first processed the mathematical description of sphere eigenmodes) from NPs having the forms of spheres, or quasi-spheres, are now well established. Thanks to increasing theoretical efforts, the understanding of NP eigenmodes has quickly evolved beyond the simple case of free nanospheres: eigenmodes from ellipsoidally distorted shapes and/or embedded nanospheres are now well documented. A few years ago [5], the use of higher resolution spectroscopic instruments allowed to resolve detailed features in the low frequency Raman spectra from Au NPs, that had probably been unseen previously. The early analysis of these features pointed out an effect due to the inner crystalline structure of the NPs ("elastic anisotropy"), thereby opening up the possibility of probing the crystalline quality of NPs through the detection of their eigenmodes. In the present works, we will see how the elastic anisotropy effect adds to the value of low frequency Raman characterization, illustrating it as a central point in the study of non-embedded Au nanocrystals and more secondarily through the

studies of embedded bimetallic AuAg and Cu NPs. While the investigation of bimetallic NPs has enabled the first identification of high order overtones from NP modes in the low frequency Raman spectra, making it possible to test calculations predicting Raman *intensities*, the study of Cu NPs essentially uses the Raman probe as a tool to characterize the several types of NPs which can be produced through different annealing conditions of an initially Cu-atom doped transparent glass.

Based on the well advanced comprehension of low frequency modes from solid NPs, several papers emerged in the past 5-10 years, stating the possible existence of similar modes in biological globular structures. Viruses emerged as the best candidates to test the existence of NP modes in spherical shaped biological nanostructures. Indeed, viruses are compact nano-objects, with well defined and highly monodisperse morphologies and a vast part of them are of quasi-spherical shape (like icosahedral shape). Besides, recent experimental characterizations of their elastic properties have revealed stiffnesses close to polymeric matter [6], which definitely makes the existence of NP modes in viruses a reasonable expectation. Numerous theoretical studies have already conjectured about virus eigenmodes [7, 8, 9, 10, 11]. As an illustration, Figure 1 reports recent numerical results pertaining to low frequency modes from virus-like protein assemblies. The displayed modes definitely compare with the Lamb-modes mentioned earlier in the case of solid nanospheres. A lot of justifications given for these types of studies rely on the possible role played by the NP collective dynamics in large conformational changes (like swelling) that a viral particle undergoes throughout its life cycle; detecting virus eigenmodes might therefore open the way to control key processes in their biological activity. Actually, these ideas were first developed by Nobel prize, P. G. de Gennes and co-author M. Papoular [12], who performed the first theoretical investigation on low frequency modes in nanometric biological structures back in 1969. Today, the relevance of possible eigenmodes in viral particles extends beyond biological considerations; indeed thanks to their high monodispersity, robustness and self assembling properties, viruses (or at least viral capsids) are conceived as unique tools in technological fields such as nanocaspules for drug delivery or nano-ordered templates [13, 14, 15, 16]. With respect to these latter applications, characterizing eigenmodes of viruses or virus like particles would definitely provide valuable information on their elasticity and on their behaviour in non necessarily biological environments.

Bearing in mind the above considerations, attempts to experimentally detect eigenmodes from viruses, through inelastic light scattering, were undertaken at the LPCML

several years ago. Such difficult task is also achieved by other teams [3, 17]. While the somewhat limited success reached in a previous study [5] mainly focused on small plant viruses ($D \leq 30$ nm), test studies performed with a larger virus ($D \sim 200$ nm) appeared as a potentially interesting continuation, that we achieved in the present thesis.

The present manuscript is divided into four chapters. In the first one, the basic concepts of the theory of elasticity and the derivation of vibrational eigenmodes in the case of spherical bodies is given. Mode nomenclatures as well as the influence of a surrounding medium and of elastic anisotropy on vibrational eigenmodes are described therein. The second chapter is dedicated to our main investigation technique, i.e. inelastic light scattering. In this chapter, the mechanisms of light scattering by vibrations are described, as well as the associated technology we used to perform our experiments. As "particular vibrations" (as opposed to molecular vibrations), the selection rules associated with the scattering from NP modes are discussed,comparing both cases of small ($D << \lambda$) and large ($D \approx \lambda$) spheres. Chapter three reports our several investigations of NP modes in small metallic NPs, as mentioned earlier. This chapter provides a good opportunity to get to know the ins and outs of this type of research, learning how existing theoretical tools allow to describe the main features of low frequency Raman data, including subtle effects like elastic anisotropy or the presence of an embedding medium. A rather complete study on the growth of Cu NPs in a glass illustrates the set of informations that the sole Raman probe is able to provide. Finally, the last chapter is dedicated to the studies of viruses. After a brief description of the viruses of interest, comparative studies based on small angle x-ray scattering and atomic force microscopy are made in order to verify the comparable physical behaviours of viruses and polymeric colloid samples that will serve as reference samples. Then the very low frequency light scattering data of both systems are compared, particularly considering the effect of surrounding water. It will be shown how the experimental detection of virus eigenmodes in aqueous environments remains difficult to process.

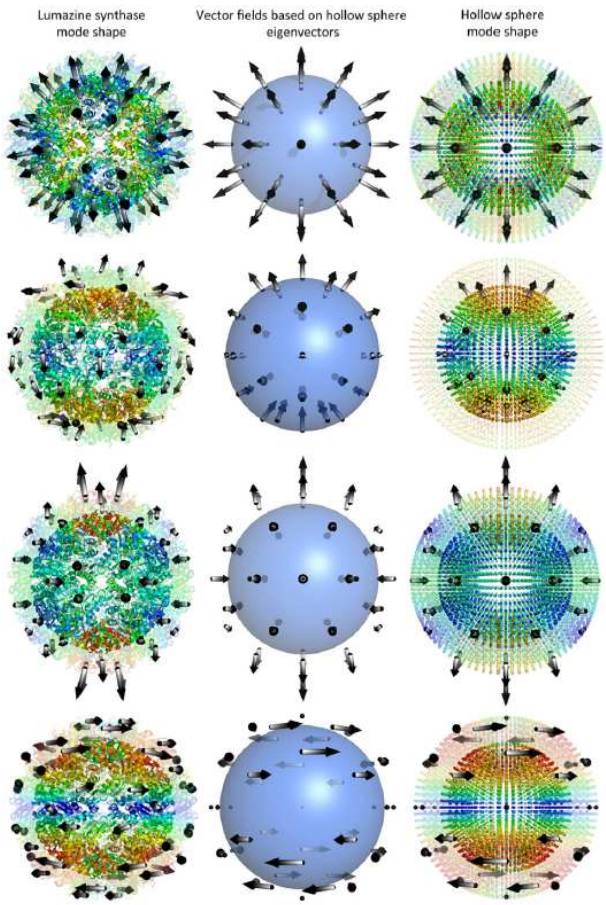

Figure 1: The diagrams on the left display the model of the modes illustrated for lumazine synthase (a protein enzyme which is capable to create an icosahedral assemblies). The arrows indicate the directions of collective motions on/above the surface. The middle and right columns display the equivalent mode shapes generated by the theory for a hollow sphere with comparable dimensions and packing density. The diagrams on the right column are also colored by the mobilities of the nodes [10].

Chapter 1

Vibrational dynamics of nano-spherical objects

This chapter has a goal to present shortly a theoretical basis of the vibrations of spherical objects. Vibrations are mechanical oscillations about an equilibrium point. These oscillations are the superposition of displacements of each atom of a solid body and have a strong connection with elastic properties of the substance. That is why the first part of this chapter will give a small review of the basic knowledge of elastic theory. The next parts are dedicated to eigenmodes of spherical bodies in a given environment. It will be shown that coupling with a medium can change the parameters of the eigenvibrations. In the last part we will consider the influence of the inner structure of NPs on their vibrations.

1.1 Basics of the theory of elasticity

The elastic theory of continuous homogeneous media is very developed in most textbooks dedicated to solid state physics and it is possible to find a lot of information about it. In our short review we were guided by [18, 19] to describe the basic items of this theory.

The classical theory of elasticity does not take into account at the first order the microscopic atomic structure of an object and assumes it as a continuum medium where any point is described by the radius vector $\vec{r}$ with coordinates (x_1, x_2, x_3) in a Cartesian coordinate system. After infinitesimal deformation this point will change its coordinates

to $\vec{r}'$ with coordinates (x_1', x_2', x_3'). The vector of deformation $\vec{u}(\vec{r})$ will be expressed by:

$$\vec{u}(\vec{r}) = \vec{r}' - \vec{r} \tag{1.1}$$

If one considers the magnitudes of these radius-vectors described above they will be: $dr = \sqrt{(dx_1)^2 + (dx_2)^2 + (dx_3)^2}$ and $dr' = \sqrt{(dx_1')^2 + (dx_2')^2 + (dx_3')^2}$. One of the most fundamental assumptions of this theory is the smallness of deformation. It means that the contribution of the energy density of the body at point $\vec{r}$ depends only on the value $\vec{u}(\vec{r})$ and thereby on the first derivative of $\vec{u}(\vec{r})$, whereas the second derivative equals zero. Writing that $du_i = \frac{\partial u_i}{\partial x_j} dx_j$ and remembering that $du_i = dx_i' - dx_i$ one can show that

$$(dr')^2 \approx (dr)^2 + 2\left(\frac{\partial u_i}{\partial x_j} + \frac{\partial u_j}{\partial x_i}\right) dx_i dx_j, \tag{1.2}$$

where the value $e_{ij} = \frac{1}{2}\left(\frac{\partial u_i}{\partial x_j} + \frac{\partial u_j}{\partial x_i}\right)$ is named the *deformation tensor*.

According to the Hooke's law of elasticity the force acted on an unit surface is named the tensile stress. In the general three-dimensional case for infinitesimal deformations, the *tensile stress* and the deformation are tensors of the second order (it means they have 9 components each) and the expression of this law is the following:

$$\sigma_{ij} = C_{ijnk} \frac{\partial u_n}{\partial x_k}, \tag{1.3}$$

where C_{ijnk} is the forth order tensor of elastic constants which has 81 components, but it is possible to show that the C_{ijnk} are symmetrical relatively to the order of indexes so that only 21 components are independent. If one considers an isotropic medium made of a cubic crystal (we deal with this type of lattice in this work) the numbers of independent coefficients decreases to two and the Hooke's law will be expressed as:

$$\sigma_{ij} = \lambda \delta_{ij} \sum_n e_{nn} + 2\mu e_{ij}, \tag{1.4}$$

where λ is the first coefficient of Lamé and μ is a shear modulus (it also called the second Lamé coefficient). These coefficients are specific to a material and are connected to the Young's modulus and the Poisson's coefficient of the material [21].

As we have mentioned before, stress is a force divided by surface. If one wants to come to volume it is necessary to use the theorem of Gauss-Ostrogradsky which connects the flow of the vector field through the surface and divergence of this field inside the volume.

Thus, we can reformulate a definition of stress saying that a divergence of stress is force acted on a unit volume and we can write that

$$\rho \ddot{u}_i = \frac{\partial \sigma_{ij}}{\partial x_j}. \tag{1.5}$$

This equation is a standard form of the equation of motion in an elastic medium with constant density. In the case of isotropic three-dimensional medium where the Hooke's law is applicable one obtains the equation of Navier:

$$\rho \ddot{\vec{u}} = (\lambda + 2\mu) \cdot \vec{\nabla} \cdot (\vec{\nabla} \cdot \vec{u}) - \mu \cdot \vec{\nabla} \times (\vec{\nabla} \times \vec{u}). \tag{1.6}$$

We can rewrite this expression in the following form:

$$\ddot{\vec{u}} = v_L^2 \cdot \vec{\nabla} \cdot (\vec{\nabla} \cdot \vec{u}) - v_T^2 \cdot \vec{\nabla} \times (\vec{\nabla} \times \vec{u}), \tag{1.7}$$

where v_L and v_T are related to the Lamé coefficients and to the density of the medium. These two coefficients have the following expressions:

$$v_L = \sqrt{\frac{\lambda + 2\mu}{\rho}}, \tag{1.8}$$

$$v_T = \sqrt{\frac{\mu}{\rho}}. \tag{1.9}$$

These parameters have dimensions of speed [m/s] and from the physical point of view they are respectively the longitudinal and transverse speeds of sound inside the medium. As these values are important parameters in our works Table 1.1 lists values of v_L and v_T for several materials[1] we will be dealing with in this work.

The equation (1.7) has a periodic solution of the following form:

$$\vec{u}(\vec{r}, t) = \vec{u}(\vec{r}) e^{-i\omega t}, \tag{1.10}$$

and we can rewrite the Navier equation as

$$-\omega^2 \vec{u} = v_L^2 \cdot \vec{\nabla} \cdot (\vec{\nabla} \cdot \vec{u}) - v_T^2 \cdot \vec{\nabla} \times (\vec{\nabla} \times \vec{u}). \tag{1.11}$$

[1] Data for Cu_2O were taken from reference [20].

Table 1.1: Important elastic parameters for materials of interest in the present work.

Material	$\lambda + 2\mu = C_{11}$, $N/m^2 \cdot 10^{11}$	$\mu = C_{44}$, $N/m^2 \cdot 10^{11}$	ρ,kg/m^3	v_L,m/s	v_T,m/s
Cu	1.684	0.754	9018	4799	2381
Ag	1.240	0.937	10530	3747	1740
Au	1.923	0.420	19280	3319	1236
Cu_2O	1.229	0.129	6070	4499	1363
Polystyrene	0.059	0.016	1060	2350	1210

1.2 Free sphere model

The mathematical resolution of the Navier equation for a three-dimensional body with non-specific shape is almost impossible. Further we will consider laws of vibrations of **free spheres**. We have chosen this model due to the fact that through experimental results NP modes detected by Raman investigations were interpreted with vibrations of spheres and all NPs we will consider are well approximated by spheres (unless the systems are known to differ from spheres). We will first briefly consider the oversimplified case of the longitudinal vibrations of a one dimension chain of atoms that will help us to capture a key aspect of the vibrations of finite size objects.

Let us consider a chain of atoms with length L. It means that the equation of Navier takes the form

$$-\omega^2 u = v_L^2 \frac{d^2u}{dx^2}. \tag{1.12}$$

This is a linear differential homogeneous equation of the second order with characteristic numbers $\lambda_{1,2} = \pm i\omega/v_L$. It means that the general solution can be written as a sum of cosine and sine functions with arguments $\frac{\omega}{v_L}x$. If we consider a case of a chain fixed on its ends, that means $u(0) = u(L) = 0$, then we can write

$$u_n(x) = Bsin\frac{\omega_n}{v_L}x, \tag{1.13}$$

$$\omega_n = n\frac{\pi v_L}{L}, \tag{1.14}$$

where B is an arbitrary constant. Thus, the fundamental frequency of the atom chain is

$$\nu = \frac{v_L}{2L}. \tag{1.15}$$

This simple example illustrates an important result: the fundamental vibration frequency of a finite size system is inversely proportional to its size. This peculiarity gives us an opportunity (and we will use it further) to estimate the size of investigated objects from the experimental evaluation of the vibration frequencies.

Two- and three-dimension models are more complicated to treat and demand a full-fledged mathematic analysis. An object with random shape in the 3D space is extremely complicated and to calculate its modes is almost impossible, but this task becomes rather simpler if we consider objects with high symmetry such as a cylinder or a sphere. Horace Lamb was the first one who solved this problem for the case of homogeneous elastic spheres in 1882 [4]. Thanks to the solution of the Navier equation it is possible to calculate the vibrational modes of a large range of objects of spherical shape. Indeed, the Lamb theory has been shown to apply equally well to the vibrations of planets ($\sim$ mHz) as well as the vibrations of NPs ($\sim$ GHz).

In the following, the main ingredients involved in the mathematical calculations of the eigenmodes of sphere vibrations are given. The only parameters needed to describe this model are the radius of the solid sphere, its density and the speeds of sound of the material the sphere is made of (longitudinal and transverse).

In spherical symmetry it was shown [22] that the solution of the Navier equation can be expressed as

$$\vec{u} = \vec{\nabla}\phi + \vec{\nabla} \times (\psi\vec{r}) + \vec{\nabla} \times \vec{\nabla} \times (\varsigma\vec{r}), \tag{1.16}$$

where ϕ , ψ and ς are the Helmholtz's potentials. This equation has sense only if these potentials are solutions of the following wave equations:

$$\begin{aligned} \ddot{\phi} &= v_L^2 \vec{\nabla}^2 \phi \\ \ddot{\psi} &= v_T^2 \vec{\nabla}^2 \psi \\ \ddot{\varsigma} &= v_T^2 \vec{\nabla}^2 \varsigma \end{aligned} \tag{1.17}$$

The solution of these equations is expressed by Bessel spherical functions j_ℓ and spherical functions Y_ℓ^m:

$$\begin{aligned} \phi(\vec{r},t) &= A j_\ell(qr) Y_\ell^m(\theta,\varphi) e^{-i\omega t} \\ \psi(\vec{r},t) &= B j_\ell(Qr) Y_\ell^m(\theta,\varphi) e^{-i\omega t} \\ \varsigma(\vec{r},t) &= C j_\ell(Qr) Y_\ell^m(\theta,\varphi) e^{-i\omega t} \end{aligned} \tag{1.18}$$

where A, B and C are arbitrary constants, and ℓ and m are the angular moment and projection of the angular moment on the z-axis respectively. These numbers are integers and satisfy the condition: $\ell \geq 0$ and $\mid m \mid \leq \ell$. Arguments q and Q are respectively the

longitudinal and transverse wave vectors:

$$\begin{aligned} q &= \frac{\omega}{v_L} \\ Q &= \frac{\omega}{v_T} \end{aligned} \tag{1.19}$$

Now we pass to another spherical coordinates to simplify the mathematical expression of the displacement vector $\vec{u}$. The following new basis $(\vec{e_1}, \vec{e_2}, \vec{e_3})$ is defined in replacement of the $(\vec{e_r}, \vec{e_\theta}, \vec{e_\varphi})$ one:

$$\begin{cases} \vec{e}_1 = Y_\ell^m(\theta,\varphi)\vec{e}_r \\ \\ \vec{e}_2 = \frac{\partial Y_\ell^m(\theta,\varphi)}{\partial\theta}\vec{e}_\theta + \frac{1}{sin\theta}\frac{\partial Y_\ell^m(\theta,\varphi)}{\partial\varphi}\vec{e}_\varphi \\ \\ \vec{e}_3 = \frac{1}{sin\theta}\frac{\partial Y_\ell^m(\theta,\varphi)}{\partial\varphi}\vec{e}_\theta - \frac{\partial Y_\ell^m(\theta,\varphi)}{\partial\theta}\vec{e}_\varphi \end{cases} \tag{1.20}$$

Thus, going back to the vector of deformation and using equations (1.11) and (1.16) it is possible to prove that components of the deformation in the new basis are:

$$\begin{cases} u_1 = \frac{1}{r}(A(\ell j_\ell(qr) - qrj_{\ell+1}(qr)) + C(\ell(\ell+1)j_\ell(Qr)))e^{-i\omega t} \\ u_2 = \frac{1}{r}(Aj_\ell(qr) + C((\ell+1)j_\ell(Qr) - Qrj_{\ell+1}(Qr)))e^{-i\omega t} \\ u_3 = Bj_\ell(Qr)e^{-i\omega t} \end{cases} \tag{1.21}$$

The constants A, B and C are the same as of equation (1.18), but in this case their values are fixed for every couple of numbers (ℓ, m).

Knowing the vector of deformation and using the Hooke's law (Eq.(1.4)) we can calculate the components of the tensile stress tensor σ_{ij}. But to calculate further the fundamental eigenmodes we need only components $(\sigma_{1r}, \sigma_{2r}, \sigma_{3r})$ which correspond to the force acting on an unit surface along the direction $(\vec{e_1}, \vec{e_2}, \vec{e_3})$. It is found from [22] that

$$\begin{cases} \sigma_{1r} = \frac{2\mu}{r^2}(A((\ell^2 - \ell - \frac{Q^2r^2}{2})j_\ell(qr) + 2qrj_{\ell+1}(qr)) + \\ +C\ell(\ell+1)((\ell-1)j_\ell(Qr) - Qrj_{\ell+1}(Qr)))e^{-i\omega t} \\ \\ \sigma_{2r} = \frac{2\mu}{r^2}(A((\ell-1)j_\ell(qr) - qrj_{\ell+1}(qr) + \\ +C((\ell^2 - \ell - \frac{Q^2r^2}{2})j_\ell(Qr) + Qrj_{\ell+1}(Qr)))e^{-i\omega t} \\ \\ \sigma_{3r} = B\frac{\mu}{r}((\ell-1)j_\ell(Qr) - Qrj_{\ell+1}(Qr))e^{-i\omega t} \end{cases} \tag{1.22}$$

Now let us discuss the vibrational mode of a sphere considered as "free". This model is an ideal one: the ideal sphere does not have any mechanical contact with its environment. In practice this model can be used when the NP is embedded in a matrix which has a

negligibly small influence on the particle. It means that no force acts on the surface of the particle. This condition according to the Hooke's law can be written as

$$\vec{F} = \vec{\sigma} \cdot \vec{r} = 0 \tag{1.23}$$

It means that the components of the tensile stress tensor given in (1.22) at the surface $r = R$ have to be zero:

$$\sigma_{1r} = \sigma_{2r} = \sigma_{3r} = 0 \tag{1.24}$$

Thus we obtain a system of three linear equations and its non-nil solution exists only when its determinant equals zero. Using equations (1.19) and (1.22) we can derive the eigenfrequencies from solutions for qR and QR. It is possible to show [23] that for the case $\ell = 0$ it can be obtained as the roots of following equations:

$$\frac{tg(qR)}{qR} = \frac{1}{1 - \frac{1}{4}(\frac{v_L^2}{v_T^2})(qR)^2} \tag{1.25}$$

If we consider cases with $\ell > 0$ the frequencies of the vibrational modes of the free sphere will be given by the roots of two equations:

$$\begin{aligned} &\tfrac{(qR)^2}{2}(2\ell^2 - \ell - 1 - \tfrac{(QR)^2}{2})j_\ell(QR) + (\ell^3 + 2\ell^2 - \ell - 2 - (QR)^2)qR\times \\ &\times j_{\ell+1}(qR)j_\ell(QR) + (\ell^3 + \ell^2 - 2\ell - \tfrac{(QR)^2}{2})+ \\ &+(2 - \ell^2 - \ell)qRQRj_{\ell+1}(qR)j_{\ell+1}(QR) = 0 \end{aligned} \tag{1.26}$$

and

$$(\ell - 1)j_\ell(QR) - QRj_{\ell+1}(QR) = 0 \tag{1.27}$$

These three equations (1.25), (1.26) and (1.27) lead to different categories of modes. We describe them it the next section.

1.3 Vibration modes of free spheres

1.3.1 Nomenclature of the eigenmodes

Vibrations of the solid spherical body are divided into two groups: *spheroidal* (SPH) and *torsional* (TOR). Spheroidal modes are characterized by a change of volume of the sphere along the vibrations; it means that these vibrations lead to a change of the radius (Fig.1.1). The torsional modes are vibrations that do not induce a change neither of

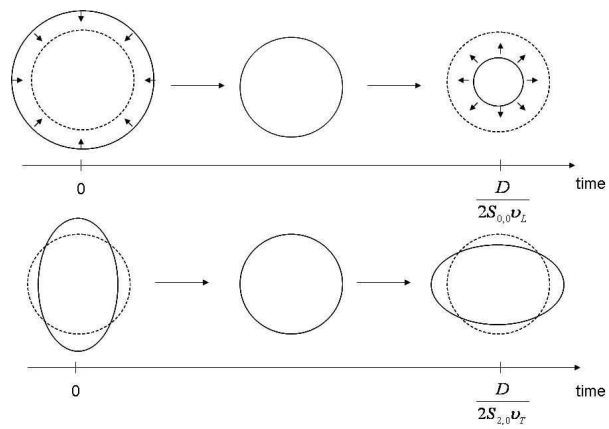

Figure 1.1: Fundamental spheroidal vibrational modes of a spherical object. **Up:** a spherical (breathing) mode $\ell = 0$; **down:** a quadrupolar mode $\ell = 2$.

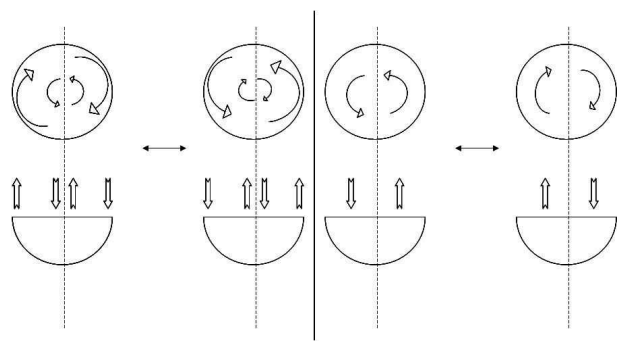

Figure 1.2: Fundamental torsional vibrational modes of a spherical object: **left:** a mode $\ell = 1$; **right:** a mode $\ell = 2$.

the volume nor of the shape. Thus they are characterized by a zero radial displacement, $u_r = 0$ (Fig.1.2).

SPH modes are described by the equations (1.25), (1.26) where the first one expresses the vibrations for $\ell = 0$ and describes the first SPH mode. This mode is named *radial* or *spherical*, in this case $\vec{rot}\vec{u} = 0$. As far as $\vec{u}(\vec{r}, \theta, \varphi, t) = \vec{u}(\vec{r}, t)$, the vector of deformation in equation (1.16) depends only on ϕ:

$$\vec{u}(\vec{r}, t) \propto \vec{\nabla}\phi(\vec{r}, t) \propto \vec{\nabla}(j_0(qr)Y_0^0(\theta, \varphi)e^{-i\omega t}). \tag{1.28}$$

Knowing that $Y_0^0(\theta, \varphi) = \frac{1}{2}\sqrt{\frac{1}{\pi}}$ and $j_1 = -j_0'$ we can rewrite this expression as:

$$\vec{u}(\vec{r}, t) \propto j_1(qr)e^{-i\omega t}\vec{e_r}. \tag{1.29}$$

This equation describes a breathing process of the sphere that is why the spherical mode

is also called the *breathing* mode. As far as the deformation in this mode has zero curl it is purely longitudinal (see Table 1.2).

Equation (1.26) gives the frequencies of the spheroidal modes which involve both torsional and radial motions. In this case the constant C in equation (1.18) equals zero and the vector of deformation depends on only two Helmholtz's potentials: $\vec{u} = \vec{u}(\phi, \psi)$. The detailed mathematical description of this mode can be found for example in ref. [22].

The roots of equation (1.27) give the pure TOR modes. The deformation in this case is a function of only one Helmholtz's potential, so, $\vec{u} = \vec{u}(\varsigma)$. This mode is purely transverse. It is also worth to note that a TOR mode with angular momentum $\ell = 0$ does not exist.

Table 1.2: Nature of the displacement $\vec{u}$ involved in SPH and TOR modes.

Type	SPH	TOR
$\ell = 0$	$\vec{rot}\vec{u} = 0$ $div\vec{u} \neq 0$	Does not exist
$\ell \neq 0$	$\vec{rot}\vec{u} \neq 0$ $div\vec{u} \neq 0$	$\vec{rot}\vec{u} \neq 0$ $div\vec{u} = 0$

Both types of modes, SPH and TOR, are labeled by the integer number ℓ and a natural number n. The number n marks the different modes with the same value of angular momentum. The frequency with $n = 1$ is named "fundamental" mode. Higher values of n are named harmonics (or overtones).

1.3.2 Eigenfrequencies

As we showed before the eigenfrequencies of a sphere are derived from the solutions of equations (1.25), (1.26) and (1.27) for qR and QR, i.e. the frequencies of fundamental vibrations are inversely proportional to the size of the sphere as we have recalled it in the case of 1D vibrating string. This assertion is correct even for non-spherical objects. For a homogeneous sphere the frequencies of the eigenmodes are expressed as

$$\nu_{\ell,n} = S_{\ell,n} \frac{v_{L,T}}{D}. \tag{1.30}$$

In this equation frequency is given in hertz[2], D the diameter of the particle, v is the speed of sound of the substance the particle is made of. Depending on the type of mode, equation (1.30) is preferentially expressed either as a function of v_L or as a function of v_T, bearing in mind that the exact expression of the frequency depends on both (see Eq.(1.25) – (1.27)). Saviot and Murray [24] showed that some spheroidal modes (at least fundamental ones) feature a primarily longitudinal or primarily transverse character. As a matter of fact, the fundamental *radial mode* ($n = 1; \ell = 0$) is primarily *longitudinal* while the fundamental ($n = 1; \ell = 2$) quadrupolar mode is primarily *transverse*. These aspects are important for polarization selection rules in Raman scattering, as will be seen further (section 2.2.1). The coefficient S is calculated using the solution of the previous equations. It has different values for different modes. Table 1.3 lists typical values of the S coefficient for the essential two modes ($\ell = 0$ and $\ell = 2$) which the low frequency Raman scattering technique allows to detect in the case of small ($D \ll \lambda$) particles. For $\ell = 0$ modes, v for equation (1.30) was chosen as v_L and the S coefficients are given accordingly while for the $\ell = 2$ mode v was chosen as v_T. As reported in this Table, the values of S change when the sphere is no more considered as *free*, as will be mostly considered with the samples investigated in our works. We now briefly describe the situation of embedded particles.

Table 1.3: The values of the parameter S from equation (1.30), calculated for different substances for Free Sphere/Embedded Sphere (see section 1.4) models. The embedding medium is a so-called St.Just glass (see Chapter 3) which was used in the case of Cu NPs samples.

Harmonic	Mode	Cu	Ag	Au
n=1	$\ell = 0$	0.88/0.91	0.89/0.95	0.94/0.97
	$\ell = 2$	0.84/0.95	0.84/1.03	0.85/1.07
n=2	$\ell = 0$	1.95/1.96	1.96/1.97	1.97/1.98
	$\ell = 2$	1.63/1.82	1.65/1.91	1.69/1.94
n=3	$\ell = 0$	2.97/2.97	2.97/2.98	2.98/2.99
	$\ell = 2$	2.75/2.83	2.77/2.9	2.8/2.94

[2]In Low-Frequency Raman Scattering, frequency can be expressed either in Hz (or more precise — in GHz because the typical size of the studied subjects is $\sim nm$) or cm^{-1}; 1 cm^{-1} = 30 GHz.

1.4 Sphere embedded in a matrix

The model of the free sphere shown above is a simplified model and experiments showed that this simple description is quite useful in a first approximation even if the spheres are not really free, but rather embedded in matrix. It is the case if the acoustic impedance of the matrix $Z_m = \rho_m v_m$ is much less than that of the NPs [25]. On general basis the actual coupling between NP and matrix and the actual ratio of their acoustic impedances do not allow to use the free sphere model. The opposite case of the free sphere model (FSM) is the model of a **blocked** sphere (BSM). In this model a sphere embedded in a homogeneous isotropic infinite matrix is totally blocked by it, so that no deformation on the surface of the sphere is possible:

$$\vec{u} = 0; r = R; \forall(\theta, \varphi). \tag{1.31}$$

In this case it is possible to show that for the case $\ell = 0$ the eigenfrequency can be derived by solving the following equation:

$$tg(qR) = qR. \tag{1.32}$$

The roots of this transcendental equation are well known: $qR = 4.49; 7.73; 10.9\ldots$

For the case $\ell > 0$ the frequencies of vibrational modes can be obtained from the roots of the following equation:

$$qRj'_\ell(qR)(QRj'_\ell(QR) + j_\ell(QR)) = \ell(\ell+1)j_\ell(qR)j_\ell(QR). \tag{1.33}$$

More often in practice one faces an intermediate situation: the NP is neither fully free nor completely blocked. In that case part of the vibrational energy of the NP can flow to the matrix. It means that it is necessary to use another model which takes into account the mechanical properties of the matrix and which would give a more adequate estimation of modes' frequencies of the NPs. There are several models which are able to account for the coupling between a matrix and the NP (see, for example, reference [25]). One of such models is the *complex-frequency model* (CFM) [26, 27] that we used in our work to estimate the influence of the presence of matrix. In this model the NP is surrounded by a homogeneous and isotropic matrix with known density and speeds of sounds (longitudinal and transverse). This model does not aim at describing very precisely the matrix-particle interconnection, but it replaces the mode of the NP with pseudomodes for a matrix-embedded NP [28]. The vector of deformation $\vec{u}$ becomes an outgoing traveling wave. It

implies matrix-particle interconnections that lead to a damping of the vibrations of the particle. In this model the mode frequencies are complex values, where $\omega_n = Re(\omega_n^{CFM})$ and the imaginary part accounts for a frequency linewidth[3] $\Delta\nu$ [29], which is zero for a *free* sphere. For an embedded sphere this value is inversely proportional to the lifetime of the pseudomode. For example, if a matrix and the embedded NPs have a weak acoustic impedance mismatch (their ratio is not far from 1) the reflection of the acoustic wave at the matrix-particle interface is very weak. This leads to the fact that the acoustic wave (so does vibrational energy) delocalizes out the NP and the lifetime τ of the pseudomode is very small, i.e. the damping $\Delta\nu$ is large. For a large acoustic impedance mismatch the lifetime of the vibration increases, thus the damping decreases. The case when $Z_p \ll Z_m$ streams to BSM, while the $Z_p \gg Z_m$ case can be described by FSM.

The CFM was developed in paper [27]. In our works, we used the CFM model to interpret our data. Such was done through the use of a computer program created by Lucien Saviot from Laboratoire Interdisciplinaire Carnot de Bourgogne (UMR 5209 CNRS, Université de Bourgogne, Dijon). By entering the values of the sound velocities and of the densities of both the NPs and the matrix, the program allows to evaluate the eigenfrequencies or the S coefficients of either SPH or TOR modes for a given NP size.

1.5 Degeneracy of the modes

During previous reasoning we considered NPs with spherical shapes. However in real experiments this situation is just an ideal case as synthesized NPs hardly ever adopt a purely spherical shape, depending on the synthesis method. Although very useful to describe first order effects, the spherical assumption for real NPs may, on some occasions, not be sufficient to account for more subtle effects. Among these effects, a recent development of low frequency Raman scattering has focused on the inner crystalline nature of the NPs. We now see how the breakdown of spherical symmetry at the atomic scale modifies the vibrational pattern, as exposed in paper [28, 30].

Let us consider for instance a NP of Cu, as we will be dealing with in the following chapter. Copper has a face cubic centered crystalline structure with different elastic constants along different crystallographic directions; this is called "elastic anisotropy". This anisotropy is associated with different speeds of sound along each direction. From the expression of the eigenfrequency of an isotropic sphere vibration (Eq.(1.30)), which

[3]In this work linewidth is associated with the mathematical term — the width at half maximum.

is proportional to the speed of sound inside the sphere, one can already anticipate that elastic anisotropy will result in different possible values of eigenfrequencies in the case of a sphere made of a crystalline material. Therefore the appearance of the anisotropy in the inner structure of the objects imposes to take into account all components of the elastic tensor C_{ij} instead of only two for isotropic materials (C_{11} and C_{44}). Cubic crystalline structures require to take into account one more elastic constant, i.e. C_{12} such that $C_{44} \neq \frac{C_{11}-C_{12}}{2}$. As a result one can obtain the splitting of a $(2\ell+1)$-fold degenerate mode $(n;\ell)$ into several submodes. This effect can be well explained using group theory. For the O_h point group symmetry the Raman active vibrations have three A_{1g}, E_g and T_{2g} irreducible representations [28]. Saviot and Murray [31] showed that for crystalline NPs with spherical shapes and smaller than the exciting wavelength, the degeneracy lifts according to some important rules. Firstly, the fivefold degenerated quadrupolar vibrational mode $\ell = 2$ splits up into two modes: a twofold degenerated mode E_g and a threefold degenerated mode T_{2g} (Fig.1.3). Secondly, some modes which are not active in the isotropic model become active. For example, mode $\ell = 4$ splits into four modes A_{1g}+E_g+T_{1g}+T_{2g}.

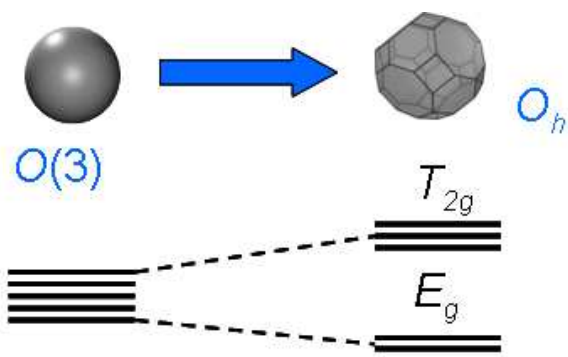

Figure 1.3: The scheme of the splitting of the quadrupolar mode occurring when the anisotropy appeases in the inner structure of NPs.

The non-degenerated spherical mode in the case of anisotropy turns out to be the A_{1g} mode whereas the modes E_g and T_{2g} are derived from the quadrupolar mode acting along the different crystallographic directions. The first one is a twice degenerated, so it has two components: **a:** displacement along the [100] and [001] directions and antiphased displacement along the [010] direction; **b:** antiphased vibrations along the [001] and [100]

directions and no motion along [010] direction. The T_{2g} mode is a three times degenerated and its three components differ only with special relations: stretching along the [011] and no motion along [100], and the vibrations of [101] and [110] directions with changing of other two directions accordingly. It means that these two modes correspond to transverse acoustic waves propagating in the [100] and [110], respectively. The computation of these modes is given in [30]. Their speeds of sound are expressed by

$$v_{E_g} = \sqrt{\frac{1}{2}\frac{C_{11} - C_{12}}{\rho}} \tag{1.34}$$

$$v_{T_{2g}} = \sqrt{\frac{C_{44}}{\rho}}, \tag{1.35}$$

where ρ is the density of the material of the particle. It means that in the case of crystalline particles we have to use v_{E_g} or $v_{T_{2g}}$ instead of the transverse speed in equation (Eq.(1.30)) to estimate the frequencies of these modes.

Since their experimental discovery [2], the theoretical description of NP modes, and the tools developed to relate them to experiments, have very much improved. From the free sphere model, it is now possible to account for their modification due to embedment or due to their inner crystalline structure. Other aspects not developed in this chapter, such as non-sphericity of NPs (oblate, prolate, cylinders, etc) have also benefited from important theoretical advances [32, 33].

In order to investigate the vibrational modes of spherical nanometric particles we use an original technique: low-frequency inelastic light scattering, which has been recently accepted as a powerful non-destructive tool allowed to detect certain modes. Following chapter is dedicated to inelastic light scattering phenomenon and to devices applying this effect.

Chapter 2

Inelastic light scattering: Raman and Brillouin scattering

There is a large variety of different techniques and methods to investigate the vibrational dynamics of nano-objects. All of them have their own advantages and disadvantages and own outputs. Our works were essentially based on the use of inelastic light scattering (Raman and Brillouin) as it has proved to be one of the most powerful techniques in this field of characterization. Of course, a proper interpretation of our Raman data requires cross-checking with other techniques such as pump-probe, TEM, AFM, etc. Some of these cross-checks will be mentioned along chapters 3 and 4. The present chapter will be devoted to the Raman and Brillouin scattering effects and their applications to the study of the nano-objects we have investigated. The structure of the chapter will be like an inverse pyramid: we will start from the base i.e. we will describe shortly the physical principles of light scattering and then progressively restrict our purpose to specific objects: spherical NPs in the first stage and, in the second stage, small metal NPs and large biological NP (viruses). In the end of the chapter the design of the apparatus we used at the laboratory and their principles of operation will be described.

2.1 Physics of inelastic light scattering

2.1.1 Short historical recall

Inelastic Raman scattering is a process where light is inelastically scattered through its interaction with the vibrations of the constituents of a substance (solid, liquid or gaseous)

causing a frequency shift of the radiation. As opposed to Rayleigh (or elastic) scattering, in the case of inelastic scattering the optical spectrum comprises additional frequencies that were not present in the exciting light spectrum. The number and energy positions of these lines are defined by the molecular structure of the scattering substance.

Several famous physicists had theoretically predicted the possibility of Raman scattering before its experimental discovery. The first one was Adolph Smekal in 1923. Independently of A. Smekal, Sir Chandrasekhara Venkata Raman found accidently some peculiarities in the polarization of light scattered by distilled water in 1921 but at the time he did not conceive what kind of effect he had observed. Within two years he showed that this fact had a strong connection with the presence in the medium of some other radiation with wavelength appreciably different from the one of incident light. Firstly luminescence was the main hypothesis for the origin of this additional radiation but this interpretation did not agree with the fact that purification of the water would not remove the effect. This latter observation led Raman to the idea that this phenomenon was of a new type and in 1923 Raman started a purposeful investigation of this "new light". In 1928 Raman assumed that the effect he observed was an analog of the Compton Effect (the scattering of photons from electrons) through which photon energy can be absorbed partially. Raman carried out the experimental inspection of this hypothesis and finally discovered the discrete spectrum of the scattered radiation. In 1930 Raman was awarded the Nobel Prize "for his work on the scattering of light and for the discovery of the effect named after him"[1].

Nowadays Raman scattering is a very powerful tool to investigate the structure of materials. This technique was developed and expanded to a lot (around 25) of separate methods. The most used ones among them are hyper-Raman scattering, coherent Stokes/anti-Stokes Raman scattering, stimulated Raman gain or loss spectroscopy, second hyper-Raman scattering, etc [34].

2.1.2 Nature of the phenomenon

In practice a Raman experiment is performed as follows: a monochromatic laser beam illuminates a sample which scatters along all directions around it. The observer detects

[1]Simultaneously with Raman the new radiation was also observed by Russian physicists Landsberg and Mandelstam. They had been carrying out their experiments independently of Raman since 1918. Nowadays in the countries of Eastern Europe this effect has the name of Combinational Scattering and Brillouin Scattering is called Mandelstam-Brillouin Scattering.

the intensity of the light scattered at some angle θ which is defined with respect to the axis of incident direction. The output spectrum consists of several components: unshifted and shifted light frequencies with respect to that of the incident radiation. The unshifted component (zero frequency[2]) refers to Rayleigh scattering. Rayleigh or elastic scattering originates from static fluctuations of the refractive index with typical fluctuation sizes of the order of the wavelength of the exciting light. The shifted components of scattered light correspond to Raman and Brillouin inelastic scattering. Brillouin scattering is a result of light modulation by the acoustic mode propagating in the substance, in other words, it originates from correlated dynamical fluctuations of the refractive index. They usually give rise to very low frequency narrow lines. For example, the Brillouin frequency shift for water is of the order of several GHz[3] (around several tenths of cm^{-1}), while glass usually gives Brillouin lines with positions approximately ranging between $15 - 30$ GHz ($0.5 - 1$ cm^{-1}). The Raman modes are a result of the scattering by vibrations and rotations of molecules and their bonds that in a crystal identify as optical modes. The highest detected frequencies can reach about 120 THz (4000 cm^{-1}).

A full typical Raman spectrum includes two sides which are symmetrical relatively the Rayleigh line (ν_0). These sides (Fig.2.1) are named Stokes (ν_S) and anti-Stokes (ν_{AS}). A photon scattered during the Stokes process corresponds to the case when a substance gets the vibrational quantized energy $h\nu$, thus we can write it as:

$$h\nu = h\nu_0 - h\nu_S \tag{2.1}$$

Conversely if during the interaction photon-substance the latter loses vibrational energy $h\nu$ this process is named anti-Stokes.

$$h\nu = h\nu_{AS} - h\nu_0 \tag{2.2}$$

We now consider this situation in more details. Let the three wave vectors $\vec{k}_0$, $\vec{k}_S$ and $\vec{k}_{AS}$ be those of the incident, Stokes and anti-Stokes photons respectively. According to the law of conservation of momentum the wave vector which corresponds to the transferred energy can be written as:

[2]As far as in Raman scattering the most important information is the difference between the scattered frequency and the exciting one, the initial frequency is usually set as zero, and the scattered frequency as $\Delta\nu = \pm\nu_{vib}$.

[3]Liquids have only one Brillouin line because there is no transverse acoustic wave.

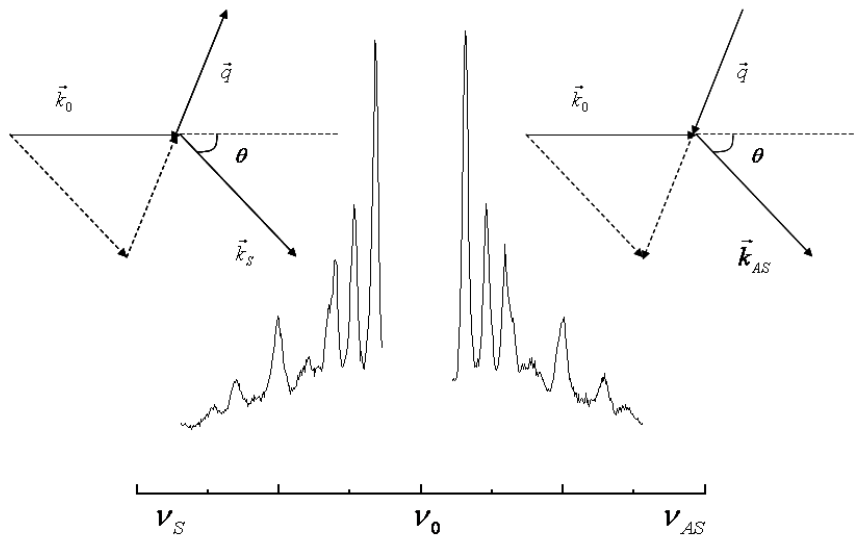

Figure 2.1: An example of a Raman spectrum at low energy. The elastic line (ν_0) is cut. The Stokes side is a Raman response to the vibrational energy transfer from a photon to the substance, the anti-Stokes side corresponds to the transfer of vibrational energy from the substance to the photon.

$$\begin{aligned} \vec{q} &= \vec{k}_0 - \vec{k}_S \\ \vec{q} &= \vec{k}_{AS} - \vec{k}_0, \end{aligned} \tag{2.3}$$

where $\vec{q}$ is the so-called *transferred wave vector*. In Figure 2.1 the process of momentum conservation is represented. For clarity we further proceed only with the Stokes process. We have:

$$q^2 = k_0^2 + k_S^2 - 2k_0 k_S \cos\theta. \tag{2.4}$$

For simplicity it is more convenient to consider the situation where the incident photon and the scattered photon belong to the same medium with a homogeneous refractive index which does not possess birefringence. Knowing that $kc = n\omega$ and $\omega_0 - \omega_S = \Delta\omega$ we can rewrite equation (2.4) as:

$$c^2 q^2 = n^2\omega_0^2 + n^2(\omega_0 - \Delta\omega)^2 - 2n^2\omega_0(\omega_0 - \Delta\omega)\cos\theta. \tag{2.5}$$

Thus, for a Stokes process we can write:

$$\frac{c^2q^2}{n^2\omega_0^2} = \frac{\Delta\omega^2}{\omega_0^2} + 4(1 - \frac{\Delta\omega}{\omega_0})\sin^2\frac{\theta}{2}. \tag{2.6}$$

For an anti-Stokes process the equation (2.6) looks similar except that the minus sign in the brackets of the right part will change to plus. In practice, the difference between Rayleigh and Stokes (anti-Stokes) lines is negligibly small in comparison with the absolute value of the initial frequency[4]. Thus, we can conclude for both processes

$$\frac{cq}{n\omega_0} = 2\sin\frac{\theta}{2} \tag{2.7}$$

and therefore (knowing that $\omega = 2\pi\nu$)

$$q = 2k_0\sin\frac{\theta}{2} = \frac{4\pi n}{\lambda_0}\sin\frac{\theta}{2}. \tag{2.8}$$

The same result can be obtained using another logical way. The changing of energy during the scattering process is so small that we can say that $k_S \approx k_0$. This means that the triangle $\Delta k_0 k_S q$ in the Figure 2.1 is isosceles, thus, the angles of the base $\vec{q}$ equal $\frac{\pi-\theta}{2}$. If we draw an altitude to the base $\vec{q}$ we will see that according to the definition of cosine

$$q = 2k_0\cos\frac{\pi-\theta}{2} = 2k_0\sin\frac{\theta}{2}. \tag{2.9}$$

It is worth noticing that if $\vec{q}$ is streaming towards zero then θ and consequently $sin\frac{\theta}{2}$ are streaming towards zero as well. It means that solving equation (2.6) we cannot use the simplification we have applied before.

We now can discuss the physicals reasons underlying inelastic scattering. We first assume the continuum behavior of the scattering medium. Indeed, supposing the size of an atom of the order of the Angströms and a typical wavelength of 0.5 μm, we can say that in a volume λ^3 the approximate amount of atoms is $\sim 10^{10}$. In such conditions our assumption is reasonable and we can consider the classical model of visible light scattering. The quantum theory of inelastic scattering exists too but in this thesis we will consider only the classical one. In the following, the main ideas of inelastic scattering are given. The purpose of this description aims at pointing the essential ingredients of Brillouin and Raman scattering, rather than processing a detailed theoretical development.

[4]In these works we deal with visible radiation, therefore, the frequency of light is $\sim 10^{14}$ Hz, whereas the considered Raman shifts will be at most of the order of $10^9 - 10^{12}$ Hz.

Let us consider a not very powerful electromagnetic wave passing through the medium (a high intensity wave would lead to another effect named hyper-Raman scattering[5] that we do not consider herein). Visible light interacts with the electrons of the atoms forcing the oscillations of polarization. The polarization in such conditions is proportional to the exciting electric field $\vec{E}(\vec{r},t)$, so that the time-dependent induced electric dipole moment vector of a molecule of the medium may be written as

$$\vec{p}(\vec{r},t) = \vec{\alpha}\vec{E}(\vec{r},t), \tag{2.10}$$

where $\vec{\alpha}$ is the polarizability second-rank tensor of the molecule. This tensor is time-dependent if molecular vibrations are involved and therefore it is a function of atoms' coordinates. **Inelastic scattering originates from the dependence of the polarization response on the vibrations of the scattering system.** For simplicity we assume a scattering non-rotating molecule whose atoms are vibrating around the equilibrium positions. The variations of the polarizability can be expressed by an expansion in a Taylor series each component of the tensor in normal coordinates [34]:

$$\alpha = \alpha_0 + \sum_i \left(\frac{\partial \alpha}{\partial Q_i}\right)_0 Q_i + \frac{1}{2}\sum_{i,j}\left(\frac{\partial^2 \alpha}{\partial Q_i \partial Q_j}\right)_0 Q_i Q_j ..., \tag{2.11}$$

where α_0 is the value of α at the equilibrium state, $Q_i, Q_j ...$ are the normal coordinates of vibrations corresponding to the molecular vibrational frequencies $\omega_i, \omega_j, ...$, etc. We will focus on one normal mode of vibration Q_i. Let us consider only the first order approximation of this expression for an electrical harmonic oscillator (as in mechanics, the force is proportional to the first order of the displacement, in electrical harmonicity the variation of polarizability is proportional to the first order of Q_i). It means that we can rewrite equation (2.11) for the general case as

$$\vec{\alpha}_i = \vec{\alpha}_0 + \vec{\alpha}'_i Q_i. \tag{2.12}$$

As far as we assume harmonic motions, we can write

$$Q_i = Q_{i_0}\cos(\omega_i t + \delta_i), \tag{2.13}$$

where Q_{i_0} is the normal coordinate amplitude and δ_i is a phase of the oscillation. Thus, using the two previous expressions and remembering that $\vec{E} = \vec{E}_0 \cos(\omega t)$ one can obtain

[5] In the case of a powerful electricity field the electric dipole described in the equation (2.10) will be proportional to square of the $\vec{E}$ and hyperpolarizability third-rank tensor β.

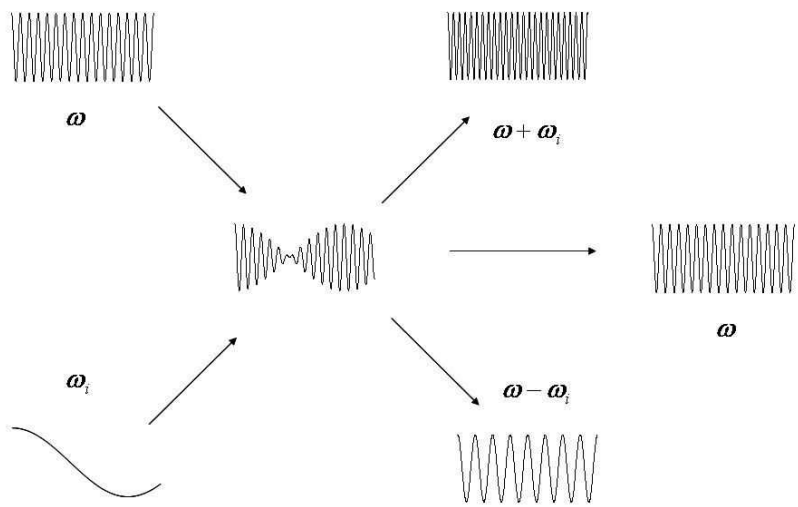

Figure 2.2: The modulation of the linear induced dipole produced by an electromagnetic field of frequency ω and scattering molecule vibrating with frequency ω_i. As an output we have three frequencies: ω, $\omega - \omega_i$ and $\omega + \omega_i$ (see Eq.(2.16)).

the following equation for the dipole vector (2.10):

$$\vec{p} = \vec{\alpha}_0 \vec{E}_0 \cos(\omega t) + \vec{\alpha}_i' \vec{E}_0 Q_{i_0} \cos(\omega_i t + \delta_i) \cos(\omega t). \tag{2.14}$$

So that

$$\vec{p} = \vec{\alpha}_0 \vec{E}_0 \cos(\omega t) + \frac{1}{2} \vec{\alpha}_i' \vec{E}_0 Q_{i_0} (\cos((\omega + \omega_i)t + \delta_i) + \cos((\omega - \omega_i)t - \delta_i)) \tag{2.15}$$

$$\Rightarrow \vec{p} = \vec{p}(\omega) + \vec{p}(\omega - \omega_i) + \vec{p}(\omega + \omega_i), \tag{2.16}$$

where the component with the frequency ω corresponds to the elastic (Rayleigh) scattering and the components with changed frequency correspond to inelastic (Raman) scattering: Stokes process for decrease of frequency and anti-Stokes for increase (Fig.2.2).

As we can see the Raman scattering arises from the electric dipoles oscillating at the shifted frequencies which appear due to a modulation of the frequency of the electromagnetic field by vibration of the molecule.

Now that we have reported a qualitative analysis of the phenomenon of inelastic light scattering we carry on the description in more details. We consider the field of incident

light $\vec{E}(\vec{r},t) = \vec{E}_0 e^{i(\vec{k}\vec{r}-\omega t)}$ scattered by a small volume of the medium and we estimate the scattered field far from the point of scattering (doing this we avoid the influence of the scattering from the other points). This field is described by Maxwell's equations and from them one can show that [35]:

$$\vec{E}'(\vec{R}) \propto \vec{rot} \cdot \vec{rot} \frac{e^{i\vec{k}'\vec{R}}}{R} \int \vec{p}(\vec{r},t') e^{-i\vec{k}'\vec{r}} dV, \tag{2.17}$$

where $\vec{R}$ is a vector joining a point inside the illuminated volume to the point of observation of the field. The wave vector $\vec{k}'$ expresses the change of the wave vector in the medium, so $\vec{k}' = n\omega\vec{l}_k/c$ with $\vec{l}_k$ a unit vector and n is the refractive index of the medium. Time t' is the retarded time $t- \mid (\vec{R}-\vec{r}) \mid /c_m$ because a value of the speed of light inside the medium (c_m) differs from that outside (c). This integral does not depend on the point of observation. Remembering that the origin of scattering is an oscillation of the polarizability (Eq.(2.12)) and assuming these oscillations very weak function of time $\alpha(\vec{r},t) = \alpha_0 + \delta\alpha(\vec{r},t)$:

$$\frac{\partial^2 \vec{p}(\vec{r},t)}{\partial t^2} = -\omega^2 \vec{p}(\vec{r},t). \tag{2.18}$$

If we plug expressions (2.12) and (2.18) into equation (2.17) assuming that $\vec{R} \gg \vec{r}$ we obtain [21]:

$$\vec{E}'(\vec{R},t) = -\left(\frac{\omega}{c}\right)^2 \frac{e^{i(\vec{k}'\vec{R}-\omega t)}}{R} \vec{l}_k \times \left(\vec{l}_k \times \int_V (\alpha_0 + \delta\alpha(\vec{r},t'))\vec{E}_0 e^{i(\vec{k}-\vec{k}')\vec{r}} d^3\vec{r}\right) d^3r. \tag{2.19}$$

This equation shows a superposition of all waves with different phases scattered by all scattering points of the medium. If the fluctuations of polarizability induced by the vibrations ($\delta\alpha$) are zero, the integral in equation (2.19) is zero too except the case of integration in the forward direction (when $\vec{k} = \vec{k}'$) when the contribution of α_0 is not zero. Indeed: as far as the integral applies for a volume and due to the symmetry and anisotropy of the volume the integration over other directions leads to the cancellation of the scattered waves (the mathematical proof can be found in [21]). Hence, we again come to the conclusion that the source of the scattering is a fluctuation of polarizability of the medium. From this expression it is also possible to single out two types of scattering: Rayleigh (if $\delta\alpha(\vec{r},t') = \delta\alpha(\vec{r})$) and inelastic (if polarizability is a function of both time and space).

Vibrations that cause inelastic scattering are divided into two groups: propagating mode (Brillouin scattering) and non-propagating modes (Raman scattering). We now briefly describe these two phenomena.

2.1.3 Raman and Brillouin scattering

Brillouin scattering

Brillouin scattering originates from plane acoustic waves that induce polarizability fluctuations. These waves arise from the collective coherent vibrational motions of the atoms and are characterized by a wavevector $\vec{q}$ which in the Debye approximation is proportional to frequency $\omega(\vec{q})$ [36]. We can apply the spatial Fourier transformation to the polarizability fluctuations appearing in equation (2.19). Summing over all acoustic branches we obtain:

$$\delta\alpha(\vec{r}, t') = \frac{1}{(2\pi)^{\frac{3}{2}}} \sum_m |d\vec{q}|\, \delta\alpha^m(\vec{q}) e^{i(\vec{q}\vec{r} \mp \omega_m(\vec{q})t')}. \tag{2.20}$$

Here $\vec{q}$ is a wave vector which corresponds to a fluctuation wavelength $\lambda = \frac{2\pi}{q}$, $\omega_m(q)$ is a frequency of these fluctuations and the plus/minus sign describes waves propagating in both negative and positive directions. The index m labels the branch in the dispersion relation connecting q and ω. Inserting equation (2.20) into equation (2.19) we obtain

$$\vec{E}'(\vec{R}, t) = -\left(\frac{\omega}{c}\right)^2 \sum_m \vec{l}_k \times \left(\vec{l}_k \times \int |d\vec{q}|\, (\delta\alpha^m(q)\vec{E}_0) \frac{e^{i(\vec{k}\vec{R} - (\omega \pm \omega_m(q))t)}}{R} \right) \frac{1}{(2\pi)^{3/2}} \int e^{i(\vec{k}_0 - \vec{k} + \vec{q})\vec{r}} d^3\vec{r} \tag{2.21}$$

with $\vec{k} = \frac{n}{c}(\omega - \omega_m(\vec{q}))\vec{l}_k = \vec{k}(\vec{q})$ is the wave vector of scattered light. The last integral in this equation is a Dirac Delta-function and it appears because the considered region of scattering is much larger than the wavelength of the radiation. In this conditions it can be written as:

$$\int e^{i(\vec{k}_0 - \vec{k} + \vec{q})\vec{r}} d^3\vec{r} = (2\pi)^3 \delta(\vec{q} - (\vec{k}(\vec{q}) - \vec{k}_0)) \tag{2.22}$$

Hence, the only wave vector of fluctuation which gives rise to scattering is

$$\vec{q} = \vec{k}(\vec{q}) - \vec{k}_0 \tag{2.23}$$

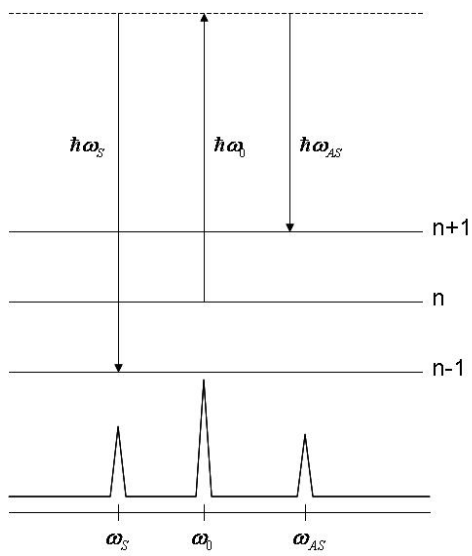

Figure 2.3: A scheme of Brillouin scattering from the quantum point of view: the Stokes process is a transfer of a quantum of acoustic phonon energy to the lattice from the photon and the anti-Stokes process is a reverse symmetrical process. Vibration levels are labeled with the index n.

This equation reminds us of equation (2.3) and it reflects the conservation of momentum between the incident photon and the scattered one with the important role of the scattering coherent fluctuation. From the definition of $\vec{k}(\vec{q})$ (Eq.(2.21)) we can see that the frequency of the scattered light and that of the incident light differ by $\pm\omega_n$ which corresponds to an exchange of quantum energy $\pm\hbar\omega_n$ between the scattering fluctuations and the incident photon (Fig.2.3). From the classical point of view these fluctuations modulate the phase of the scattered light with phase factor $e^{i(\vec{k}_0-\vec{k}+\vec{q})\vec{r}}$ or, in other words, the scattering process consists in a Bragg reflection from the lattice formed by the phases of fluctuations of polarizability.

As we know from the theory of vibrations of continuous media [18] the law of dispersion of acoustic vibrations is linear for small $\vec{q}$ (Fig.2.4):

$$\omega = qv, \tag{2.24}$$

where v is a speed of sound. This means that, using equation (2.8), the frequency shift obtained in a Brillouin experiment will be given by expression:

$$\nu = \frac{\omega}{2\pi} = \frac{qv}{2\pi} = \frac{2vn}{\lambda_0}\sin\frac{\theta}{2}. \tag{2.25}$$

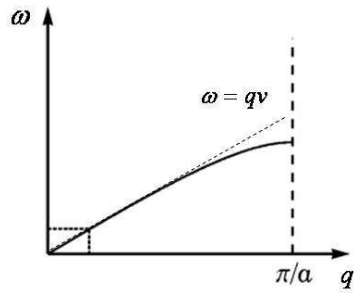

Figure 2.4: The ω-q dependence for acoustic vibrations in a crystal lattice (a is the typical atomic separation). The linear behavior depicts the Debye approximation.

From this equation it is obvious that a Brillouin frequency shift is small with respect to the incident frequency. This is due to the smallness of the transferred momentum $\vec{q}$ with visible light experiments. For instance, for $\lambda = 500$ nm, $q \approx 3 \cdot 10^{-2}$ nm^{-1} which is much lower than $\pi/a \sim 30$ nm^{-1} (Fig.2.4). Accordingly, the Brillouin shift depending on the speed of sound ($\sim 10^3$m/s) is proportional to $v/\lambda \sim 10^9$ Hz $= 1$ GHz. It is worth to note that in a Brillouin experiment the wavelength of the probed fluctuation is of the order of $\lambda = v/q \sim 200$ nm. In homogeneous media this value implies that one can consider the continuous elasticity approximation. In systems with heterogeneities of the order of $\lambda \sim 200$ nm (like opals, see chapter 4), one has to consider "particular" eigenmodes, as we will see in the following section.

It is worth to note that the frequency shift of this type of scattering depends on $\vec{q}$ through the angle θ hence on the geometry of the experiment. This fact helps us to distinguish the Brillouin signal from the Raman one (if the Raman signal derives from very low frequency vibrations) which does not depend on $\vec{q}$ (see following section) on the experimental spectrum. The largest Brillouin shift can be observed in backscattering geometry (Fig.2.5) when the scattered light is detected in the opposite direction comparing to the incident light. As it is seen on the picture in such geometry $\theta = 180°$ so that

$$q_{back} = \frac{4\pi n}{\lambda_0} \Rightarrow \nu_{back} = \frac{2vn}{\lambda_0}. \tag{2.26}$$

In 90N (normal or pure) geometry the scattered light is detected perpendicularly to incident light as it is shown in Figure 2.6. Thus $sin(\pi/4) = \sqrt{2}/2$ so that $\vec{q}$ and the frequency shift can be expressed as:

$$q_{90N} = \frac{4\pi n}{\lambda_0}\frac{\sqrt{2}}{2} \Rightarrow \nu_{90N} = \sqrt{2}\frac{vn}{\lambda_0}. \tag{2.27}$$

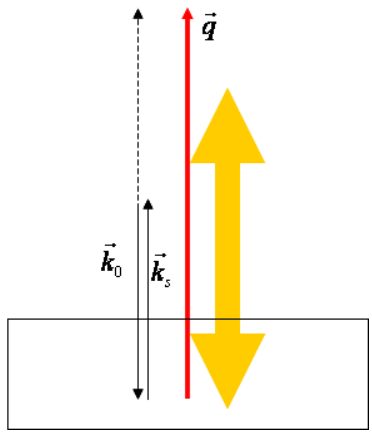

Figure 2.5: The backscattering geometry of the scattered light detection.

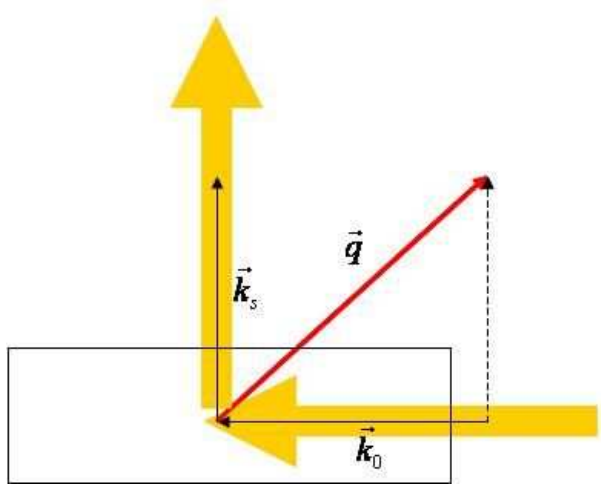

Figure 2.6: The 90N geometry of the scattered light detection.

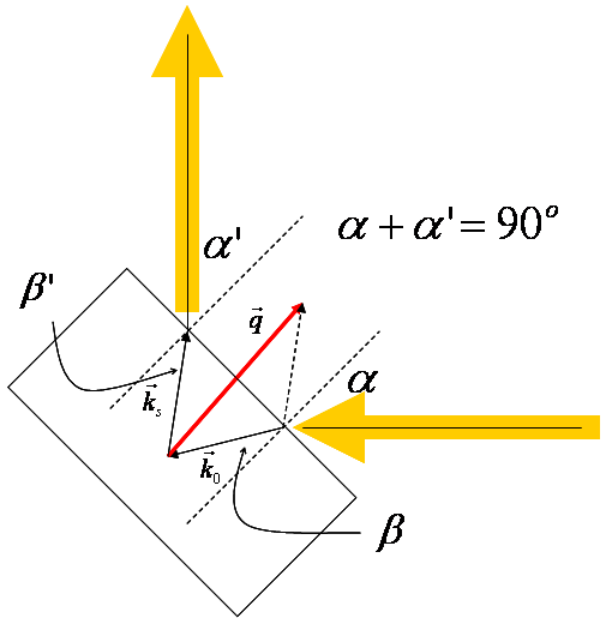

Figure 2.7: The 90R geometry of the scattered light detection.

There are two additional versions of the perpendicular scheme: 90R and 90A. In the 90R ("R" means "reflection") geometry the inelastic scattering emerges in the same direction as the elastic reflection of the light (although in practice we try to remove the elastic line from the detection direction). As it is shown in Figure 2.7, $\alpha + \alpha' = 90°$. Based on a geometry of the light path we can assume that $\alpha \approx \alpha'$ and $\beta \approx \beta'$. Hence, remembering the Snell's law, one can show that $\sin(\frac{\beta+\beta'}{2}) = \frac{1}{\sqrt{2}n}$. From the diagram we can see that $\theta = \pi - (\beta + \beta')$. So that the frequency shift for the 90R geometry of the experiment can be expressed as:

$$q_{90R} = \frac{4\pi n}{\lambda_0}\sqrt{\frac{4n^2-2}{4n^2}} \Rightarrow \nu_{90R} = \frac{v\sqrt{4n^2-2}}{\lambda_0}. \tag{2.28}$$

In 90A geometry ("A" means "absorption") the elastically reflected light is "absorbed" by the medium of the sample (Fig.2.8). In this scheme $\theta = \beta + \beta'$, so that one can write

$$q_{90A} = \frac{4\pi}{\lambda_0}\frac{\sqrt{2}}{2} \Rightarrow \nu_{90A} = \frac{v\sqrt{2}}{\lambda_0}. \tag{2.29}$$

The main advantage of the latter configuration is the independence on the refractive index of the sample. Using this scheme in combinations with the others one can estimate the refractive index and as a landmark of Brillouin scattering the speed of sound of the

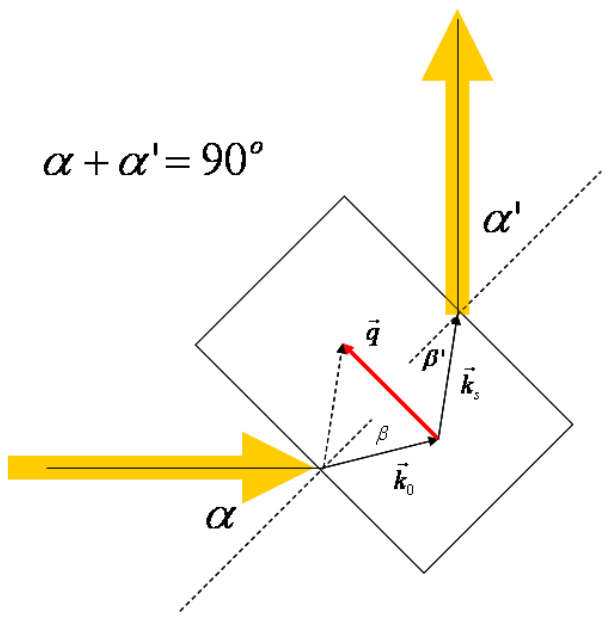

Figure 2.8: The 90A geometry of the scattered light detection.

sample substance. In fact we applied Brillouin scattering to evaluate the speed of sound in glass matrices used as embedding media of NPs (see chapter 3)

Raman scattering

This type of scattering is produced by non-dispersive optical modes for which the frequency hardly depends on $\vec{q}$, i.e. $\omega(q) \approx \omega_0$ (Fig.2.9) unlike acoustic modes. The frequency of optical phonons with wave vectors such as those transferred from visible light (and these vectors typically lie at the center of Brillouin zones, as emphasized previously) is almost a constant. Due to this the frequencies of the Stokes and anti-Stokes components do not depend (or weakly depend) on the scattering geometry and equal essentially ω_0. The Raman terms usually appear due to so-called *localized modes* whereas Brillouin scattering corresponds to *propagating modes*.

2.2 Inelastic scattering from modes of spherical NPs

In the theoretical descriptions of inelastic light scattering given above, focus was essentially made on the mechanism of scattering by vibrations in a general way (collective vibrations or molecular vibrations). We have distinguished between Brillouin and Raman scatterings that significantly differ from each other through the delocalized and localized

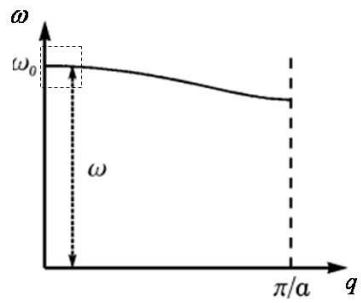

Figure 2.9: The ω-q dependence for the optical branch of lattice vibrations.

(acoustic and optical) nature of the scattering vibrations respectively. From the description of low energy modes from nano-spheres (section 1.3), one may realize that these modes can hardly be identified as either completely delocalized or completely localized. Indeed, they are described in terms of parameters that usually refer to acoustic vibrations (namely the speed of sound) while the finite size effect confers these types of modes with an optical-like character. This observation is to be related to the fact that inelastic scattering from NP modes emerges in a spectral window lying between those of Brillouin and Raman scatterings. As mentioned earlier, both types of scattering obey selection rules that essentially restrict the information to a certain type and hence certain vibrational modes. In the following, we relate about the selection rules that pertain to inelastic scattering from neither completely acoustic nor completely "molecular" modes, i.e. from NP modes.

2.2.1 Selection rules for nanoparticle modes

These rules were first established by Duval [37] in 1992 on the basis of group theory. Let us consider a solid **spherical NP** with size negligibly **lower than the wavelength** of the exciting laser. The symmetry group of a sphere is the group of rotations that is isomeric to O(3). The irreducible representations of the rotation group O(3) have dimension $2\ell+1, \ell = 0, 1, 2, ...$ Moreover there is only one such representation, which is denoted by D^ℓ and for spheres they are marked as D^ℓ_g and D^ℓ_u [38] where g is for even representations and u is for odd ones. According to the Wigner's theorem[6] each vibration fundamental mode corresponds to its own representation (D^ℓ_g or D^ℓ_u) and the degeneracy of this mode is the

[6]A theorem of fundamental importance in spectroscopy and angular momentum theory which provides both: a form for the dependence of all matrix elements of irreducible tensors on the projection quantum numbers and a formal expression of the conservation laws of angular momentum.

same as the dimension of the corresponding representation [39]. In paper [37], it was proved that *spheroidal modes* transform into representations D_g^0, D_u^1, D_g^2 and *torsional modes* — into D_g^1, D_u^2, D_g^3. Considering the operator of the Raman scattering process as a tensor of polarizability it was shown (see [37]) that its components transform into the sum of irreducible representations $D_g^0 + D_g^2$. This means that only two spheroidal modes: spherical D_g^0 and quadrupolar D_g^2 ones are active for Raman scattering by eigenmodes of a sphere with radius $R \ll \lambda$. Also it is worth to note that Raman scattering through the breathing mode (SPH $\ell = 0$) does not change the polarization of the light whereas the light scattered by the quadrupolar mode (SPH $\ell = 2$) is totally depolarized. This fact allows to distinguish between these two modes by controlling the polarization of both incident and scattered collected lights (see next chapter). In spite of vain contradictive theoretical attempts [40], the selection rules established by Duval in the case of small ($D \ll \lambda$) NPs, have always been confirmed by theory [41] and experiments.

In the present works, we have studied both "small" NPs, i.e. metal NPs (chapter 3), but also **"large"** NPs, namely viruses (chapter 4). Both systems, in a first approximation, can be described as "nanospheres". In addition to the fact that as non-noble metal NPs low frequency Raman scattering from viruses is non resonant (see further), the size of the viruses we have investigated (~ 200 nm) is comparable with exciting wavelength, so $\lambda \sim R$ or $qR \sim 1$. This definitely falls out of the range of applicability $qD \ll 1$ (the case of small NPs). One difficulty that emerges switching from the study of "small" NP to the study of "large" NPs is the modification of the selection rules. Indeed, upon considering NPs with sizes $D \gg 10\%\lambda$, Brillouin type scattering mechanisms should be taken into account, in addition to Raman mechanism. Such statement is the starting point of recent theoretical developments of Montagna [42] who first attempted to rationalize the selection rules for large NPs. Montagna showed that the contribution of the ith mode with frequency ω_i to the Stokes part of a spectrum can be expressed in a compact form:

$$I^i_{\alpha\beta}(\vec{q}) \propto \frac{n(\omega_i, T) + 1}{\omega_i} C_{\alpha\beta}(\omega_i, \vec{q}), \tag{2.30}$$

where α and β are the directions of polarization of incident and scattered photons respectively, $n(\omega_i, T)$ is the Bose-Einstein factor and $C_{\alpha\beta}(\omega_i, \vec{q})$ is the coupling coefficient which depends on the tensor of polarizability (Eq.(2.12)). $C(\omega_i, \vec{q})$ is the sum of two components: the first one describes the polarization fluctuations due to acoustic vibrations (this mechanism is responsible for polarized Brillouin scattering), the second component describes the motion of the surrounding dipoles and change of the atomic distances. This effect

leads to contributions to both the polarized and depolarized (longitudinal and transverse phonons) Brillouin signal and it also induces Raman scattering. The Brillouin mechanism has a negligibly small contribution in the case of small NP ($R \ll \lambda$) because the density fluctuations produced by the vibrations of the NP and the change of the phase of the incident light are insignificant. As a matter of fact it was shown [42] that the dependence of the Brillouin intensity for small values of qR is of the order of $(qR)^4$. Upon size increase, the Brillouin contribution becomes more significant and the scattering is produced by the longitudinal spheroidal mode with frequency $\omega = qv_L$. According to Montagna, in large spheres ($qR \gg 1$) light scatters by "dynamical Bragg grating" associated with the modes of the sphere and created by both angular and radial oscillations. The period of this imaginary grating is inversely proportional to the numbers n and ℓ. The most intense scattering takes place when the exciting wavelength matchs the period of grating (or when the frequency of the mode is equal to qv_L). The same approach has to work in the case of medium NPs ($qR \sim 1$). The Brillouin scattering in the case of large NPs ($qR \gg 1$) is dominant in the polarized spectrum because it is the case of ordinary Brillouin scattering of the bulk material.

Raman scattering of large NPs has also different selection rules. Vibrational modes of higher ℓ and n become stronger and active with increase of the NPs' size. This type of scattering is produced by longitudinal phonons ($\omega_L = qv_L$) and transverse phonons ($\omega_T = qv_T$). Also the TOR modes may become active as well in the case of large spheres. They produce only depolarized scattering (because of the fact that torsional modes do not contain any radial displacement) but the experimental detection of the TOR modes has not been observed yet.

It is worth to note that equation (2.30) expresses the inverse dependence of the scattered light intensity on Raman shift frequency ω. According to that inverse frequency dependence, the larger the mode frequency is, the lower its contribution to the Raman spectrum becomes. This partly explains the usually low (if not zero) intensities of vibration modes with large n values (harmonic ranks). For this reason only the first mode ($n = 1$ and $\ell = 0; 2$) are detected for the majority of systems. However, we will show that one specificity of Raman scattering from NP eigenmodes harmonics is that their respective intensities do not scale monotonically with the inverse of their respective ranks (see section 3.1).

Once we have outlined the main differences between low frequency inelastic scattering from "small" and "large" NPs, we now turn to further specificities that arise from the

"electronic" nature of the scattering medium that makes up the nanoparticles. We will see how low frequency inelastic scattering turns to be notably powerful (in terms of scattering efficiency) in the case of noble metal NPs.

2.2.2 Raman scattering from metal nanoparticles

Metal NPs as objects of investigation by low frequency Raman scattering are in fact very special cases. Such became clear after the Surface-Enhanced Raman Scattering effect (SERS) was discovered in 1974 [43] according to which molecules adsorbed on a silver surface produce a Raman signal notably larger than it was expected. The origin of this effect is an enhancement of the dipole moment of the molecule by the electric field of a surface plasmon excitation formed through coupling with incident light. The precise theoretical discussion of this effect can be found in [44]. The basic ingredient of the SERS effect, which turns out to be an essential feature of any metal NP, is that if a metal object is reduced to nanometric dimensions some new electronic properties appear. One of the most significant properties is the Surface Plasmon Resonance (SPR) which plays a notable role in resonant low frequency Raman scattering from noble metal NPs. In this section, we relate on the specificity of the SPR in low frequency Raman scattering from metal NPs.

Surface plasmon resonance

Firstly we consider a bulk of a metal. The electric field propagating along the z direction in a medium with refractive index n can be written as $\vec{E} = \vec{E}_0 \exp i(\omega t - kz)$ where $k = n\omega/c$. In the case of a metal n is complex ($n = \sqrt{\epsilon}$; Eq.(2.33)) and can be written as $n = n_1 - in_2$. Then $\vec{E}$ takes the following form:

$$\vec{E} = \vec{E}_0 e^{i\omega\left(t - \frac{n_1 z}{c}\right)} e^{-\frac{\omega n_2 z}{c}} \tag{2.31}$$

This expression shows that the imaginary part of the refractive index (also named as the "extinction term") leads to the exponential damping of the electric wave penetrating into the medium, while the real part of the refractive index is responsible for the phase velocity of the wave front. The damping of the field is associated with the absorption coefficient $\alpha(\omega)$ entering the Beer-Lambert law: $I = I_0 e^{-\alpha(\omega)z}$, where z is the propagation direction. From equation (2.31) ($I = E \cdot E^*$) one has

$$\alpha(\omega) = 2\frac{\omega}{c} n_2(\omega). \tag{2.32}$$

According to the Drude model (see, for example [45]) the metal can be assumed as a system of motionless fixed ions with an ideal electronic gas in between them. The electric field produced by the ions accelerates electrons whereas collisions with defects, with ions, and with each other, brake them. Due to the isotropy of the metal the average vector of the electric field (in the absence of an external field) is equal to zero. If the metal is placed into an electric field, the free electrons of the metal move against this field and produce a local electrical field directed against the external field. The superposition of these fieldsleads to the absence of the electrical field inside the metal and the only place where it differs from zero is the surface of the metal. The electric wave of an incident light causes the oscillations of the free electrons. These electric collective oscillations are named *plasmon*.

In general, the electrical response of a medium is characterized by the relative permittivity ϵ. Let $\epsilon(\omega)$ be the relative permittivity of the bulk metal. Within the Drude model, the dielectric function can be written as:

$$\epsilon(\omega) = 1 - \frac{\omega_p^2}{\omega(\omega + i\Gamma)}, \tag{2.33}$$

where $\omega_p = \sqrt{\frac{Ne^2}{m_{eff}\epsilon_0}}$ is the plasma frequency, N is the number of the conduction electrons of the metal per a unit of volume, m_{eff} is the effective mass of these electrons and Γ is a relaxation rate due to collisions. From equation (2.33) the dielectric constant of the metal is a complex value and taking into account the fact that for visible optical frequencies $\omega \gg \Gamma$ we can write the real and imaginary respectively parts as:

$$\epsilon_1(\omega) \approx 1 - \frac{\omega_p^2}{\omega^2} \tag{2.34}$$

and

$$\epsilon_2(\omega) \approx \frac{\omega_p^2}{\omega^3}\Gamma \tag{2.35}$$

These two parameters, as will be shown further, are determinative in the absorption of a metal.

In the case of noble metals (and in this work we deal with them: Cu, Ag, Au), one needs to take into account the contribution of the d-electrons in the metal polarizability. Interacting with incident light a nd-electron can make an interband transition to the $(n+1)sp$-band of the higher energy level. The Drude theory cannot describe this situation correctly, so another term taking into account the polarization of the core electrons has to be added in the dielectric function [46]:

$$\epsilon_{nm} = \epsilon^D + \epsilon^d - 1. \tag{2.36}$$

where ϵ^D is a term associated with conduction electrons (Drude model) and ϵ^d is a term describing the contribution of the core d-electrons. Appearance of the ϵ^d term affects mainly the imaginary part of ϵ (ϵ_2 in Fig.2.10) giving rise a steep increase, off the Drude approximation, near 4 eV and 1.9 eV for Ag and Au respectively. The position of this minimum corresponds to the interband transition threshold.

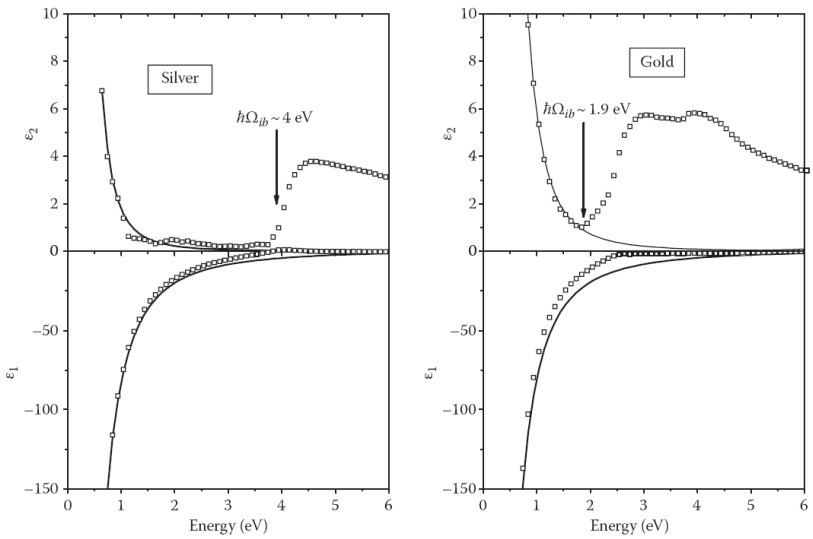

Figure 2.10: Real and imaginary parts ϵ_1 and ϵ_2 of the dielectric function of silver (left) and gold (right). Comparison between the Drude model (solid lines) and the experimental measurements (squares). The influence of d-core electrons is patent in the imaginary part of ϵ where an increase of ϵ_2 appears around 1.9 eV for gold and 4 eV for silver corresponding to the interband transition threshold. Retrieved from [46].

Now we consider a **metal nanosphere** interacting with such electric field **in vacuum**. Specifying "nano" we understand that the size of the sphere is much smaller than the wavelength of the incident light. Due to this, $kr = 2\pi n/\lambda \ll 1$ therefore $\vec{E}$ from the equation (2.31) can be written as $\vec{E} = \vec{E_0}e^{-i\omega t}$, i.e. it depends only on ω. This ensures the validity of the quasi-static approximation. The electric field changes the charge distribution of the sphere. To compensate this redistribution and to keep a NP neutral the induce dipolar electric field appears. This field can be derived within the quasi-static approximation by the superposition of non-concentric oppositely charged spheres (Fig.2.11):

$$\vec{E_O} = \frac{1}{4\pi\epsilon_0} Ne \frac{4}{3}\pi r^3 \frac{\vec{r_1} - \vec{r_2}}{r^3} = \frac{Ne}{3\epsilon_0}\vec{R}, \tag{2.37}$$

where $\vec{r_1}$ and $\vec{r_2}$ are radius-vectors of the sphere centers and $\vec{R} = \vec{r_1} - \vec{r_2}$. Under the

influence of the local electric field electrons of the NP oscillate with the frequency ω_{sp} (plasmon oscillations), therefore, the vector $\vec{R}$ also oscillates with the same frequency, so

$$\vec{R}(t) = \vec{R}_0 e^{-i\omega_{sp}t}. \tag{2.38}$$

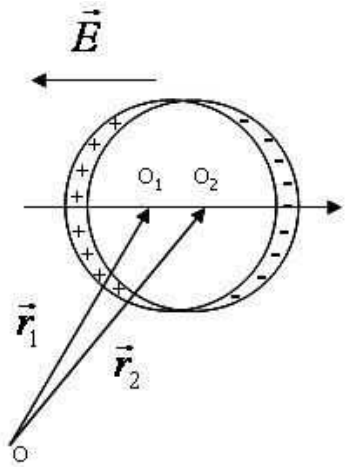

Figure 2.11: A scheme of the dipolar charge redistribution in the metal nanosphere under influence of electric field with $\lambda \gg D$.

The second law of Newton for electrons in this case has a following view:

$$m_{eff}\frac{d^2R}{dt^2} = -eE_O = -\frac{Ne^2}{3\epsilon_0}R. \tag{2.39}$$

Remembering the definition of ω_p from the expression (2.33) and considering the limit conditions ($R(0) = R_0$) we can solve this equation that gives us a frequency of plasmon oscillation in a free metal sphere:

$$\omega_{sp}^{vacuum} = \frac{\omega_p}{\sqrt{3}}. \tag{2.40}$$

The optical frequency ω_{sp} is called *the surface plasmon resonance* (SPR). The light with frequency lower than ω_{sp} will be reflected due to the shielding of the electric field of the wave by the electrons of the metal, whereas the light with frequency higher than ω_{sp} will be transmitted because the response of the electrons will not be rapid enough to compensate the external electric field. Light with frequency $\omega = \omega_{sp}$ will be absorbed and, therefore, $\alpha(\omega)$ will achieve its maximum.

If now we consider that a metal **NP** is **embedded in a transparent dielectric matrix** with dielectric constant ϵ_m (purely real), the internal electric field is modified with respect to the vacuum case:

$$E_{int} = \frac{3\epsilon_m}{\epsilon + 2\epsilon_m} E. \tag{2.41}$$

It comes out that the absorption coefficient of the composite medium (in the case of small metal volume fraction and non interacting metal spheres) is [46]:

$$\alpha(\omega) = 9q\frac{\omega}{c}n_m^3 \frac{\epsilon_2(\omega)}{(\epsilon_1(\omega) + 2\epsilon_m)^2 + \epsilon_2^2(\omega)}, \tag{2.42}$$

where q is a volume fraction of the metal NPs in the medium. From this expression $\alpha(\omega)$ tends to a maximum when $\epsilon_1(\omega) \to -2\epsilon_m$ ($\epsilon_2(\omega)$ is negligible at optical frequencies because $\Gamma \ll \omega$ and $\frac{\partial \epsilon_2}{\partial \omega} \approx 0$). Therefore from equation (2.34) we can obtain the expression for the resonance frequency of a simple metal NP embedded in a dielectric matrix:

$$\omega_{sp}^{embedded} = \frac{\omega_p}{\sqrt{1 + 2\epsilon_m}}. \tag{2.43}$$

This equations shows that resonance frequency ω_{sp} essentially depends on the refractive index of the matrix ($n = \sqrt{\epsilon_m}$).

The resonance frequency of noble metals is expressed as:

$$\omega_{sp}^{noble} = \frac{\omega_p}{\sqrt{2\epsilon_m + \epsilon_1^d(\omega_{sp})}}. \tag{2.44}$$

As an illustration of SPRs, we now discuss the three cases dealt with in this work: Ag, Au and Cu. Figure 2.12 compares the absorption spectra calculated by the discrete dipole approximation (DDA) for Ag, Au and Cu NPs of size of 10 nm embedded in a glass matrix with refractive index $n = 1.5$ (the experimental spectra of the similar systems are published somewhere else [47]). All three NP types demonstrate a clear SPR peak in their spectra within the visible range: around 420 nm for silver, 530 nm for gold, and 580 nm for copper. As mentioned before, these positions depend on the refractive index of the matrix. The visibility of the SPR maximum is different for the different metals. This is due essentially to the interband transition, whose threshold for silver NPs is around 311 nm [48]. This is quite far from the SPR and so it does not influence the silver's SPR in the absorption spectrum. The threshold of the interband transitions of gold and copper are similar, around 617 nm but they possess different amplitudes and slope ratios of the $\epsilon_2(\omega)$ dependence increases and therefore contribute differently to the SPR peaks.

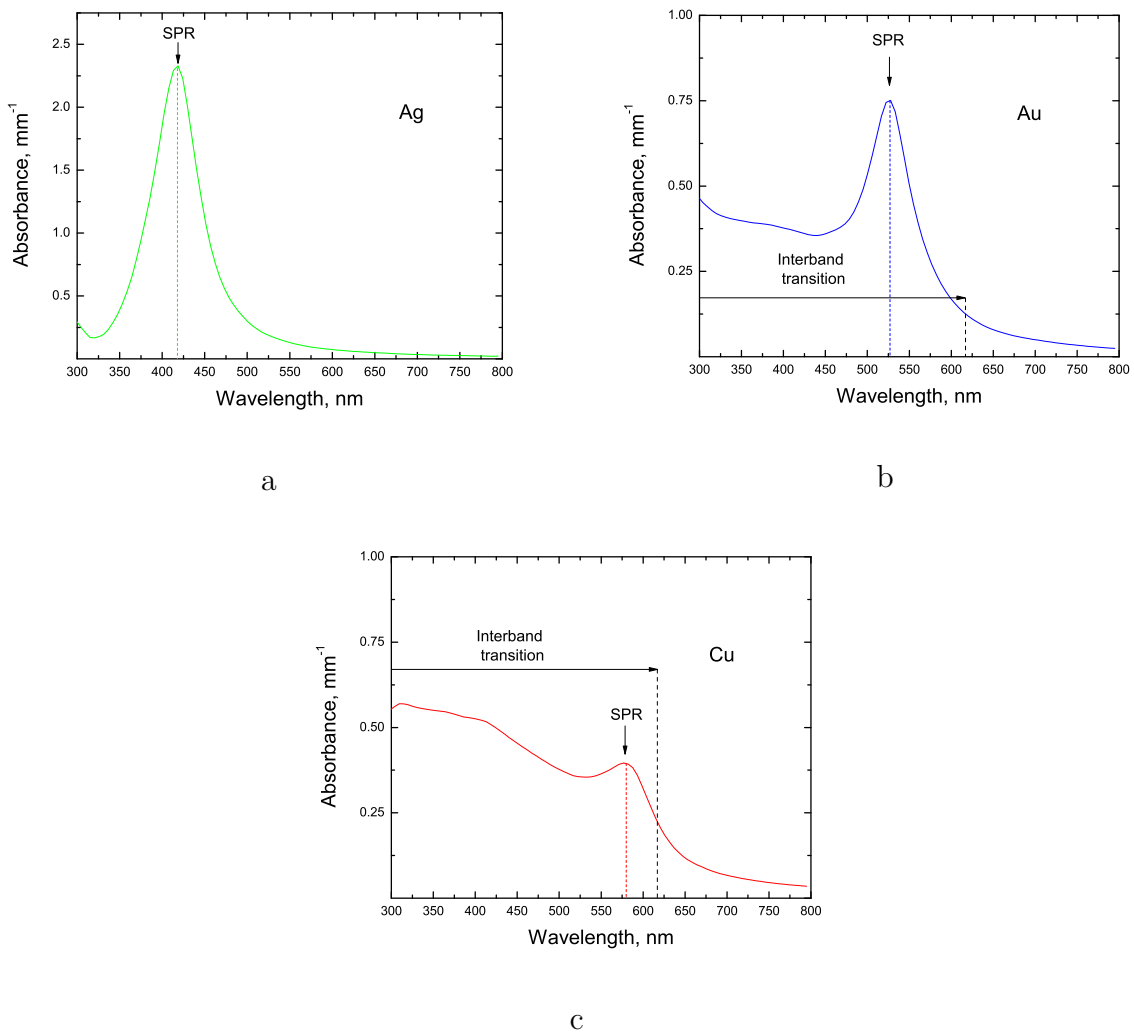

Figure 2.12: Theoretical absorption spectra of silver (**a**), gold (**b**) and copper (**c**) NPs of size of 10 nm embedded in a glass matrix with refractive index $n = 1.5$. These spectra were calculated by P. Yang and H. Portales (LM2N, University Paris 6, Paris, France) with the DDA method.

The strong absorption of metal NPs at ω_{sp} has a major consequence on the detection of NPs vibrations through Raman scattering if the incident light has a frequency which is not far from the surface plasmon resonance.

Influence of the SPR on Raman scattering

Theoretical developments have shown that the Raman scattering amplitude is very large if the frequency of the exciting light matches (or nearly matches) that of the SPR

[49]. It happens because the dipolar plasmon is the essential feature that is responsible for the absorption of the visible light.

Electronic plasma oscillations in spherical NPs reflect spherical symmetry [28] and the plasmon corresponds to a strong electronic dipolar moment with which the incident light strongly interacts. Due to this the selection rules for the Raman scattering process for metal NPs are the same as for non-resonance Raman. But the nature of the plasmon-phonon coupling for radial vibrations differs from that for quadrupolar ones. The "breathing" mode modulates the volume of the particle which leads to the modulation of the dielectric susceptibility [50] which, in turn, leads to a coupling with plasmon. The coupling with the quadrupolar mode comes from the dependence of the plasmon frequency from the shape of the NP which modulates the electronic dipole. The stronger coupling of the plasmon with quadrupolar modes leads to a larger Raman signal than that from the spherical modes. Thanks to strong plasmon-phonon coupling one can observe Raman scattering signal even from poor concentrations of metal NPs embedded in the matrix. Indeed, we will see that typical volume concentration of NPs (q from the equation (2.42)) as $\sim 10^{-5}$ is sufficient to generate visible colors, arising from the SP absorption (see next chapter).

Due to the peculiarities of Raman scattering from metal NPs, during the last 30 years, this topic was significantly developed and demonstrated a lot of perspectives. The current situation in this field is briefly described in following section.

Current knowledge about low frequency Raman scattering from metal nanoparticles

The first paper dedicated to low frequency Raman scattering from metal NPs was published in 1980 [1]. In this paper the authors reported the first observation of low frequency vibrations from a rough silver surface which could not be observed from a smooth surface. Although incompletely at that time, the low frequency Raman signal was then correctly attributed to the acoustic vibrations localized over "surface protrusions". This early finding opened the way to more detailed investigations of the vibrational modes of metal NPs with enhanced impetus after the low frequency Raman technique was asserted as a definite good probe of vibrational eigenmodes of spherical NPs [2], together with the derivation of the related selection rules [37]. Over the past two decades, the strong low frequency Raman response from metal NPs was used as a very valuable tool in the characterization of NP modes either in the specific case of metallic ones or in the more

general case of non-metallic NPs. On a very general basis, the specificity of metallic NPs is important when dealing with the intensities of the observed low frequency Raman lines while it is not relevant (at least at first order) when the interest is essentially focused on their frequency positions. We cite thereafter several works on metal NPs where the low frequency Raman probe was used for other purposes than simple size determination.

The works [51, 52] are dedicated to the study of the selective resonant excitation of the surface plasmon. It was demonstrated that the plasmon-phonon coupling that occurs in the case of metal NPs allows to investigate the dependence of the Raman response on the excitation wavelength. Due to the splitting of the dipolar plasmon with an ellipsoidal distortion the NPs, selective excitations with either of the two split components favors the Raman response from NPs with non-spherical shape.

The strong optical absorption of metallic NPs which essentially arises from that of the electrons can also be used as a probe of metal NPs vibrations. Such is performed in time resolved pump-probe spectroscopy where the NP vibration is probed by recording the very small ($\sim 10^{-7}$) relative change of the optical transmission (near the SPR), that follows an intense short excitation of the conduction electrons [50]. This technique essentially probes the radial breathing mode $\ell = 0$, thereby allowing a comparison with Raman scattering from the same type of mode. On this basis Portales *et al* [53] have identified the Raman scattering from the breathing mode of silver NPs, together with its first two harmonics. Also in these works it was shown that the impact of SPR resonant Raman scattering on the relative Raman intensities of the $\ell = 2$ band in metal NPs derives from the strong sensitivity of the plasmonic dipolar excitation to ellipsoidal distortions (splitting of the SPR). Since the fundamental $\ell = 2$ mode by its very nature consists in such dynamical distortions, the coupling with the surface plasmon is large. The weaker contribution of the $\ell = 0$ modes to the Raman spectrum originates in the periodic volume changes that this mode induces. Such modulation affects the dielectric permittivity associated with interband transitions which are at the origin of the resonance process for the breathing mode.

Even though the strong optical response of metallic NPs allows to probe very diluted amounts of NPs, the low frequency Raman scattering technique in its present technological development stage is bound to the study of NPs assemblies, as opposed to single particle spectroscopies. In most samples investigated through low frequency Raman scattering, the observed bands are inhomogeneously broadened due to the size distributions of the probed assemblies. When the size distribution is sufficiently narrow, NPs may be assembled in the

form of compact organized structures (supracrystals). Courty et al [54, 55] investigated the behavior of the $\ell = 2$ modes in supracrystals of silver nanocrystals (NCs) (of 5 nm diameter) functionalized with alkane chains. Thanks to the large Raman signal of the silver NCs, combined with high densities of NPs due to the supracrystalline structure, variations in the spectral widths of the Raman bands could be detected as a function of the extent of supercrystallinity. This observation evidenced the signature of inter-NP coherence which essentially shows up as a narrowing of the Raman band in ordered assemblies.

The rather rich low frequency Raman spectrum obtained from metallic NPs makes it possible to focus interest on the intensities of the Raman scattering. Studying the relative intensities of the Raman active bands is important in identifying the scattering mechanism and the parameters that are relevant for Raman activity. Theoretical calculations on both resonant (metallic NPs, semiconductor NPs) and non-resonant (dielectric NPs) Raman scattering from NPs modes have been performed by different authors [56, 57]. In chapter 3, we will see how calculations performed for metal NPs compare to our experimental data.

Recent advances

An important experimental limiting factor in low frequency Raman scattering from NP modes is the ability of the used spectrometers to resolve low intensity inelastic frequency bands from the strong elastic (Rayleigh) or quasielastic scattering. As shown in a previous PhD work [5], the use of a multipass Tandem Fabry-Perot interferometer has proved as a very adequate tool in this type of spectroscopy. Using this system, significant breakthrough in the field of low frequency Raman scattering from NP modes could be achieved, especially in the field of so-called large NPs (i.e. of the order of $\sim 100 - 300$ nm) [58]. Recently, the use of a multipass Tandem FP interferometer enabled a fine characterization of low frequency modes from Au NPs with size greater than ~ 6 nm. This characterization allowed to disclose the effect of elastic anisotropy on the quadrupolar band of both embedded [59] and non-embedded Au NPs [30]. Elastic anisotropy, which directly derives from the crystalline quality of the NPs induces a splitting of the quadrupolar mode (see section 3.1). An important part of our experimental works exposed in chapter 3 are precisely dedicated to further studies of elastic anisotropy in metal NPs. Another important part was the extension of LFRS to the study of particles of submicron dimensions, as developed over the past decade with a relative success [60].

The specificity of the submicron particles we have chosen to study is that they consist of biological matter rather than solid state.

2.2.3 Recent extension to nanoparticle modes from large viruses

NP mode characterization through inelastic scattering has essentially been focused over the past two decades on solid NPs, being produced either embedded in matrices or non-embedded. One main point of such characterization is a non destructive determination of NP sizes although the technique is also sensitive to NP shape, NP inner crystalline structure, NP environment, etc. The many aspects the LFRS technique addresses, or at least potentially addresses, prompt us to use it as a probe for NPs other than solid ones. As mentioned in the introduction and further illustrated in chapter 4, viruses may be considered as "nanoparticles" due to their compact and nanometric morphologies. Tracking NP modes from viral globules may lead to dynamical characterizations that structural investigations cannot de facto, account for. In turn, this dynamical characterization can be relevant in biological activity. Viruses have been predicted to possess modes of vibration (similar to solid NPs), involving the coherent motions of their main constituents in paper [12] and after this assumption was developed in papers [61, 9]. With these ideas in mind, Raman investigations of viruses have been initiated at the LPCML a few years ago.

Raman investigations of viruses are rather well developed, at least in the range of conventional Raman spectroscopy where the information pertains to the constituent or inner proteins of a virus (see, for example [13, 62]). The search of low energy modes from viruses is much scarcer. The low frequency modes were predicted long time ago through theoretical calculations [7, 63, 11] and also were admitted as potentially important ingredients of the dynamical and elastic behaviors of viruses. But in the same time they have proved difficult to be detected experimentally. In previous works, Stephanidis *et al* [64] explored the possibility of detecting virus NP modes from considered "small" viruses (15 – 30 nm). One main difficulty met in these works is the very low concentrations possibly obtained from suspensions of viruses. Indeed, although highly concentrated solution of viruses could contain as much as 10^{13} pc/ml, the smallness of the studied viruses induced very low viral volume concentrations. Such was circumvented investigating microcrystals of the Sattelite Tobacco Mosaic Virus ($D = 15$ nm) which allowed the determination of the elastic constant of a viral crystal. However, no NP modes from the viruses could be clearly identified from the microcrystal spectra. A possible explanation for this non-observation is the too strong coupling between viruses within the crystalline arrangement

that tends to delocalize the NP vibration. Such explanation was also derived from the study of 2D layers of the Wiseana Iridescent Virus [3]. In spite of the inconclusive results obtained on small viruses, test studies performed on suspensions of a "large" virus (190 nm, PBCV-1) [5] revealed the existence of a very low frequency inelastic signal that could have been identified as a "Raman" signal. In chapter 4, we will report further studies on large viruses aiming at identifying this signal, using reference colloids and other large viruses.

As already mentioned with the study of fine effects like elastic anisotropy, it is important to have spectroscopic tools with adequate performances for low frequency Raman/Brillouin scattering. This is all the more necessary when studying NP modes from large nano-spheres, with rather weak elastic constant, like viruses. We present the unique spectroscopic tool that we used to record the inelastic light scattering spectra of both small metal NPs and large viruses.

2.3 Experimental Raman and Brillouin techniques

The low frequency Raman and Brillouin measurements reported in these works were essentially carried out with a Fabry-Perot interferometer (Tandem) constructed by J.R. Sandercock. This setup and its underlying theoretical development are described in details in [65, 66, 67, 68]. The Tandem allows to record Brillouin and low frequency Raman spectra with a resolution that cannot be reached with grating monochromators. This section will be dedicated to the design and features of this device. We will briefly see its principle of operation and make a comparison with a five-grating monochromator.

Theory of Fabry-Perot resonator

The heart of a tandem is a Fabry-Perot resonator (FP) [69, 70]. Fabry-Perot resonators (Fig.2.13) nowadays are ones of the main devices used in high-resolution spectroscopy. Its principle is based on the transmission of light between a set of two parallel high reflective surfaces along the axis of the resonator. The most common resonator is made by two facing mirrors with air space between them. Light manifold reflected from these mirrors forms parallel beams. The path difference Δ_0 between two beams illuminating the resonator is

$$\Delta_0 = 2dn\cos\varphi, \tag{2.45}$$

where n is the refractive index of the medium between the mirrors, φ is an angle of the incident light respectively to the vertical axes to the plane of mirrors and d is the distance between the mirrors; and the conditions for the constructive interference is

$$2dn\cos\varphi = p\lambda \Rightarrow \nu = \frac{pc}{2dn\cos\varphi}, \tag{2.46}$$

where p is positive integer, λ and ν are the wavelength and the frequency of the transmitted light. Actually, this condition is identical to that for any set of parallel planes but in ordinary plane the reflection coefficient r is around 3 – 5 % [70] which leads to the rapid decrease of the rays' intensity with the number of reflections. In a FP resonator r is close to 100% so that the intensity of each reflected ray does not appreciably differ from that of the previous one. In result the total number of interfering rays is quite large and that explains the high resolution of such a construction.

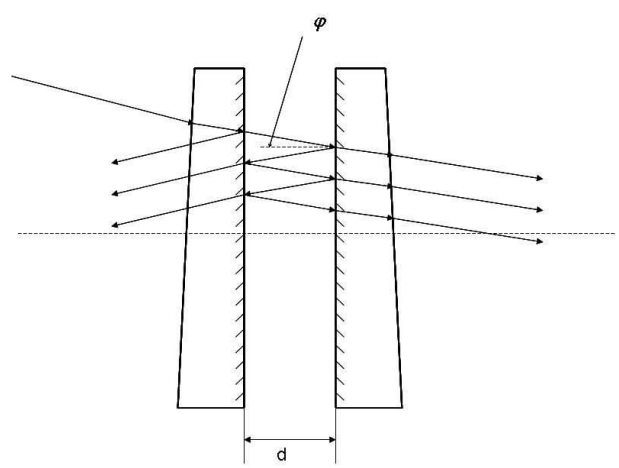

Figure 2.13: The manyfold reflection of a light beam in a Fabry-Perot resonator with air space between mirrors.

The intensity transmitted by one resonator is given by the Airy function:

$$I = I_0 \frac{\tau^2}{(1-r)^2 + 4r\sin^2(\frac{\delta}{2})}, \tag{2.47}$$

with τ is the transmission[7] through the plane and $\delta = 2\pi\Delta_0/\lambda$ is the phase shift associated with the path difference Δ_0. According to equation (2.47) maxima of the transmitted intensity I occur if $\delta/2 = p\pi$ which corresponds to $\Delta_0 = p\lambda$. In such case

[7] τ and r are defined in terms of the intensity of the light wave, i.e. $\tau = \frac{I_\tau}{I_0}$ and $r = \frac{I_r}{I_0}$ respectively.

$$I_{max} = I_0 \frac{\tau^2}{(1-r)^2}. \tag{2.48}$$

In the ideal case where there is no absorption loss inside a mirror $(1 - r = \tau)$ $I_{max} = I_0$, i.e. all the energy from the source in the direction of maximum passes through the cavity.

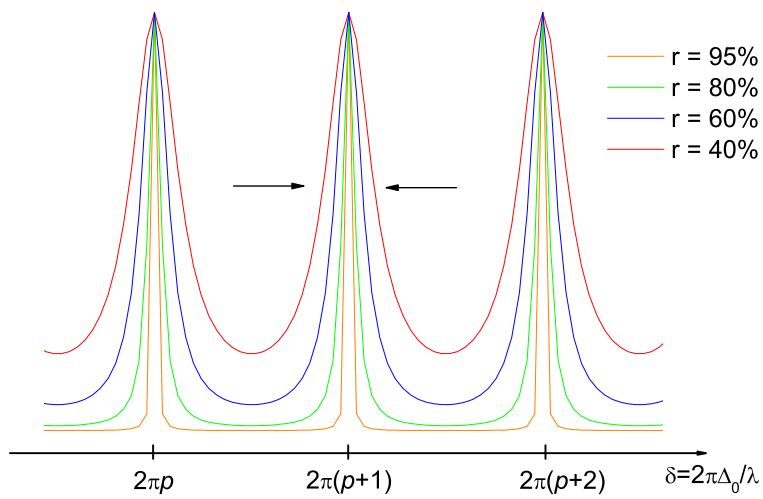

Figure 2.14: The distribution of the relative intensities I/I_{max} in the interference of a FP resonator as a function of δ for different values of the reflection coefficient r.

The minima of the transmission function, according to equation (2.47), correspond to $\sin(\delta/2) = 1$, and the intensity of transmitted light is

$$I_{min} = I_0 \frac{\tau^2}{(1+r)^2}. \tag{2.49}$$

The ratio of maximal and minimal transmitted intensities defines the contrast γ:

$$\gamma = \frac{I_{max}}{I_{min}} = \frac{(1+r)^2}{(1-r)^2}. \tag{2.50}$$

According to that expression, the contrast of a FP resonator is controlled by the value of r: the closer r is to unity, the more defined the resonance. Typical contrast values of each Tandem's resonators FP is $\approx 10^3$.

Figure 2.14 shows a spectrum of transmission of one FP resonator calculated according to expression (2.47) assuming the absence of absorption loss. It is clear that the reflec-

tion coefficient controls the width of the transmission line, hence the so-called "resolving power" $\delta\lambda$. Indeed, the resolving power of a cavity FP is expressed by

$$\frac{\lambda}{\delta\lambda} = \frac{2\pi d}{\lambda}\frac{\sqrt{r}}{1-r}. \tag{2.51}$$

If we deal with high quality cavity so that r is close to 1, then $\sqrt{r} \approx 1$ and with negligible error an estimate of the width is

$$\frac{\lambda}{\delta\lambda} \approx \frac{6d}{\lambda(1-r)}. \tag{2.52}$$

This means that resolving capacity is proportional to the distance between the mirrors, but that distance cannot be increased indefinitely because of the difficulty of maintaining a perfect parallelism between two mirrors. In our setup the limit mirror spacing is ~ 2 cm. The mirror spacing also influences the *free spectral range* (FSR) of the cavity. The FSR is a frequency distance between two consecutive maxima of the transmission function. Assuming the angle $\varphi \longrightarrow 0$ in the equation (2.46) we can write

$$FSR = \Delta\nu = \Delta p\frac{c}{2d}. \tag{2.53}$$

For neighboring maxima $\Delta p = 1$, thus the FSR is inversely proportional to mirror spacing. The FSR is widely used in FP experiments because it is a very important instrumental parameter which being changed, controls the extant of the spectral part one can record. As the FSR is inversely proportinal to mirror spacing d, it is evident (Eq.(2.51)) that it is inversely proportional to the resolution. The ratio between $\Delta\nu$ and $\delta\nu$ is called the *finesse*:

$$F = \frac{\Delta\nu}{\delta\nu}. \tag{2.54}$$

This parameter is very important as it defines the quality of the resonator and so that of the experimental results. Using equations (2.51) and (2.53) and also remembering the relations $\frac{\delta\lambda}{\lambda} = \frac{\delta\nu}{\nu}$ one can show that

$$F = \frac{\pi\sqrt{r}}{1-r}. \tag{2.55}$$

From this expression it is clear that the finesse depends only from the reflection coefficient.

Unfortunately, one FP resonator does not possess sufficiently high contrast. Therewith the intensities of all orders of transmitted light are approximately similar which can lead to overlaps of identical inelastic spectra belonging to different transmission orders.

Figure 2.15 illustrates such confusing situation from the Brillouin scattering of silica. Typically, the Brillouin spectra should look like that from Figure 2.3: one elastic component (Rayleigh scattering) and two (Stokes and anti-Stokes) inelastic (Brillouin) signals (in the present case, where both longitudinal and transverse Brillouin lines are observed, one expects two inelastic signals apart the Rayleigh one). One observes in Figure 2.15 that the Stokes part of p-th order overlapq with the anti-Stokes part of the $(p+1)$-th order (labeled with primes). To avoid such overlap, and improve the resolution, one may use a tandem of FP which consists in a set of two resonators.

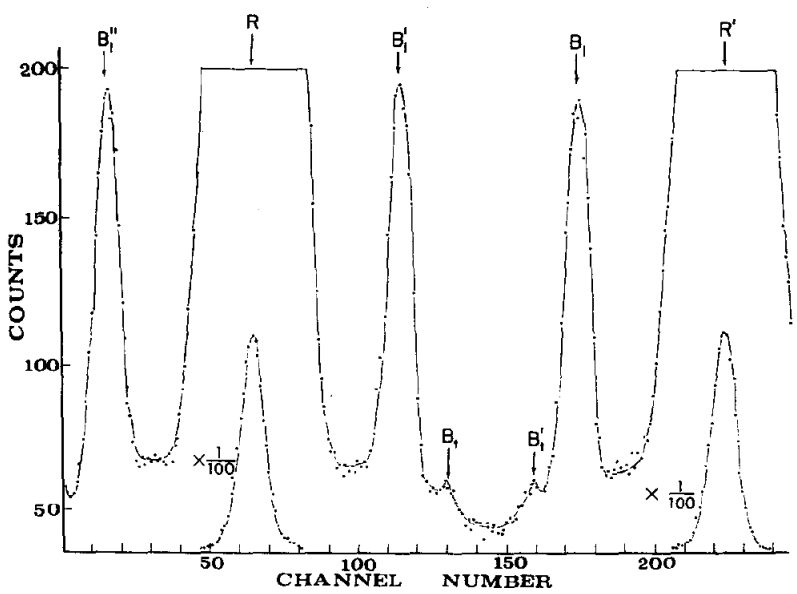

Figure 2.15: Brillouin scattering spectrum of a glass made by one FP spectrometer [71]. The free spectral range is 22.43 GHz. R designates the Rayleigh line and B_l and B_t the longitudinal and transverse Brillouin components, respectively. The second-order lines are indicated by a prime and one line of a third order is indicated by a double prime (B_l''). The Rayleigh peaks scaled down by a factor of 100 are also shown.

Theory of a Tandem

If the beam passes through two FP cavities placed sequentially and adjusted on the same resonance frequency with mirror spacings in a ratio ~ 1, then the contrast and the resolution of such system is notably higher than those of a single FP. The FSR of this tandem is defined by the FP with the smallest mirror spacing, and the resolution is defined by the FP with the largest mirror spacing. The contrast of the tandem is the product

of the contrasts of both FPs, as the transmission is $I = I_1 I_2$. Figure 2.16 shows the resulting transmission of a tandem FP after setting of two resonators. The main outcome of the tandem set is that non-coinciding orders produce a nearly zero transmission so that mixing of different lines with respect to different orders is nearly suppressed. As far as the intensity of the background between maxima of a cavity is not exactly zero, the transmission function of the tandem shows "extra" double-maxima (ghosts). Usually the intensity of a ghost is γ times weaker than that of the main maximum, where γ is a contrast of the whole system.

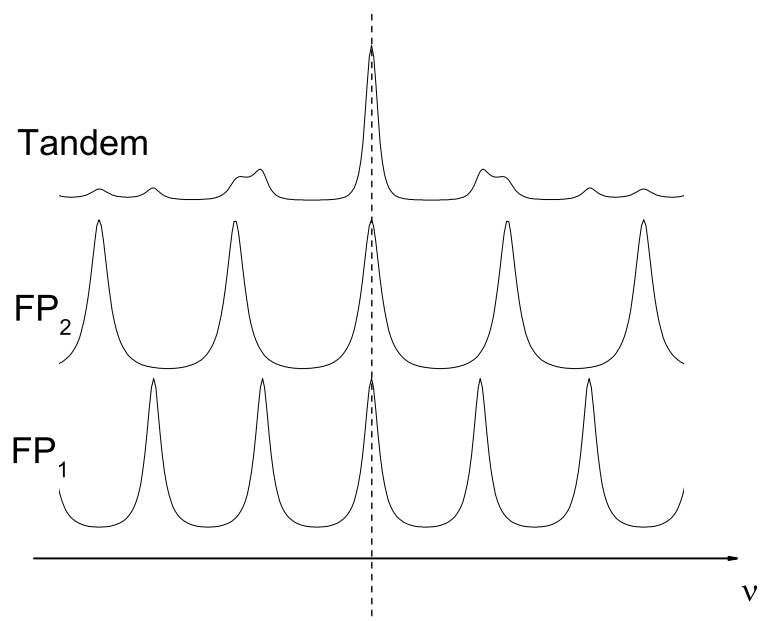

Figure 2.16: Transmitted intensity of a tandem made of two sequential resonators FP: $I = I_{FP_1} I_{FP_2}$. The intensities of the single FP are in linear scales, the intensity of the tandem is in logarithmic scale.

In the Tandem FP designed by J.R. Sandercock the light passes three times through each cavity. It means that theoretically the resulting intensity of the whole system is $I_T = I^3_{FP_1} I^3_{FP_2}$. The contrast of the whole system is also the product of the contrasts of both resonators FP: $\gamma_{2FP} = \gamma_1 \gamma_2$, so that in the Tandem FP after three passes: $\gamma_T = \gamma_1^3 \gamma_2^3$. Due to the total three passes through one FP the theoretical value of the contrast increases to 10^{18}. The experimental measurements of this parameter [5] showed a value of more than 10^{10}. This notable increase of the contrast makes the system very sensitive and

allows to observe very subtle spectroscopic effects.

Design of the Tandem

Two resonators in the Tandem FP are arranged sequentially along the light path at the angle α to each other on a common stage as shown in Figure 2.17. One mirror of each resonator (the second for the FP_1 and the first for the FP_2) is fixed on a common translation stage which is able to shift precisely. The axis of FP_1 lies along the direction of the translation stage motion. Thus, the ratio between two mirror spacings is expressed by

$$d_2 = d_1 \cos\alpha. \tag{2.56}$$

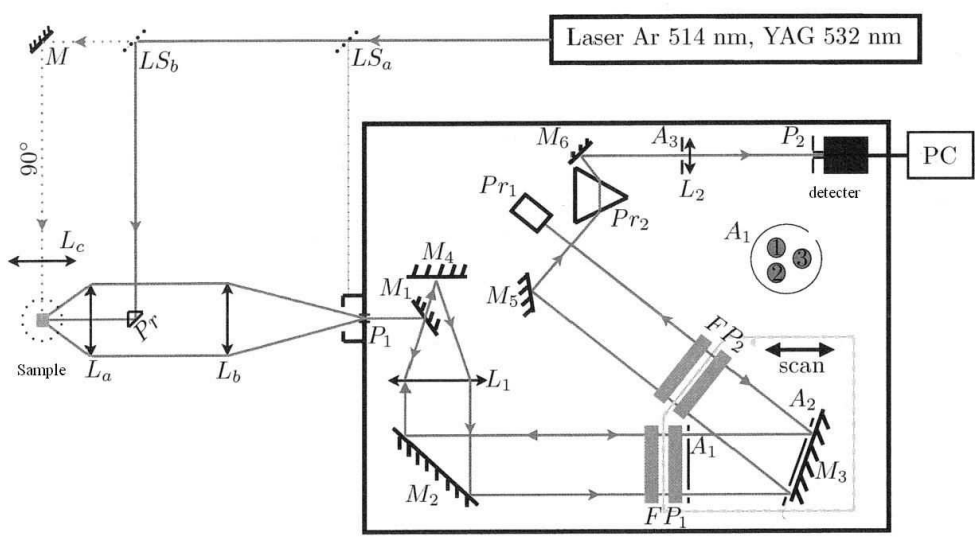

Figure 2.17: The scheme of the Tandem FP.

To achieve an optimal suppression of the higher order of transmissions (Fig.2.16), this ratio is set to 0.95, so that $\alpha = 18°$. Translating the whole stage by δd_1 produces a change of spacing δd_1 in FP_1 and of $\delta d_1 \cos\alpha$ in FP_2. As $\delta d_1/\delta d_2 = d_1/d_2$, the two interferometers scan synchroneously. As the translation stage is moved off the coinciding order position, one allows light with wavelengths $\lambda' \neq \lambda_p$ to be transmitted by the system. A scan of the translation stage about the central position allows to cover both Stokes and anti-Stokes sides.

In practice the environment of the Tandem (temperature, air pressure, humidity) can change either the optical length of a resonator FP or the spatial localization of the mirrors. This means that to repeat the scan, the stability of the Tandem has to be controlled with a high precision. In fact this has been a major technological challenge in the development of FP interferometers. To compensate for these factors one of the two mirrors of each FP is fixed by three ceramic piezoelectric elements which control the positioning of the mirror (around vertical and horizontal axes) and help to reach the parallelism of mirrors in each FP better than $\lambda/100$. Using another piezoelectric element we can change the mirror space of each FP for several wavelengths. This gives an opportunity to adjust both FPs in resonance at the same frequency.

We now consider the optical path of the beam inside of the Tandem FP (Fig.2.17). The light scattered from the sample is collected and focused on the input pinhole P_1 of the Tandem. After successive reflections (M_1, M_2) the light passes through FP_1 then (via M_3[8]) trough FP_2. The 90° prism Pr_1 deflects the beam in the vertical plane, redirecting it into FP_2 and FP_1 for a second pass. The third pass is enabled by a cat's eye mirror M_4 which deflects the beam in the horizontal plane. Passing both cavities the beam reflects from mirror M_5 and comes to the detector through the system that consists of the prism Pr_2, mirror M_6 and lens L_2. As a detector a Si avalanche photodiode (SPCM-AQR, Perkin Elmer) is used. It is very sensitive in the range of wavelength from 400 to 1060 nm and has a dark noise level less than 1 photon/ms/channel. The passes are separated from each other by aperture diaphragms A_1, A_2 and A_3. The scheme of A_1 (Fig.2.17) shows the spatial distribution of the rays.

Table 2.1 summarizes the technical characteristics of the Tandem FP.

Controling systems of Tandem

As mentioned before, the mirror spacing and the parallel alignment of the mirrors are very sensitive to the environment conditions but from the opposite side they should not vary with time during the experimental work otherwise the alignments of the resonators are lost. This requires dimensional stabilities of the order of 20 Å [68]. For these purposes an automatic stabilisation system of the Tandem FP was created.

A small fraction of the incident laser light, so-called reference beam, is taken out (LSa in Fig.2.17) and focused onto a side pinhole where through light is injected for

[8]The mirror M_3 has comparably low reflective index $r = 90\%$. Due to this the influence of the cavity consisting of the second FP_1 mirror and the first FP_2 on the resulting system is negligible.

Table 2.1: Main characteristics of the Tandem FP built by J.R. Sandercock, together with those of the exciting sources used at the LPCML.

Parameter	Value (Type)
Wavelength of exitation, nm	Ar^+ laser lines: 514.5; 488; 476.5 YAG laser line: 532 Semiconductor laser line: 561
Power, mW	0 – 150
Finesse	>100
Contrast	$>10^{10}$
FSR, GHz	5 – 2000
Mirror spacing, mm	0.03 – 20
Scanning range, μm	$0 - 2.5 \pm 0.0001$
Maximum mirror tilt during scan, rad	10^{-8}

purposes of dynamical alignment. Two shutters, one in the light path of the reference beam, another in the path of the light from the sample, control the light flow entering the interferometer. They are alternatively switched by the computer at a rate of the order of tens of milliseconds. During the scan procedure the shutter of the reference beam is closed and that of the probe beam is opened. When the scan passes through the position of the elastic line the sample beam shutter closes and the reference beam shutter opens. This provides both protection of the detector from the powerful elastic line scattered by the sample and stabilization of the interferometer's mirror positions. The system traces the signal [65] of the last scan over the central elastic peak, i.e. the integrated counts of the peak center N_c and the counts of the left N_{c-} and right N_{c+} half of the central peak. While N_{c-} and N_{c+} are needed to evaluate a possible drift (drift stabilization) of the transmitted reference signal, N_c is needed to optimize any possible loss of alignment of the resonators through the control of the piezoelectric elements (finesse optimization).

The drift stabilization comes according to a correcting algorithm which calculates the correction value:

$$Z_c = C_c \frac{N_{c+} - N_{c-}}{N_{c+} + N_{c-}}, \tag{2.57}$$

with C_c is a properly chosen constant. Z_c is applied as a change of offset to the scan

voltage.

The finesse optimizer algorithm is more complicated because of the five degrees of freedom of the Tandem stability: two axis of the mirrors of each resonator FP_1 — X_1 and Y_1, and FP_2 — X_2 and Y_2, and ΔZ — the difference of the spacings d_1 and d_2. It takes 12 scans in pairs for a full stabilization cycle: within two consecutive scans the voltage for axis X_i is set to $X_i - \delta$ in the first scan and to $X_i + \delta$ in the second scan. Due to its high sensitivity the ΔZ alignment steps are performed twice during a full alignment cycle. The corresponding finesse signals are $N_c(-\delta)$ and $N_c(+\delta)$. The algorithm calculates the following value:

$$Z_F = C_F \frac{N_c(+\delta) - N_c(-\delta)}{N_c(+\delta) + N_c(-\delta)} \delta, \tag{2.58}$$

with C_F a properly chosen parameter. After, the algorithm adds this value as an offset to the corresponding parameter.

Such sensitive mechanism requires a vibration free environment. For example, the vibrations coming from the scanning process have an order of frequency of 12 GHz. They and other incoming vibrations are suppressed by the anti-vibrational module installed beneath the scan stage and consists of two systems: static and dynamical. The static system is a traditional solution to vibration problems using very soft passive springs. The dynamical isolation system uses feedback control and is installed directly on the optical table, therefore its components are, in general, not sensitive to external vibrations.

Ambient air refractive index fluctuations are minimized by enclosing the Tandem FP in a protective box. To avoid any changing of the length of the optical paths of the rays, the Tandem FP has to be installed in a room with temperature control: fluctuations of temperature $\pm 2°$C can lead to destabilization of the apparatus.

Optical setup outside the Tandem

The Tandem FP is installed on an optical table and included in the optical scheme of the experiment as it is shown in Figure 2.17. The vertically polarized laser beam radiated by the laser passes through the splitter LS_a and splits up into two beams of different powers. The weakest one (around 5% of the original power) comes to the input pinhole P_1: it is used as a reference beam. The main part of the beam goes to the sample. The light scattered by the sample is collected by the objective L_a and focused by the lens L_b to the input pinhole. In order to control the polarization of the scattered light, a polarizer is placed before the input pinhole. Hence, we can record polarized (VV) (vertical-vertical:

parallel polarizations of excitation and detection) spectra and depolarized (VH) (crossed polarizations) spectra. The differences between these spectra can give information about the nature of the vibrations (see next chapter).

The angle between light incident on the sample and the axis of the detection of the scattered light gives a name to the scheme of experiment. The most famous one is backscattering geometry (Fig.2.5), also 90°-schemes (Fig.2.6 – 2.8) are very widely used. In the backscattering scheme, the 90° prism Pr is used. The angle of experiment allows to carry out the investigations with different vector $\vec{q}$ as it was described in the section dedicated to Brillouin scattering. Carrying out the experiments with "small" NPs (this means we investigate pure Raman scattering so that there is no q-dependence) we prefer to use the backscattering scheme as the scattered signal in this geometry is the most convenient.

As it was mentioned before, the mirrors of the FPs have to be of very high quality, with special dielectric coating. Such type of mirrors can be used only in a restricted interval of wavelengths. In our Tandem FP, we use the set of mirrors allowed to work with blue, green and yellow wavelengths. The sources of monochromatic light are essentially three: the green line is a line of the second harmonic of a YAG laser with wavelength 532 nm; occasionally the blue lines are those of gas Ar^+ laser: 476.5 and 488 nm (also it is possible to readjust this laser on the wavelength 514.5 nm); the yellow line is a line of semiconductor laser with wavelength 561 nm.

Non-Tandem techniques. Monochromator Z40

Before the acquisition of a Tandem FP, most low frequency Raman scattering studies at the LPCML were performed using a quintuple monochromator. The five-grating monochromator Z40 is an apparatus, made by Dilor, puprposely designed for the investigation of both the low frequency Raman scattering and classical Raman scattering. It consists of five gratings with 1800 traits/mm located along the same rotating axis and a system of parabolic mirrors with focus distance equals to 80 cm (Fig.2.18). The scattered light passes through the input slit of the device and comes to the first grating. Changing the angle between grating and incident light it is possible to select a unique wavelength. After the reflections from all gratings light comes to the photomultiplier (PM). In order to decrease the level of the dark noise of the PM, the latter is cooled down by Peltier elements. Spectra are recorded step by step, as defined by the user. Its technical characteristics are listed in Table 2.2.

The Z40 was worked out earlier than the Tandem FP. Although of high performance with respect to grating monochromator tt has a lower resolution and cannot approach as close to the elastic line as the Tandem FP can but it is still very useful to measure the range of spectrum between ~ 5 and 200 cm^{-1}. The Tandem FP is not specially meant to measure this range and modern classical Raman spectrometers usually do not come towards elastic line closer than 50 cm^{-1} (using Notch filters).

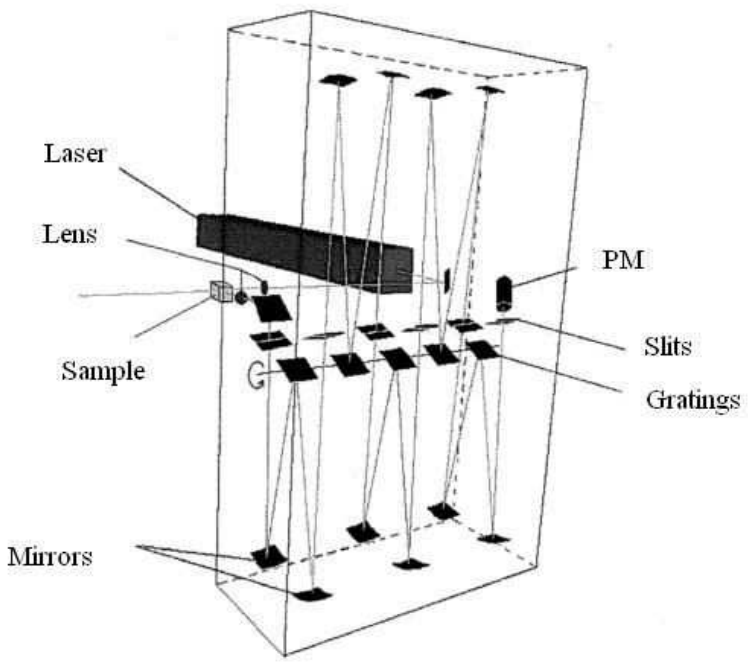

Figure 2.18: The five-grating monochromator Z40 [72].

In our experiments with large viruses we were able to use only the Tandem FP: due to the large size of the viruses the vibrational eigenmodes of the virus were expected at 5 – 10 GHz which is impossible to detect by Z40. For investigations with metal NPs we used both devices: the notably high resolution of Tandem FP allows to observe a fine effects [59] such as the splitting of quadrupolar mode whereas Z40 helped us to confirm high frequency vibrational modes which are hardly visible in the spectra recorded by Tandem FP. In Figure 2.19 a comparison between two signals detected by the two devices from the same sample is represented. Clearly, the Tandem FP is an asset for very low frequency investigations.

Table 2.2: Some important characteristics of Z40

Parameter	Value (Type)
Wavelength of exitation, nm	Ar^+ laser lines: 514.5; 488; 476.5 Kr^+ laser line: 647.1; 676,4
Power, mW	$0 - 500$
Minimal step of scan, cm^{-1}	0.1
Geometry of experiment	Backscattering, 90°, 90°R, 90°A

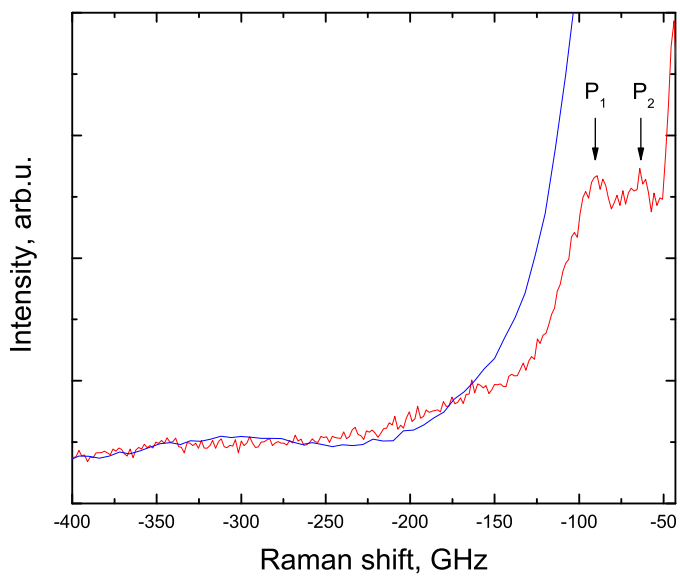

Figure 2.19: The comparison of spectrum quality between the Z40 (**blue**) and the Tandem FP (**red**). Both spectra are the scattered signal from copper nanoparticles of size of ~ 21 nm. The Z40 spectrum was recorded with exciting wavelength 514.5 nm whereas the Tandem's spectrum was made using the YAG line 532 nm. It is clear that the Tandem's spectrum contains two peaks which are not resolved in the Z40 spectrum.

Chapter 3

Low frequency Raman scattering from the metal nanoparticles

This chapter is dedicated to Low Frequency Raman Scattering (LFRS) investigations of metal NPs. As mentioned before, the design of high-resolution devices such as the Tandem FP made it possible to inspect fine vibration effects associated with the crystalline inner structure of the vibrating nano-objects. The elastic anisotropy stemming from the crystalline atomic arrangement inside the NPs leads to a lift of degeneracy of the quadrupolar mode, that may have been unseen in "old" data [59]. There are several possible explanations for this fact:

- the frequency splitting of the quadrupolar mode is too small to be resolved by the used spectrometers; this adds to the experimental difficulty of low frequency Raman scattering from NP vibrations, as it is already difficult to resolve small inelastic signals from the large elastic one.

- the probe NPs are not "perfect" nanocrystals. As we will see, this can either come from the fact that LFRS probes polydisperse assemblies of NPs or from the fact that the crystalline structure of the NP is not "perfect". Both effects tend to smear out the observability of the splitting.

In this chapter, we report investigations aiming at better understanding the LFRS from either embedded or non embedded NPs, on the grounds of the recently established effect of elastic anisotropy. Essentially three types of metal NPs were studied:

1. *Bimetallic NPs of AuAg grown in a vitreous matrix.* Carrying out experiments with these objects the splitting of the quadrupolar mode of highly crystalline NPs was

confirmed. Also we managed to observe for the first time high frequency harmonics of the quadrupolar mode. This latter finding allowed to perform a comparison with theoretical predictions on the Raman activity of NP modes. The related results are published in paper [73].

2. *Au nanocrystals deposited on a surface.* In this case, the controlled synthesis of the NPs allowed to investigate the influence of cristallinity on the splitting of quadrupolar mode. The good crystallinity of the studied nanocrystals enabled a reliable quantitative evaluation of the frequency splitting. The dependence of the LFRS on the excitation wavelength is found to be consistent with the selective excitation of Au NPs with different crystalline structures and related shapes. This investigation is the continuation of the works reported in [30]. The results are published in ref. [74].

3. *Cu NPs grown in a vitreous matrix.* In this work we investigated the influence of the preparation conditions on the LFRS signal, in order to deduce information on the structure of the copper NPs. It will be shown that the annealing temperature plays a key role in the formation of the different types of NP structures.

3.1 Bimetallic silver-gold nanoparticles embedded in a glass matrix

3.1.1 Sample presentation

Bimetallic AuAg NPs were produced in a multicomponent silica glass of the St.Louis factory. The composition of the glass together with its elastic parameters derived from Brillouin measurements are given in Tables 3.1 and 3.2. It is worth to notice the rather large density of the St.Louis glass (usual density of SiO_2 glasses is around $\rho = 2.2$ g/cm^3) due to the Pb content. The NPs were prepared according to a standard method [75]: the metals were added to the raw materials as a solution of tetrachloroauric acid or potassium dicyanoaurate. Upon melting at about 1400°C the metals dissolve and are dispersed in the atomic form in the quenched glass. After this procedure the prepared glass is transparent and colorless. Only during prolonged annealing at the temperature sufficiently close to the glass transition temperature T_g (490°C) the glass acquires an amber shade as a result of the nucleation and growth of small metal particles which strongly absorb in the blue

part of the spectrum due to the SPR.

Table 3.1: Composition of the St.Louis glass.

Substance	Mass, %	Substance	Mass, %
SiO_2	53	TiO_2	0.1
PbO_2	30	Al_2O_3	0.02
K_2O	12	Cl	0.006
Na_2O	2	Fe_2O_3	0.005
Sb_2O_5	1.8	CaO	0.003
As_2O_3	1	Au	< 0.1
SnO_2	0.2	Ag	< 0.1

Table 3.2: Several important characteristics of the St.Louis glass.

Density, g/cm^3	$\rho = 2.97$
Speed of sound, m/s	$v_L = 5020$ $v_T = 3010$
Refractive index	$n = 1.59$
Transition glass temperature, °C	$T_g \approx 490$

The studied samples are small glass squares of about 1 cm^2 of 2 mm of thickness (Fig.3.1). They were annealed at 490°C over 8, 16, 32 and 64 hours. The change of the color indicates a change of the SPR with annealing, as we discuss now in the next section.

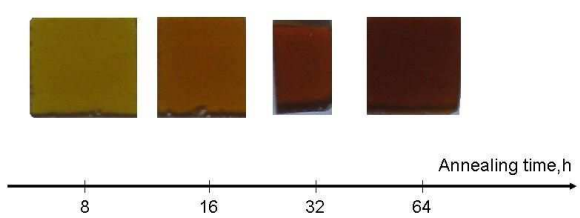

Figure 3.1: AuAg samples annealed during 8, 16, 32 and 64 hours at the temperature of 490°C.

3.1.2 Optical characterization. Discussion about the type of NPs

In the process of growing of NPs in a glass containing two different types of atomic metals the first question is: what is the structure of the formed NPs? Theoretically three cases are possible: coexisting pure gold and pure silver NPs, core-shell NPs (possibly with silver as a core due to the greater diffusion coefficient of silver), and NPs formed of an alloy of the two metals. The results of optical absorption measurements may help clarify this situation using the behavior of the SPR as a probe.

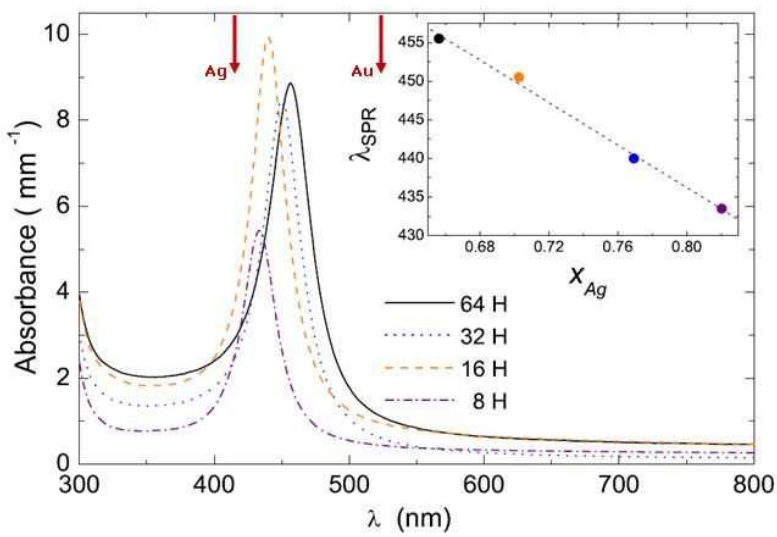

Figure 3.2: Absorption spectra of the AuAg samples annealed during 8, 16, 32 and 64 hours at 490°C. Red arrows mark the positions of the SPR peaks of pure gold and pure silver NPs of the same sizes. **Inset:** the dependence of the SPR peak position on the values of x (atomic ratio of Ag in the NPs)

.

Figure 3.2 shows the results of these measurements. All curves were normalized with respect to the thickness of the samples. These data show a single SPR peak around 445 nm. This value lies between that of pure silver (414 nm [51, 76]) and that of pure gold (529 nm [59]) when particles of comparable sizes are embedded in a matrix with similar refractive index. As we observe a single narrow peak we can conclude that the distribution of NPs is homogeneous and NPs are bimetallic: two sorts of NPs would give two distinct plasmon peaks. The alloy or core-shell structure of the formed AuAg NPs is more delicate to firmly establish, as the influence of a core-shell structure on the SPR of embedded NPs

is itself poorly characterized. Two observations can be made from Figure 3.2:

- the SPR is remarkably narrow ($\lambda/\Delta\lambda \sim 14$) in comparison with that reported for comparable systems [77, 78, 79, 80]. Looking at experimental SPR curves of core-shell AuAg NPs [81, 82], it appears that the alloy SPR is systematically narrower. One may therefore interpret the narrowness of the observed SPR as coming from alloy rather than core-shell NPs.

- Upon increasing annealing time, the measured SPR position shifts towards the pure gold SPR position. This shift is usually interpreted [77, 78] in terms of an alloy behavior such that

$$\lambda_{Ag_xAu_{1-x}}(t_a) = x\lambda_{Ag}(t_a) + (1-x)\lambda_{Au}(t_a), \tag{3.1}$$

where $\lambda_{Ag}(t_a)$ and $\lambda_{Au}(t_a)$ are the pure Ag and pure Au SPR peak positions respectively and x is the atomic fraction of Ag in the alloy NP. On the basis of this relation, we have derived the variation of x with annealing time. The value of x is found to vary between 0.82 and 0.66 as the annealing time increases from 8 to 64 hours (see inset of Fig.3.2). This variation reflects an Au enrichment of the NPs with increasing annealing time. Overall, the AuAg NPs are found to be Ag-rich, rather than Au-rich. This may be at the origin of the obtained remarkable Raman results.

3.1.3 Low frequency Raman scattering experiments

The LFRS experiments were carried out in backscattering geometry (as the most convenient one to obtain enough signal). The chosen FSR was set to 550 GHz. All spectra were recorded at room temperature thanks to the Tandem FP interferometer using the exciting radiation of the YAG laser 532 nm, i.e. a little bit off the SPR maximum. The main results are displayed in Figure 3.3 where the polarized (i.e. VV) spectra of the four samples are shown. The most distinctive feature is that these spectra have remarkably many components. If we make a comparison with most Raman data reported for metal NPs (see chapter 3) we see that they usually show only two bands which correspond to the quadrupolar and the spherical modes whereas in the given spectra we can indentify four components, located at approximately 75 GHz, 150 GHz, 300 GHz and 460 GHz. Among these four components, the straightforwardly identifiable one is the fundamental quadrupolar mode (near 75 GHz) which is known to dominate the low frequency Raman spectrum from metallic NPs; in spite of many erroneous assignments [83, 84, 85], the

quadrupolar mode is definitely the lowest frequency mode among the Raman active ones [86].

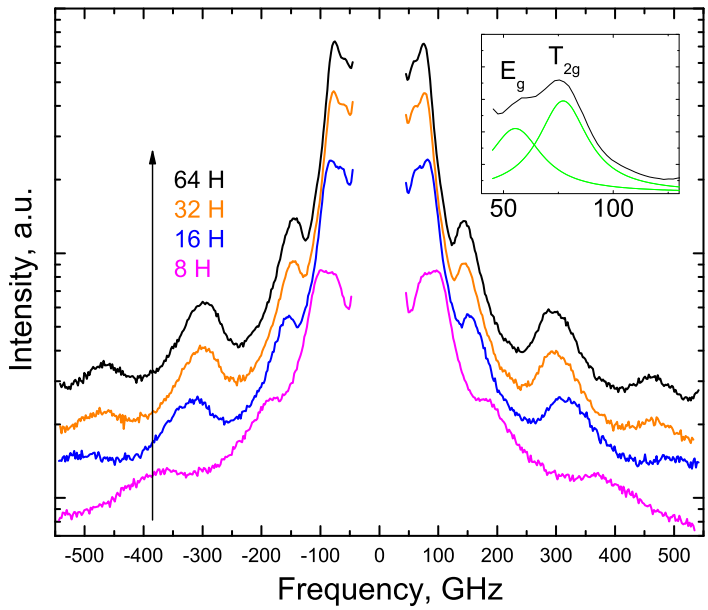

Figure 3.3: LFRS VV spectra of the AuAg samples annealed during 8, 16, 32 and 64 hours at the temperature of 490°C. Spectra are normalized on maximum and shifted along vertical log-scaled axes for clarity. **Inset:** the zoom of the the lowest frequency line demonstrates a splitting of the quadrupolar mode.

A close inspection of the quadrupolar band profile shows a double component structure (Inset of Fig.3.3) which is similar to that observed for pure Au NPs, produced in the same type of glass, using a similar protocol [59] (Fig.3.4). This double structure was interpreted for the first time as the signature of elastic anisotropy, which, as explained in section 1.5, partially lifts the degeneracy of the quadrupolar mode. The observation of more components in the case of AuAg NPs allows to refine this first interpretation.

In order to identify the many components of the AuAg low frequency Raman spectra, we compare the polarized (VV) and depolarized (VH) spectra of a same sample. As stated in section 1.3, while the polarized spectra feature the contributions of both $\ell = 0$ and $\ell = 2$ modes, only the $\ell = 2$ modes can contribute to the depolarized spectrum. Figure 3.5 displays the comparison of the VV and VH spectra of the sample annealed at

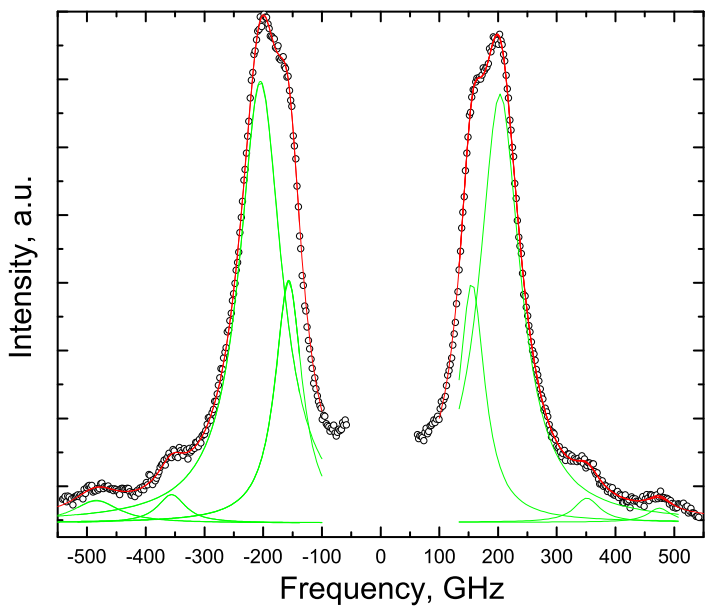

Figure 3.4: LFRS high-resolution spectrum of Au NPs embedded in St.Louis matrix [59].

64 hours. Testing different spectra normalizations with respect to the different maxima reveals that band profile changes are essentially observed around the 150 GHz and the 300 GHz regions (Inset A of Fig.3.5). As will be seen later, they can be ascribed to the contributions of the spherical mode. It turns out that most of the bands observed either in the VV or VH spectra come from the fundamental and harmonic vibrations of the quadrupolar mode. In the following, we proceed to the identification of these harmonics.

The quadrupolar mode

A multi-Lorentzian decomposition of the VH spectrum (Fig.3.6; the experimental frequency positions are listed in column "Exp" of Table 3.3) reveals the previously mentioned 5 components, two of them forming the intense lower frequency doublet evidenced thanks to the high resolution Fabry-Perot setup. The observed frequency ratio between the lower and the larger components of the E_g/T_{2g} doublet $\frac{\nu_{T_{2g}}}{\nu_{E_g}} \simeq 1.4$, is close to the value expected for either free Au or free Ag (~ 1.6). A more detailed investigation of the E_g/T_{2g} splitting will be reported in section 3.2, with the study of non-embedded Au NPs.

In order to identify the three remaining higher frequency components approximately

Rank n	Exp		Calc Free		Calc Emb		
	ν_n	ν_n/ν_1	ν_n	ν_n/ν_1	ν_n	$\Delta\nu$	ν_n/ν_1
E_g	55	0.83	-	-	-	-	-
T_{2g}	77	1.17	-	-	-	-	-
1	77	1	77	1	77	9.7	1
2	146	**1.9**	152	1.97	145	10.6	**1.88**
3	-	-	253	3.29	221	9.2	2.87
4	293	**3.8**	346	4.49	296	10.0	**3.84**
5	-	-	379	4.92	319	16.5	4.14
6	-	-	447	5.80	378	10.6	4.90
7	464	**6.02**	538	6.99	454	10.6	**5.90**
8	-	-	599	7.78	505	17.3	6.56
9	-	-	633	8.22	532	11.0	6.90
10	-	-	724	9.40	609	10.8	7.91

Table 3.3: Comparison of experimental (Exp) and calculated (Calc) harmonic frequency positions and harmonic-to-fundamental frequency ratios for the quadrupolar mode of a $Ag_{0.66}Au_{0.34}$ nanoparticle with 20.5 nm diameter in the embedded (Emb) case (CFM) and 17.2 nm diameter in the case of a *free* sphere. The bold values emphasize the correspondance between experimental and calculated values.

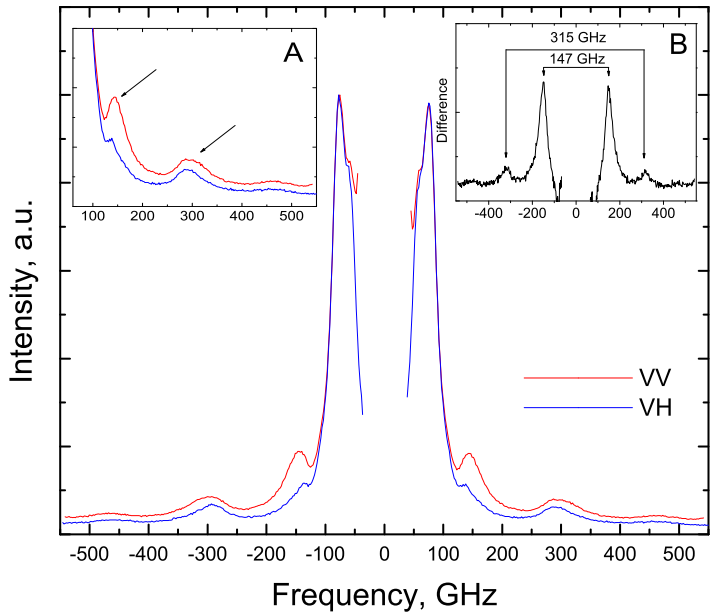

Figure 3.5: Comparison of the VV and VH spectra of the richest Au sample (64H annealing). The intensities were scaled with respect to the most intense line. **Inset A:** Enlargement of the Stokes side; the arrows point the modified regions. **Inset B:** The difference spectrum (VV-VH) unveils the contributions from the spherical mode.

located at 150, 300 and 460 GHz, we first compare the experimental positions to those calculated from the CFM which allows to determine the eigenfrequencies of a nanosphere embedded in a matrix as well as the corresponding lifetimes (expressed in frequency $\Delta\nu$) of the eigenmodes [25, 87]. These calculations require the input of the matrix parameters (density $\rho = 2.97$ g/cm^3; $v_L = 5020$ m/s and $v_T = 3010$ m/s, as derived from Brillouin light scattering measurements on the same samples) together with those of the alloy NPs that were assumed to obey linear relationships as a function of x according to:

$$P_{Ag_xAu_{1-x}} = xP_{Ag} + (1-x)P_{Au}. \tag{3.2}$$

where the alloy property P_a is either the density ρ_a, the longitudinal v_L^a or transverse v_T^a sound velocity using $\rho_{Ag} = 10.5$ g/cm^3, $\rho_{Au} = 19.28$ g/cm^3, $v_L^{Ag} = 3747$ m/s, $v_L^{Au} = 3319$ m/s, $v_T^{Ag} = 1740$ m/s, $v_T^{Au} = 1236$ m/s.

Finally, the CFM calculations require the knowledge of the NP size. Ideally, one would prefer to rely on an independent evaluation of the NPs average size, determined

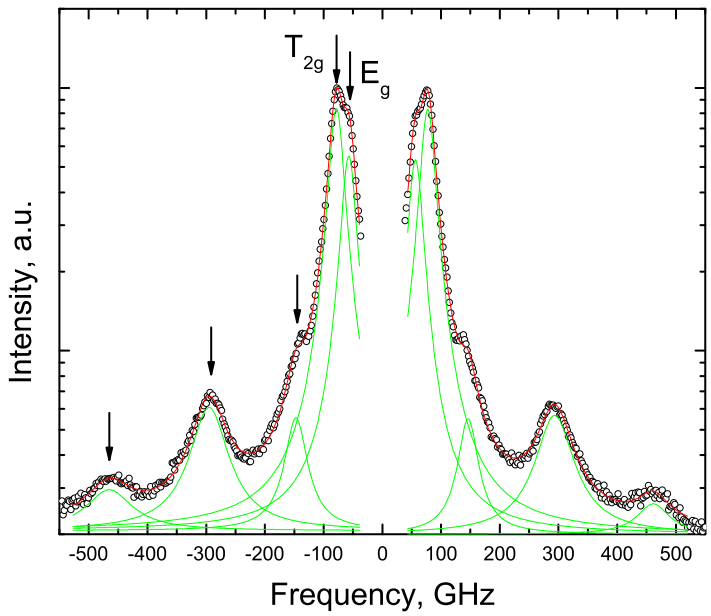

Figure 3.6: Five Lorentzian fit of the VH spectrum of the sample annealed for 64 hours ($Ag_{0.66}Au_{0.34}$). The non-labeled arrows point the detected high order harmonics.

for instance from Transmission Electron Microscopy (TEM). It occurs that TEM proves difficult to use with this kind of sample, as already experienced with embedded Au NP's [5]. This is essentially due to the buried nature of the NPs. In these conditions, the main difficulties met with TEM are the following:

- due to the very small initial content of metal incorporated in the glass (less than 0.1 mole%), the concentration of formed NPs is small. This means that spotting one NP within the TEM sampling is rather difficult and measuring a reliable size distribution virtually impossible;

- in order to obtain a good quality of TEM observation, one would need a very thin flat glass sample ($\sim$ 50 μm). Homogeneous thinning of a relatively hard glass sample, through successive steps of mechanical abrasion and eventually long time ion sputtering, has not yielded convincing results with respect to the invested time;

- TEM observations from microchips of samples obtained from diamond tip scratching remains as a possible alternative, although the non flatness of the microchips does

not favor the quality of the observations. Further in this chapter we will show TEM characterization attemps made with Cu-glasses; in the case of AuAg, none of these could be reliably used for the Raman analysis.

In the absence of sufficiently reliable TEM data, the mean diameter of the NPs has to be derived from the best agreement between the calculated and experimentally observed frequencies. Although in its present stage of development the CFM cannot account for the elastic anisotropy of the NPs (which we know is present from the observation of the E_g/T_{2g} doublet), we use it as a first evaluation tool. In these conditions, one criterion is to search a diameter value which provides the maximum of matchings with bands observed in the experimental spectra (Table 3.3). Taking into account the parameters of the embedding glass, this value is found to be 20.5 nm for the 64H sample. Using this diameter value, the "isotropic" fundamental quadrupolar mode lies at 77 GHz, which occurs to match the frequency of the T_{2g} component. This agreement might be explained by the fact that the T_{2g} mode is the one that least departs from the five-fold degenerated component upon splitting (see section 1.5). The agreement with the three higher frequency band positions is remarkably good: it comes out that the observed bands identify with the second ($n = 2$), fourth ($n = 4$) and seventh ($n = 7$) harmonics for which the relative difference between the CFM and experimental values (ν_2/ν_1, ν_4/ν_1 and ν_7/ν_1) are of the order of the percent. Had the effect of the matrix not been taken into account (column "Calc Free" of Table 3.3), with a size such that the "isotropic" fundamental quadrupolar mode lies at 77 GHz, the agreement would have been less satisfactory. The comparison between the free and embedded cases demonstrates that taking into account the embedding medium strongly modifies the harmonic-to-fundamental frequency ratios, which is due in the present case to the relatively large mass density of the glass. Finally, the CFM results are found to equally well describe the band positions for the samples with different x values (Fig.3.7).

The Raman activity of only selected harmonics ($n = 2, 4, 7$ from the CFM) of the quadrupolar mode was theoretically predicted with different methods [24, 49]. Our experimental observation overall agrees with these predictions in the sense that it confirms the unequal Raman activity among the harmonics: some harmonics are Raman active while some are silent. Both theoretical approaches pointed out that the key ingredient for the Raman activity of the quadrupolar mode (or at least affiliated ones in reference to the free nanosphere case) is the surface deformation induced by the mode. Using CFM, Saviot and Murray [24] identified this behavior through the mean square radial surface displacement ("URS") induced by each of the harmonics; indeed only harmonics whose

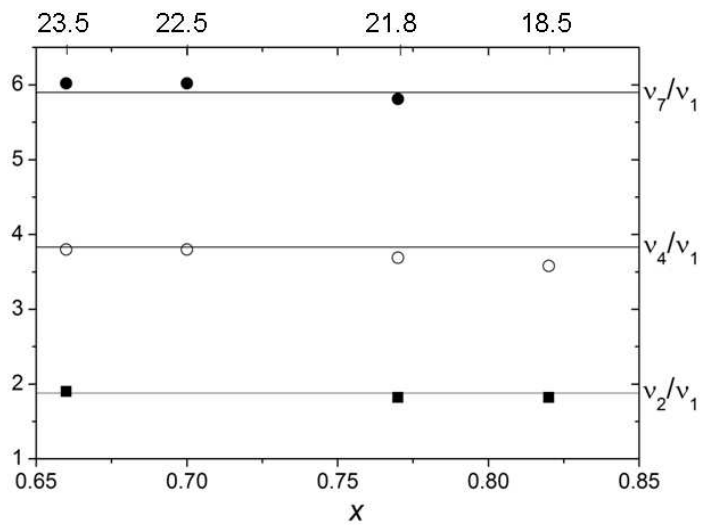

Figure 3.7: Comparison of the experimental (symbols) and the CFM calculated (lines) values of the harmonic-to-fundamental frequency ratios of the Raman active harmonics of the $\ell = 2$ mode, for the four different samples ($x = 0.66, 0.7, 0.77$ and 0.82). The top scale indicates the corresponding diameters, as deduced from the T_{2g} component.

URS are significant are found to contribute to the Raman spectrum. Such can be observed by visualizing the animations of the quadrupolar mode vibrations made by L. Saviot [88]. A similar conclusion was drawn from quantum calculations [49], where the gradient of the displacement field at the surface of the NP was identified as the main indicator of Raman activity. As explained below, this latter method enables a rather complete description of the entire spectrum, both in terms of band positions and intensities.

Comparison with Raman scattering intensity (RSI) calculations

G. Bachelier [49, 89] developed a theoretical approach to calculate the low frequency Raman spectrum from metallic NPs, taking into account the resonant Raman process with the dipolar surface plasmon. Before using the outcomes of these calculations, we briefly describe the physical mechanisms that these calculations revealed as relevant for Raman scattering.

The initially reported Raman scattering intensity calculations for metallic NPs [49] were developed for *free* NPs. The low frequency Raman spectrum is calculated through the computation of the Raman transition probabilities of a three-step scattering process:

(1) the surface plasmon-polariton (SPP) state (ω, L, M) is excited by the incoming photon where (L, M) the integer numbers associated with the spherical harmonic functions;

(2) the SPP decays into another SPP state (ω', L', M') through the emission or absorption of a confined (n, ℓ, m) vibration;

(3) the emission of the scattered photon.

Such scattering process involves two Hamiltonians: H_{ph-SPP} which corresponds to the photon-SPP interaction and $H_{vib-SPP}$ which describes the vibration-SPP interaction.

Along the computation of these interactions, essentially two effects turn out relevant: volume effects and surface effects. The *volume mechanism* is rooted in the modulation of the metal dielectric function by the NP lattice vibrations, through the deformation potential interaction. One finds that the change of dielectric susceptibility due to the interaction with the lattice vibrations essentially arises from *interband excitations*. In the calculation, the corresponding term features the interband dielectric function, the divergence of the displacement field associated with the vibration and the deformation potential energy, which is independent of the NP surface.

Unlike the volume mechanism, the *surface mechanisms* are involved whenever the shape of the NP changes along the vibration. Changing the shape of the NP leads to a change of the distribution of the polarization charges at its surface, with respect to that described in the static case (section 2.2.2). The computation of this term requires to quantitatively evaluate the variation of the surface polarization charge density with the oscillation of the NP shape. It occurs that a purely diverging displacement field yields a zero contribution in the surface mechanism. Basically, this mechanism is essentially sensitive to the displacement field at the surface of the NP, as was mentioned earlier through the evaluation of the URS within the CFM.

Considering the Raman active vibration modes ($\ell = 0$ and $\ell = 2$), it occurs that the two effects described above are separately dominant in the two types of modes (Fig.1.1). Since the radial vibration $\ell = 0$ induces a volume change of the NP with no shape deformation, its Raman activity is essentially controlled by a volume mechanism. Differently, the quadrupolar vibration $\ell = 2$ induces a surface deformation of the NP through a constant volume process and is therefore Raman active through a surface modulation effect.

The important advantage of the quantum calculation method developed by Bachelier *et al* is the prediction of the Raman intensities. As an illustration, calculations performed

for the quadrupolar mode of a *free* silver nanosphere of 5 nm diameter (Fig.3.8) already show good qualitative agreement with our experimental data on our embedded AgAu NP's (Table 3.3, Fig.3.6) although they concern obviously different systems. By "qualitative agreement", we essentially refer to the fact that approximately the same harmonics as those found by the CFM contribute to the Raman spectrum, with an intensity of approximately one order of magnitude lower than that of the fundamental mode.

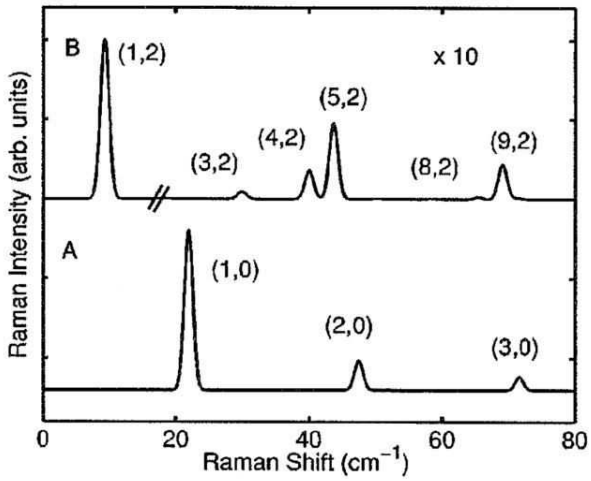

Figure 3.8: Normalized Raman spectra of silver NPs calculated with $R = 2.5$ nm, excitating wavelength is 496.5 nm. **A:** A spectrum corresponding to the volume coupling mechanism; **B:** A spectrum corresponding to the surface coupling mechanism, the frequency range 16–80 cm^{-1} is zoomed in 10 times. The figure was taken from [49].

In order to account for the effect of an embedding medium, G. Bachelier modified his calculation method so that the calculated frequency spectrum no more consists of a discrete set but rather of a continuum. As within the CFM, a perfect contact between the particle and the matrix is assumed in order to apply the standard boundary conditions between the two media. Figure 3.9 shows the results of these calculations for the quadrupolar mode of the 64H sample ($Ag_{0.66}Au_{0.34}$), using the same alloy and matrix parameters as those used for the CFM estimations, with the corresponding SPR wavelength as additional input parameter. As with the CFM, the Raman scattering intensity calculations do not account for the elastic anisotropy effects. In these conditions, the best overall agreement, which now relies on the barycenters of the bands rather than on their positions only (see previous comparison with CFM) is obtained by using a diameter of 23.5 nm. With such value, the fundamental quadrupolar vibration lies at an average position of the E_g/T_{2g} doublet. Once again, comparing the Raman intensity calculations

of the embedded case with those of the sphere case (vertical bars in Figure 3.9) shows that the presence of the matrix has a signficant effect; an estimation of the particle size based on the free sphere model would result in a $\sim 20\%$ smaller diameter.

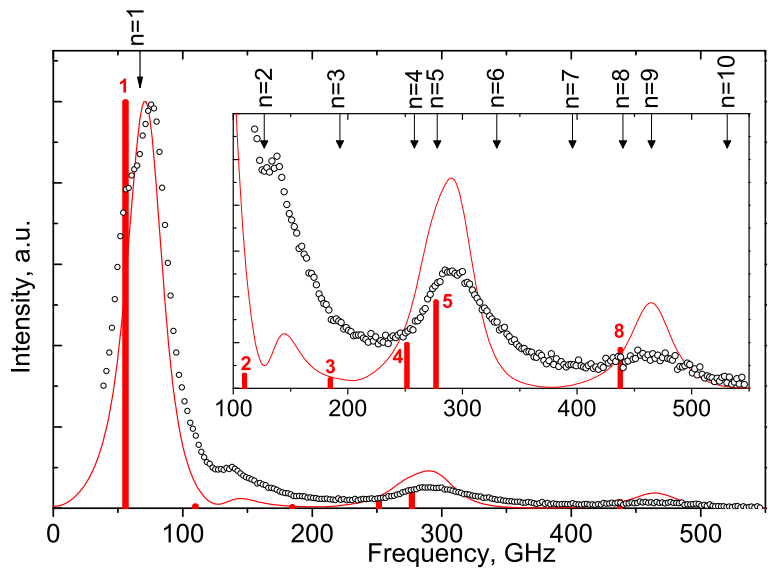

Figure 3.9: LFRS VH spectrum of the AuAg sample annealed during 64 hours at the temperature of 490°C. The size of the corresponding NPs is approximatelly 23.5 nm. Red solid curve is the RSI prediction of the Raman spectrum for NPs embedded in the matrix; red solid bars are the RSI prediction for the quadrupolar mode and its harmonics of free NPs; black arrows are the CFM predictions. **Inset:** Zoom of the the higher frequency part of the spectrum.

If one compares the outcomes of the RSI calculations for the continuum (embedded) and discrete (free) approaches, it is possible to filiate the observed bands with nearly the same overtones as those previously identified using frequency positions only. The main overtone contributions identify with the harmonic groups $n = 4, 5$ and $n = 8$, while CFM had pointed out overtones $n = 4$ and $n = 7$. This minor disagreement between CFM and RSI calculations would not have been noticed if the criterion used in the first place to estimate the agreement with CFM had been different. Indeed, paying attention to the damping of the modes derived from CFM (column $\Delta\nu$ of Table 3.3), one remarks that the $n = 5$ and $n = 8$ harmonics exhibit a damping which is signicantly larger than that of the other harmonics; this means that these modes couple significantly with the embedding medium. From the comparison with the RSI results, it appears that this

coupling may be used as a good indicator of Raman activity for embedded NPs. Had the diameter value of 23.5 nm been chosen for the CFM calculations (instead of 20.5 nm), the agreement in terms of band positions with predictions of the CFM would have been slightly less satisfying (yet still within 5%; top arrows in Figure 3.9) while favoring an identification primarily based on the coupling of the modes with the matrix. In fact, this latter aspect sheds new light on the weak peak that emerges on the high energy foot of the fundamental quadrupolar band (near 150 GHz). In a previous study of pure Au NPs embedded in the same glass, a similar peak was assigned to the T_{2g} component of the lowest frequency doublet [59]. From the present RSI calculations, it comes out that this component rather filiates with the second harmonic of the quadrupolar mode. Although predicted of negligible intensity in the free sphere case, its intensity is enhanced by a factor 4 in the embedded case so that coupling with the matrix reveals again as an important parameter, not only for band positions, but also for band intensities. One should however mention that the direct comparison of the $n = 2$ mode with the experimental data is biased due to its immediate vicinity with the T_{2g} component, that neither the CFM nor the RSI calculations are able to account for at the present stage. In fact, taking into account the redistribution of nanosphere modes due to elastic anisotropy, which also has an impact on the distribution of overtones (as recently investigated for free nanospheres [31]), might lead in a future to a refinement of the interpretation scheme given above.

As mentioned at the beginning, the quadrupolar mode contribution to the polarized LFRS spectrum of the investigated AgAu embedded NP system accounts for almost 90% of the observed features. Once we have interpreted it in a rather complete way, it is worth analyzing the ∼10% overlapping contribution of the radial mode and check the consistency of the information derived from the quadrupolar mode.

The radial mode

From the extraction of the radial mode contribution (Fig.3.5, inset B) of the 64H sample, essentially two components are observed at 147±5 GHz and 315±5 GHz. These positions are found to hardly vary with a reasonable choice of the scaling factor k used to perform the subtraction $I_{VV} - kI_{VH}$. Comparing the so derived radial mode contribution with that obtained from the RSI calculation proves very satisfactory (Fig.3.10), quantitatively in terms of band positions (as additionally confirmed by CFM predictions) and qualitatively considering relative intensities. The observed components are therefore assigned to the fundamental and second overtone of the radial mode (actually, the third

overtone may also be distinguished).

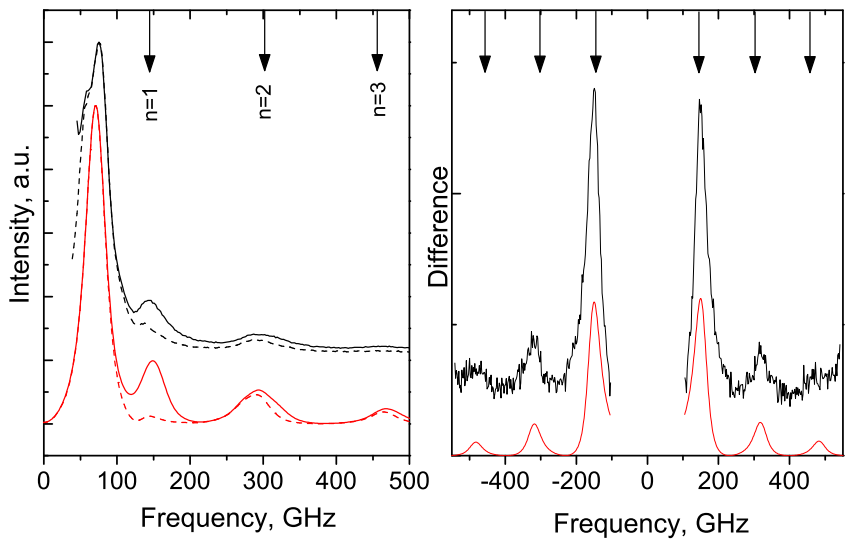

Figure 3.10: **Left:** The RSI calculated (red) and experimental (black) VV (solid line) and VH (dashed line) Raman spectra of the $Ag_{0.66}Au_{0.34}$ NPs. The spectra are normalized with respect to the quadrupolar mode. **Right:** The RSI calculated (red) and experimental (black) Raman difference spectra ($I_{VV} - kI_{VH}$). Black arrows are the CFM prediction of the positions of the spherical mode and its harmonics.

In order to cross-check these findings, independently from their Raman response, femtosecond pump-probe experiments were achieved (courtesy of N. Del Fatti and F. Vallée, LASIM, Lyon, France). In these experiments, one follows the energy decay of nanoparticles shortly after an intense IR pulse excitation, through the time modulation of the SPR absorption induced by the spherical mode oscillations [90, 91]. In the present case, the pump radiation was at 842 nm with a power of 80 mW, while the probe pulse was a 421 nm radiation, with 3.6 mW power. The fundamental mode frequency derived from a one component fit of the observed oscillations ($\nu^{\ell=0,n=1} = 1/T = 146$ GHz) turns out to perfectly match that derived from the Raman difference spectrum (Fig.3.11). A further analysis of the data, using an additional spectral component associated with the first harmonic of the spherical mode yields an equally consistent value, i.e. $\nu^{\ell=0,n=2} = 305$ GHz. Such good agreement between pump probe and Raman observations definitely assesses the correctness of the $Ag_{0.66}Au_{0.34}$ nanoparticle diameter, initially derived from the depo-

larized spectrum analysis. This agreement is further confirmed by the analysis of other samples (Fig.3.12).

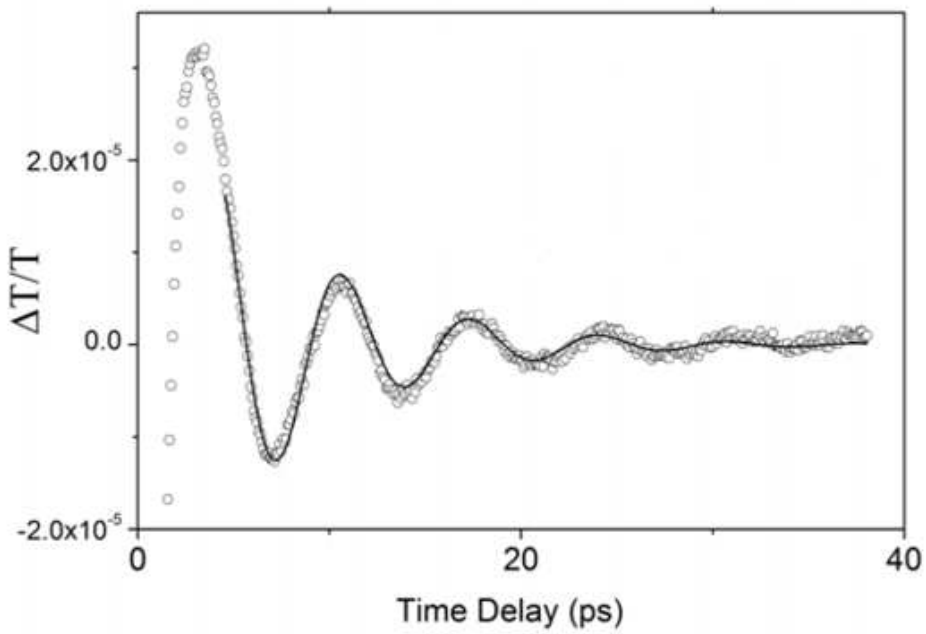

Figure 3.11: Relative change of the transmission of the 64H sample, as measured through pump probe spectroscopy. The pseudoperiod derived from a single vibration component ($T = 6.8$ ps) agrees well with that derived in the frequency domain from the Raman spectrum (inset B of the Fig.3.5).

3.1.4 Summary

As a result of this work with glasses containing two types of metal atoms, gold and silver, it was shown that an annealing close to the glass transition temperature of the glass allows the formation of bimetallic NPs of about 15 nm to 25 nm diameter. Most likely, these NPs are alloys, which is enabled by the close crystallographic radii of the Ag and Au atoms. The high resolution low frequency Raman spectra of these samples indicates that the crystalline quality of the NPs is good, according to the observation of the E_g/T_{2g} doublet. The first experimental detection of high frequency overtones of the quadrupolar mode has enabled a quantitative comparison of existing theoretical approaches that have been developed to interpret the low frequency Raman data from metallic or non-metallic NPs. In spite of still missing aspects (like the influence of elastic anisotropy on the activity

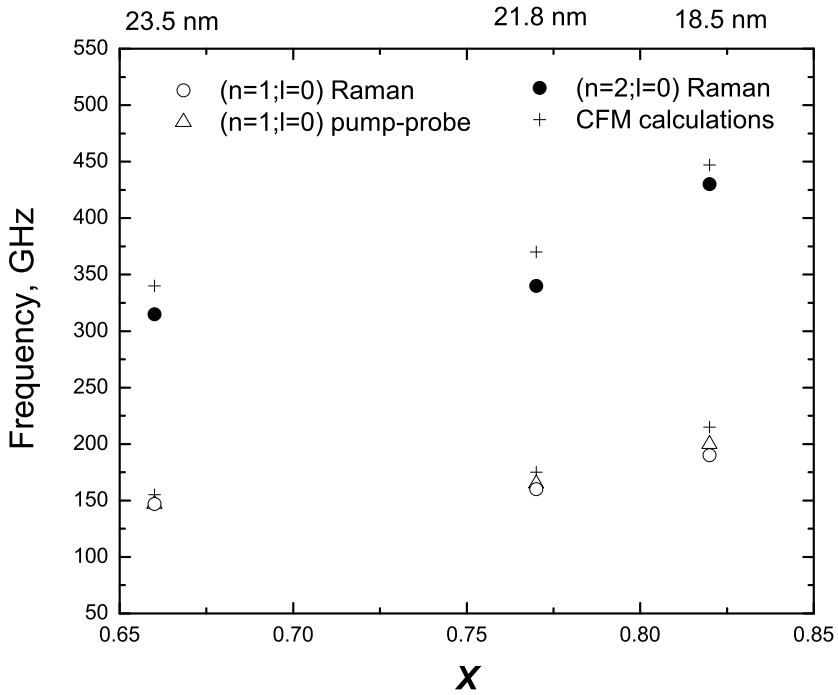

Figure 3.12: Spherical mode frequency values (fundamental and second harmonic), as derived from Raman experiments (circles), pump probe experiments (triangles) and CFM calculations (crosses), for three different samples ($x = 0.66, 0.77$ and 0.82). The top scale indicates the corresponding diameters, as deduced from the ($\ell = 2, n = 1$) mode.

of the overtones)[1], the good comparison of our experimental data with the calculations confirms which parameters and mechanisms are relevant for the Raman response.

The study of the vibrational properties of Au [5] and AuAg NPs nucleated in glasses through annealing has revealed a good nanocrystallinity, as attested by the observation of the elastic anisotropy splitting. Althgouh initially detected on these systems, the detailed investigation of the effect of elastic anisotropy in nanocrystals should ideally be performed from non-embedded NPs (as the coupling with a matrix may add complexity) with controlled, or at least characterizable, morphologies and inner structures. Such was performed with the study of assemblies of Au nanocrystals, as reported in the following section.

[1]Very recent works [31, 92] yet do treat these aspects.

3.2 Gold nanocrystals deposited on the surface

The splitting of the quadrupolar modes observed in LFRS spectra of embedded AuAg NCs, attributed to the crystalline structure of NPs, was firstly discussed, as we already mentioned, in [59] for Au NPs embedded in a glass matrix and further developed in the case of non embedded Au NCs [30]. In this latter case, the experimental observation of the splitting is very clear, due to high crystallinity and narrow size distributions of the observed NP assemblies. Although these NP assemblies are probably very different from those dealt with in the case of NPs grown in glasses, their study enables a more detailed characterization of the elastic anisotropy effect. As a continuation of [30], we report below further studies of non-embedded Au NCs which allowed to refine the interpretation of the LFRS data in terms of NP nanocrystallinity. These studies were performed in collaboration with H. Portalès from Laboratoire des Matériaux Mésoscopiques et Nanométriques, Université Pierre et Marie Curie Paris 6. In the following, the essential results of these works are given in order to illustrate the most updated experimental understanding of the elastic anisotropy effect; details can be found in reference [74].

3.2.1 Investigated samples. Optical characterization

Gold nanoclusters were produced at te LM2N (Paris 6) using a procedure described in [93]. The samples consist of ordered assemblies of Au NCs deposited on highly oriented pyrolitic graphite (HOPG). Details about the chemical synthesis of Au NCs are given in [30]. Basically, the Au NCs are initially produced in a toluene solution with dodecanethiol molecules. Immersing the HOPG substrate in the solution and through slow evaporation of the solvent results in the formation of ordered assemblies of the coated NCs (Fig.3.13). The TEM and optical characterizations of the NCs are performed from the solution samples whereas the LFRS experiments are achieved from the deposited assemblies. Assemblies with three sizes of Au NCs were studied: 4.3, 5.1 and 5.3 nm.

Figures 3.14a,b show the bright field and dark field scan TEM images of the sample containing Au nanocrystals of size 5.3 nm. From these pictures it was derived that a part of the NPs (∼30% of total amount of 2000 NPs investigated by TEM) are single domain — monocrystals with form of a cuboctahedron or a truncated octahedron [94]. The major portion (∼65%) of NCs are so-called multiply twinned particles (MTPs) — polycrystals [95] which apparently have forms of a decahedron and of an icosahedron. The rest 5% of investigated NPs are poorly twinned nanocrystals. The large variety of the structures

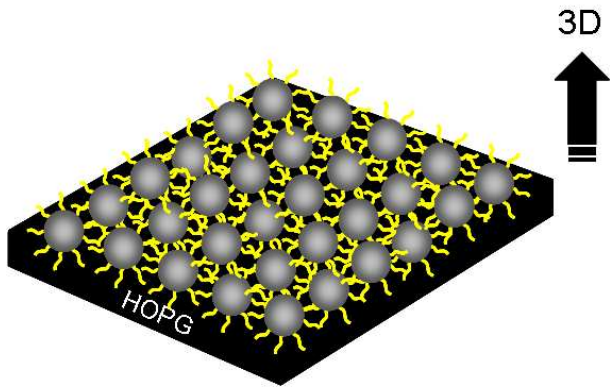

Figure 3.13: 3D scheme of the Au NCs deposited on HOPG.

does not influence the size distribution of the particles which is characterized by a very low polydispersity around 5%.

This TEM information is very important because the spatial geometry of the metal NP, as it was assumed in [30], may influence the LFRS spectrum which occurs due to strong coupling of exciting photons with SPR of the particle [49]. To estimate this influence the extinction spectra of the different crystal shapes represented in Figure 3.14 were calculated using the discrete dipole approximation (DDA) method [96]. For the calculations the NPs were assumed to be embedded in a host medium with refractive index equaled to that of the coating agent ($n = 1.46$). The calculated spectra are shown in Figure 3.15 and compared to that obtained experimentally from the solution of 5.3 nm Au NCs. All calculated curves are in good agreement with the experimental one. Their SPR peaks are located in a small wavelength interval centered around 530 nm whereas the maximum of the experimental curve is 520 nm. The only exception is the spectrum calculated for decahedral NCs: it is shifted towards the red part and broader than all the other spectra. It is obvious that the spectra of the icosahedron, of the cuboctahedron and of the truncated octahedron are rather similar to the spectrum of the sphere. In fact the decahedron spectrum differs from the rest due to its *oblate* shape [97]. As during the calculations the spatial orientations of the decahedral particles were calculated as random, these NCs are capable to excite selectively their SPR with changing of the excitation wavelength.

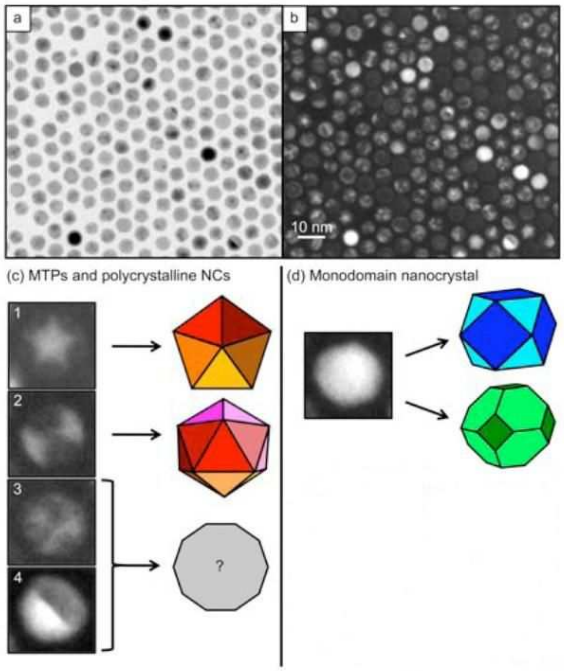

Figure 3.14: **A:** Bright field scan TEM image of Au NCs of 5.3 nm; **B:** Dark field scan of the same NCs; **C:** Several zoomed areas of the TEM image presented different types of the NC shapes: 1. decahedron, 2. icosahedron, 3. undefined polycrystal, 4. single-twinned particle; **D:** Zoomed zone of the TEM image presented the monocrystal NPs: of cuboctahedral shape and of truncated octahedron shape. Retrieved from [74].

3.2.2 Low frequency Raman scattering experiments of gold nanocrystals

Experimental observations

In paper [30] the specific vibrational behavior of gold monocrystals was demonstrated. It was explained, as in [59, 73], by their anisotropic elasticity. The two bands observed in both VV and VH scattering geometries which demonstrated a solid dependence on the NC sizes were attributed to E_g and T_{2g} modes. In addition, one broad line in a middle position was observed and this phenomenon was interpreted as a "pure" quadrupolar mode from NPs where elastic anisotropy is ineffective, i.e. NP with poorer crystallinity than single NCs. This latter type of NPs can be viewed as "badly" crystallized particles (defects) or polynanocrystals, among which are MTPs. Figure 3.16 shows the LFRS of the samples described in the previous section (three different NC sizes), illustrating these

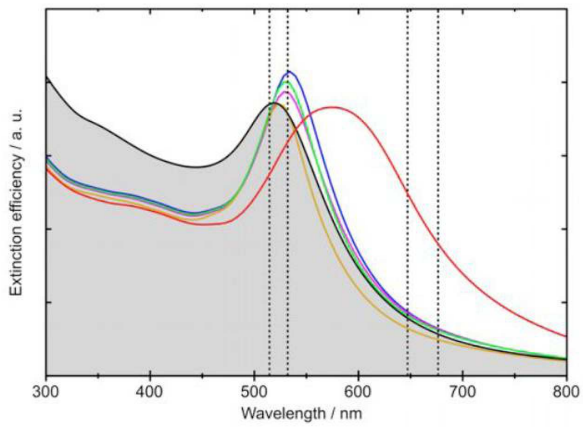

Figure 3.15: Experimental UV-vis extinction spectrum (filled black curve) of the colloidal Au solution plotted along with those calculated by using the DDA method for nanoparticles of different shapes: cuboctahedron (blue curve), icosahedron (violet curve), truncated octahedron (green curve), decahedron (red curve) and sphere (orange curve). The vertical dotted lines indicate the wavelengths of the various laser lines used as excitation sources for the LFRS experiments. Retrieved from [74].

results.

According to the TEM characterization described in the previous section, although all highly crystalline, all samples contain single NCs on one hand and polyNCs and/or MTPs on the other hand. White single NCs are responsible for the E_g/T_{2g} doublet, polycrystals and/or MTPs, where elastic anisotropy "'cancels out" through orientational averaging, are associated with the middle broader line described as an "average" $\ell = 2$ mode. Due to the *resonant* conditions of LFRS from metal NPs, one may expect that the singular SPR of decahedral MTPs (with respect to that of the nearly spherical counterparts) reflects on the wavelength dependence of the LFRS spectra. Figure 3.17 shows how the spectra of the deposited 5.3 nm Au NCs do indeed evolve with different wavelength excitations. These spectra were recorded using the Dilor Z40 five-grating monohromator (section 2.3) with three excitation lines of Ar^+ and Kr^+ lasers: 514.5, 647.1 and 676.4 nm. All these spectra show the same profiles as those of Figure 3.16, in spite of a slightly lower resolving power (the middle band appears slightly less resolved) due to the use of the five-grating monochromator, instead of the Tandem FP.

As it is seen in the figure, the profile of the LFRS spectrum depends significantly on the excitation wavelength: the relative intensities of all three contributions change from one excitation to another. The evolution points towards an increasing intensity of the

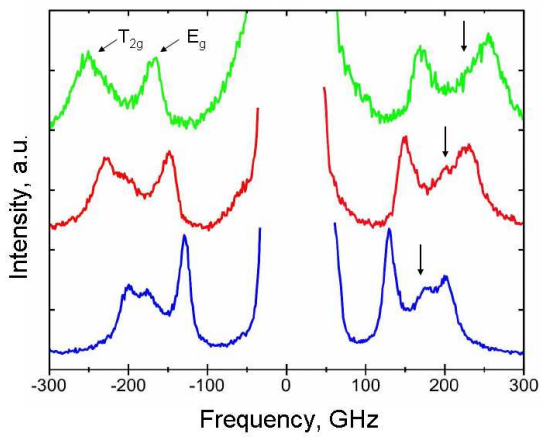

Figure 3.16: LFRS spectra of Au NCs measured from three samples of Au NCs: 4.3 nm (green curve), 5.1 nm (red curve) and 5.3 nm (blue curve). The excitation wavelength is 532 nm. All spectra are shifted along vertical axis for clarity. Black arrows at the anti-Stokes side point the middle band. Retrieved from [74].

middle band, going from 514.5 nm to 676.4 nm excitation. On the other hand we do not observe any frequency shift of these components unlike previous observations of this phenomenon, for example in [51], which showed a shift of the quadrupolar component towards lower frequency increasing the excitation wavelength. This latter result was explained by the additional presence of NPs with significantly ellipsoidally distorted shapes. Such interpretation cannot be given in the present case since the studied NCs have very narrow size and shape distributions, as stated in the preceding section. Considering the results of Figure 3.15, it is natural to interpret the wavelength dependence of the middle band as a signature of specific coupling with decahedral MTPs. Several arguments based on band positions, widths and relative band intensities support this interpretation; we briefly describe them below (see the paper [74] for details).

Quadrupolar modes from decahedral MTPs: frequency analysis

In order to confirm these results, the same LFRS measurements were carried out by Tandem FP possessing higher frequency resolution. Due to technical peculiarities of the Tandem FP only one exciting wavelength could be used in these experiments. The Stokes side of the spectrum recorded for an excitation at 532 nm is shown in Figure 3.18. It is obvious that the profile of the spectrum consists of three components which were successfully fitted by Lorentzian profiles.

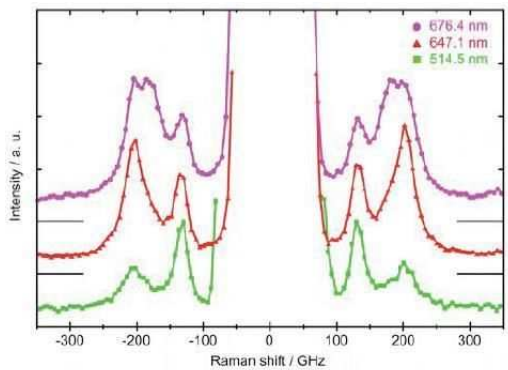

Figure 3.17: LFRS spectra of 5.3 nm Au NCs. The wavelengths of the different laser lines used as the excitation sources are 514.5, 647.1, and 676.4 nm, from the bottom to the top. Spectra have been vertically shifted and amplitudes normalized to the maximum of the lowest frequency band for clarity. Retrieved from [74].

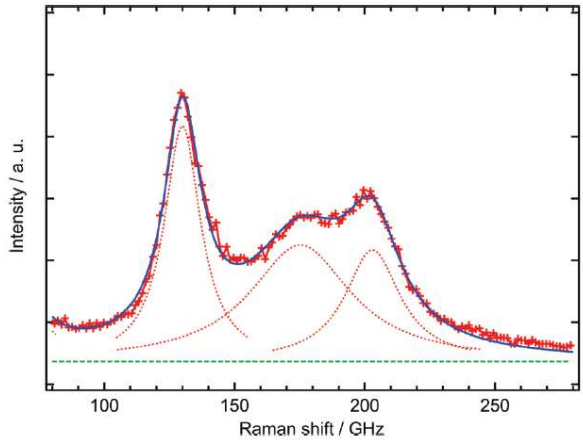

Figure 3.18: High-resolution Stokes LFRS spectrum of 5.3 nm Au NPs recorded for an excitation at 532 nm. Retrieved from [74].

A three component fit of the spectrum yields the positions reported in the last column of Table 3.4. While the frequency of the E_g/T_{2g} doublet agrees well with theoretical predictions for a 5.3 nm NC [30], the position of the middle band agrees with that of the quadrupolar mode of an isotropic nanosphere of identical size. Assuming an icosahedron instead of a sphere does not lift the degeneracy of the fivefold degenerated quadrupolar mode (the third line of the Table 3.4). Such is no more the case assuming a decahedron. Indeed, the decahedral morphology adds two peculiarities: the partial lifting of degeneracy of the quadrupolar mode and mixings of the quadrupolar mode with low-frequency modes

affiliated with TOR type motions which are not Raman active for a sphere with isotropic elasticity. In the case of the decahedron the quadrupolar mode splits into two twofold degenerate E (E_1'' and E_2') modes and one A (A_1') mode which are found to be Raman active. An additional E mode (E_1'') comes from the mixing wit ha TOR mode, which becomes Raman active. The theoretically predicted frequency positions of these modes are represented in Table 3.4. According to calculated values and taking into account a minimum bandwidth for each mode of around 20 GHz, as measured for the E_g mode of monodomain NCs, all discussed modes for the decahedron lie in a narrow frequency range which is close to that of the fivefold quadrupolar mode of an isotropic sphere with the same volume. Therefore, the Raman signals scattered from icosahedra and decahedra can be attributed with the band observed at around 183 GHz, so that it is not possible to distinguish between them based on the measured Raman frequencies.

Table 3.4: Comparison of the vibrational frequencies of 5.3 nm Au NCs measured by LFRS with those calculated by using the RUS approach for objects with different elastic properties and shapes.

Types of NC	Elasticity	Shape	Modes	ν_{calc}	ν_{exp}
cuboctahedron	anisotropic	sphere	E_g	141	137 ± 10
			T_{2g}	227	210 ± 10
icosahedron	isotropic	sphere	$\ell = 2$	200	183 ± 10
decahedron	isotropic	decahedron	E_2'	167	—
			E_1''	192	—
			A_1'	202	—
			E_1''	219	—

It is worth noticing that the linewidth of the middle band is significantly larger than those of the E_g/T_{2g} lines. This is in agreement with the multiple possible origins for this band: polycrystalline NCs and MTPs. For both types of particles, the "imperfect" crystallinity is expected to reduce the vibration lifetimes, hence the corresponding frequency width.

SPR coupling with MTPs: intensity changes

Qualitatively, the growing intensity of the middle band changing the laser excitation from 514.5 nm to 676.4 nm can be understand if one considers that MTPs partially contribute to it. If we consider the extinction spectra (Fig.3.15) we see that decahedral particles absorb light at 514.5 nm mainly through interband electronic transitions which was shown not to enhance the Raman signal [52]. In contrast monodomain NCs contribute a lot to the LFRS spectrum because this wavelength matches with the maxima of their SPRs thereby leading to selective excitation via plasmon-vibration coupling. Therefore we can assume that at 514.5 nm the Raman scattering from monodomain NCs is dominant so that the intensity of the middle band is relatively low. The contribution of decahedral MTPs in this case has to be negligible. When changing the excitation wavelength towards red lines one observes (Fig.3.15) that light is preferentially absorbed by the SPR of decahedral MTPs, so that the *resonant* Raman mechanism selects the response from this type of "imperfectly crystalline NPs", thereby leading to an increase of the middle band. It should be noted that the Raman response of NCs (E_g/T_{2g} doublet) still dominates the spectra, although the red excitation lines lie far off the SPR maxima of single NCs (cuboctahedra or truncated octahedra). This probably arises from a very efficient plasmon-vibration coupling, related to a very high interatomic vibrational coherence within highly crystalline structures [98].

3.2.3 Summary

The investigation of Au NCs with a high size monodispersity and different crystalline qualities has enabled us to analyze in more details the special region associated with the splitting of the quadrupolar mode, due to elastic anisotropy. Basically, it was shown that the Raman response from off-spherical shape MTPs, which consists of a single non-split quadrupolar line, can be selected by tuning the resonant Raman excitation. Such result could be obtained thanks to the narrow size distribution of the probed Au NC assemblies. In NP assemblies where not only the size distribution is expected to be large, but also the shape and crystalline quality distributions, this effect would have been virtually impossible to demonstrate, due to inhomogeneous broadening. In spite of the expected smearing out of the three-component Raman profile (E_g, T_{2g} and $\ell = 2$ bands) in systems with large size/shape/crystallinity distributions, the strong signature of the E_g/T_{2g} frequency splitting can be considered as a reliable probe of NP high crystallinity,

as has been mentioned in the case of AuAg NPs grown in glass. We will see now how this signature can be used to discuss the evolution of Cu NP crystallinities nucleated through different annealing conditions of their embedding glassy medium.

3.3 Copper nanoparticles embedded in a glass matrix

As we have described it with Au and AuAg systems, the large Raman signal due to resonance conditions with noble metals allows to probe fine effects of NP's structures. Since the Raman characterization proves to be quite useful in the case of embedded NPs we undertook the study of another type of metal NPs which should lead to comparable successful results. We set our choice on copper NPs due to the fact that copper, being a noble metal of the same group of the periodic table as gold and silver, exhibits similar optical properties. The SPR of Cu NPs embedded in a vitreous matrix lies at about 560 nm, which makes it appropriate for a visible light scattering study. As it was mentioned in section 2.2.2, Cu NPs possess small amplitude of the SPR due to its interband transition (Fig.2.12). This is the reason for the different shades generated in glasses containing Cu NPs ("copper ruby") and Au NPs ("gold ruby"). The similar behavior of the SPRs for all represented metals makes us expect to obtain results from Cu NPs that are comparable with those obtained with Au and AuAg NPs.

In terms of crystalline structure, as silver and gold, copper crystallizes in a face centered cubic crystal structure; in terms of elastic anisotropy, one expects comparable behavior with Ag and Au. Indeed, if one considers the elastic anisotropy which can be quantified through the Zener ratio: $\frac{2C_{44}}{C_{11}-C_{12}}$, it is observed that the Zener ratio for Cu is 3.2, i.e. close to that of Au (2.9) and Ag (3.1).

As we will see, one important difference between copper and gold/silver is that at the temperatures of the treatments considered in this section, copper easily oxidizes which makes the Raman analysis more complex in particular with respect to the coupling with the SPR.

What we have considered as an important advantage for our study on Cu NPs is the availability of Cu-doped glass. Like Au and AuAg glasses obtained from the St.Louis factory, Cu red glasses were obtained from the color glass factory — St.Just [100]. Collaborators from St.Just provided us with a significant amount of transparent Cu-doped glass from which we prepared many samples, particularly in order to investigate the influence of preparation conditions. NPs were grown in the silica glass by annealing it at

a temperature such that the defects in the matrix act as nucleating centers and then a nucleation process takes place. During the annealing process the particles (formed after nucleation) with radius exceeding the critical one, grow streaming to minimize their surface-to-volume ratio and therefore minimize their surface free energy (Ostwald ripening) [101]. Depending on the time and on the temperature of annealing and on other preparation conditions we can control the growth of the NPs. The basic aim of our works on Cu NPs was to study the evolution of the Raman spectra (in order to interpret them in terms of the structure of the NPs) with the preparation conditions because we assumed the temperature to be the main factor influencing the structure of prepared NPs. A good probe of the crystalline structure quality is supposed to be the splitting of the quadrupolar mode like it was observed for Au or AuAg embedded NPs.

In order to study the influence of the preparation conditions we prepared three series of samples which differ from each other only through the temperature of annealing: below the glass transition temperature of the matrix — T_g, slightly above T_g and well above T_g. The glass transition temperature of the glass was chosen as a bench mark due to the fact that the mechanical and structural properties of the glass change importantly at this temperature and so does the diffusion coefficient of the metal atoms. Therefore we expect to observe different NPs structures with changing of the annealing temperature because they have to form in different environments. As we will see the observed low frequency Raman scattering spectra from the obtained Cu NPs in each series demonstrate noticeable differences in their profiles. This means that the NPs populations formed at different annealing temperatures are different in terms of sizes, size distributions and crystalline quality. While the three first batches of samples were produced at fixed annealing temperature over different times, a forth series of samples annealed at different temperatures, for a fixed period of time was also studied.

As already exposed with AuAg and Au NPs, the characterization of the embedded Cu NPs will be performed using:

- optical absorption in the UV-visible range as a first identification means of the NPs formed in the annealing process and also in order to estimate some physical parameters of the system (chemical composition of the NPs and their volume fraction);

- low frequency Raman scattering; as demonstrated before it allows us to investigate the vibrational dynamics of metal NPs through the comparison with theoretical calculations (CFM, RSI);

- TEM technique in our work is an additional attempt to check the results obtained with the LFRS.

3.3.1 Sample presentation

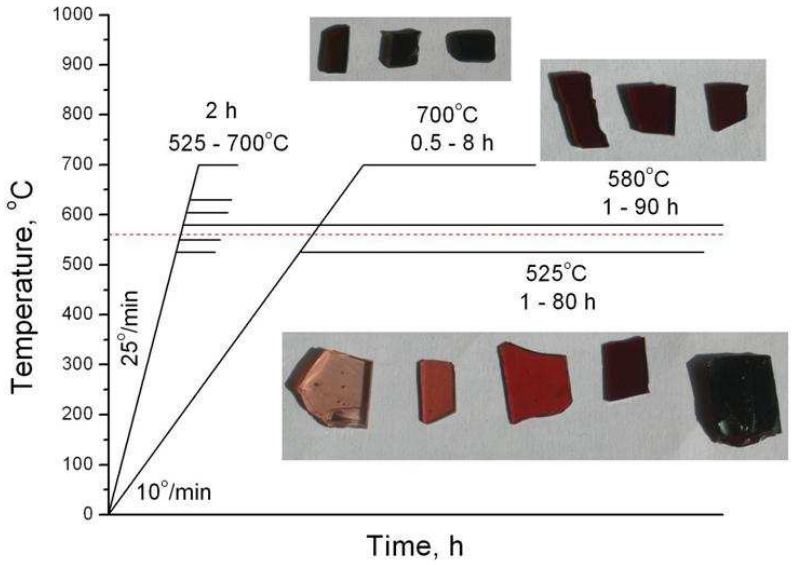

Figure 3.19: Temperature/time conditions of the differently prepared samples preparation. The red line marks T_g temperature of the glass.

Copper NPs were grown in a multicomponent silica glass produced in the St.Just factory. The initial copper oxide (I) (Cu_2O) weight content was 0,166%. The basic composition of this glass is $84SiO_2$-$19NaO_2$-$12CaO$-K_2O-Al_2O_3. The method of preparation of the glass with incorporated copper atoms is rather similar to that described in section 3.1.1. More detailed content of the glass composition is shown in Table 3.5. The peculiarity of this glass is that in this composition carbamide is considered as the main reducing agent, while tin dioxide is considered as a developer (without tin dioxide the red color does not strike). It is worth to notice the extremely low content of Cu so that theoretically the maximal volume fraction of Cu can be estimated as 0.04%.

The most important elastic parameters of the glass matrix are given in Table 3.6. Speeds of sound (longitudinal and transverse) and the density of the matrix, as we mentioned before, play a key role in the theoretical calculations of the CFM and of the RSI

Table 3.5: Composition of the St.Just glass.

Substance	Mass, %	Substance	Mass, %
SiO_2	72.1262	SnO_2	0.225
Na_2O	14.9	Cu_2O	0.166
CaO	9.388	MgO	0.052
K_2O	1.527	Bi_2O_3	0.045
Al_2O_3	0.959	Carbamide	0.0238
B_2O_3	0.3	Fe_2O_3	0.014
P_2O_5	0.29	SO_3	0.0072

models. The speeds of sound were derived from Brillouin light scattering measurements of the same samples (see equation (2.26)) using for the refractive index an experimental value determined from M-line spectroscopy [102] at $\lambda = 543.5$ nm. The density of the matrix was determined from buoyancy measurements. The glass transition temperature T_g was found by Differential Scanning Calorimetry (DSC) method. Figure 3.20 shows the DSC curve of the transparent glass and how the chosen annealing temperatures compare to T_g.

Table 3.6: Several important elastic parameters of the St.Just glass.

Matrix	St. Just
Density, g/cm^3	$\rho = 2.48$
Speed of sound, m/s	$v_L = 5730$ $v_T = 3480$
Refractive index	$n = 1.5228$
Transition glass temperature, °C	$T_g \approx 560$

As we mentioned before, different series of samples (see Table 3.7 and Figure 3.19) were prepared to investigate the influence of the preparation conditions on the evolution of the Raman scattering from the grown Cu NPs through:

- annealing at the temperature of 525°C which is below T_g ("$T_a < T_g$"), over different times ranging from 1 to 80 hours;

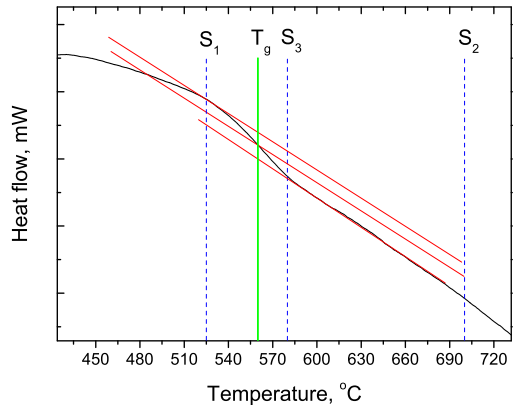

Figure 3.20: Determination of the T_g temperature of the St.Just glass by the DSC method. The green vertical line is a middle of the transition zone; the blue dashed lines are the temperatures used to anneal the samples.

- annealing at the temperature of 580°C which is slightly above T_g ("$T_a > T_g$"), over different times ranging from 0.5 to 16 hours;
- annealing at the temperature of 700°C which is well above T_g ("$T_a \gg T_g$"), over different times ranging from 0.5 to 90 hours;
- annealing at different temperatures from 525°C to 700°C, during a fixed time of 2 hours.

Table 3.7: Cu-glass sample description.

Series number	Sign symbol	Time of annealing, h	Temperature, °C	Rate, °C/min	Color after preparation
S_1	"$T_a < T_g$"	1 – 80	525 ($< T_g$)	10	Ruby → dark red
S_2	"$T_a \gg T_g$"	0.5 – 16	700 ($\gg T_g$)	10	Brown
S_3	"$T_a > T_g$"	0.5 – 90	580 ($> T_g$)	25	Ruby → dark red
S_4	"$T_{a:525-700}$"	Fixed: 2	525 – 700	25	Ruby → brown

All annealings were performed **in air**, with a heating rate of 10 or 25 degrees per minute. After the annealing procedure, the samples were let cool down inside the furnace

with an approximate rate of 100°C/hour. This rate is very slow so that in the samples prepared at temperatures significantly higher than T_g the NPs formation may significantly continue after the shutdown of the furnace, during several hours. To estimate the influence of this post-annealing cooling two additional samples annealed at 630 and 700°C and rapidly quenched at room temperature were prepared. As testified by the color aspect of the different samples (Table 3.7 and Figure 3.19), the different annealing procedures yield different shades, going from red to brown. These shades were characterized through optical absorption.

3.3.2 Absorption: results and discussion

Absorption

Absorption spectra of the samples were recorded with a Perkin-Elmer Lambda 900 spectrometer in both the visible and near UV range. All spectra were recorded at room temperature. All samples had comparable thicknesses around 1 mm.

Absorption spectra of the samples annealed below T_g ("$T_a < T_g$") (Fig.3.21a) demonstrate clear SPR peaks located in the region around 557 nm which is typical for Cu embedded in SiO_2 glass [103] (Fig.2.12). In this Figure only several samples from this series, with annealing times from 1 to 40 hours, are presented. The intensity of the SPR peak increases with annealing time, i.e., as we will see later, with the growth of the NPs. This can be easily explained from the equation (2.42) which shows that the absorption coefficient, and thus the absorption intensity, is proportional to the volume fraction q of the metal NPs in the sample. As it is well seen on the spectra the interband transition characterized by a steep rise in the UV ranges influences a lot the SPR of copper that leads to the damping and broadening of the SPR peak for the smallest NPs (i.e. smallest annealing time) [46].

In order to estimate the NP concentration, these spectra were compared with curves[2] theoretically calculated by the Maxwell-Garnett theory [104]. These calculations allow us to estimate the volume fraction q of the Cu involved in the formation of the NPs in the glass. According to the Maxwell-Garnett theory the dielectric permittivity of the composite medium {glass + NPs} is replaced by an effective dielectric permittivity:

$$\epsilon_{eff}(\omega) = \frac{\epsilon_m(2q+1)\epsilon_{Cu}(\omega) + 2(1-q)\epsilon_m}{(1-q)\epsilon_{Cu}(\omega) + (2+q)\epsilon_m}, \tag{3.3}$$

[2]These calculations were made by E. Cottancin, University Lyon 1, LASIM, Lyon, France.

where ϵ_m and ϵ_{Cu} are the relative dielectric permittivities of the glass and of copper respectively. The calculated curves appear in good qualitative agreement with the experimental ones (Fig.3.21b). The disagreement (SPR positions, profile below 550 nm) between experimental and theoretical SPR peaks may be explained by the small error in the measurements of the refractive index of the matrix (see Table 3.6) which was measured for only one wavelength: 543.5 nm.

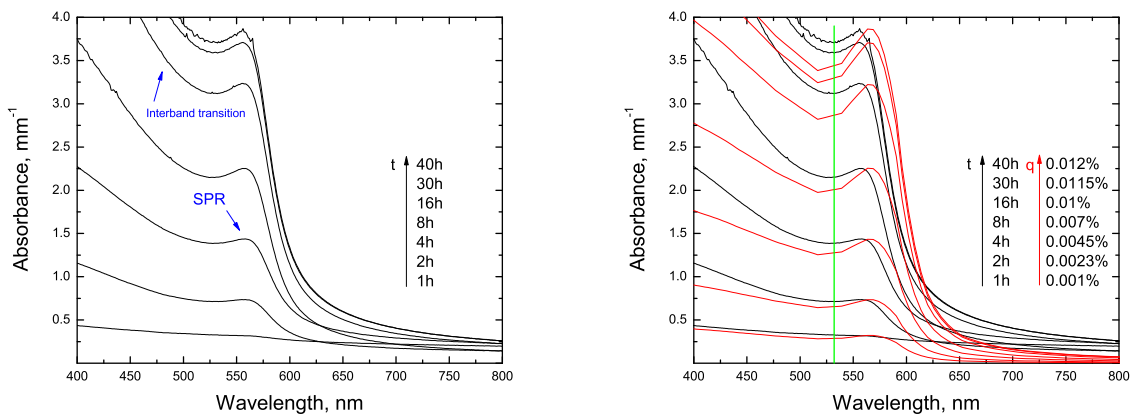

a b

Figure 3.21: **a:** Absorption spectra of Cu NPs grown through annealing below T_g over times ranging from 1 to 40 hours (batch S_1). **b:** The same spectra in comparison with theoretically calculated spectra (red curves). The volume fraction q of the Cu involved in the formation of the NPs in the glass is found to increase from 0.001% to 0.012%, while the annealing time increases from 1 to 40 hours. The green line at the position of 532 nm is the excitation line used in the LFRS investigations.

Absorption spectra of the samples annealed at a temperature slightly above T_g ("$T_a > T_g$") are shown in Figure 3.22a. As observed on the spectra of the samples annealed below T_g, these samples also demonstrate a visible SPR peak at the position around 557 nm, thereby proving the existence of Cu NPs. In general, the absorption of the "$T_a > T_g$" samples behaves like that of the "$T_a < T_g$" samples (Fig.3.21). The main visible feature is that in spite of the higher temperature of annealing, the absorbances at the SPR maxima of the "$T_a > T_g$" samples are lower than those of the "$T_a < T_g$" samples (Fig.3.22c). The key of this phenomenon is in the peculiarity of copper's behavior under temperature.

The NPs grown in the St.Just glass were prepared at different heating rates (Table 3.7). Sample annealed at differing heating rates theoretically have to contain the NPs of

different average sizes but the volume fraction q of the metal involved in the formation of NPs has to be the same for both samples. If one compares the values of copper volume fractions q for the "$T_a < T_g$" and the "$T_a > T_g$" samples we can observe that the increase

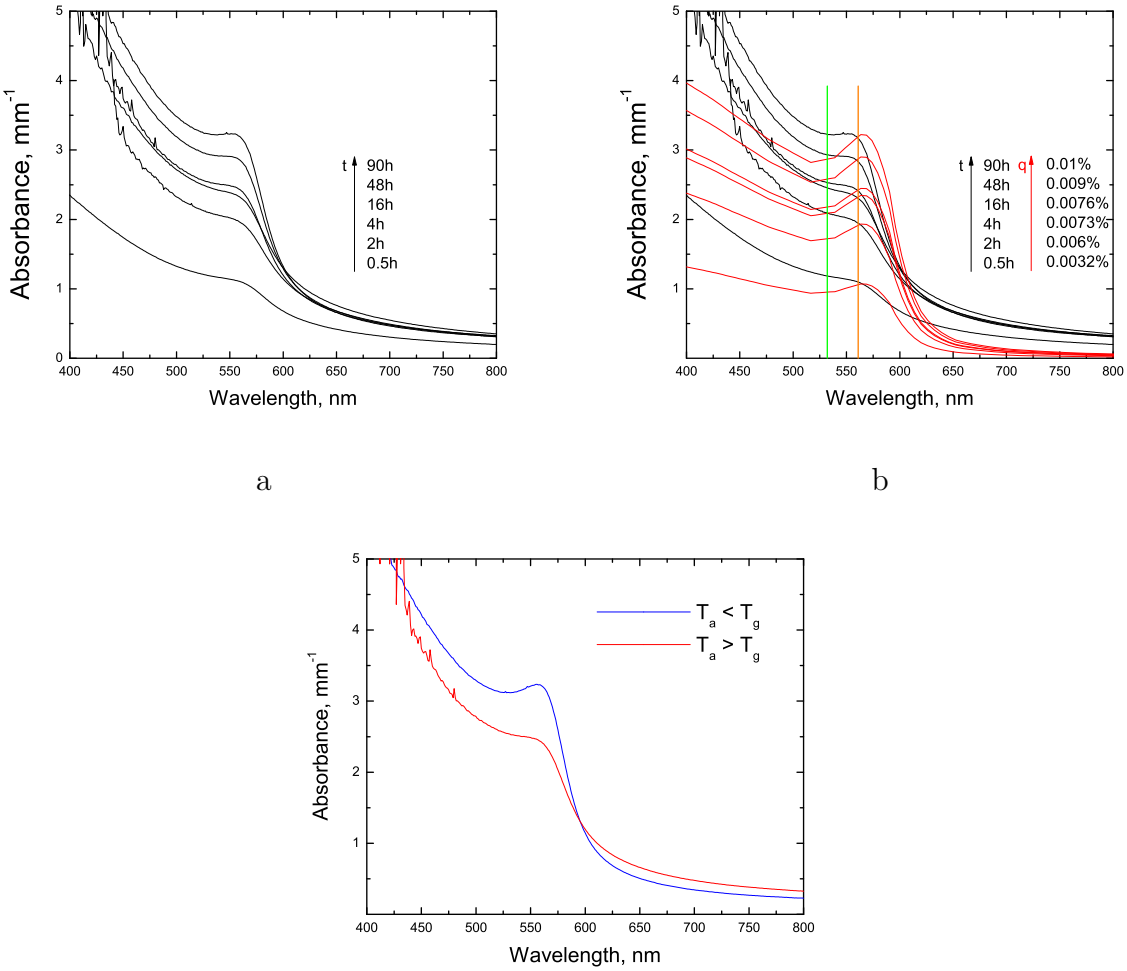

a b c

Figure 3.22: **a:** Absorption spectra of Cu NPs grown at 580°C for annealing times ranging from 0.5 to 90 hours (batch S_3). **b:** Same spectra in comparison with theoretically calculated spectra (red curves) with different values of the volume fraction q of the Cu involved in the formation of Cu NPs in the glass in the range of 0.0032% to 0.01%. Vertical lines at the positions of 532 and 561 nm are the excitation lines used in the LFRS investigations of these samples. **c:** Comparison between two samples annealed during 16 hours at temperature below T_g (blue curve) and slightly above T_g (red curve).

of q processes differently (Fig.3.23). During the several first hours of annealing the amount of copper involved in Cu NPs is higher for the "$T_a > T_g$" samples. This is quite logical since the copper atoms have more kinetic energy at the higher temperatures, and above T_g copper atoms can diffuse more efficiently in the disordered less rigid glass structure than below T_g. At 30 – 40 hours annealing time, the sample annealed below T_g shows a higher Cu NP volume fraction. It is a sign that in the sample annealed above T_g part of the copper atoms are not involved in the formation of Cu NPs. Indeed, a competitive process of Cu NP formation is Cu oxidation which is expected to be enhanced at higher temperature.

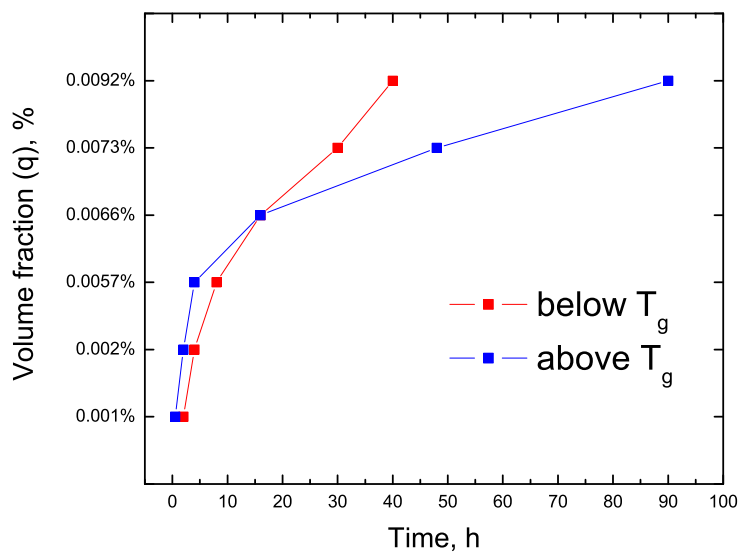

Figure 3.23: Evolution of the volume fraction of copper engaged in Cu NPs, as a function of annealing for the samples annealed at 525°C (red curve) and 580°C (blue curve).

The assumption of active oxidation of copper can be supported by the absorption results of the series of the "$T_a \gg T_g$" samples annealed at a temperature well above T_g (Fig.3.24). A remarkable feature of these curves is the absence of the SPR peak. Visually, these samples are brown while the two previous series are red (see Fig.3.19). The same result was obtained in ref. [105] and it was interpreted as an absorption signal of Cu_2O. In Figure 3.24 the theoretical calculated absorption curves for two copper oxides, CuO and Cu_2O, are shown. It is worth to notice that it is impossible to fit the experimental curves correctly neither by both oxide models nor by a model of the mixture of oxides and

pure metal. Therefore one can hardly identify the exact origin of the observed absorption curves and hence the actual composition of the formed NPs, nevertheless it is obvious that Cu oxide is present in the samples annealed well above T_g.

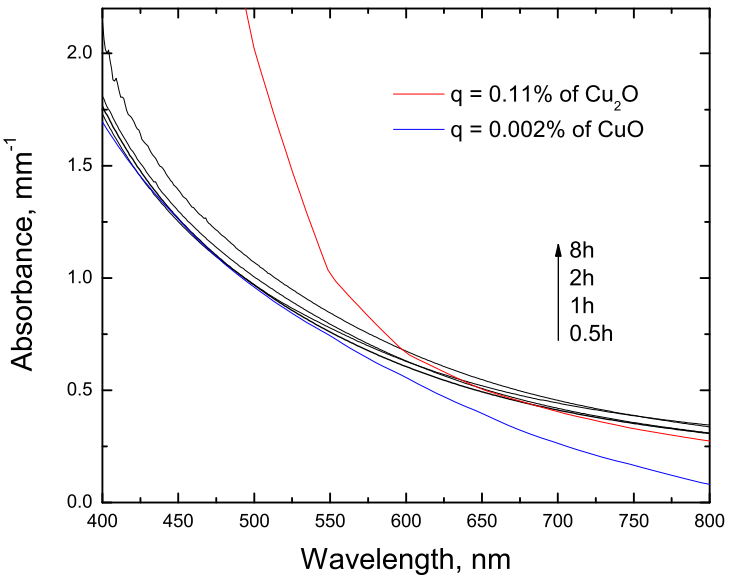

Figure 3.24: Absorption spectra of the NPs grown at 700°C for annealing times ranging from 0.5 to 8 hours. The red curve is the theoretically calculated spectrum for Cu_2O NPs and the blue curve is the theoretically calculated spectrum for CuO NPs.

To follow the dynamics of NP formation as a function of temperature, a series of samples annealed in the range of temperatures ("$T_{a:525-700}$") over a fixed time of 2 hours was prepared. Figure 3.25 presents the absorption spectra of the samples from this series. The obvious SPR peak is observed only for the samples annealed at temperatures lower than or close to T_g while it becomes less and less visible with increase of the annealing temperature. This result attests that the higher the annealing temperature the more Cu atoms oxidize. When temperature rises above 605°C the absorption signal does not show a SPR maximum any more so that we believe the formation of copper oxide prevails. The larger absorbance of the sample annealed at 630°C than that of the one annealed at 700°C is a result of more active formation of copper oxide particles to the detriment of Cu atoms and Cu NPs. The dashed lines in Figure 3.25 are the absorption spectra of the samples annealed at the corresponding temperatures and quenched rapidly down to room

temperature immediately after the annealing procedure. These samples were prepared to understand the influence of the time over which samples cool down after the shutdown of the furnace. The same shape of the curve of the quenched and of the slowly cooled down samples indicates that the additional annealing during slow cooling does not appreciably influence the type of the formed NPs.In order to correctly conclude which type of particles we face, one have to consider an important property of copper appeared at temperature treatment: oxidation.

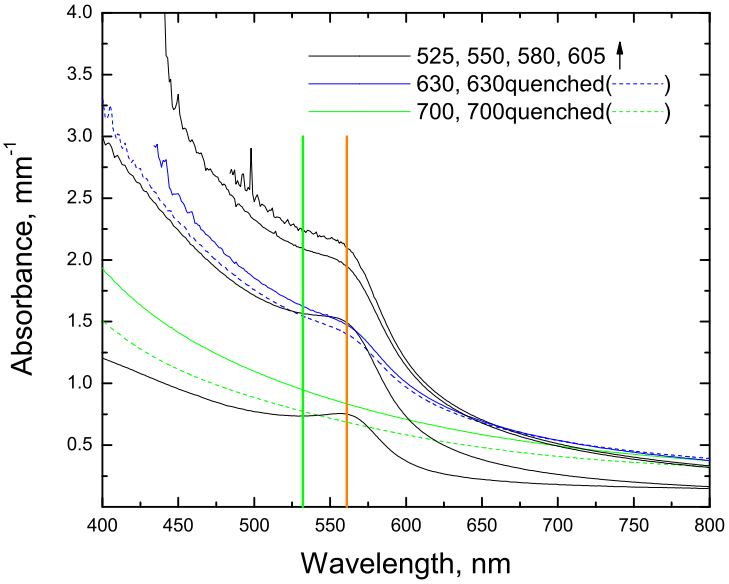

Figure 3.25: Absorption spectra from the NPs annealed at fixed time (2 hours) over a temperature range between 525°C to 700°C. Vertical bars are the positions of the exciting lines used for the LFRS investigations.

Oxidation

The observed SPR signals prove that with annealing Cu NPs are formed but simultaneously the absorption spectra demonstrate that Cu NPs are not the only contributors to the absorption. Indeed, it is known [106] that during heating at temperatures lower than 1100°C in an atmosphere with high content of oxygen, Cu reacts with oxygen and forms copper oxide (II):

$$2Cu + O_2 \longrightarrow 2CuO. \tag{3.4}$$

Cupric oxide is not very stable and under the influence of temperature it is reduced to copper oxide (I):

$$4CuO \longrightarrow 2Cu_2O + O_2 \uparrow . \tag{3.5}$$

Simultaneously with these reactions the following one is possible:

$$4Cu + O_2 \longrightarrow 2Cu_2O. \tag{3.6}$$

Cupreous oxide has a dark-red shade and it is more stable than oxide (II). The formation of Cu_2O NPs in silica glasses at the same time with Cu ones is known [107, 108]. Due to this we assume that our samples can contain some fraction of NPs made of copper oxide (I). The absorption of Cu_2O NPs is weaker than that of Cu NPs however the presence of cupreous oxide can slightly change the absorption curve of the sample. In Figure 3.26 the influence of a Cu_2O admixture is demonstrated on the example of the "$T_a < T_g$" samples. It is clear that taking into account the presence of Cu_2O more adequately describes the experimental curve, at least below 550 nm.

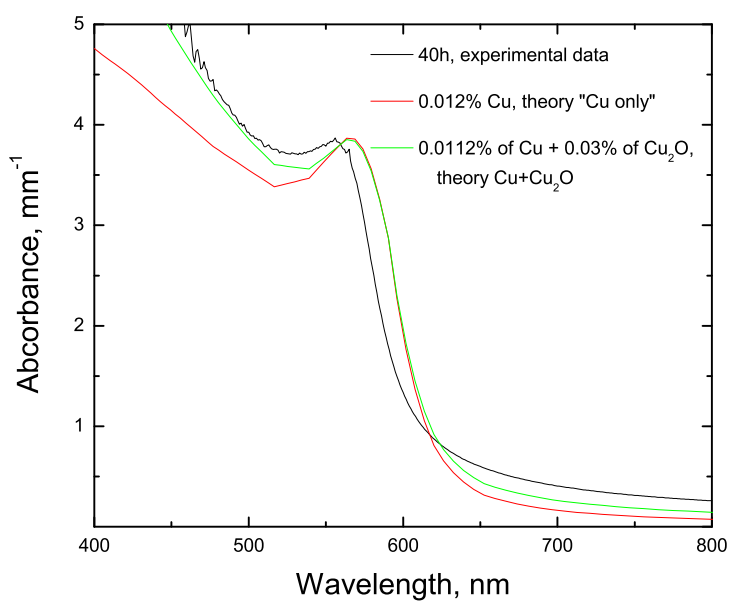

Figure 3.26: Absorption spectrum of the Cu NPs grown at 525°C during 40 hours (black curve). Red and green curves are theoretically calculated spectra assuming Cu NPs only and coexisting {Cu + Cu_2O NPs} respectively.

CuO is very rarely mentioned in the formation of NP from annealing of Cu doped glass, at least when annealing are performed in air as we did. On the assumption of this, we can suppose that two types of substances can be found in the annealed glass: Cu and Cu_2O. Core-shell NPs (core of Cu, shell of Cu_2O) for our samples probably are not formed under such conditions because according to our knowledge [109] such type of core-shell NPs gives a visible SPR peak while the content of Cu_2O in the core-shell NPs is lower than 98%. This fact cannot be the truth in our case even for the samples which do not demonstrate the SPR peak (batch S_2): according to Table 3.5 the possible maximum value of the volume fraction q of copper NPs is 0.04%; the one of cupreous oxide NPs is 0.046% whereas the calculations of q of Cu_2O for the experimental curves of the "$T_a \gg T_g$" samples give the values around 0.11%. As we will show further by the LFRS experiments the samples of this series are very close to saturation, i.e. almost all copper atoms have to be involved in a formation of any type of NPs. Therefore the content of the cupreous oxide in the NPs is less than 98%. In spite of this we do not observe the SPR peak for these samples, hence the core-shell NPs are not formed in the samples.

This makes us assume the parallel formation of two types of NPs: Cu and Cu_2O, which quantity ratio depends on the annealing temperature. Attempts to characterize the state of oxidation of Cu were performed using X-ray Photoelectron Spectroscopy (XPS). However no successful results could be obtained, probably due to the very small Cu concentration. Similarly x-ray diffraction is unable to detect the presence of crystalline Cu within the glass for the same reasons (see Fig.3.27). In spite of this we, nevertheless, managed to observe the informative LFRS from our samples which will be described in next section.

3.3.3 Low frequency Raman scattering studies

This section is dedicated to the investigation of the vibrational modes from the Cu NPs embedded in the glass described in the previous section.

Batch S_1

The LFRS spectra (VV configuration) of the samples annealed below T_g (batch S_1) are presented in Figure 3.28a. The excitation wavelength is 532 nm (see Fig.3.28b) and the FSR was set to 432 GHz. Each spectrum contains only one broad peak which can

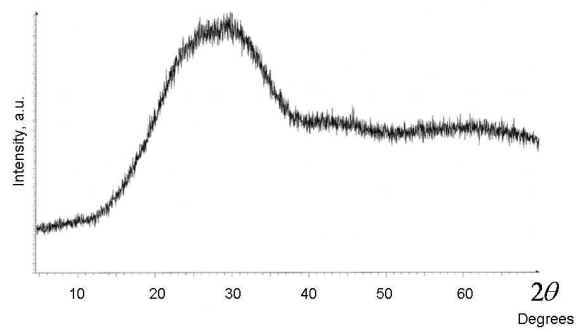

Figure 3.27: X-ray diffraction spectrum of Cu NPs grown at 700°C during 8 hours. This curve does not contain any Bragg peak attributed to copper crystals. The large peak around 30° is the first sharp diffraction peak attributed to the scattering from Si–O bonds.

be attributed to the quadrupolar mode ($\ell = 2; n = 1$) of the NPs as this peak is not suppressed in the VH configuration. In this trend one can observe the red shift of the position of the quadrupolar mode for the samples annealed during longer times which proves that the average size of the NPs increases with an increase of the annealing time.

As in the previous sections, the frequency position ν of the quadrupolar fundamental mode ($n = 1; \ell = 2$) allows to estimate an average size $< D >$ of the Cu NPs using equation (1.30), assuming the NPs as nanospheres:

$$\nu_{1;2} = S_{1;2} \frac{v_T}{< D >}, \tag{3.7}$$

where v_T is the transverse speed of sound of Cu and, for the considered glass, $S_{1;2} = 0.95$ (see Table 1.1 and 1.3). The left inset of Figure 3.28a shows the evolution of the average radius as a function of annealing time. Basically two stages are identified: in a first stage (2 hours $\rightarrow$ 16 hours) the NPs average radius increases quite rapidly (0.2 nm/h), with respect to a second stage (30 hours $\rightarrow$ 80 hours) where the radius only very slightly increases (0.003 nm/h). This two stage evolution is also found in the dependence of the relative spectral width $\Delta\nu/\nu$ ($\Delta\nu$ is the full width at half maximum derived from a lorentzian fit of the data) of the Raman band with annealing time (right inset of the Fig.3.28). The value of $\Delta\nu/\nu$ is found to strongly decrease for annealing times ranging between 2 hours and 16 hours while it remains almost constant for longer annealing.

The two step evolution observed in the LFRS complies with the scenario generally involved for the growth of NPs during isothermal annealing [110]. In a first regime NPs grow according to a precipitation process of a supersaturated solution. Once the size of the NPs is fairly large as the degree of supersaturation becomes very small, large particles

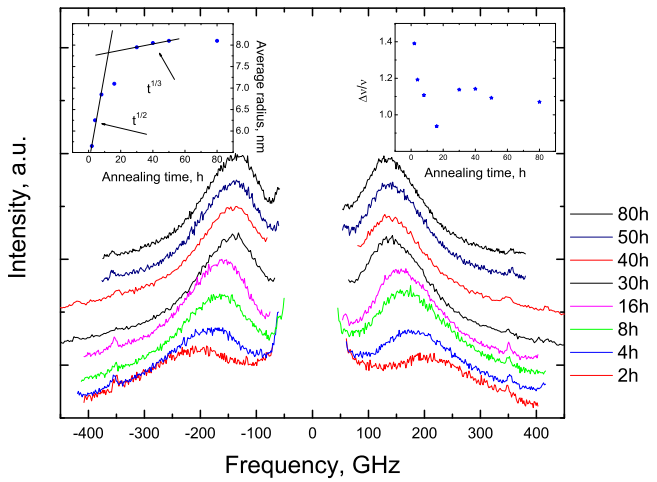

a

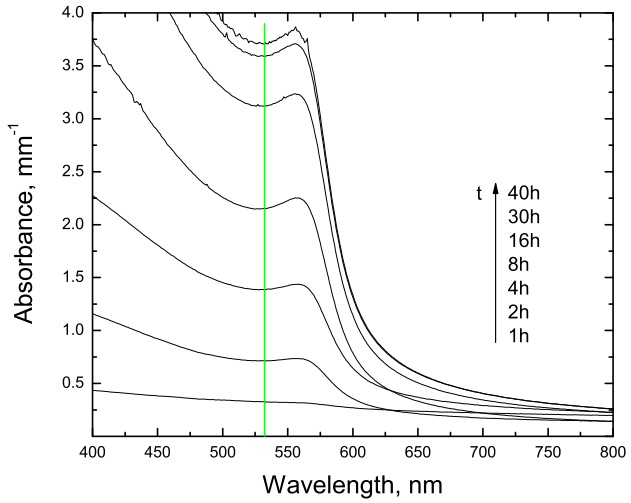

b

Figure 3.28: **a:** LFRS VV spectra from samples annealed below T_g (batch S_1). The spectra are normalized on the maximum and shifted along the vertical axis for clarity. **Left inset:** Evolution of the NP average radius with annealing time: two stages of growing may be distinguished (see text). **Right inset:** Dependence of the ratio $\Delta\nu/\nu$ on the annealing time. **b:** Recall of the absorption spectra of the same samples (see section 3.3.2).

further grow at the expense of smaller ones that dissolve. This latter stage is called *coarsening*, or Ostwald ripening and is basically governed by a Gibbs-Thomson effect according to which smaller NPs (or clusters) have a higher solubility.

The main growth stage is a pure diffusional process; in this regime the evolution of the average radius obeys a $(Dt)^{1/2}$ law [110] where D is the diffusion coefficient of the Cu atoms and t is the diffusion time. The inset of Figure 3.28a shows that this trend is indeed qualitatively observed. Besides the rapid growth of the NPs in this first regime, the significant reduction of the Raman band width seems to indicate that in the same time, the size distribution of the NPs significantly narrows.

In the following stage, both the average size and the size distribution of the formed NPs hardly evolve. In this "ripening" process, the Cu transfer occurs from the smaller clusters ("evaporation") to the largest ones. The apparent non-evolution of the Raman band profile, which we assume as a probe of size dispersion, indicates that the dissolving smallest aggregates initially had a negligible contribution to the observed Raman signal. Such is reasonable if one considers that due to the resonant Raman process, the coupling with the surface plasmon excitation favors the response of the larger NPs, as the polarisability of a NP is proportional to its volume [111]. In the coarsening regime, the average radius should scale with a $(Dt)^{1/3}$ law. Qualitatively, this trend is observed in our data (left inset of Fig.3.28a). On the basis of this, it is interesting to check if the increase of the NP's average size in the coarsening regime is consistent with the Cu volume fractions determined from the fits of the absorption spectra. According to its definition (equation (2.42)) the NP Cu volume fraction for a given annealing time t_a can be approximated by:

$$q_{t_a} \sim \frac{N_{t_a} < V_{t_a}^{1NP} >}{V_{glass}}, \tag{3.8}$$

where N_{t_a} is the number of NPs with average volume $V_{t_a}^{1NP}$, embedded in the glass volume V_{glass}. Considering that in the ripening process, the number of dominating NPs is almost unchanged, one obtains

$$\frac{q_{t_1}}{q_{t_2}} \approx \frac{R_{t_1}^3}{R_{t_2}^3}. \tag{3.9}$$

Using the values found for 30 hours and 40 hours of annealing, the ratio $\frac{q_{40h}}{q_{30h}} \approx 1.043$, derived from the absorbance data, is found to compare reasonably well with $\frac{R_{40}^3}{R_{30}^3} \approx 1.038$ as derived from the positions of the Raman bands. Finally, one may convert the q-values into NP concentrations using the average size value:

$$C_{t_a} = \frac{N_{t_a}}{V_{glass}}. \tag{3.10}$$

The typical concentrations obtained in the coarsening regime are of the order of 10^{20} m^{-3} ($\sim$ 100 NPs per 1 μm^3).

If we make a comparison with the previous observations of metal NPs through Raman scattering (sections 2.2.2) we can conclude that the single Raman band observed in the present case likely reflects a quite large size distribution of Cu NPs. Because of it, it is impossible to probe fine details of the NP structure and to detect the spherical mode. As we will see now, this situation significantly differs by annealing the samples well above T_g.

Batch S_2

The LFRS spectra (VV configuration) of the "$T_a \gg T_g$" samples annealed at 700°C are represented in Figure 3.29. The excitation wavelength is 532 nm. Each spectrum contains several peaks marked in the figure by P_1 (around 100 – 120 GHz), P_2 (around 200 – 230 GHz) and a much less visible one marked P_3 (around 370 GHz). It is obvious that the main peak P_1 is significantly narrower than that of the samples from the "$T_a < T_g$" samples. Comparatively to Figure 3.28 the red shift of the observed bands with increasing annealing time is small.

The different components of the spectra (P_1, P_2, P_3) are identified by comparing the VV and VH spectra. Figure 3.30 shows this comparison with the largest annealing time sample. As can be seen, P_1 and P_3 are depolarized while P_2 is completely polarized. Therefore P_1 can be identified as the fundamental quadrupolar mode ($n = 1; \ell = 2$) while P_2 is ascribed to the fundamental spherical mode. Note that, unlike the case of AuAg NPs, the depolarized spectrum does not show the presence of a depolarized signal in the vicinity of the polarized spherical mode band (this signal was assigned to the second harmonic of the quadrupolar mode). The observation of the spherical mode confirms the narrow size distribution of the formed NPs and their good cristallinity, as previously observed with Ag embedded NPs [53]. The identification of the weak P_3 band is less straightforward; a comparison with calculation may bring further information.

As already commented on, the optical absorption spectra (Fig.3.29a) do not unambiguously unveil the presence of Cu NPs due to the non-visibility of a SPR peak. The smooth absorption curves are suspected to reflect the presence of Cu_2O and/or CuO. The assumption of pure CuO NPs and the core-shell structures were discarded (section 3.3.2). In the following, we compare calculations performed with either pure Cu NPs or pure Cu_2O NPs in the hope it will help discriminate between the two possibilities.

Figure 3.30 indicates the frequency positions calculated using the CFM, with the appropriate matrix parameters (Table 1.3). The size of the NPs was set such that the position of the main P_1 peak coincides with that calculated for the $(n = 1; \ell = 2)$ mode. The comparison with the Cu_2O and Cu assumptions are respectively performed on the

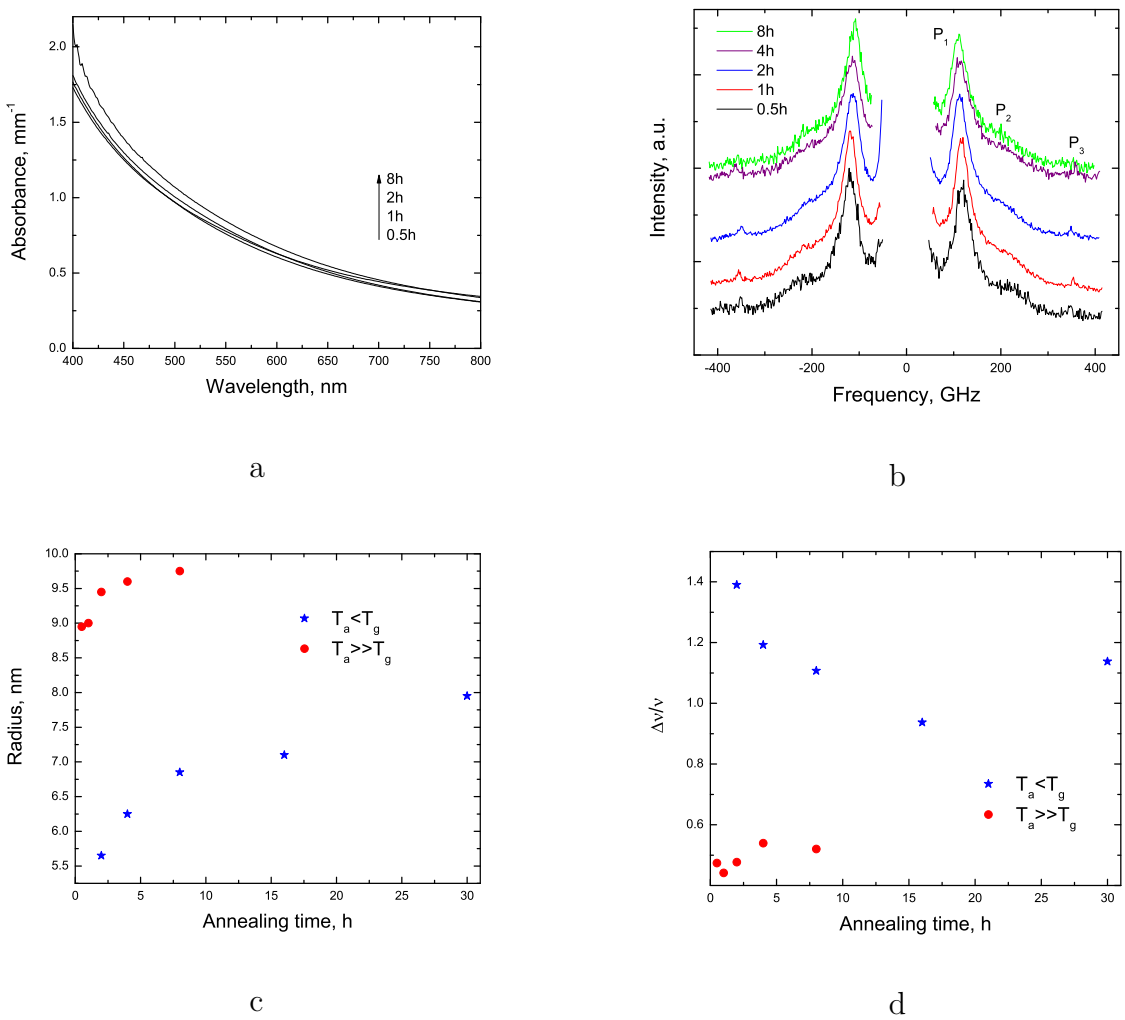

Figure 3.29: **a:** Recall of the absorption spectra from the samples annealed well above T_g (700°C) over time ranging between 0.5 and 8 hours. **b:** LFRS VV spectra from the same samples. The spectra are normalized on the maximum and shifted along the vertical axis for clarity. **c:** Evolution of the average radius as a function of annealing time assuming Cu NPs for the two series of the samples: "$T_a < T_g$" (blue stars) and "$T_a \gg T_g$" (red circles) as derived from the P_1 peak. **d:** The dependence of the ratio $\Delta\nu/\nu$ for the P_1 peak on the annealing time for the same series of the samples.

Stokes and anti-Stokes sides.

As can be seen from Figure 3.30a, better agreement is obtained with the Cu NPs assumption. Indeed, once the size of the NP is fixed, through the position of the quadrupolar mode, it occurs that the associated frequency of the spherical mode better matches the experimental one assuming Cu NPs. The assignment of the weak P_3 band is less clear. According to Figure 3.30b, the position of the band matches with an overlap of the third and the forth harmonics of the quadrupolar mode. Such assignment should not be considered as firmly established since the P_3 band is located close to a known Raman band from air molecules (at 330 – 420 GHz).

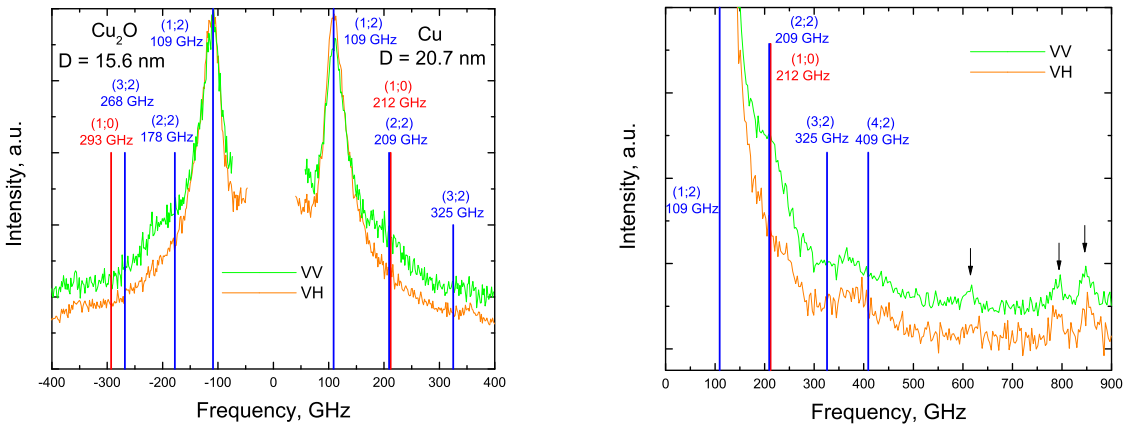

a b

Figure 3.30: Polarized/depolarized low frequency Raman spectra from the sample annealed at 700°C during 8 hours (batch S_2). The spectra are normalized on the maximum intensity. Red bars are the theoretical CFM predictions of the spherical mode ($\ell = 0$); blue bars are those for the quadrupolar mode ($\ell = 2$). The heights of the bars are irrelevant to intensities. **a:** Cu_2O and Cu NPs assumptions are respectively indicated on the Stokes and anti-Stokes sides. **b:** Same spectra recorded over a broader frequency range, using the Z40 quintuple monochromator (anti-Stokes side only). Vertical bars correspond to the Cu assumption. The double peak structure (black arrows) between 800 – 910 GHz and the peak near 620 GHz are due to Raman scattering from air contained in microbubbles.

Considering these facts we can conclude that in spite of the presence of copper oxide in the sample, which is strongly suggested by absorption measurements, the analysis of the Raman signal suggests that the detected vibrational modes arise from metallic Cu

NPs.

One possible interpretation of this situation is that the volume fraction of Cu NPs produced through annealing is very small in comparison with copper oxide, so that the associated SPR signal is masked in the absorbance spectra. On the other hand, due to the resonant Raman conditions, the selective response of the Cu NPs is observed.

Once the data of Figure 3.29 are interpreted with the assumption of Cu NPs, we derive that the size of the NPs increases from $D \approx 17.9$ nm to $D \approx 19.5$ nm between 0.5 hours and 8 hours of annealing at 700°C (Fig.3.29c). Besides the fact that these sizes are only 30% to 60% larger than those produced through annealing below T_g, the overall Raman profile is very different as testified by the $\Delta\nu/\nu$ values (Fig.3.29d). The narrow profile of the quadrupolar mode ($\Delta\nu/\nu \sim 0.5$) appears definitely as a prerequisite for the observation of the spherical mode.

In order to check the morphology of the Cu NPs, we tentatively performed TEM measurements, using the diamond tip scratching method. Figure 3.31 shows a TEM micrograph obtained on the sample of batch S_4 annealed during 2 hours at the same temperature as samples of batch S_2, i.e. 700°C (it will be shown later that the different heating rates of the two series have no influence on the observed Raman spectra). The size deduced from the TEM observation is 19±1 nm, i.e. in very good agreement with that deduced from the Raman spectrum (Fig.3.29c). It is worth noting that the TEM picture shows ring-like structures with sharp electron density contrast that appear much larger than the detected NP. These unidentified structures might be responsible for the smooth absorption curves (Fig.3.29a).

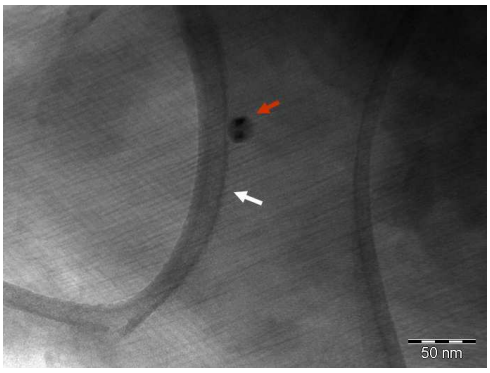

Figure 3.31: TEM image of the NPs embedded in St.Just glass and prepared through annealing at 700°C during 2 hours. One Cu NP is spotted by the red arrow. The white arrow points to large ring like structure of unidentified nature.

Although the sizes of the formed Cu NPs at 700°C compare with those of the AuAg system (section 3.1), no effect of elastic anisotropy could be detected: the quadrupolar mode consists of a non-split single narrow line. This suggests that the Cu NPs are not single nanocrystals but rather polycrystalline or at least MTPs. One essential difference between the AuAg samples reported in section 3.1 and the present Cu sample batch is that the former was produced through the annealing close to T_g. In order to check whether the detection of the elastic anisotropy effect relates to an annealing closer to T_g we now focus on the results obtained from samples annealed slightly above T_g (batch S_3).

Batch S_3

The polarized/depolarized LFRS spectra of this series are represented in Figure 3.32. Each VV spectrum contains four components (P_1, P_2, P_3, P_4) among which one (P_3) appears polarized from the VV/VH comparison. Comparing these spectra with those recorded for samples annealed below T_g and well above T_g, the following remarks can be made:

- the main contribution to the spectrum ($\nu < 350$ GHz) definitely shows a double component structure, similar to that observed for the AuAg NPs (Fig.3.3). It is therefore natural to interpret it as a sign of elastic anisotropy.
- the barycentre of this double component feature typically lies at frequencies larger than those observed for the previously investigated samples. This means that the corresponding NPs size is smaller.

Considering the absorption results obtained for the present series of samples (Fig.3.32a), and from the previous analysis performed for samples annealed well above T_g, it is natural to discard from the outset an interpretation of the Raman data based on Cu_2O NPs. As indicated by Figure 3.33, interpreting the lowest frequency peak P_1 as a unique ($n = 1; \ell = 2$) mode from a NP of diameter 9.5 nm, within the CFM, fails to reproduce the frequency positions of the P_2, P_3 and P_4 bands. One therefore turns to the elastic anisotropy effect. Fitting the four observed components with lorentzian profiles allows to evaluate the frequency ratio of the T_{2g}-E_g doublet[3]. The average value of this ratio obtained from fits of the five curves displayed in Figure 3.32 is $\nu_{T_{2g}}/\nu_{E_g} \approx 1.53$. From

[3]Bearing in mind that the T_{2g}-E_g doublet may comprise an underlying contribution of isotropic NPs (see section 3.2). Nevertheless, we expect this additional contribution to have a negligible effect on the value of the frequency T_{2g}/E_g ratio.

the elastic constants of fcc Cu, the theoretical value is $\nu_{T_{2g}}/\nu_{E_g} = 1.79$ (see Table 1.1). The small disagreement between these two values is of the same order as that found for the AuAg systems (section 3.1), while it is practically not observed in the case of the non-embedded Au NCs (section 3.2). It is very probable that the difference between the theoretical and experimental values of the T_{2g}/E_g frequency ratio is due to the presence of the embedding medium. In the present stage of development of the CFM, it is not possible to theoretically account for both the effects of the matrix and of the T_{2g}/E_g splitting[4]. Therefore in order to predict the positions of the spherical mode and of the quadrupolar mode harmonics, as with the AuAg system, the T_{2g}/E_g doublet is modeled as a single band with a barycenter that takes into account the degeneracy of the E_g and T_{2g} components:

$$< \nu_{E_g - T_{2g}} > \approx \frac{2\nu_{E_g} + 3\nu_{T_{2g}}}{5}. \tag{3.11}$$

The results are shown as vertical bars on the anti-Stokes side of Figure 3.33 spectrum. Obviously, the agreement with experimental data is very satisfactory and summarizes as follows:

- the P_1 and P_2 peaks respectively arise from the E_g and T_{2g} components of the split $(n = 1; \ell = 2)$ quadrupolar mode. The NP size is evaluated of 11 nm.
- the P_3 peak observed in VV configuration only arises from the fundamental $(n = 1; \ell = 0)$ spherical mode. Note that the P_3 peak position coincides with that of the $(n = 2; \ell = 2)$ mode, but unlike the AuAg case, the latter is not observed in VH configuration.
- the P_4 weak peak can be ascribed to the forth harmonic of the quadrupolar mode $(n = 4, \ell = 2)$, similarly to what was observed with AuAg NPs.

As previously observed with Au NCs (section 3.2), the T_{2g}/E_g intensity ratio evolves with the wavelength of excitation, due to the presence of oblate NPs (non-spherical shapes). Although most spectra reported below were recorded with $\lambda = 532$ nm (i.e. in the high energy tail of the SPR), the late acquisition of a 561 nm laser made it possible to record several spectra in nearly exact resonance with the surface plasmon of Cu. In

[4]In fact, very recent calculations [92] allow to account for the effect of the matrix on the T_{2g}/E_g frequency ratio; in the case of Cu NPs embedded in St.Just glass this ratio is expected to be 1.51, i.e. in very good agreement with the value derived from our fits.

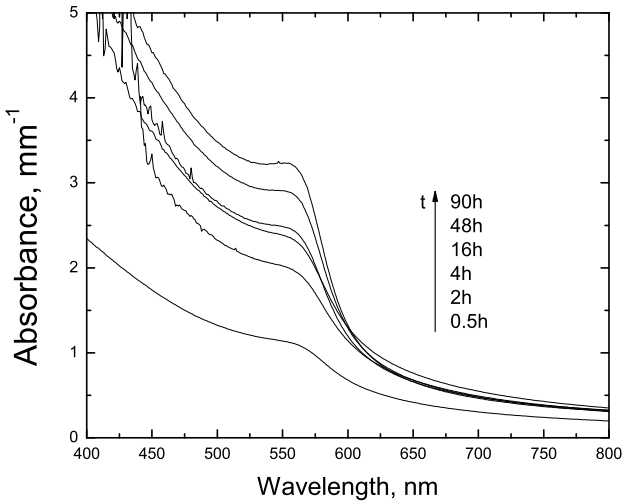

a

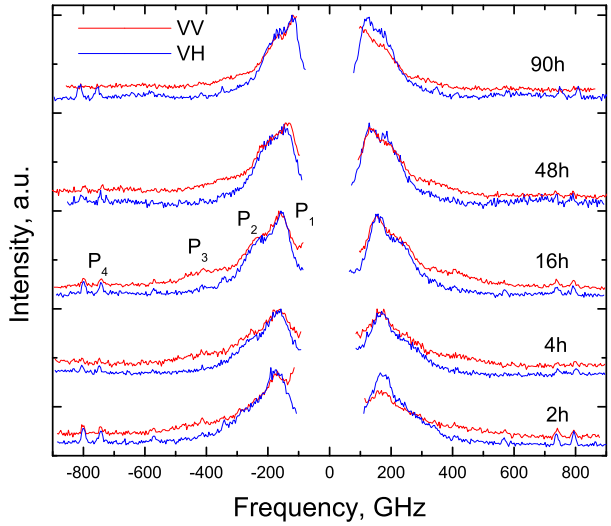

b

Figure 3.32: **a:** Recall of the absorption spectra from the samples annealed slightly above T_g (580°C) over time ranging from 2 to 90 hours (batch S_3). **b:** LFRS spectra from the same samples. The spectra are normalized on the maximum and shifted along the vertical axis for clarity.

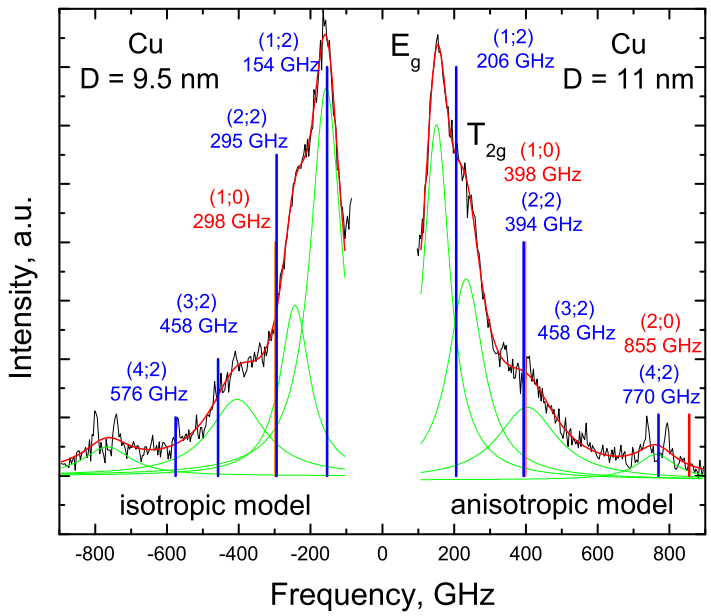

Figure 3.33: Polarized/depolarized LFRS spectra from the sample annealed slightly above T_g (580°C) during 16 hours (batch S_3). Red bars are the CFM predictions of the spherical mode ($\ell = 0$); blue bars are those for the quadrupolar mode ($\ell = 2$). **a:** The CFM hypothesis of the NPs of isotropic Cu NPs (Stokes side) and of anisotropic Cu NPs (anti-Stokes side).

order to check this effect, spectra similar to Figure 3.32 were recorded with $\lambda = 561$ nm, still using the Tandem FP interferometer[5]. Figure 3.34 compares the spectra recorded with a green (532 nm) and a yellow (561 nm) line from the sample annealed during 16 hours at 580°C ("$T_a > T_g$"). Qualitatively, the same behavior as that observed with Au NCs is found: going from 532 nm to 561 nm, the intensity ratio increases in favor of the apparent T_{2g} component. According to the interpretation given for Au NCs, this observation implies that what has been considered up to now as a "pure" T_{2g}-E_g doublet features in fact an underlying contribution associated with the isotropic ($n = 1; \ell = 2$) mode from MTPs. Unlike the non-embedded Au NCs case, this additional contribution cannot be resolved in the case of glass embedded NPs [59, 73]. As mentioned before, it

[5]Measurements with a red line are, in the present stage, not possible with the Tandem FP due to inadequate cavity mirror coating while measurements with a red line using the 5-grating monochromator does not enable to resolve, in the case of glass embedded Cu NPs, the lowest frequency Raman signal from the quasielastic line.

is not expected to have a major impact of the experimental determination of the T_{2g}/E_g frequency ratio, as testified by the good agreement with a recent theoretical estimation (see footnote 4 of this section).

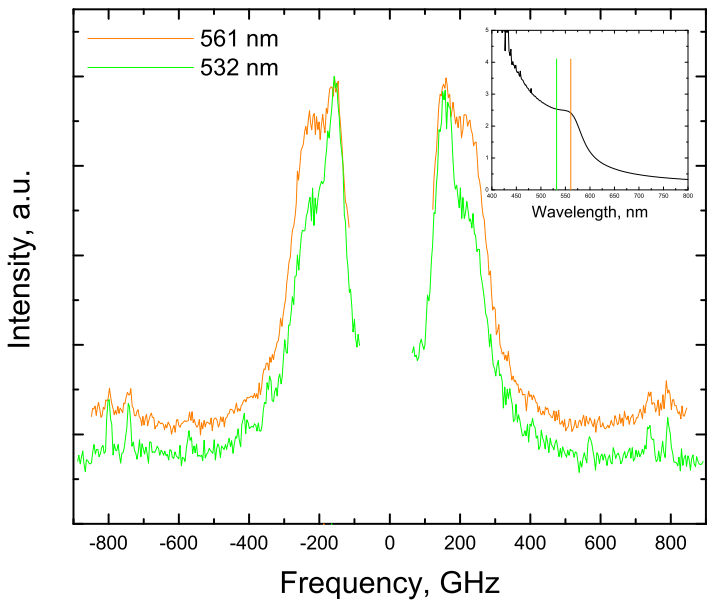

Figure 3.34: Depolarized LFRS spectra from the NPs annealed at 580°C during 16 hours. Spectra were recorded with exciting lines: 532 nm (**green**) and 561 nm (**orange**). **Inset:** Absorption spectrum of the same sample with marked positions of the exciting wavelengths.

Batch S_4

The study of the "$T_a > T_g$", "$T_a < T_g$" and "$T_a \gg T_g$" sample batches reveals that the formed NPs significantly depend on the annealing temperature.

Annealing the transparent glass well above its glass transition temperature leads to the formation of large NPs, comparing to lower temperature annealing. However the size is not the only parameter to change. While the elastic anisotropy effect appears clearly when the annealing is performed close to T_g, it is no more observed when the annealing is performed far above T_g ("$T_a \gg T_g$"). Before proceeding to a structural interpretation of these observations, we present the results obtained on samples (batch S_4) annealed during a fixed time of 2 hours and with fixed rate of annealing at temperatures ranging between

lower that T_g and well above T_g. As we will see, this series captures the progressive transition between three previously studied series.

Figure 3.35 shows the LFRS of sample annealed during 2 hours at different temperatures. As seen from the upper panel, the evolution of the size of the formed NPs (associated with a red shift of the main Raman band with increasing annealing temperature) requires to change the FSR of the Tandem FP in order to be able to record the full spectrum (bottom panel). These measurements are consistent with those obtained from the previous series at 2 hour annealing. As we observed it with the three previous batches of samples, the NPs annealed below T_g have a very poor Raman response with a very large single peak in the spectrum. In the end portion of the T_g zone, i.e. 580 – 605 °C one can observe the splitting of the quadrupolar mode with a T_{2g}/E_g ratio of 1.53 – 1.54, i.e. close to that already observed (Fig.3.34). Passing to higher temperatures the Raman spectrum shows a narrow quadrupolar mode with no more signature of elastic anisotropy.

In order to further check the consistency of the results obtained from the S_4 series, TEM characterization attempts were made with the sample annealed at 605°C (Fig.3.36). From the shown TEM picture the sizes of the detected NPs are of the order of 13 nm. This size occurs to be in good agreement with that derived from the corresponding LFRS data (Fig.3.37): from the position of the barycenter of E_g-T_{2g} doublet (Eq.(3.11)), CFM calculations predict a size of 13.8 nm, using the elastic parameters of Cu.

A close look at the comparison VV/VH spectra for the same sample (Fig.3.37) unveils the presence of a polarized signal which is only evidenced in the difference spectrum $I_{VV} - kI_{VH}$ (inset of Fig.3.37). The position of this signal is very close to that obtained by CFM (red bar) for the spherical mode ($n = 1; \ell = 0$) of the Cu NPs with size $D = 13.3$ nm. Such Raman activity of the radial mode was also observed with AuAg NPs embedded in the St.Louis matrix (section 3.1.3) but, in contrast, the polarized spectra of the Cu-glass annealed at 605°C does not demonstrate this contribution so obviously. Definitely, it appears from Figure 3.35 that the visibility of the spherical mode strongly depends on the width of the quadrupolar line (or its corresponding E_g-T_{2g} doublet): the broader the quadrupolar contribution, the weaker the spherical mode signal. One observes that once a minimum linewidth is reached, or as soon as the annealing is performed above T_g, the lines turn sufficiently narrow for the spherical mode contribution to materialize. This trend could not be observed from the S_2 batch (Fig.3.29b) since from the very first sample (0.5H annealing), a minimum linewidth appeared to be already reached (from Figure 3.29d the linewidth remains contrast for longer annealings). On the other hand, it is possible to

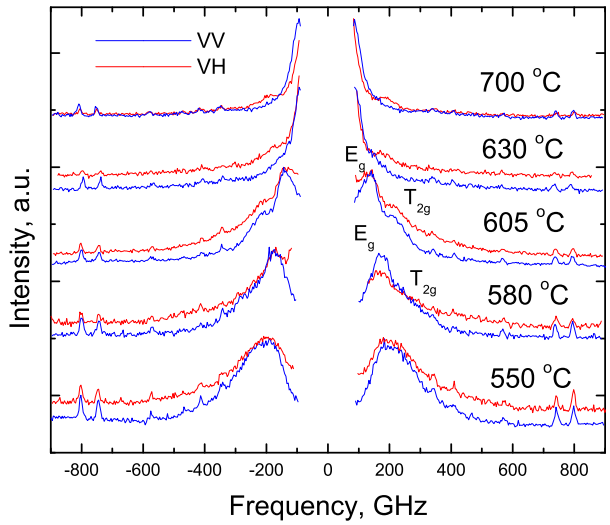

a

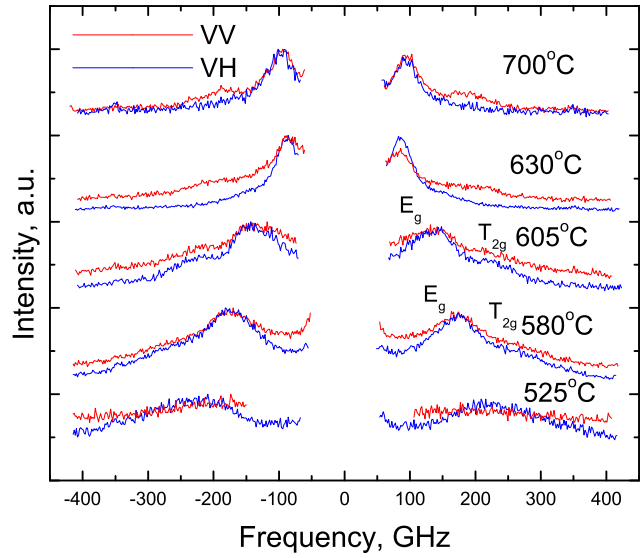

b

Figure 3.35: LFRS spectra (exciting line is 532 nm) from the NPs prepared through annealing between 525°C to 700°C during 2 hours (batch S_4). The lower panel was recorded with a lower FSR in order to resolve the inelastic signal for higher temperature of annealing.

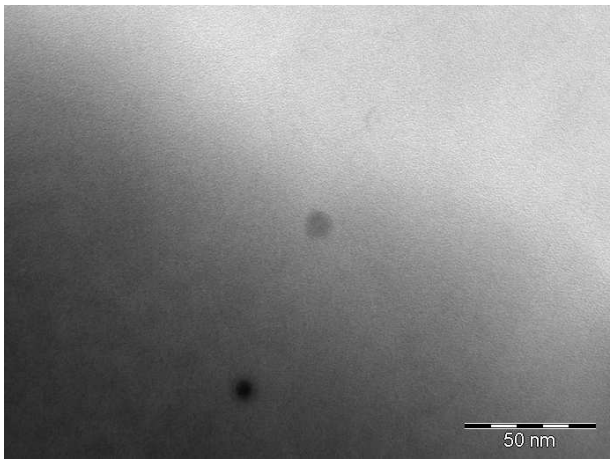

Figure 3.36: TEM image of the sample annealed at 605°C during 2 hours (batch S_4).

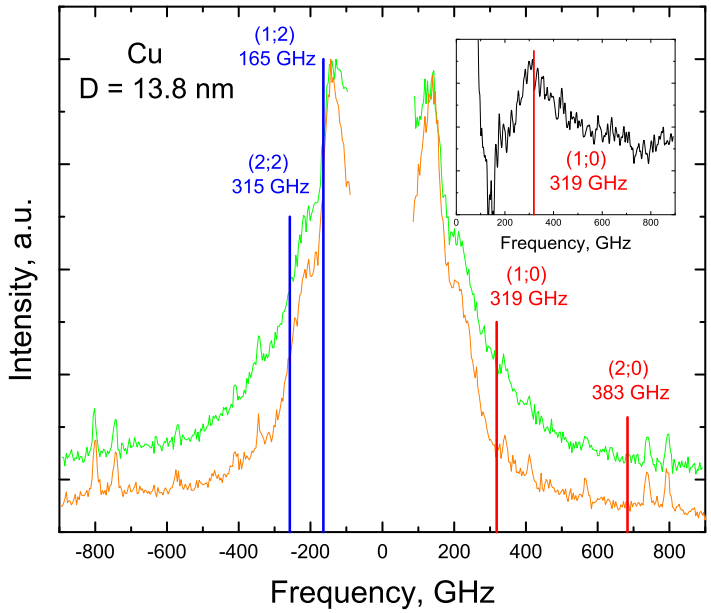

Figure 3.37: LFRS VV and VH spectra (exciting line is 532 nm) from the NPs annealed at the temperature 605°C during 2 hours and the theoretical CFM prediction of the frequency positions of the vibrational modes and their harmonics for Cu NPs with average size 13.8 nm with the assumption that the NPs are crystals. **Inset:** The difference spectrum $I_{VV} - kI_{VH}$, where k is a normalizing coefficient.

observe the effect by comparing two samples annealed at the same temperature (above T_g) for the same duration but cooled down differently: while one was quenched, the other one was cooled down in the furnace at a rate of 100°C/hour, therefore experiencing a longer heat treatment.

Figure 3.38 compares the VV and VH Raman spectra of quenched and non quenched subsamples originating from a sample annealed at 630°C for 2 hours. Basically, the observed profiles are similar, close to identical; the positions of the observed lines are equal within 1 GHz. The same behavior is observed for the samples annealed at 700°C except that the difference between quadrupolar mode positions is a bit higher: 10 GHz. These observations, together with absorption investigations (Fig.3.25), allow us to conclude that cooling time does not dramatically influence the Raman spectra. Yet, a careful examination of Figure 3.38 reveals that both VV and VH spectra display a slightly narrower quadrupolar line (and also a more "defined" radial mode signal) in the case of the non quenched sample. This can be interpreted either as a size distribution reduction or/and as a "healing" of the NP intracrystallinity which was shown to influence the Raman profile [98], as the single quadrupolar line testifies the NPs as MTPs or polycrystals. We discuss this latter aspect in the following summarizing section.

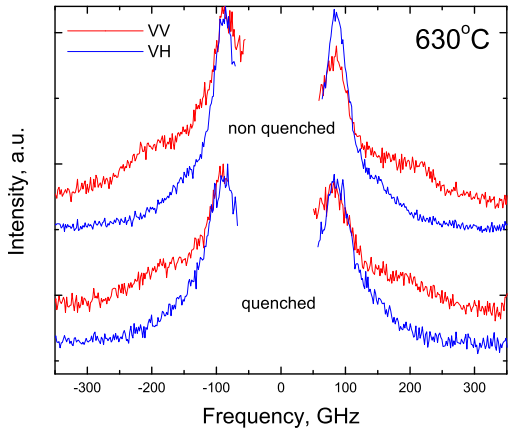

Figure 3.38: LFRS spectra of the sample annealed at 630°C and after cooled down with the rate of 100°C/h (**up**) or rapidly quenched (**down**).

3.3.4 Discussion

The results obtained on the forth batch of sample (S_4), as we noted above, have allowed to follow the evolution of the LFRS spectra, from low to high temperatures, reproducing the spectra of the first three series of sample ($S_1 - S_3$). From there, we are able to draw a general scheme on the formation of embedded Cu NPs through annealing.

Figure 3.39 summarizes the size derived for the four batches of samples and gives a basic schematic representation of the corresponding Raman profiles.

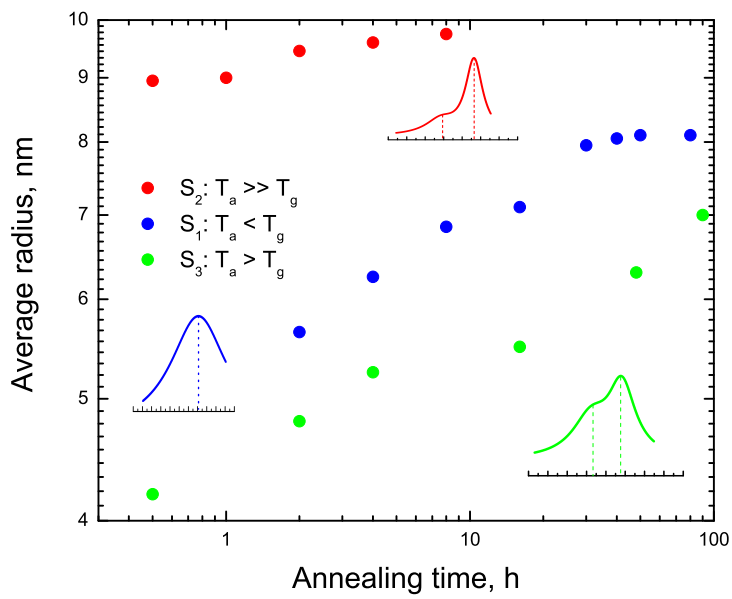

Figure 3.39: Evolution of the average radius as a function of annealing time assuming Cu NPs for the three series of the samples: "$T_a < T_g$" (blue), "$T_a \gg T_g$" (red) and "$T_a > T_g$" (green) — and corresponding schematic profiles of the lowest frequency modes.

Starting from a colorless, Cu-doped glass **annealing at temperatures lower that** T_g, the LFRS spectra consist of a single broad band attributed to the quadrupolar mode of Cu NPs. The width of the quadrupolar mode reflects the large size distribution of the formed particles. Obviously, at temperatures lower than T_g, the still solid-like behavior of the glass network hinders the diffusion of Cu atoms so that the formed NPs are likely to be poorly crystallized and hardy spherical, with a large size distribution. While this situation yields a poor Raman signal, it is worth noting that the associated optical response is rather well defined, with a clear SPR. Furthermore, prolonged annealing below T_g does

not substantially improve the quality of the Raman signal, while a maximum average size of about 16 nm is reached. In order to significantly modify the Raman profile, one needs to increase the annealing temperature.

Annealing the glass **slightly above its glass transition temperature** leads to a mode structured Raman response. The single broad maximum observed at lower annealing temperature transforms into a double component structure. The two components identify with the E_g and T_{2g} modes that arise from the splitting of the quadrupolar mode when the NPs are NCs, i.e. featuring elastic anisotropy (as observed with non-embedded Au NCs (sectiion 3.2) or embedded AuAg NPs (section 3.1)). At this temperature of annealing, the viscosity of the glass is such that the diffusion of Cu atoms is facilitated and they have sufficient energy to organize into crystal structures. The sizes obtained from the average position of the E_g/T_{2g} doublet, i.e. using an isotropic model of embedded nanospheres, are somewhat smaller than those obtained through annealing below T_g. It may be that in this regime, the use of the isotropic CFM model, which is not meant to describe elastically anisotropic structures, is a too crude approximation, thereby leading to a misestimate of the NP sizes. The second reason might be the higher heating rate used to anneal this batch of the samples (25°C/min versus 10°C/min, Table 3.7). Finally, the observation of elastic anisotropy, which goes with a narrowing of the Raman lines, is concomitant with the progressive observability of the spherical mode, which as a non-degenerated mode is helpful in the determination of the size.

Annealing at temperature well above T_g produces essentially narrow Raman lines. The E_g/T_{2g} doublet structure of the quadrupolar mode is no more observed and the spherical mode contribution is clearly visible in the polarized spectra; higher order harmonics of the quadrupolar mode may also be detected. In a sense, the LFRS spectra get closer to those expected from elastically isotropic nano-spheres, with a quite narrow size distribution. In comparison with lower temperature annealings, the obtained sizes are larger. From the clear observability of the radial mode signal, one can conclude that the NPs formed at high temperature have a good crystallinity. Such derives from the volume mechanism which is responsible for the scattering by the radial modes (see section 3.1) whereby the NP lattice vibration modulates the metal dielectric function. On the other hand, the non-observation of the E_g/T_{2g} doublet testifies that NPs cannot be identified as single NCs. Therefore, these NPs are most likely polycrystals, or MTPs, of relatively large size, as opposed to the small NCs produced through annealing slightly above T_g. One may further suggest that the shapes of the polycrystalline NPs formed at high temperature are

more spherical, in contrast to facetted NCs, for interfacial energy minimization purposes. Unfortunately, our TEM attempts were not successful enough to conclude on this matter.

3.4 Conclusion

In this chapter we showed the results of works dedicated to investigation of the vibrational modes of metal NPs: AuAg and Cu NPs embedded in vitreous matrix and Au NCs deposited on a surface. Through these works we proved that low frequency Raman scattering from the vibrational modes of metal NPs is a very powerful and sensitive probe due to the resonance conditions with the surface plasmon resonance. The unique setup based on the Tandem FP allows to record highly resolved spectra in a wide range of free spectral ranges and hence from a wide range of NP sizes. In the works described in this chapter we managed to show that:

- the probing of the crystalline quality of metal NPs through the lift of degeneracy of the quadrupolar mode ($n = 1; \ell = 2$) is now established as an additional advantage of LFRS characterization. The splitting is clear cut in single NCs while it overlaps with its degenerate counterpart in the additional presence of non single NCs (MTPs, polycrystals). In the latter case, selective wavelength excitations may help distinguish between the two types of signals, provided the probed NP assemblies are highly monodisperse in terms of size and overall crystalline quality. In the presence of NP assemblies featuring larger size and crystallinity distributions, as is probably the case with NPs grown in glass, the detection of the splitting confines to qualitative information.

- LFRS spectra of metal NPs may contain several components including, besides the fundamental spherical ($\ell = 0$) and quadrupolar ($\ell = 2$) modes, high order harmonics. As the fundamental modes, the several harmonics can be identified through their polarization dependence. Probing high order overtones of NP modes has allowed to check for the first time theoretical predictions for Raman *intensities*. The "irregular" Raman actives of the high order harmonics ($n < 9$), i.e. not regular scaling as $1/n^2$ for instance, is a consequence of both coupling with the surface plasmon excitation and specific deformation modes associated with the NP modes.

- the growth process of NPs nucleated in a matrix through annealing at high temperature can be followed LFRS: annealing below the glass transition temperature of the

glass generates large distribution of NPs (size, shape, and/or poor crystallinities) characterized by a featureless single Raman broad band, annealing slightly above T_g (AuAg, Cu) results in the appearance of the elastic anisotropy splitting effect, hence associated with the formation of single NCs. Annealing much above T_g products large sizes of NPs, with no more detectable elastic anisotropy effects, so that the NPs cannot be considered as NCs any more. With this respect, large NP sizes favor defective crystalline structures, at least when grown in matrices.

Chapter 4

Raman and Brillouin Scattering from Large Viruses

From their rigid and compact globular structures, viruses can be considered as "biological particles" whose elastic and dynamical properties are, in contrast to structural properties, hardly known. As such, they are expected to feature the low frequency vibrational modes that we have dealt with in details from solid NPs as described in the previous chapter. In viruses, these low frequency modes were predicted a long time ago [112] through theoretical calculations and also were admitted as potentially important ingredients of the dynamical and elastic behaviors of viruses. But in the same time they have been proved hard pressed to be detected experimentally. Our works aim at detecting these modes through low frequency inelastic light scattering.

At the LPCML, the investigations of virus vibrational modes have already been carried out by Stephanidis *et al.* [64]. The study of the small ($D \ll \lambda$), of the order of 17 nm, Satellite Tobacco Mosaic Virus (STMV) led to conclusion that at this stage of development of the low frequency Raman scattering techniques, it is almost impossible to detect the NP modes from small virus, whether they are dispersed in a solution or arranged within a microcrystal. In the first case the elastic and quasielastic scattering from the embedding liquid contribute significantly more to the spectrum than the expected inelastic scattering from viruses whose concentration in the solution is not high enough to grow over the signal of the liquid. In the case of microcrystals [5], the reasons for the non-observation of the virus signal are less clear. One reason could be that in spite of the high concentration due to the crystalline arrangement, the still significant water content contributes to a significant damping of the expected vibration modes. Another reason is that this damping

is enhanced by the strong interaction between closely packed viruses, as was also suggested in [3]. In contrast to the study of small viruses like the STMV, B. Stephanidis [5] showed that the low frequency inelastic scattering signal from suspensions of large ($D \sim 200$ nm) viruses could be more promising. In this case, the milky aspect of the solutions, unlike the transparent solutions of small viruses, testifies already a stronger interaction with light (Mie scattering). However, working with large viruses where the probe wavelength and size of virions are comparable leads to less restrictive selection rules (see section 2.2.1) making the interpretation of the obtained signal not be very trivial. The changing of the selection rules and poor knowledge about low frequency inelastic scattering from viruses make the spectrum decoding almost impossible without a reference object of comparable size. In order to ease this interpretation, polymeric molecules packed in nanospheres with dimensions similar to large viruses were admitted as a good reference samples. Although colloidal NPs have nearly perfect spherical morphology, in contrast to the icosahedral shape of viruses, they can be considered as very close, at least as far as concerned NP vibrational modes are. In addition, the colloidal polymeric molecules are expected to have similar mechanical properties, but in opposite to viruses which can be studied only in "wet" conditions, it is possible to investigate the polymeric spheres in both "wet" and "dry" states. This particularity gives the opportunity to follow the change of the polymeric sphere vibrational dynamics when it passes from "wet" to "dry" conditions, the latter is well identified. This, by turn, should allow to help to interpret the data obtained form pellets of viruses. The idea to use polymeric colloids as a reference for virus low frequency inelastic scattering experiments is not new. For example, Hartschuh *et al.* [3], in their experiments with WIV virus (140 nm), made a comparison with 300 nm PMMA colloids. In the present work we used polystyrene (PS) spheres as reference. This choice was set due to the fact that the PS colloids used have dimensions very close to the investigated viruses and also there are several publications [58, 113] dedicated to the low frequency Raman/Brillouin scattering from dry PS NPs describing the low frequency inelastic scattering spectra from these NPs in details.

Low frequency inelastic scattering investigations of large viruses were initiated at the LPCML by Stephanidis [5] from the *Paramecium Bursaria Chlorella* virus type 1 (PBCV-1) of the order of 190 nm. He studied liquid suspensions of the virions (it is impossible to crystallize PBCV-1) and managed to observe a large q-independent band which could be attributed to the inelastic signal of the virus. We took this result as a starting point of our experiments. In order to check whether the low frequency inelastic scattering signal

obtained from PBCV-1 was reliable, and not virus-dependent, we investigated other large viruses. The *Chilo Iridescent Virus* (CIV) was chosen as a good counterpart of the PBCV-1 due to its similar size (185 nm) and similar overall icosahedral architecture. What we considered as an interesting property of CIV is its ability to self assemble into a paracrystalline order, just like the PS colloids. The self assembly property might be an advantage in the sense that it may result in an enhanced vibrational coherence of the NP modes (as observed from Ag NPs in supracrystals [55]), thereby easing its detection, although we mentioned earlier that such did not seem to be the case for small viruses studied in the form of microcrystals.

As we mentioned before (see section 2.2.1), when the size of the NPs is comparable with the probe wavelength the important parameter influencing the number of modes active in the inelastic scattering is the product qR, where q is the transferred wave vector and R is the radius of the scattering spherical object. Due to multiple scattering processes inside large NPs all q from 0 to $4\pi n/\lambda$ contribute to the inelastic spectrum. In order to change the qR product, i.e. in order to change the active mode composition and their integrated contribution to the Raman/Brillouin spectrum by the changing of the maximal value of qR product (Fig.4.1), we have to use another exciting wavelength or change the radius of the NP, i.e. investigate a virus with a different size (the refractive index does not critically change from virus to virus in this work). From this consideration, we investigated another virus with different radius, *Wiseana Iridescent Virus* (WIV), whose diameter of 140 nm is 1.32 times lower than that of the CIV virus. WIV is a virus of the same family as CIV exhibiting similar self assembling properties. **The underlying expectation studying a similar virus with a different size is to observe a shift of the vibrational spectrum in accord with the basic relation $\nu \sim \frac{v}{D}$.** As we will see, such behavior turns out to be not so clear.

This chapter is dedicated to low frequency inelastic scattering from vibrational modes of large viruses and PS colloids. First, we briefly review short biological and physical description of the studied viruses and of the prepared samples, of their peculiarities and properties. Next, we provide a description of additional techniques we used to give a morphological characterization of our samples. The last part of the chapter presents the Raman results and their analysis.

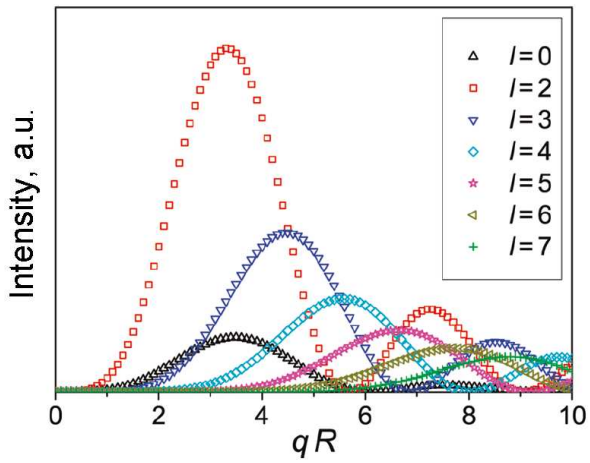

Figure 4.1: Inelastic intensity of the fundamental ($n = 1$) vibrational eigenmodes with $\ell = 0$ and $2 \leq \ell \leq 7$ for a free vibrating polystyrene latex sphere as a function of the product of scattering wavevector q and radius R [114].

4.1 Biological description of the studied viruses

A single virus particle outside of the host cell is usually called virion. A virion contains the genome of the virus (Fig.4.2). All viruses are divided into four groups differing according to their genomes: double-stranded DNA (dsDNA), single-stranded DNA (ssDNA), double-stranded RNA (dsRNA) and single-stranded RNA (ssRNA). The genome has a protein protection which is named a capsid. The main function of the capsid is to protect the genome and to provide the latter to penetrate into the cell. In spite of the fact that the virion is very small (10 – 200 nm) it is very efficient. For example a single virus infected cell can produce 10^5 virions, and a person infected with the human immunodeficiency virus (HIV) might produce 10^{11} virions per day.

The capsid is a very important part of virion. Besides its protective function it also must recognize and attach to a host cell inside which the virus can be replicated. The capsid has to be enough strong to survive in the extracellular environment. One of the most famous fundamental works dedicated to capsid structures is the paper of Caspar and Klug [115] where they show that capsids of polyhedral viruses adopt icosahedral shapes as this configuration has the largest surface-to-volume ratio among all polyhedra. Also they showed that the total number of proteins contained in a capsid is always a result of the product $60T$ where T is the so-called *triangulation number* such as $T = h^2 + hk + k^2$ and h and k are non-negative numbers characterizing the operations of translation on the

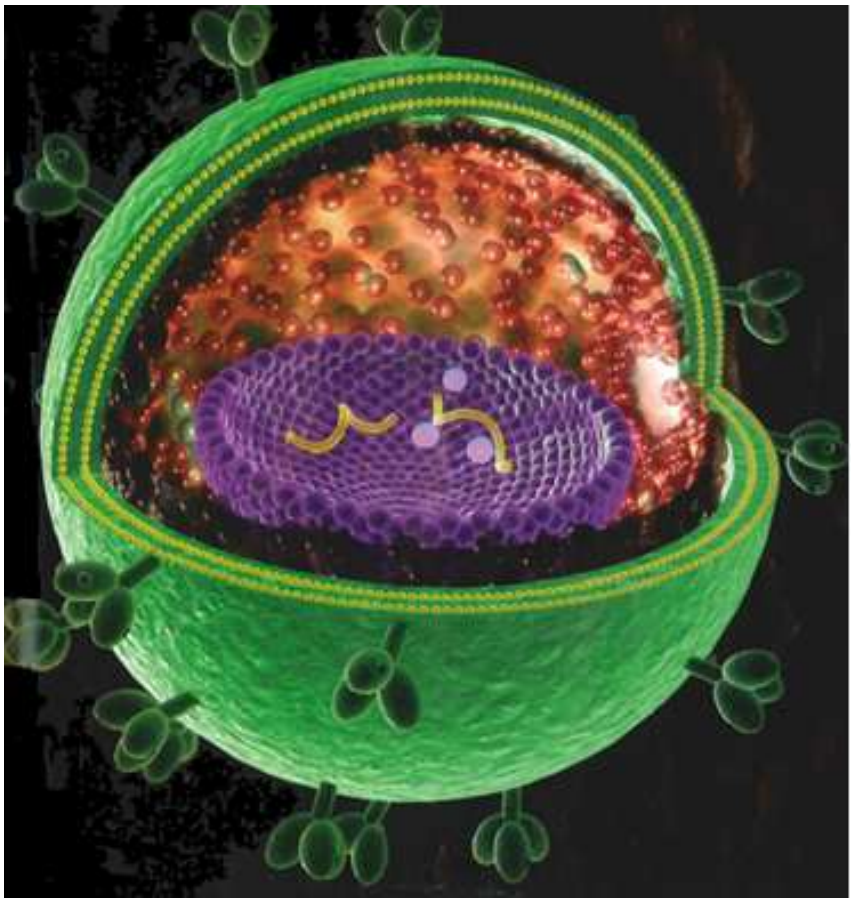

Figure 4.2: Schematic inner structure of a spherical virus.

2D hexagonal structure on the icosahedron surface [116]. The T number displaying the symmetry of protein locations is an important characteristic of viruses, as much as its size and genome. The structure of capsid, or more exactly its elastic properties, directly influences the vibrations of whole virion and therefore it is very important for us to know the peculiarity of the outer capsule. Below we shortly introduce biological structures of viruses we worked with.

4.1.1 PBCV-1

Paramecium Bursaria Chlorella virus type 1 (PBCV-1) (Fig.4.3) was discovered in 1981 in chlorella symbiotic with the protozoan *Paramecium Bursaria* and was labeled to the large category of algal viruses (genus *Chlorovirus*, family *Phycodnaviride*). Now it is well-know that it infects unicellular, eukaryotic, chlorella-like green algae and is common worldwide in fresh water. It is a virus of 175 – 190 nm in diameter of a polyhedron

shape, similar to the icosahedral [117], with multilayer capsid [118]. One specificity of PBCV-1 virus as recently discovered [119], is that one vertex of the icosahedral structure is decorated with a spike of 20 – 25 nm (Fig.4.3b). The virus, whose estimated mass is 1 GDa, consists of about 64% of proteins (at least 50 structural and 4 of virion surface), 21 – 25% of dsDNA and 10 – 15% of lipid and has a density 1.25 – 1.3 g/cm^3. Its genome has 330 kbp[1], it is linear and non-permuted. PBCV-1 is a quite popular among researchers because of its size and prevalence in the world. Its size was precisely measured by cryo-EM [120]. The crystal structure of the PBCV-1 major capsid protein, Vp54 organized into 1680 trimers as a pseudo $T = 169d$ quasi-equivalent lattice, was determined to 0.2 nm resolution by X-ray crystallography and fitted into a three-dimensional cryo-EM map of the PBCV-1 virion [121]. It was shown that it has a pseudo-hexagonal symmetry and the outer diameter of the viral capsid is 165 nm measured along the two- and threefold axes and 190 nm along the fivefold axes.

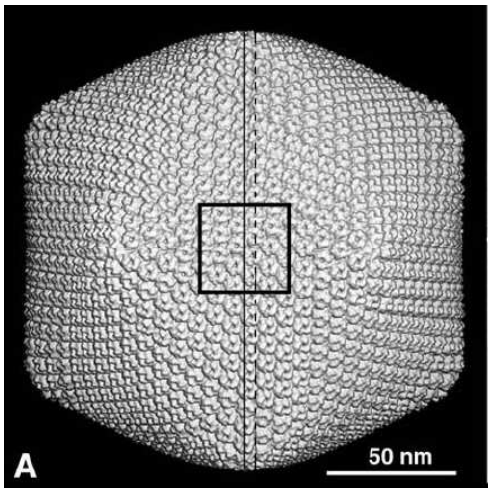

a

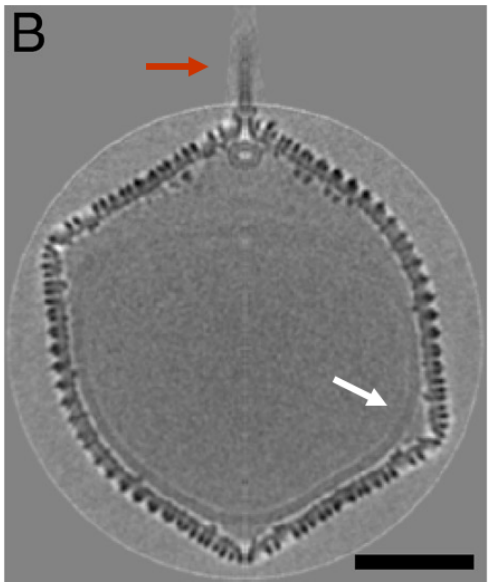

b

Figure 4.3: **a:** Shaded surface view of PBCV-1 3D reconstruction at 15Å resolution, viewed along a 2-fold axis [122]. **b:** Central cross-section of the cryo-EM density (scale bar: 500 Å) [119]; the red arrow points to the spike-structure, the white arrow indicates the inner lipid layer.

PBCV-1 virus samples were isolated, purified and provided in a Tris buffer solution (pH= 7.8) for us by James Van Etten from the department of Plant Pathology, University

[1]BP — base pair, a pair of complementary nucleotides of DNA or RNA molecules: adenine (A)/thymine (T) (for RNA — uracil (U)), and guanine (G)/cytosine (C).

of Nebraska, Lincoln, Nebraska, USA.

4.1.2 Iridescent viruses

CIV

Chilo Iridescent Virus (CIV) or *Iridovirus* type 6 (IV6) (Fig.4.4a) is an icosahedral, double-stranded DNA virus belonging to the genus *Chloriridovirus*, the family *Iridoviridae*. It is a large, $\sim$ 1 GDa, icosahedral (around 185 nm) insect virus with a blue iridescence [123]. The first IV was isolated from the larvae of the crane fly *Tipula Papudosa* by Claude Rivers in 1954 in Great Britain. The infection generated by this virus leads to a blue-opalescent coloration of the insect (Fig.4.4b) hence the term "iridescent". After several types of iridescent viruses were isolated; CIV was reported the sixth one in 1966 by Fykaya and Nasu who isolated it from dead bodies of larvae of rice stem borer [124]. It has a 209 kbp linear, circularly permuted genome, surrounded by a lipid membrane which represents 9% of the total virion weight [125] and by a capsid which consists of the major capsid protein (MCP), protein P50 and that of PBCV-1, Vp54. Its protein capsid consists of 12 pentavalent (pentamer) and 1460 hexavalent (trimer) capsomers, arranged with T=147 (h = 7, k = 7) icosahedral, quasi-equivalent symmetry [126]. The average density of CIV is 1.26 - 1.33 g/cm^3. CIV forms quasicrystalline hexagonal arrays (Fig.4.4c) in which neighboring virions are separated by 40 – 60 nm [120]. In paper [125] the structure of CIV was studied by cryo-EM; the computed reconstruction of the CIV virion based on these results is shown in Figure 4.4a. According to this reconstruction the outer diameters of the viral capsid are 165 nm along the two- and threefold axes and 185 nm along the fivefold axis. The similarities of CIV and PBCV-1 viruses (including the capsid structures) noted in [120] allow us to expect similar collective vibrational behaviors of these viruses.

Preparation of CIV suspensions

The isolation and purification of CIV takes approximately one day. It is isolated from the body of larvae of *Galleria mellonella* — a parasite of bees' hives. These larvae were infected before the purification by the injection of about 9μl of the virus solution into each individual. This virus kills the insect over 10 days. After its death, the insect will be frozen, so that its body can be used as a container for storing viruses. According to Williams and Smith [127], after the death, around 25% of the dry weight of the insect's

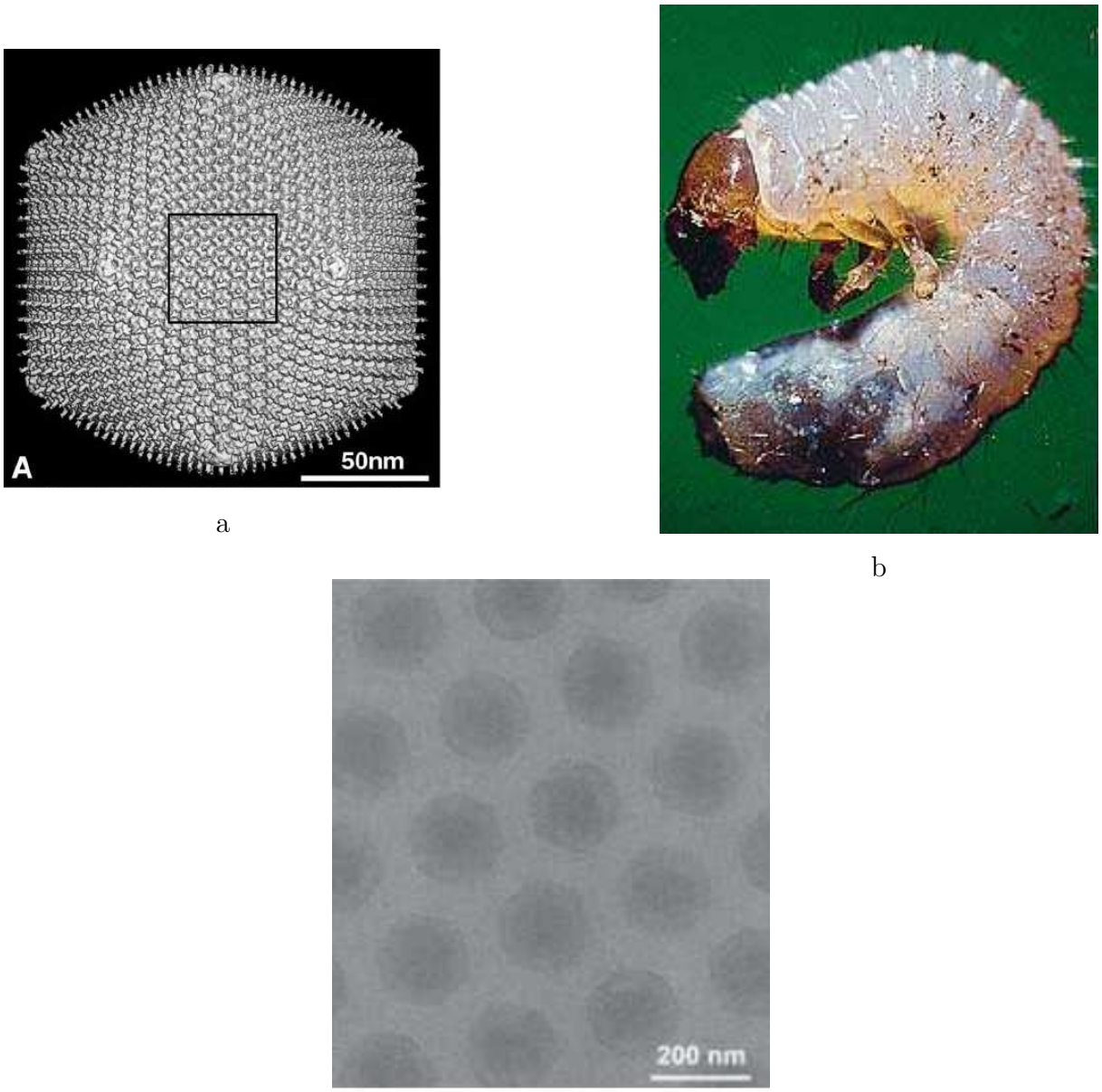

Figure 4.4: **a:** Shaded surface view of CIV 3D reconstruction at 13Å resolution, viewed along a 2-fold axis [125]. **b:** Insect infected by CIV demonstrates the opalescent shade due to CIV self organization. **c:** Micrograph of vitrified CIV virions suspended over a hole in a carbon support film [129].

body is indebted to viruses and, taking into account the approximate weight of the particle for this virus family ($2 \cdot 10^{-15}$ g [128]), one can affirm that in one dead body there are

around $2 \cdot 10^{12}$ particles [130]. This fact makes the purification procedure very simple.

The dead bodies of Galleria mellonella are pounded in distilled water. This stage, as all stages of the purification, has to be performed at low temperature around 4°C to avoid melanisation — a process by which microbes destroy anti-microbial peptides and other proteins involved in the humoral response. Then the prepared solution is placed in the centrifuge and spun there during 10 minutes with an acceleration of the order of 2500g. This centrifugation separates large fractions and remains of the insects. The filtered solution is placed again in centrifuge for 30 minutes with an acceleration of the order of 23000g. After this stage one can observe the blue trail of the viruses at bottom of the flask. The obtained solution has to be shaked and left in the cold for one hour to make the suspension more homogeneous. If the process goes on correctly the liquid has to be as white as milk.This suspension is passed through a ECTEOLA column with a cellulose filter in order to obtain a solution is the solution of purified virus. The average concentration of viruses in the final water solution prepared by the method described above is approximately 6 – 7 mg/ml. A TEM image of the pellet of the isolated virions is displayed in Figure 4.5.

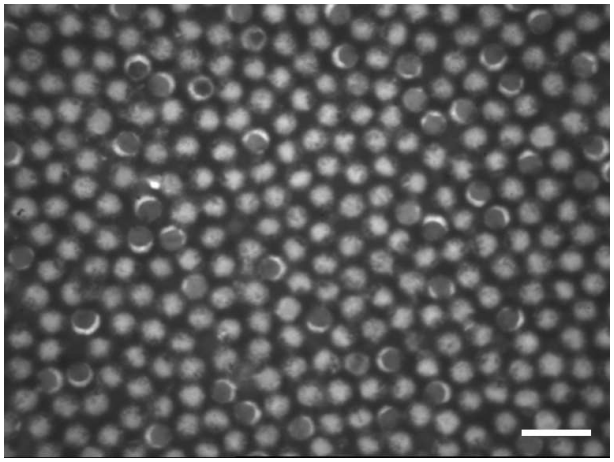

Figure 4.5: TEM image of a CIV pellet. The white bar corresponds to the scale of 460 nm.

The CIV virus samples were isolated with the help of Max Bergoin from Unité de Biologie Intégrative et Virologie des Insectes of Montpelier II University, France.

WIV

Wiseana Iridescent virus (WIV) or *Iridovirus* type 9 (IV9) is a double-stranded DNA virus belonging to the genus *Iridovirus*, the family *Iridoviridae*. It is a large insect virus

of the size of 140 nm with blue to purple iridescence (Fig.4.6a). The first WIV was isolated in 1971 by Fowler and Robertson [131] from *Wiseana* larvae. This virus also has icosahedral shape (Fig.4.6b). Its capsid containing a 4 nm lipid bilayer protects a 132 nm in diameter double-stranded DNA core. The exact surface structure of the WIV virus is not known [132]. Both CIV and WIV capsids exhibit a halo of fibrils (Fig.4.6b) which, as we will see, seem to be determinant for self assembly. The procedure of isolation and purification described for CIV can be applied to WIV. The WIV virus was initially provided by Vernon Ward from the Department of Microbiology, Otago School of Medical Science University of Otago, New Zealand. It was produced in large amounts thanks to the help of M. Bergoin.

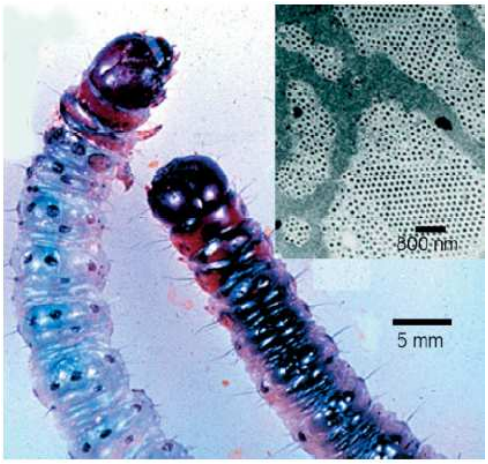

a

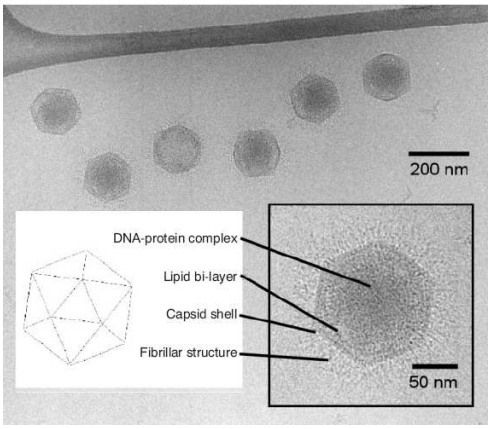

b

Figure 4.6: **a:** Insect infected by WIV (**left**) and uninfected one (**right**). TEM image (**inset**) showes closed-packed arrays of viruses within the cell cytoplasm [132]. **b:** Cryo-TEM of dispersed WIV particles. The image shows six particles viewed along a threefold symmetry axis. The higher magnification inset shows features corresponding to the fibrillar structure, emanating from the proteinaceous capsid [132].

4.2 Physical characterization of the samples

In our experiments we have studied two types of samples: virus suspensions (virions diluted in liquid) and pellets of viruses — the highly concentrated jellylike solution of viruses which is characterized by high viscosity and iridescent tints.

4.2.1 Virus solution

As mentioned before, previous low frequency inelastic scattering experiments with suspensions of small viruses are not very fruitful [5]. Considering large viruses with similar concentration values as those of small viruses ($\sim$ units of mg/ml) we can expect a more intense Raman signal from the virions because large viruses means higher volume fraction in the solution. PBCV-1, CIV and WIV viruses were diluted in liquids with values of concentrations ranging from several tenths to units of mg per ml.

UV-light absorption measurements are a good probe to determine the virion concentration in a solution and to conclude whether the virions are intact [133]. Absorption spectra of CIV suspensions of different concentrations are shown in Figure 4.7. The spectra demonstrate a broad peak with maximum around 258 nm. This feature is well known in virology [134, 135] where this band is attributed to the absorptions of the nucleic acids of virus DNA (RNA) [136]. Its presence is a sign of the fact that the DNA (RNA) of virions, and so that the virions, are not defective. The ratio A_{260}/A_{240}, where A_λ is absorption intensity at the corresponding wavelength, is usually used to estimate the virion concentration. In our case this ratio is lower than unit (0.78, 0.80 and 0.86 respectively to increase of concentration) that corresponds to very low concentrations (Fig.4.7).

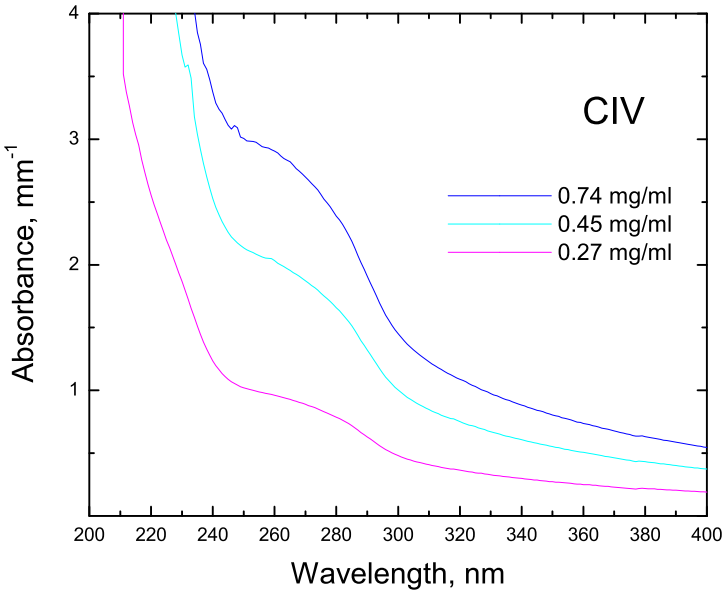

Figure 4.7: Absorption spectra of CIV suspensions with different virion concentrations.

4.2.2 Virus pellets

As we mentioned before, investigating the pellets of viruses we were guided by two reasons. First, the high concentration of virions is supposed to enhance the scattered intensity of the virus signal with respect to that of the liquid due to the increase of virus volume fraction. Second, the self assembled virions may vibrate coherently so that we may expect the increase of the Raman response from virus vibrational modes.

The pellets were prepared by the centrifugation (rotor SW41) of the origin solution with an acceleration around $23000g$ during 30 minutes that allowed to separate the virions from the liquid. Although the centrifugation leads to a substantial removal of the embedding liquid the pellet still contains a significant amount of water. Unlike the suspensions where most of the water can be considered as bulk water, the remaining water in pellets interpenetrates the virus aggregative structures, thereby ensuring its cohesion. It is a fact that water is intrinsically part of biological architectures so that a complete removal of water leads to their disruption. As we will discuss it later, this might have important consequences for the existence of NP modes in viruses.

Figure 4.8 shows the bottom of the tube after the centrifugation of the CIV solution. The virus concentrate subsided during the separation procedure displays iridescent properties, testified by an opalescent green shade in scattered light turning to a pronounced red color in absorbed light. These tints are typical of opal structures characterized by a regular array of submicron particles. This ordering property of CIV, derived from macroscopic optical behavior, meets that found from cryo-electron microscopy (Fig.4.4c).

While WIV pellets display the same iridescent properties as the CIV ones, it is not the case with PBCV-1: its pellets appear totally white. The absence of iridescent behavior with PBCV-1 most likely indicates the absence of long range ordering. This specificity will be discussed in the USAXS and AFM studies.

4.2.3 Polystyrene spheres

As the vibrational dynamics of the viruses is little-explored it was decided to find some non-virus polymeric NPs of similar sizes to make a comparison with. The first objects we chose as a reference were NPs of polylactic acid (PLA). PLA NPs (produced by IBCP laboratory, University Lyon-1, France) were first considered because they could be provided with sizes close to those of the investigated viruses and also because PLA is biocompatible and envisaged as a good material to form “artificial” capsids. Unfortunately, a USAXS

a b

Figure 4.8: CIV pellets obtained through centrifugation of the virus suspensions. **a:** View in reflected light. **b:** View in absorbed light.

check of PLA NP solutions (Fig.4.9) immediately revealed that the size distribution of the produced suspensions was very polydisperse (see next section), against the provider expectations.

As substitute of PLA NPs, we turned to polystyrene (PS) NPs which present several advantages:

- highly narrow size distribution PS colloids can be commercially found, within a quite large range of sizes that includes that of our investigated viruses.
- PS colloids that are provided in solutions can easily be "dried out" through the evaporation of the solvent, thereby offering the possibility of studying the effect of the liquid embedding medium.
- low frequency Raman/Brillouin measurements and their interpretation on PS colloids is well developed [58, 113] so that they may serve as a reliable basis for similar measurements on biological NPs such as viruses [3].

PS suspensions (grade "Estapor") were purchased from Merk at typical concentrations of the order of 10^{13} pc/ml. As with viruses both solutions and pellets were studied. The pellets were obtained by centrifugation at 23000g.

The pellets of PS prepared analogous to those of investigated viruses are also viscous jelly-like substance with iridescent tints. As the studied viruses are of different sizes

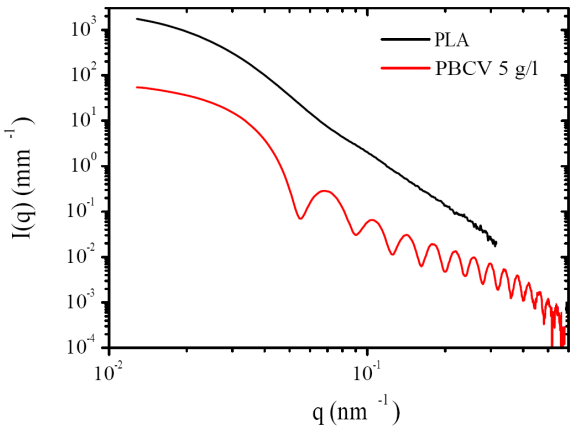

Figure 4.9: USAXS from a suspension of PLA NPs and from a PBCV-1 solution. These curves show that PBCV-1 viruses are monodisperse spheres whereas PLA NPs possess a high polydispersity and therefore they cannot serve as proper references for our low frequency inelastic scattering experiments.

(so that the maximal values of the qR products are different for different viruses), we considered PS NPs of two sizes: 187 and 297 nm (named PS-187 and PS-297 respectively).

As exposed briefly in the forthcoming sections, the structure of viruses such as PBCV-1, CIV and WIV are well established, essentially from electron microscopy and x-ray diffraction observations (see for example [119]). These latter characterization techniques imply sample conditions that differ from our light scattering measurements. For instance, the cryogenic conditions used in TEM do not compare with room-temperature light scattering measurements performed from liquid suspensions or pellets. These different methods might possibly probe different states of the viruses (e.g. conformational states) associated with slightly different sizes. For these reasons and also in order to complete the physical characterization of the viruses and of their polymer colloid counterparts, we performed Atomic Force Microscopy (AFM) and Ultra Small Angle X-ray Scattering (USAXS) experiments. These techniques allow to characterize the samples we have investigated with inelastic light scattering. As we will see, they enable to characterize the morphology of the viruses but also their self assembled organizations.

4.3 Morphological characterization

Prior to the presentation of our results, the main principles of AFM and USAXS characterizations are given.

4.3.1 Techniques

Atomic force microscopy

Atomic Force Microscopy (AFM) is a very high-resolution type of microscopy which can achieve nanometer scales. It was developed from the scanning tunneling microscope invented by Gerd Binning and Heinrich Rohrer who were awarded a Nobel Prize in 1986 for "their design of the scanning tunneling microscopy". The AFM apparatus (Fig.4.10) contains a sharp nanotip made from silicon or silicon nitride. When the tip touches the surface of sample, interaction forces lead to a deviation of the tip which can be measured by a laser spot reflected from the top surface of a tip holder. Scanning the surface and processing the vibrations of tips it is possible to make a visual picture of the sample surface with very high resolution. AFM topographs have a lateral and a vertical resolution of ~ 10 and ~ 1 Å, respectively [137]. Although AFM measurements can be performed in a liquid environment [138], the AFM apparatus we used for our virus characterization was not equipped for such measurements. Basically, our AFM measurements were performed from centrifuged pellets of viruses, depositing a drop of the viscous pellet onto the AFM stage. All measurements were made at the CLYM center of INSA-Lyon, thanks to A. Descamps.

Ultra small angle X-ray scattering

Small Angle ($< 10°$) X-ray Scattering (SAXS) and its variety Ultra Small Angle ($\sim 0.1°$) X-ray Scattering (USAXS) are well developed non-destructive techniques to probe the structure of nano-objects. The X-ray scattering at small angles is provided by electron density fluctuations in the investigated objects. This technique is capable to sense the length-scale of supermolecular aggregations at the level of the nm up to hundreds of nm. Although typical SAXS measurements can be performed with compact x-ray sources, USAXS, which addresses the case of large particles (50 - 500 nm), definitely requires synchrotron sources. Accordingly, our investigations of large viruses were performed at the European Synchrotron Radiation Facility (Grenoble, France) on the ID2 beamline.

According to the SAXS theory [140] the intensity scattered by an assembly of NPs is expressed by the equation:

$$I(q) = NV^2 \Delta\rho^2 P(q) S(q), \tag{4.1}$$

where N is the amount of the NPs per unit volume in the zone of illumination, V is the

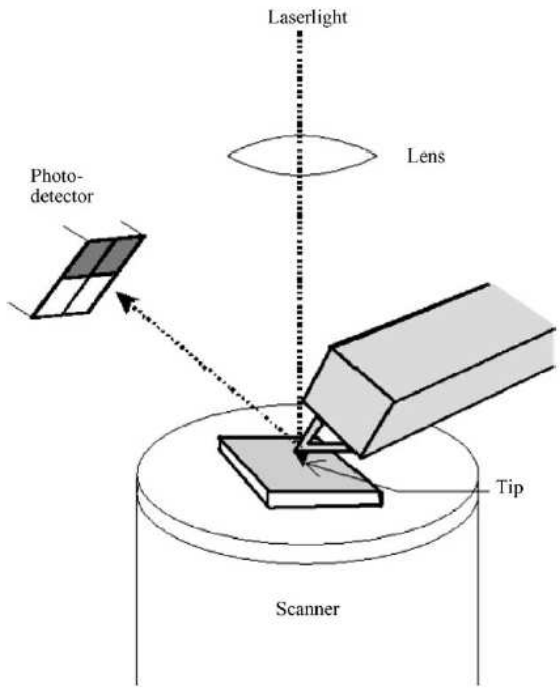

Figure 4.10: Schematic of an atomic force microscope [139].

volume of one NP, $P(q)$ and $S(q)$ are the form- and structure factors respectively and $\Delta\rho$ is the contrast electron density (the difference between the NP and its surrounding). The form-factor $P(q)$ is a function describing the scattering from a single object depending on its shape using the Bessel function. In the case of spheres which are monodispersed the form-factor is expressed as

$$P(q) = \left(\frac{3(\sin(qR) - qR\cos(qR))}{(qR)^3} \right)^2 . \tag{4.2}$$

The USAXS spectrum from a monodisperse spherical system is shown in Figure 4.11. It consists of sharp oscillations, inherent to equation (4.2), but real systems possess a finite polydispersity in size. For example, for the systems described by equation (4.2) the zeros turn to minima in the scattered intensity and for the particles with inner uniform electron density these minima can be used to determine the average radius. Polydispersity is entered in the equation as a size distribution function $D(R)$ which is normalized according to $\int D(R)dR = 1$. The resulting scattering function is expressed as

$$I(q) = N\Delta\rho^2 \int_0^\infty D(R)V^2 P(q,R)S(q,R)dR. \tag{4.3}$$

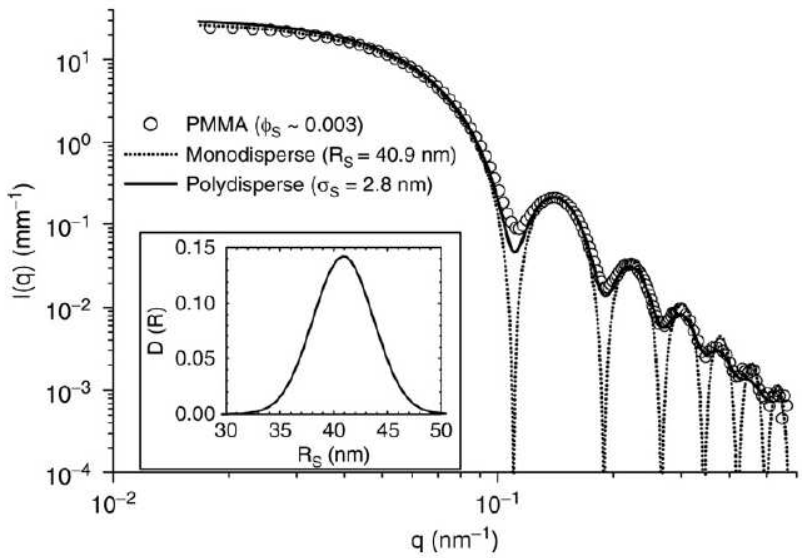

Figure 4.11: USAXS intensity from a dilute suspension of PMMA NPs with $R = 40.9$ nm (volume fraction $\phi_S = 0.3\%$). The dotted line is a fit of the spectrum by monodisperse model. The continuous line is a fit to polydisperse sphere function given by equation (4.3) for Gaussian size distribution with deviation 2.8 nm [140].

The structure factor $S(q)$ accounts for the interaction between NPs in the system, and in dilute non-interacting systems its value streams to 1, $S(q) \approx 1$. $S(q)$ is a function of the interaction potential [140] which can be expressed through the pair correlation $g(r)$ — the probability to find a particle at a distance r from another particle.

$$S(q) = 1 + 4\pi N \int_0^\infty (g(r) - 1) \frac{\sin(qr)}{qr} r^2 dr. \tag{4.4}$$

Interpreting the results of USAXS requires a lot of modelling calculations of the electron density, structure factor, etc. In our case we used it to reveal the NPs size, their quality of monodispersity and to qualitatively evaluate the interaction between the NPs. For our data analysis we used the program "SAXSutilities" provided by M. Sztucki (ESRF, ID2) [141].

4.3.2 USAXS and AFM sample characterization

Solutions of CIV and PBCV-1

The structural and dispersity characteristics of viruses were investigated by USAXS at ESRF (Grenoble, France) on the ID2 beamline. Figure 4.12 shows the one-dimension scattered intensity spectra of CIV diluted in water and PBCV-1 diluted in Tris buffer. The operating energy was 12.5 keV, i.e. a wavelength of the order of 1 Å, for a photon flux of 10^{13} photons per second and a beam size of 0.3 mm per 0.8 mm. Each presented spectrum is the averaged of ten spectra recorded at different sample points illuminated during 0.05 and 0.06 seconds for CIV and PBCV-1 respectively. Spectra were normalized to the intensity of the incident beam and the scattering of the buffer was subtracted. The PBCV-1 concentration in this experiment is 8 mg/ml, i.e. its volume fraction in the solution is approximately 1.7%. For such values of volume fractions the particles in the solution can be assumed as non-interacting and therefore the structure factor $S(q) \to 1$ and the only parameter critically influencing the scattered intensity is the form-factor $P(q)$. The USAXS spectrum of PBCV-1 demonstrates the oscillations that are very typical for a monodisperse (or at least quasimonodisperse) solution of spherical NPs as shown in Figure 4.11 for PMMA spheres whose volume fraction is close to that of PBCV-1. The spectrum of CIV slightly differs from that of PBCV-1 in the q range from 0.06 to 0.15 nm^{-1}. This feature might reflect interactions between virions. Indeed, the CIV concentration in this experiment is 15 mg/ml which corresponds to 2.9% of virions volume fraction in the solution. This, relatively high density of virus particles can generate the formation of the nearest neighbour shells (conglomerates) of virions. In spite of this, the low-q range of the spectrum proves that extended structures definitely do not exist in the virus solution whereas the uniform oscillations of the scattered intensity along the q-axis are the sign of the extremely narrow size distribution of the scattering virions. According to this, we can conclude that both virus samples possess high monodispersity which is definitely an asset with respect to our low frequency inelastic scattering investigations.

The correct and rigorous fitting of these curves is not a trivial task, even in spite of the fact that for both systems the structure factor $S(q)$ can be accepted as 1. The form factor for an icosahedron is very complex for an analytical solution [132] which demands the knowledge of the electron density map within the viral structure. Along previous works [142], we use here only the spherical approximation which has been shown to capture the essential aspects of quasispherical structures. For the PBCV-1 spectrum (Fig.4.13a) the

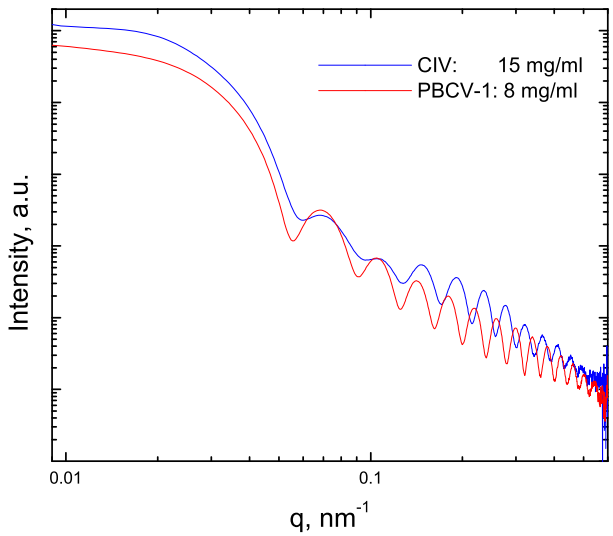

Figure 4.12: USAXS spectra of CIV (blue curve) and PBCV-1 (red curve) virus solutions of the concentrations of 15 and 8 mg/ml respectively. Both axes are log-scaled.

fitting applying the hard sphere model matches satisfactorily in the low-q part which can be considered as enough for a reliable estimation of the size. Further discrepancy of the fitted curve and experimental data may be a result of the icosahedral form of real virions [132]. The fitting of the CIV curve using the hard sphere model cannot be accepted as satisfactory because the disagreement with the experimental spectrum is too strong. In Figure 4.13b the fitting with a core-shell sphere model is shown. This model fits the experimental data more adequately but still not perfectly. This fact can be due to the structure factor $S(q) \neq 1$. It is worth to note that for both CIV and PBCV-1 spectra the best fitting takes place only when the diameter of sphere equals the outer diameter of the virus measured along the two- and threefold axes. It means that if diluted viruses are assumed to be spheres the diameters of these spheres have to be taken as 165 and 160 nm for PBCV-1 and CIV respectively.

Pellets of CIV and PBCV-1

The qualitative ideas about the structurization of the virions in the pellets concluded from optical properties find confirmation in the USAXS measurements. Figure 4.14a shows the comparison between the x-ray scattering spectra from the diluted suspensions

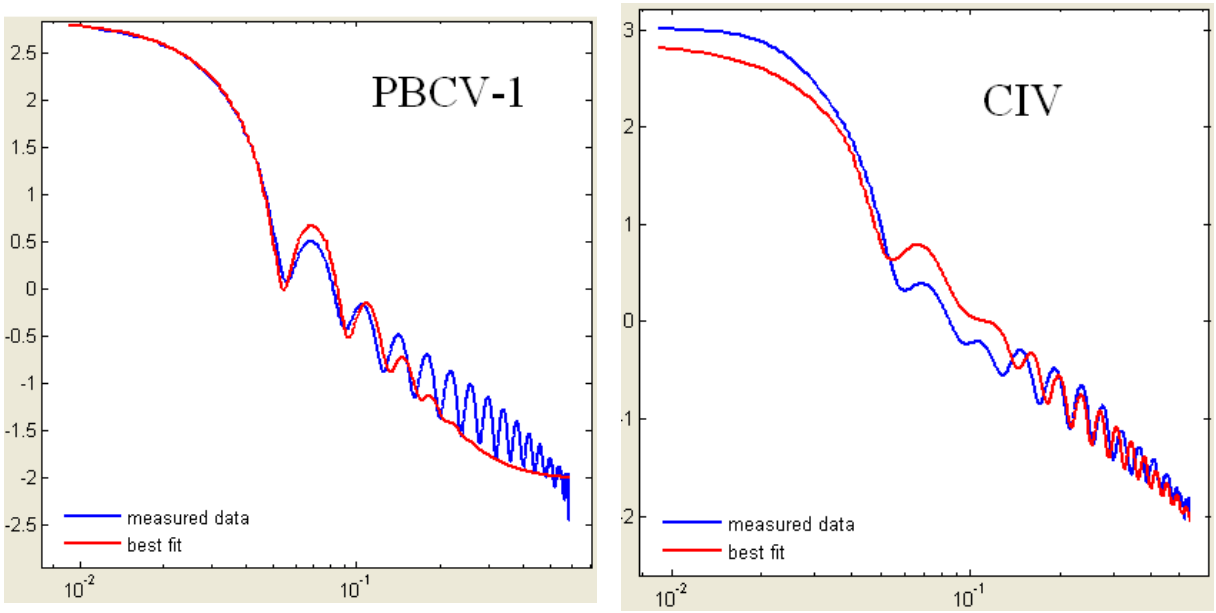

a b

Figure 4.13: USAXS experimental data (blue curves) and the best fits (red curves) for PBCV-1 (**a**) and CIV (**b**) solutions. In order to fit the PBCV-1 data a hard sphere model was used, for CIV data — core-shell sphere model.

and from the pellets of CIV. The main difference between these spectra is located in the low-q part which characterizes the long-range structure. As the scattered signal is a product of the form- and structure factors (Eq.(4.1)) and since for the same NPs, i.e. when the shape of the particles and the size distribution are identical, the form-factor is supposed to be the same both in the diluted suspension and in the pellets, therefore only the structure factor, i.e. the interaction between NPs and thus their organization, was changed after centrifugation.

The symmetrical and discrete pattern observed in Figure 4.14b gives information on the type of crystalline structure. Like with diffraction from atoms arranged in a crystal, one crystalline lattice is associated with one precise distribution of diffraction spots on a 2D projection. In the present case, the diffraction spots are not sharp but rather diffuse, which indicates the presence of several crystalline structures oriented differently but lying in the same plane. A quick way of identifying the lattice is to list the q-points of the Bragg peaks identified in the low-q regions of differently oriented 1D cross sections. Table 4.1 lists the values of the ratios of the Bragg peak positions with respect to the lowest one found for CIV (the displayed values are obtained from azimuthally averaged 2D patterns

recorded in the same conditions).

Table 4.1: Theoretical values of the ratios of the Bragg peak positions for different types of crystal structure [140] and those derived from USAXS experiments of CIV and PS-187 pellets.

fcc	bcc	hcp	CIV	PS-187
1	1	1	1	1
$\sqrt{3}$ (1.73)	$\sqrt{2}$ (1.41)	$\sqrt{3}$ (1.73)	1.68	1.62
2	$\sqrt{3}$ (1.73)	2	?	1.91
$\sqrt{8}$ (2.83)	2	$\sqrt{7}$ (2.65)	2.58	2.62
$\sqrt{11}$ (3.32)	$\sqrt{5}$ (2.24)	3	2.93	2.85
$\sqrt{12}$ (3.46)	$\sqrt{6}$ (2.45)	$\sqrt{12}$ (3.46)	3.45	3.82
4	$\sqrt{7}$ (2.66)	$\sqrt{13}$ (3.61)	3.79	—

Obviously, the best agreement is obtained with the hcp structure, even though the 1 : 2 peak cannot be detected. The value of the lattice parameter derived from the absolute values of q's is $a \approx 230$ nm. The a parameter compares reasonably well with the inter-virus distance found from TEM observation (Fig.4.4c and Fig.4.5). AFM characterization attempts on CIV pellets were unsuccessful in evidencing the long-range order (Fig.4.15b). This is certainly due to the viscosity of the samples which confers the AFM pictures a blurry aspect in the early stages of the AFM measurements. Upon removal of the virus pellet drop, after the AFM measurements, we noticed the drop had dried out. This can be due to the white light used in the AFM experiments.

Unlike CIV and WIV [132], the USAXS pattern of PBCV-1 pellets is nearly identical to that of the solution. Obviously PBCV-1 is unable to self organize, at least over as large distances as CIV does. A small peak observed near 0.03 nm^{-1} in the azimuthally average intensity (Fig.4.14c), i.e. close to that of the first peak observed in CIV pellets (Fig.4.14a), can be interpreted as a primitive first order organization of the virions. Such can be seen in the AFM pictures of PBCV-1 pellets, where one can identify quasispherical structures of about the same sizes as that of PBCV-1, regularly spaced by 150 – 200 nm (center-to-center separation). The self organization of particles is at first order permitted by a very narrow size distribution (for spherical NPs, polydispersity should be lower than $\sim 5\%$ [140]). The naturally monodisperse size of viruses, as attested by the many observable oscillations from low q to high q in the USAXS pattern (Fig.4.13), makes them ideal

particles for self organization. Comparing the self organization properties of CIV (and WIV) with those of PBCV-1 it turns out that long distance self assembly does not only rely on a size monodispersity. One essential difference between CIV (or WIV) and PBCV-1 with respect to long range ordering is the presence of thin fibril structures (hair-like) that emanate from the capsids in the case of CIV and WIV, and not of PBCV-1 [119]. The interaction between the fibril halos of different virions is expected to play a major role in the stabilization of the 3D assembly. In fact, this behavior is very similar to that observed with the formation of supracrystals of metallic NPs coated with alcane chains (Fig.3.13). The impossibility of PBCV-1 to form long-range ordered arrays might also be due to its capsid structure, which although of icosahedral symmetry, bears a "spike" structure at one vertex of the icosahedron. This feature (Fig.4.3b) has been recently discovered and seems to be observable from our AFM measurements. Indeed, looking at Figure 4.16a, one observes that a significant fraction of the pseudospherical structures that are assumed as the virions are centered with a bright spot which indicates a narrow protrusion which can be associated with the spike structure. Due to this specific spike structure, and in the absence of an outer fibril structures, it appears natural that PBCV-1 is unable to form long range paracrystalline order, at variance with CIV and WIV.

Both USAXS and microscopic techniques confirm the size of the virions, their narrow size distribution and their quasispherical morphologies. They also show that highly concentrated pellets of virions are able to form regular structure with paracrystal order. The above-listed features are positive for low frequency inelastic scattering measurements because monodisperse self-organized structures are, as opposed to solutions, coherent and highly concentrated assemblies. Before showing the low frequency inelastic scattering results obtained from the different virus samples we present the result of morphological characterization of the PS colloids that will serve as "reference large NPs".

Polystyrene samples

USAXS spectra of PS NPs diluted solutions are displayed in Figure 4.17. All spectra prove high monodispersity of the PS colloids with nearly no super structure (aggregation) in the diluted state. In order to fit these spectra, we used the hard sphere approach which allows to approximate all curves with a good agreement. As all studied viruses have a size close to 200 nm, we present the fitting results only for PS-187 NPs (Fig.4.18) although all results described below apply to the other size. The agreement between model and

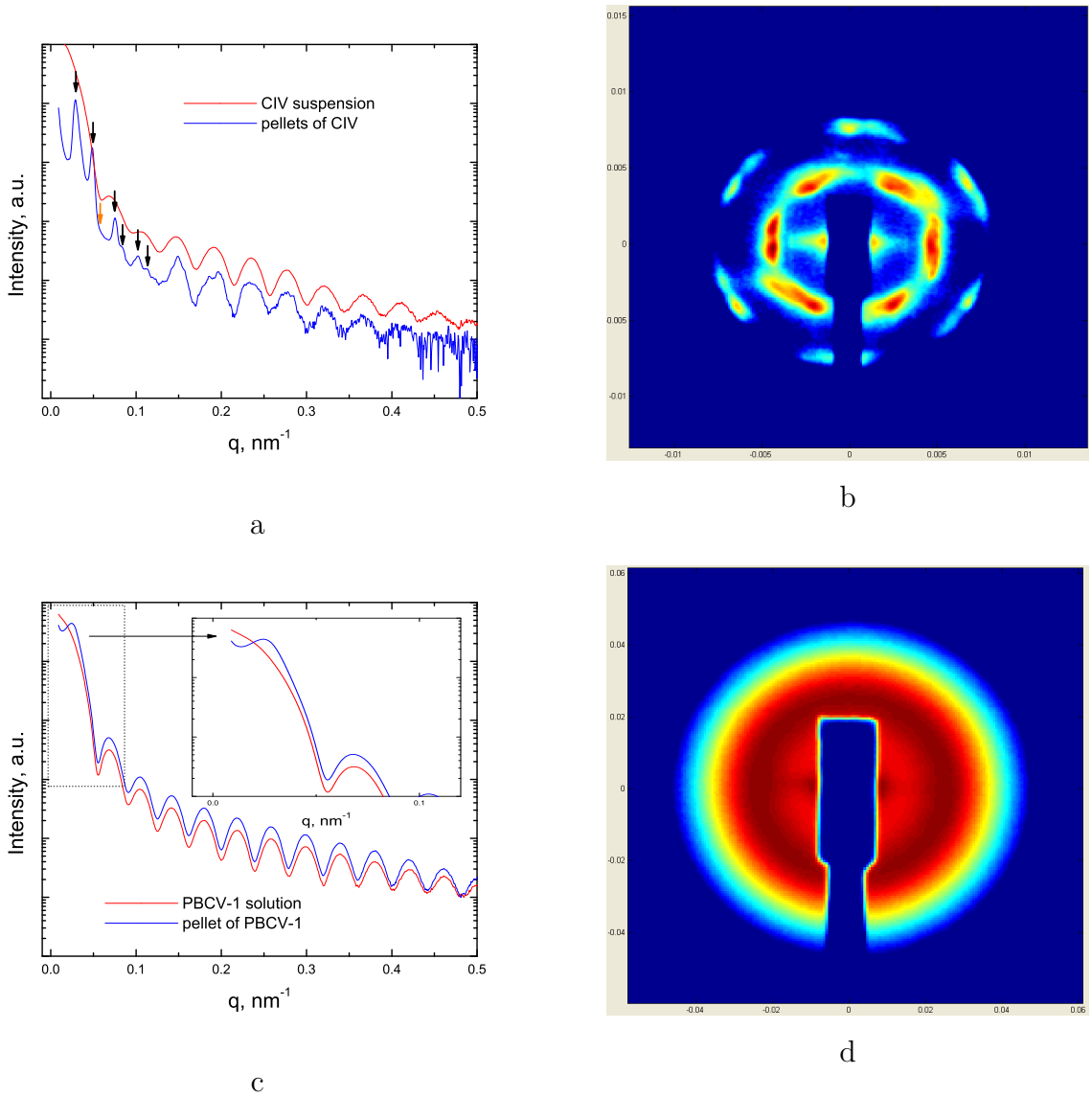

Figure 4.14: **a:** Comparison of the USAXS 1D azimthal averaged profiles from the diluted suspensions of CIV (red curve) and pellets of CIV (blue curve). Black arrows mark the Bragg peaks which were used for Table 4.1, the orange arrow is the theoretical position of the third order Bragg peak. Vertical axis is log-scaled. **b:** Characteristic two-dimensional pattern of the higly concentrated CIV. **c,d:** Same as (a,b) for PBCV-1.

experiment is good enough at intermediate q values. The weak oscillation at the lowest q-values observed in the fitting curve is artificial: it fails to reproduce the smooth rise of intensity for $q \to 0$. The right image of Figure 4.18 represents the structure factor derived as a result of fitting. Not far from zero its value oscillates around 1 and at the high values

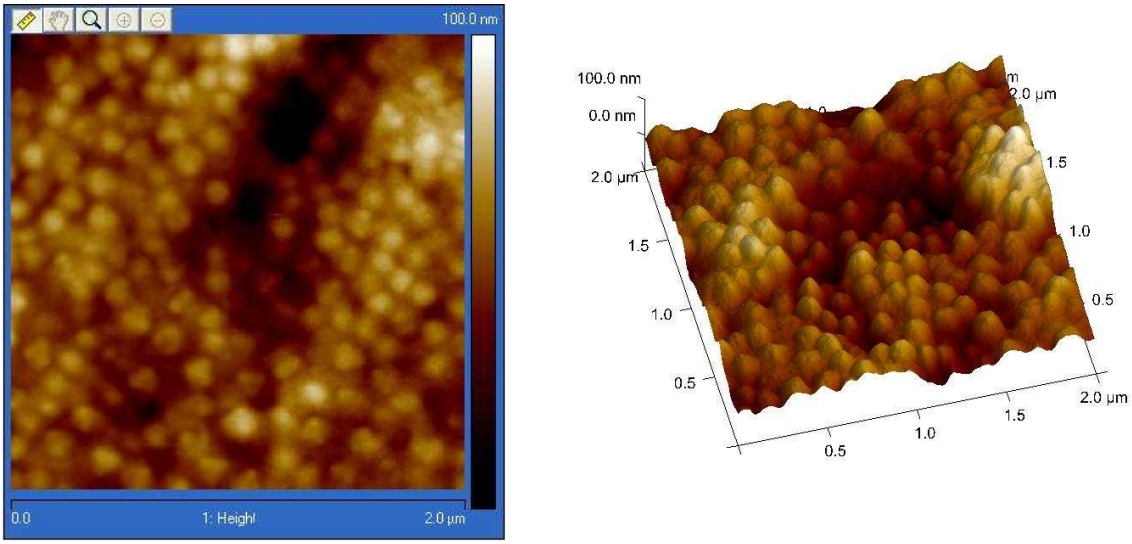

a b

Figure 4.15: AFM image of a pellet (probably dried) of CIV: **a:** 2D; **b:** 3D.

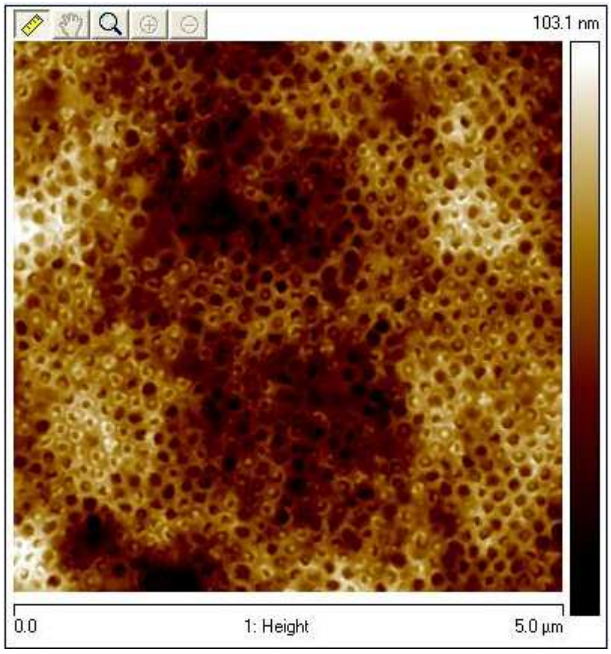

Figure 4.16: AFM height-contrast image of the PBCV pellet.

of q it asymptotically streams to 1. Basically PS NPs do not self organize in solution.

As for PBCV-1 and CIV, PS colloids solutions dried rather quickly under the AFM investigations. Nevertheless, in this case, the evaporation of the solvent does not alter

the morphology of the NPs: AFM confirms the spherical shape, as well as the size of the PS colloids. In the AFM images (Fig.4.19) the spherical particles with size of 187±2 nm are well observed.

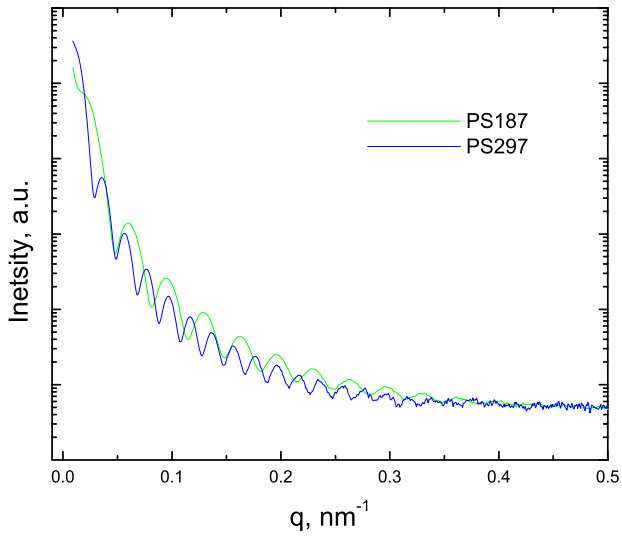

Figure 4.17: USAXS spectra of PS NPs solutions: PS-187 (green curve) and PS-297 (blue curve). Vertical axis is log-scaled.

The USAXS spectra of the highly concentrated PS-187 pellets is presented in Figure 4.20a where also the spectrum of diluted PS-187 NPs is given for comparison. As with CIV pellets, strongly pronounced Bragg peaks appear in pattern revealing the close packing arrangement within the PS pellets. Again the paracrystalline order corresponds to hcp organization as derived from the ratios between the q-positions of the peaks (1 : 1.62 : 1.91 : 2.62 : 2.85 : 3.82) and through the two-dimensional USAXS pattern (Fig.4.20b). It is worth to note that the ratios between the q-positions of the peaks are closer to ideal values of a hcp structure than those of the CIV USAXS spectrum (Table 4.1); in addition the two-dimensional USAXS pattern of PS-187 pellets is not so spread and allows to observe the third order of diffraction. These facts show that PS NPs form a more extended paracrystalline order than CIV particles do. This might be explained by the shape of the PS colloids which are definitely spherical whereas CIV are icosahedra.

From our morphological characterizations we can conclude that PS NPs, characterized by a high monodispersity and close to ideal spherical shapes and capable to form

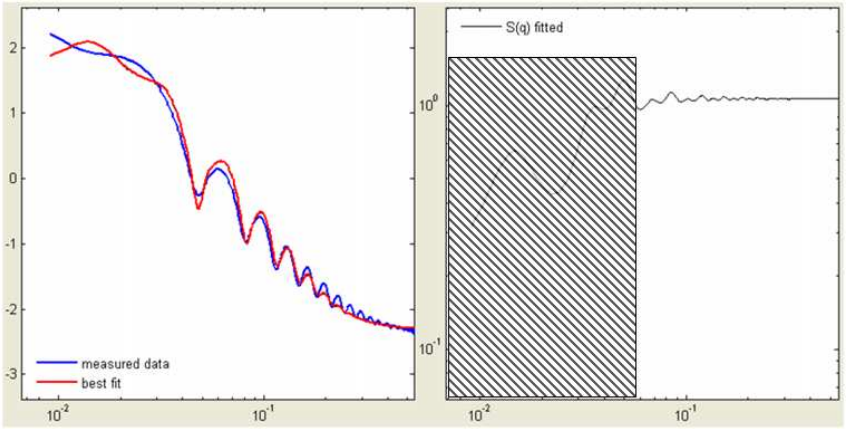

Figure 4.18: **Left:** Experimental (blue) and fitted (red) USAXS spectra of PS-187 NPs in water solution. **Right:** Structure factor of PS-187 NPs diluted in water obtained as a result of the fitting.

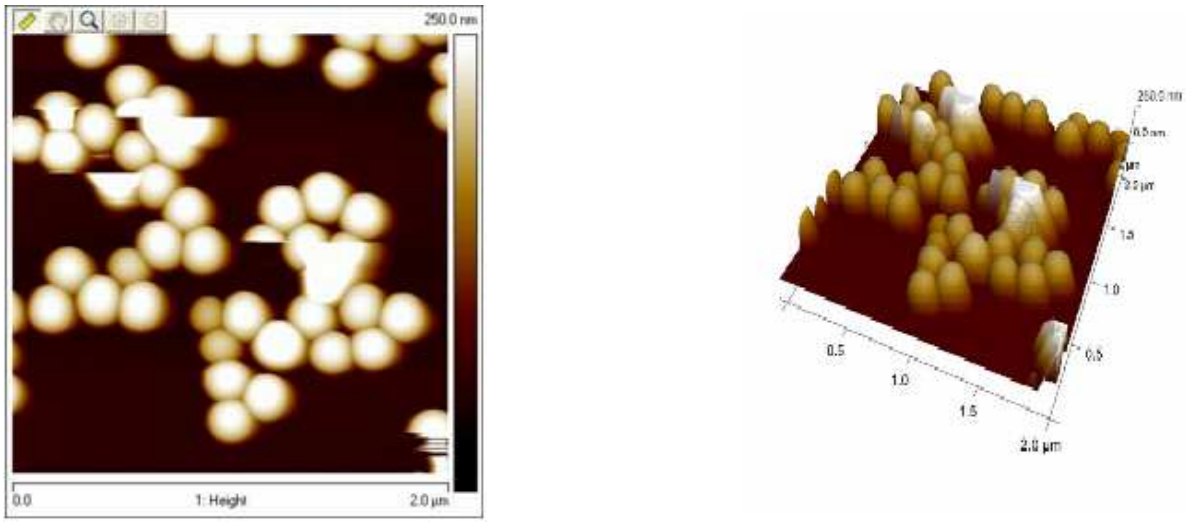

a b

Figure 4.19: AFM images, two-dimensional (**a**) and three-dimensional (**b**) from a drop of PS-187 NP solution dried on a glass substrate. The distortion of the spheres can be explained by the mechanical motion of the scanning tip of the AFM which sometimes may push NPs.

superstructures close to those formed by our studied viruses, can be admitted as a good reference for our low frequency inelastic scattering experiments which will be considered in the next section.

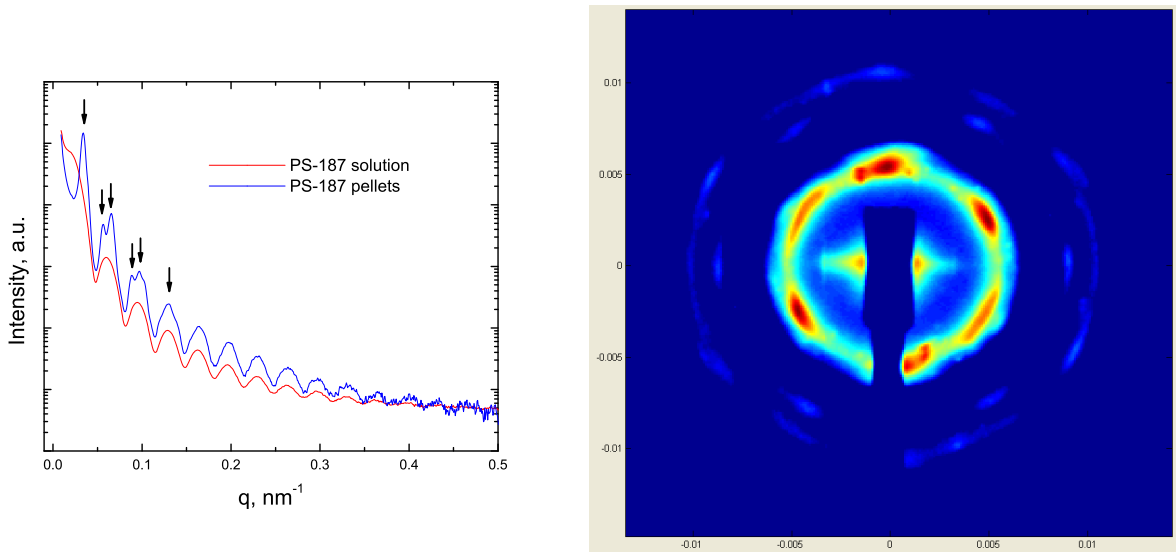

a b

Figure 4.20: **a:** Azimuthally averaged USAXS spectra of PS-187 NPs in solution (red curve) and in pellets (blue curve). Vertical axis is log-scaled. **b:** Associated 2D pattern of the pellets.

4.4 Low frequency inelastic light scattering from large viruses

As stated on several occasions before, our purpose has been to experimentally detect the eigenmodes of viral particles, whose existence (and relevance) is taken for granted by many theoretical and simulation works. Morphological characterization of the studied viruses, as reported in the preceding section, confirm that physically they can be regarded as sufficiently defined NPs in order to expect the existence of corresponding "nanoparticle modes". The following results show that unambiguous evidence for the existence of virus eigenmodes is hard-pressed to obtain, at least when viruses are studied within a liquid environment, which basically justifies the interest for such research.

4.4.1 Experimental details

All inelastic light scattering experiments reported thereafter were performed using the Sandercock interferometer 2.3, essentially using the 532 nm laser line as excitation, at room temperature. Most data were recorded with a FSR of 15 GHz, with an exciting power of 10 mW to minimize a possible radiation damage.

Unlike the *Raman* studies we have dealt with in Chapter 3, the systems to be in-

vestigated here are liquids or liquid-like (pellets). Different containers have been used: capillaries (0.3 mm outer diameter and 0.01 mm thickness of the wall) and a "sandwich" of two thin silica slides in between which a drop of sample was placed and flattened. The "sandwich" was used for pellets or "dry" samples to investigate different scattering geometries (90A, 90R, backscattering, see section 2.1.3) (Fig.4.21). In backscattering geometry, capillaries turned out to be most convenient for either types of sample, so that most of the results below were obtained with capillary containers.

Figure 4.21: "Sandwich" with PS pellet in reflected light.

4.4.2 Results and discussion

First experimental overview

Figure 4.22a displays VV and VH experimental low frequency spectra of virus and PS-187 **suspension** samples: CIV, WIV and PS-187 are diluted in water with concentration 4, 5.93 and 15 mg/ml respectively while PBCV-1 is diluted in Tris buffer ($C_4H_{11}NO_3$, refractive index is $n \approx 1.3$ [143]) with concentration of 1 mg/ml. All spectra are normalized on the maximum intensity for clarity however real intensity maximum of polarized spectra is ~ 10 times higher than that of the depolarized spectra. All VV spectra exhibit an obvious sharp peak around 7.3 GHz. This frequency position nearly matches that of the Brillouin line from longitudinal modes in pure bulk water in the same conditions of experiment [144]. Changing the Brillouin scattering geometry (Fig. 4.22b), this peak shifts according to the variations expected from the change of the q transfer (section 2.1.3).

In contrast to the VV spectra, the VH spectra of the solutions display a broad band, centered about 6 GHz. On a very simple basis, this value can be considered as within

the right order of magnitude for low frequency modes for a virus-like particle. Such can be estimated by modelling the virus as a full nanosphere, taking a longitudinal speed of sound v_L equal to 1920 m/s, as derived from Brillouin measurements in virus crystals [64] and assuming a ratio $v_L/v_T \simeq 2$. In the case of a *freely* vibrating sphere, the lowest frequency spheroidal mode, i.e. the quadrupolar mode ($n = 1, \ell = 2$), which will be shown to be the expected dominating one in the spectra (see further), is then given by $\nu \simeq 0.85 v_T/D$, i.e. 4.3 GHz and 5.8 GHz for 190 nm and 140 nm diameter particles respectively. Throughout our further developments, we will see that these values have a very limited reliability for our investigations.

If the position of the VH broad band can first be considered as compatible with a possible virus eigenfrequency, it occurs unfortunately that it does not show a significant size dependence (Fig.4.23a,c) (WIV has a diameter of 140 nm, while the diameters of PBCV-1, CIV and PS-187 are close to 190 nm). Yet, what may be interpreted as a sign of an eigenmode signal is that the position of the broad band turns out to show no significant q dependence when testing different scattering geometries (Fig.4.22b). It is worth to notice that although the narrow line observed in VV conditions is strongly suppressed in VH, remains of it can be traced in the VH spectra (blue arrows in Fig.4.22b and also for low concentrations of virus in Fig.4.22a); this can be due to a leakage of the polaroid used in our experiments.

Figures 4.22c,d represent the spectra of the **pellets** of viruses and PS-187. All spectra were recorded under the same conditions as those of the solutions. Except for PS-187 these spectra basically show a similar situation as with the solutions: a single q-dependent narrow line in VV conditions, while a broad maximum in VH that hardly shifts with the scattering geometry, nor with the size (Fig.4.23b). A notable difference with the solutions though is a poorer definition of the broad maximum due to an increase of scattering on its low frequency wing (towards $\omega \to 0$), which is clearly observable for CIV, WIV, PS-187 and PS-297, and less pronounced for PBCV-1. Since the essential difference between CIV, WIV and PS with PBCV-1 is the ability to form long range organized assemblies (Fig.4.14,4.20), one may ascribe the increase of scattering at low frequencies in the pellets to enhanced particle interactions. For pellets of PS one observes that the signal does not feature anymore the narrow VV line; in addition the broad band features substructures that we will discuss in details further.

The spectra of Figure 4.22 cannot be straightforwardly interpreted at first sight. The narrow line observed in VV conditions strongly suggests a Brillouin signal from longitudi-

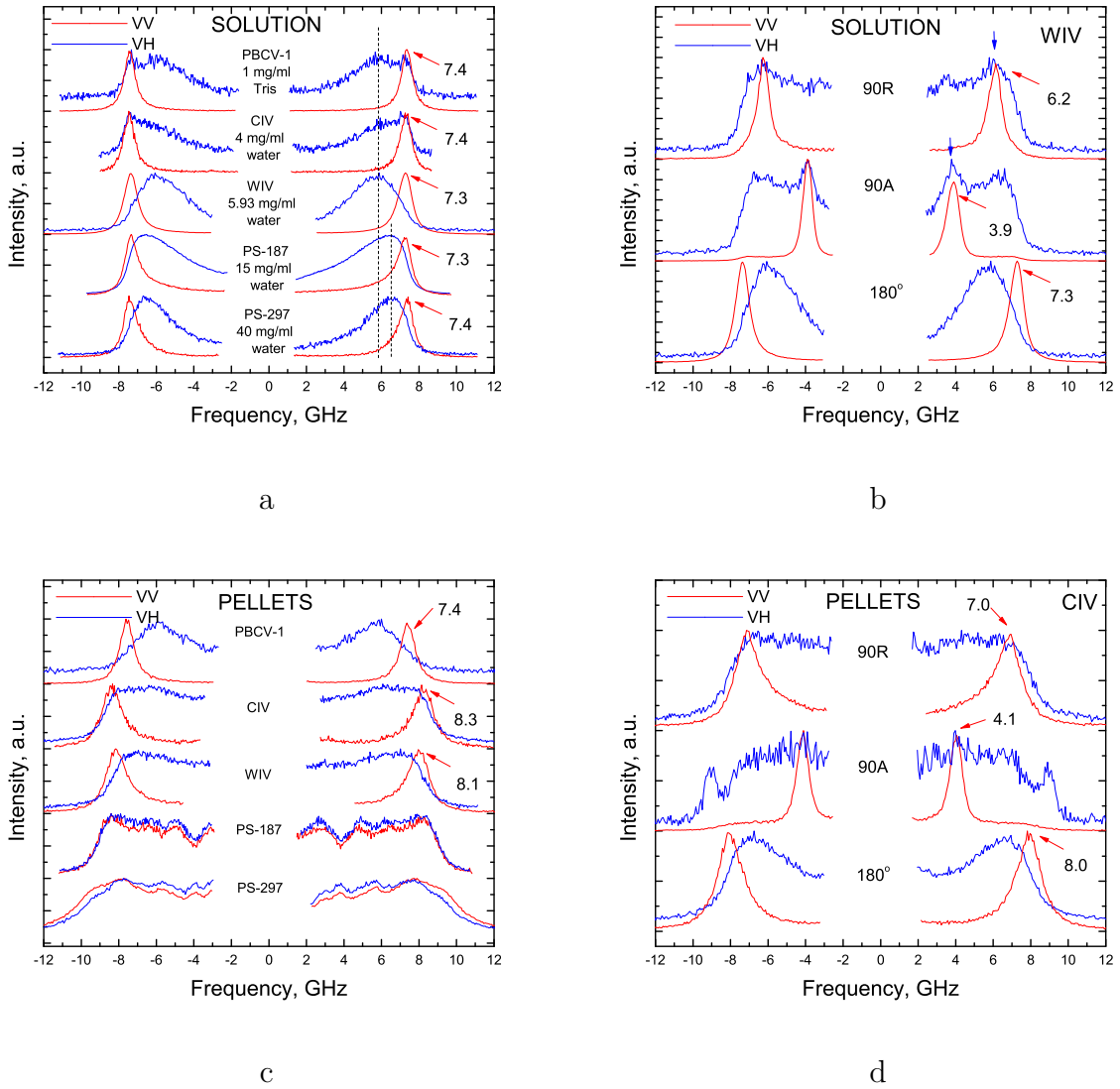

Figure 4.22: Low frequency inelastic scattering spectra, VV (red) and VH (blue) of PBCV-1, CIV, WIV and PS-187. All spectra are normalized on maximum intensity and shifted along vertical axis for clarity. **a:** Low frequency inelastic scattering spectra of CIV, WIV and PS-187 diluted in water and PBCV-1 virus diluted in Tris buffer of pH 7.8 in backscattering geometry of experiment. **b:** Low frequency inelastic scattering spectra of WIV virus water solution in backscattering, 90A and 90R geometries of experiment. **c:** Low frequency inelastic scattering spectra of CIV, WIV, PBCV-1 and PS-187 pellets. Viruses' spectra are recorded in backscattering geometry of experiment whereas PS-187 spectrum is represented in 90A geometry. **d:** Low frequency inelastic scattering spectra of CIV pellets in backscattering, 90A and 90R geometries of experiment.

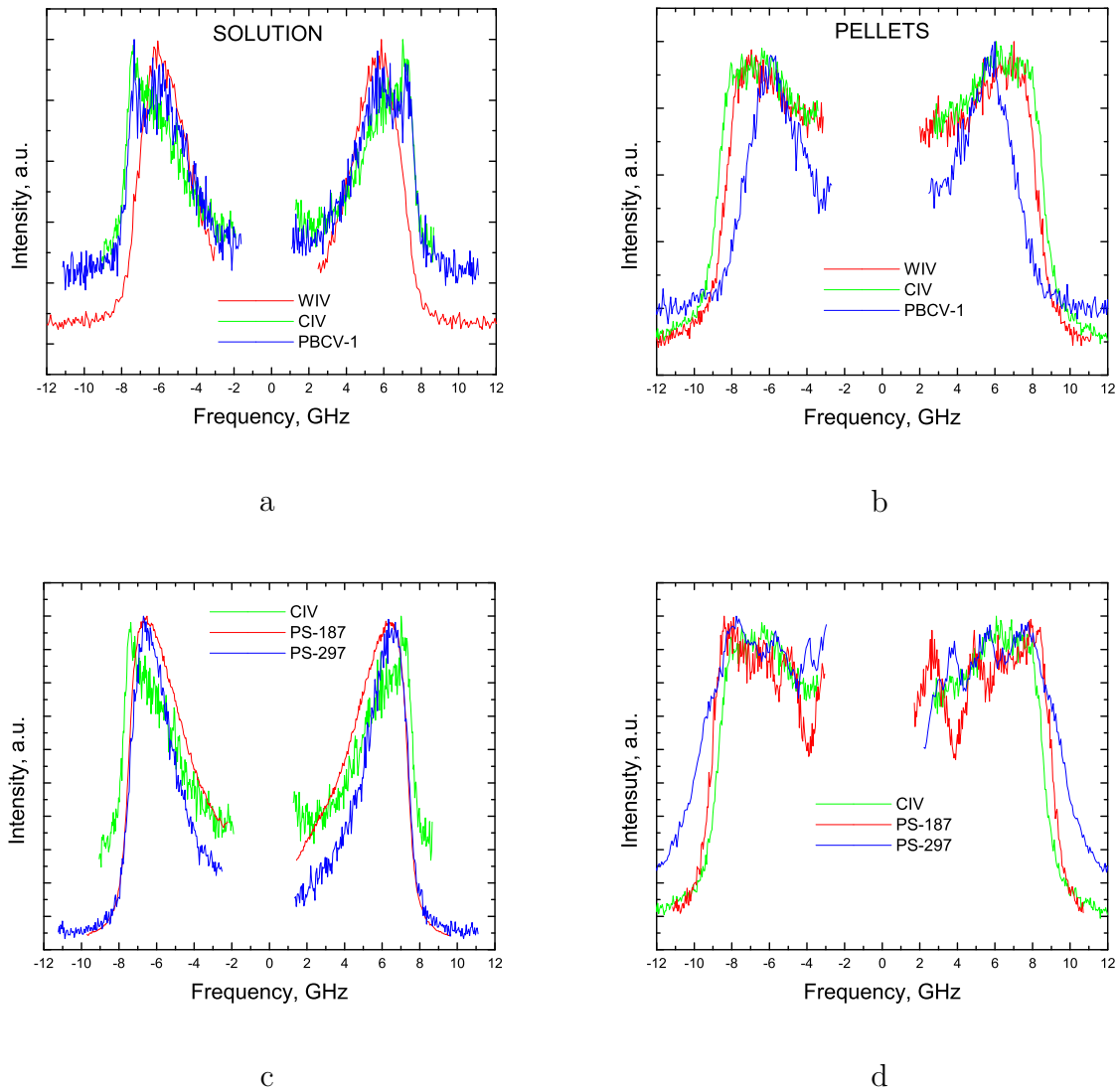

Figure 4.23: Inelastic scattering VH spectra recorded in backscattering scheme of: **a:** CIV, WIV and PBCV-1 solutions; **b:** CIV, WIV and PBCV-1 pellets; **c:** CIV, PS-187 and PS-297 solution; **d:** CIV, PS-187 and PS-297 pellets.

nal modes of the water solvent, due to its position, q-dependence and strong polarization. The behaviour of the lower frequency broad band is more intriguing. Had it been a low frequency Raman signal from *nanoparticle modes*, one would expect a change of its position with the size of the virus (scaling rouglhy as $\nu \sim 1/D$), which is not observed. Although the polarization of light is poorly defined in turbid samples like ours, due to multiple scattering processes in strong Mie scattering systems, there still remains a strong

difference between VV and VH conditions. One may therefore relate the VH signal to scattering from modes featuring a transverse character, which cannot be assigned to the liquid solvent. In other words, the presence of large nanoparticles (virus or PS) in the solution would confer the mixture the possibility of sustaining transverse-like vibrations. However, in spite of the apparent non q-dependence of the broad band (Fig.4.22b,d), the localized or non-localized nature of these excitations is difficult to assess since multiple scattering strongly reduces the information on a possible q-dependence.

In order to further check whether the broad band signal is really q-independent, the same spectra were recorded with differing wavelengths (Eq.(2.8)). Figure 4.24a displays the VH spectra of a PBCV-1 solution with concentration of 2.5 mg/ml made using two exciting wavelengths: 532 and 476.5 nm. Both the narrow line (as a remain of VV signal) and the broad band appear to shift to larger frequencies going from the green to the blue wavelength. The same effect is observed in the VH spectra of the virus pellets (Fig.4.24b), using in addition a yellow wavelength. For both solutions and pellets, the observed shifts quantitatively agree with the change of the magnitude of the transferred q, i.e. $\nu_1/\nu_2 = \lambda_{0_2}/\lambda_{0_1}$. Therefore, it appears that the broad band signal detected in VH conditions behaves like a Brillouin signal, i.e. arising from excitations with a delocalized character.

Overall the spectra of both virus and PS solutions and pellets feature Brillouin signals, the narrowest one most likely reflecting the behaviour of longitudinal modes in a material essentially made of water. The broader signal seems to originate from the presence of the nanoparticles (whether viruses or PS colloids). This origin is confirmed studying the influence of particle concentration on the spectra. Figure 4.25 displays the VV and VH spectra of PS-187 suspensions with different concentrations. All shown spectra, recorded in the very same conditions, were normalized with respect to an identical number of scans. Through this figure one can see that with the increase of PS colloid concentration, i.e. with increase of the volume fraction of NPs, the intensity of the VV narrow band decreases while that of the VH broad band *increases*, without significant changes of the frequency positions nor of the spectral profiles. This behaviour clearly relates the VH broad band signal to the nanoparticles, while the VV narrow line is ascribed to the bulk behaviour of the dominating solvent.

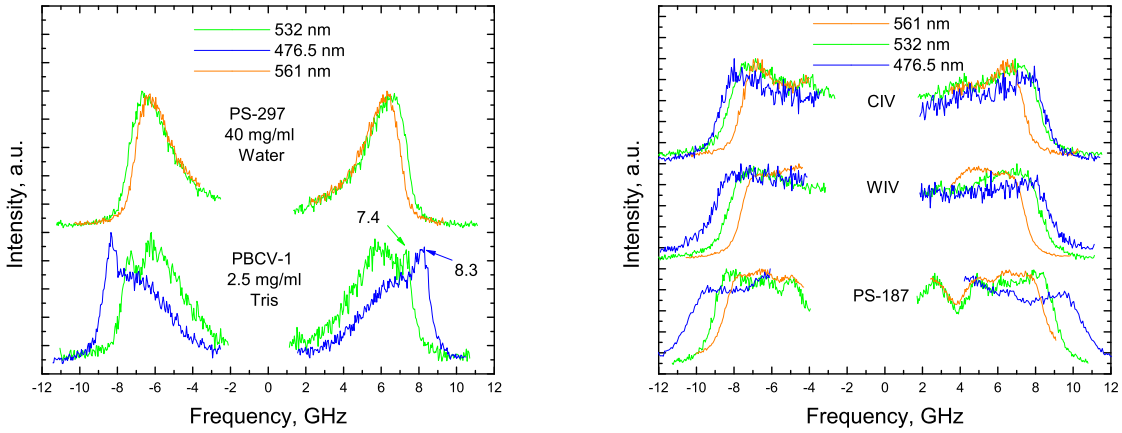

a b

Figure 4.24: **a:** Inelastic scattering spectra of PS-287 PBCV-1 solutions recorded at different wavelength excitations. **b:** The same but for PS-187, CIV and WIV pellets.

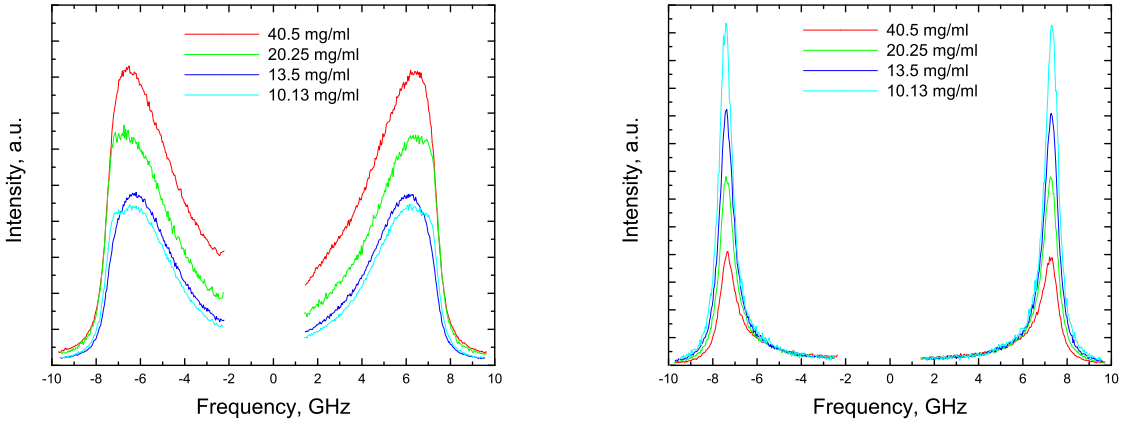

a b

Figure 4.25: Depolarized (**a**) and polarized (**b**) low frequency inelastic scattering spectra of PS-187 solutions of different concentrations. All spectra are normalized on the amount of scans.

Characterization of the broad band using the PS colloid reference.

The comparison of the VH spectra obtained for the solutions and for the pellets (Fig.4.22a and Fig.4.22c) evidences differences in the profile of the band, at least in the case of the nanoparticles that develop long range ordered structures (CIV, WIV and PS-

187). The clear inelastic shape of the band observed in the solutions is stretched over the low frequency side, forming a continuum of frequencies towards the elastic line. However, no evolution from an "inelastic-like" to a "continuum-like" profile can be detected in Figure 4.25, i.e. when working with solutions where the volume fraction of the NPs is rather low ($< 5\%$). In order to study the effect of higher volume fractions, we used the PS colloids which offer the advantage of being available in large amounts, unlike the virus samples.

Figure 4.26 represents a comparison of the VH spectra of PS-187 suspensions of different concentrations with pellets of the same particles (we assume that in pellets the volume fraction of PS colloids streams to 100%). This figure shows how the profile of the broad band considerably deforms upon increase of the volume fraction, i.e. increase of interaction between the NPs. More interestingly, one observes that once a high volume fraction is reached (74% in the present case), substructures appear within the continuum profile of the band; it is tempting to ascribe these substructures to poorly defined pre-signatures of NP modes. In order to test this possibility, Figure 4.27 compares the VH spectra of PS-187 and PS-297 colloid suspensions of comparable high concentrations ($\sim$75%). As already observed from the diluted solution spectra (Fig.4.23c), the maximum of the observed bands (near 6 GHz) are essentially identical while in addition, in the present case, the continuum-like low frequency wing of the bands evidences substructures of non-coinciding positions. These substructures are found to persist in the 100% pellet spectra (Fig.4.22c). Evaluating the ratio of the frequency positions of the substructures (see marked bands in Fig.4.27) reveals that this ratio does not conform to the ratio of the respective colloid sizes ($297/187 \sim 1.6$); in other words, interpreting the substructures as signatures of nanosphere modes remains at this stage unsatisfactory, at least within the used simplest interpretation scheme according to which $\nu \sim 1/D$.

From the study of the VH broad band in highly concentrated conditions, several early conclusions may be drawn:

1. the broad inelastic band observed in VH conditions, in diluted suspensions, is irrelevant to possible eigenmodes of NPs as its frequency position remains unchanged with the NP size

2. increasing the interaction between NPs results in the transformation of the band profile into a "continuum-like" profile, which, from the study on the wavelength dependence, appears to infer from delocalized excitations

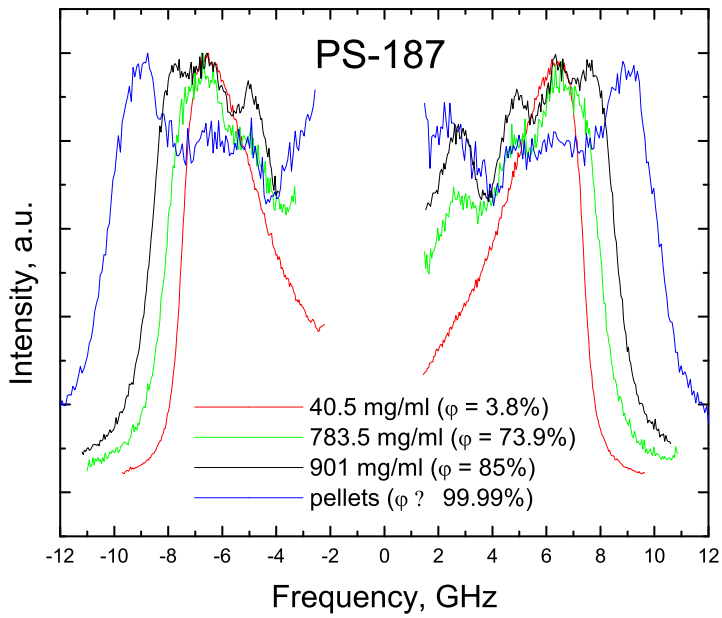

Figure 4.26: Inelastic light scattering VH spectra of PS-187 of different volume fractions.

3. substructures appear in the continuum profile, however they cannot be directly related to size dependence

In order to further elucidate the origin of the substructures, we now explore the evolution of the continuum profile as the liquid solvent is progressively removed.

Evolution of the broad band into a discrete spectrum.

Starting from "wet" pellets of PS colloids, a series of VH spectra were recorded as a function of time during which water progressively evaporates off the samples (the excitation power was increased to 40 mW). Figure 4.28 shows the evolution of the spectra recorded at regular time intervals for PS-187 and PS-297. For both systems, one clearly observes the pellet "continuum" spectra transforming into sets of discrete narrow lines, reached in the dry state where the spectra no more evolve. These narrow lines are known as eigenmodes of the nanospheres [113], as we describe it in the following.

Interpretation of the discrete spectra from "dry" assemblies of PS nanoparticles. The very low inelastic light scattering spectra from submicron colloids have long

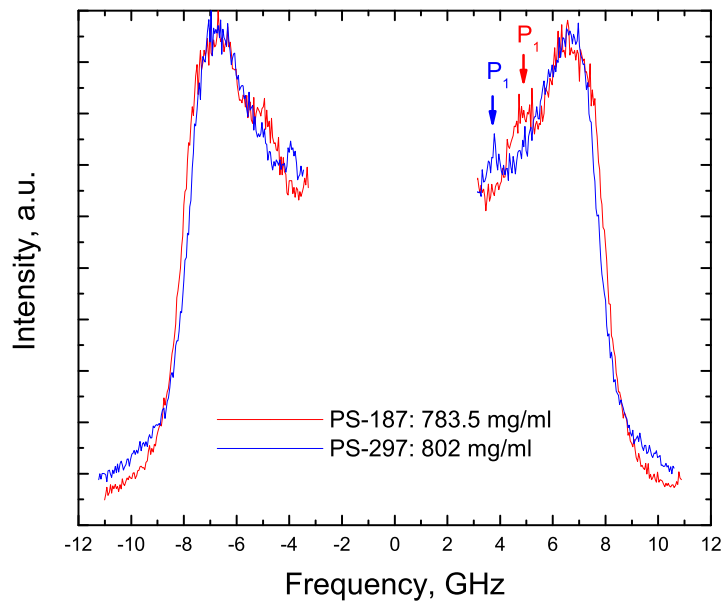

Figure 4.27: Low frequency inelastic scattering spectra of PS-187 and PS-297 colloid suspensions of high concentration (the PS volume fraction is around 75%). The P_1 band is hardly seen on the anti-Stokes side because of an asymetry of the elastic laser line.

been reported by the groups of Fytas and Kuok [58, 85] over the past decade. Very recent works, performed in collaboration with M. Montagna, provided a convincing rationalization for the interpretation of such spectra, that we use now as guideline to interpret our findings.

As exposed in section 2.2.1, according to the theoretical works of Montagna [42, 114], the low frequency scattering spectra from colloidal spheres with $\lambda \approx D$ may feature the contributions from all possible spheroidal eigenmodes, unlike the case of Raman scattering from small particles ($D << \lambda$) where restrictive selection rules reduce the contribution to only two modes ($\ell = 0$) and ($\ell = 2$). Note that because of a $1/\omega^2$ factor in the scattered intensity, the larger the eigenmode frequency (and hence roughly the larger the (n, ℓ) indices), the lower its contribution to the spectrum (in the higher frequency range). In turbid samples made of large nanospheres, where the q information is basically lost, the respective contributions of the spheroidal eigenmodes to the spectra are obtained by integrating the computed q-dependent scattering intensities. These intensities are reported as a function of the product qR ($R = D/2$) in Figure 4.29. This figure is

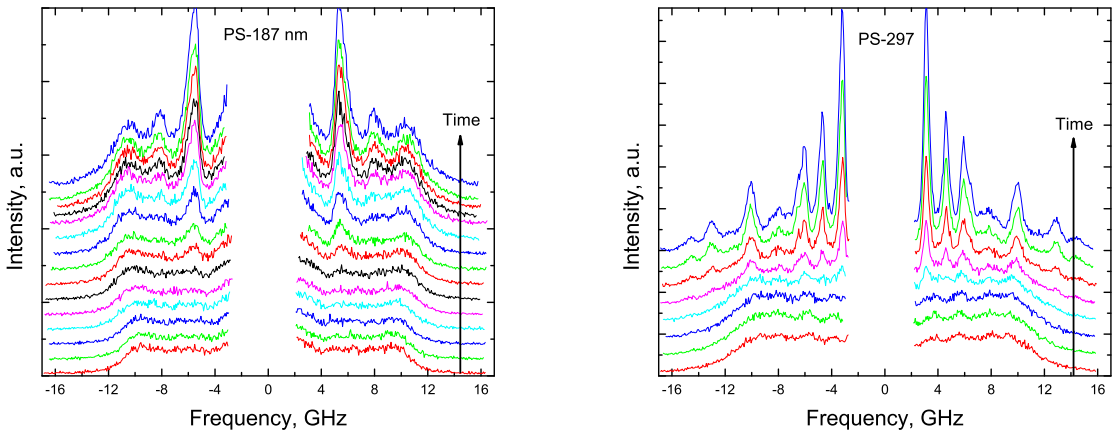

a b

Figure 4.28: Evolution of the low frequency inelastic scattering spectra of placed in "sandwich" PS-187 (**a**) and PS-297 (**b**) caused by the extinction of the PS pellets.

specifically computed for a given ratio of longitudinal to transverse speeds of sound, i.e. $v_L/v_T = 1.94$ in PS. For a given size, the inelastic light scattering spectra can be computed by integrating the several eigenmode contributions up to the maximum q value $q_{max} = 4\pi n/\lambda$, where n is the refractive index of the material the sphere is made of. Taking $n = 1.59$ for PS, the limits of integration for PS-187 and PS-297 are respectively $q_{max}R = 3.5$ and $q_{max}R = 5.6$ at 532 nm (vertical lines in Figure 4.29). One observes from Figure 4.29 that in the case of PS-187, essentially three modes contribute to the low frequency spectrum, i.e. $\ell = 0, 2, 3$, with a stronger intensity for the $\ell = 2$ mode. For PS-297, the further integration limit brings additional contributions from the $\ell = 4, 5, 6$ modes and high order harmonics of the $\ell = 2$ mode. As an illustration of Montagna's calculations, Figure 4.30 reports the detailed interpretation of PS colloids with $D = 360$ nm [114]; it is very comparable to the one we obtained for PS-297 (Fig.4.28b, top spectrum). Note that the observed very good agreement is obtained assuming non-interacting *free* nanospheres, which indicates that in the dry state, the interaction between the colloidal spheres can be considered as negligible.

The application of Montagna's approach[2] to our PS-187 dry sample is reported in Figure 4.31a (the results obtained for PS-297 being very close to those displayed in Figure 4.30 are shown in Figure 4.31b). Essentially three lines make up the spectrum: $(n = 1, \ell =$

[2]private communication

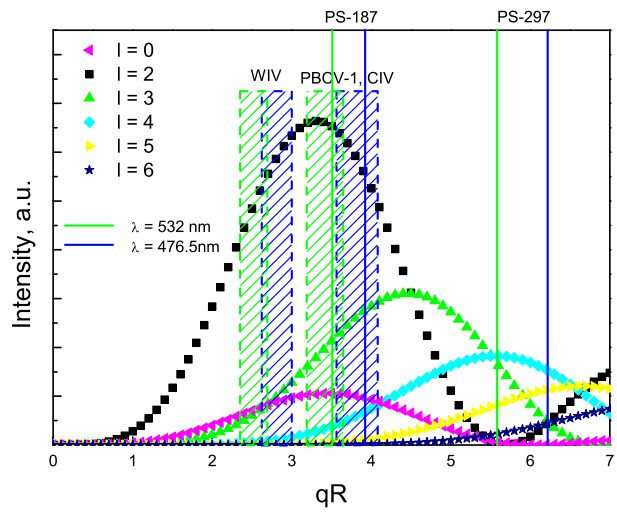

Figure 4.29: Scattered intensity of the fundamental ($n = 1$) vibrational eigenmodes with $\ell = 0$ and $2 \leq \ell \leq 7$ for a free vibrating polystyrene latex sphere as a function of the product of scattering wavevector q and radius R. Vertical lines correspond to $q_{max}R$ values for PS-187 and PS-297 for excitations of 476.5 nm (blue) and 532 nm (green). Vertical shaded rectangles are supposed to mark the $q_{max}R$ value for viruses; their width corresponds to estimated range of virus refractive index.

2), ($n = 1, \ell = 3$) and ($n = 1, \ell = 0$) in decreasing intensity order. The discrete spectra of the dry samples are mostly q-independent (notwithstanding minor relative intensity changes), as experimentally verified using different wavelengths (Fig.4.32). Also, it is worth being noticed that once the modes are well identified in the dry state, the frequency ratio of identical modes (e.g. ($n = 1, \ell = 2$)) for the two colloids matches the inverse of the diameter ratios[3], at variance with what has been observed with the not so well identified substructures of highly concentrated "wet" samples (Fig.4.27). A possible filiation of these substructures with the well identified eigenmodes observed in the dry state is now discussed.

Can the broad band observed in "wet pellets" be filiated with the nanosphere eigenmodes observed in the "dry" state? Looking at Figure 4.28, it appears ob-

[3]Note that in order to properly describe the frequency positions of the experimental discrete spectrum from PS-297, an actual size of $D = 319$ nm had to been entered, differently from the Estapor announced size of 297 nm ($\sim 7\%$ difference)

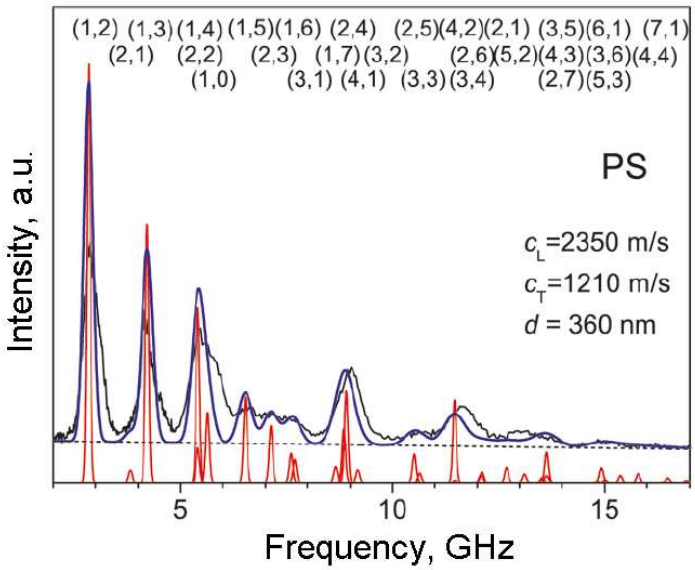

Figure 4.30: Comparison between experimental (black solid line) and calculated (blue) spectra of silica and PS spheres using the sound velocities (c_L, c_T) and diameter d given in the plots. The sharp (red) lines denote the contributions of the individual modes (n, l) labeled above the spectrum. The blue line is the sum of all modes broadened with a Gaussian line shape and corrected for a linear background (dashed line). For clarity, only the anti-Stokes side is shown [114].

vious that the defined eigenmodes of the dry PS colloids emerge out of the broad band observed from "wet" pellet samples. However, juxtaposing the first ("wet") and last ("dry") spectra of Figure 4.28 (Fig.4.33) discloses the difficulty in drawing a clear filiation : *(i)* the high frequency "edge" of the continuum-like broad band (i.e. $\sim$ 10 GHz for both colloid sizes) matches with positions of different eigenmodes in the dry state ($(n = 1, \ell = 0)$ for PS-187 and $(n = 2, \ell = 4)$ for PS-297); *(ii)* the frequency positions of the substructures observed within the broadband do not all find a clear correspondence with the narrow lines observed in the dry states; *(iii)* although of comparable intensities in the "wet" pellets, the intensity of the substructures evolve differently, at different stages of the evaporation.

This difficult correspondence between wet and dry spectra makes obvious the need of theoretical works describing the influence of a liquid embedding medium on the inelatic light scattering spectra. A first step in this direction was performed by Saviot *et al* [145] who estimated the effect of an aqueous environment on the frequencies and dampings of low frequency eigenmodes ($\ell \leq 2$) from solid nanospheres. Qualitatively, two results

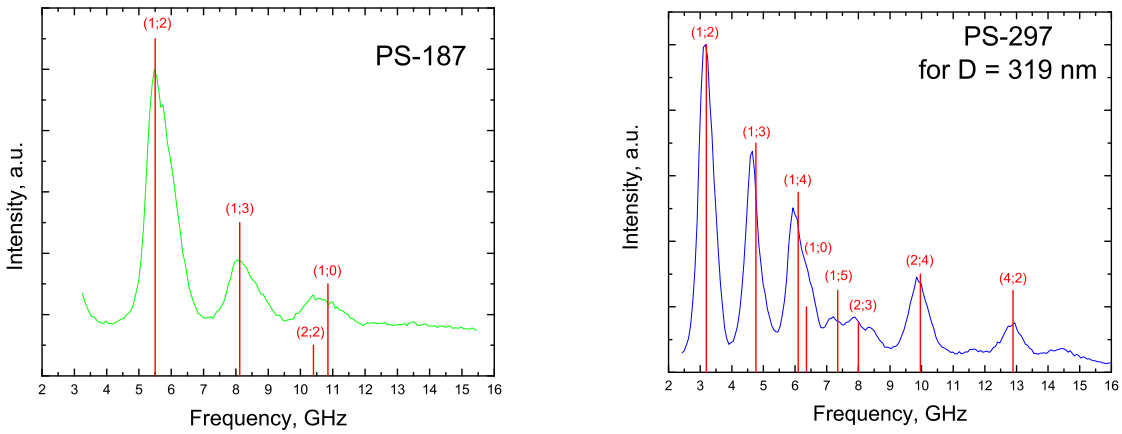

a b

Figure 4.31: Anti-Stokes sides of the inelastic spectra of PS-187 (**a**) and PS-297 (**b**) "dry" NPs for exciting wavelength 532 nm ($q_{max}R = 3.51$ and 5.58 respectively). Red bars are the theoretically predicted SPH modes made by the FSM calculations with intensities (bar heights) predicted by M. Montagna with help of its method [114]. According to the FSM calculations the real size of PS-297 is about 319 nm.

emerge from this study:

- the effect of an embedding liquid is at first order dependent on the acoustic mismatch between the nanoparticle and the embedding liquid, as with nanoparticles embedded in a solid matrix. For instance, the dampings of the eigenmodes (including their overtones) of PMMA nanospheres embedded in water are much larger than those of "harder" CdSe nanoparticles.

- the damping effect depends on the type of mode: while shear viscosity has principally an impact on eigenmodes with a transverse character, bulk viscosity mainly affects modes with a longitudinal character.

Considering the case of PS colloids embedded in water, the acoustic mismatch is similar to that of PMMA nanospheres in water, i.e. one should expect a rather significant damping of the modes. For instance the ratio $\delta\nu/\nu$ for the fundamental breathing mode ($n = 1, \ell = 0$) of a 100 nm PMMA sphere in water is about 55% while it is 30% for the quadrupolar mode ($n = 1; \ell = 2$) [145]. According to the evaluation of the longitudinal/transverse character of several eigenmodes [24], it occurs that most of the lowest frequency eigenmodes which

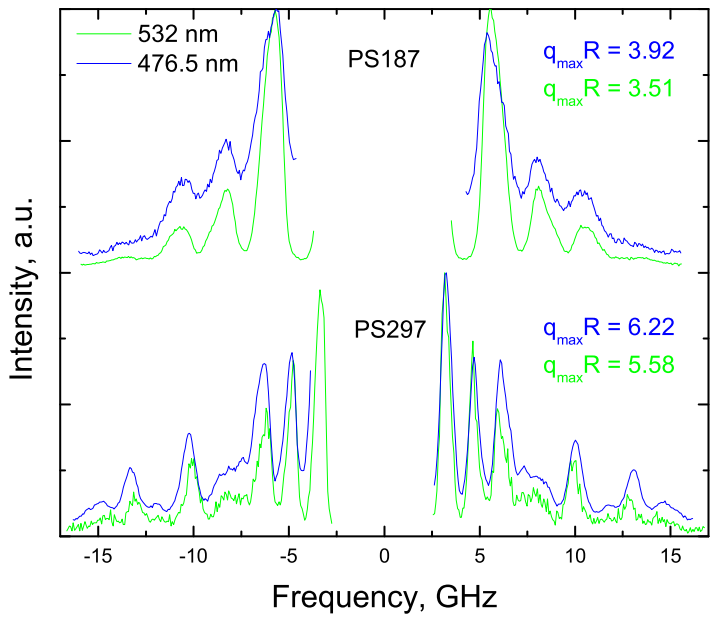

Figure 4.32: Low frequency Raman spectra of the PS-187 and PS-297 NPs for two exciting wavelengths: 532 and 476.5 nm.

contribute to the spectrum (like $(n = 1, \ell = 2)$ and $(n = 1, \ell = 3)$, Fig.4.30) have a dominating transverse character, except the breathing vibration $(n = 1, \ell = 0)$ which is more longitudinal. Even in the presence of a weak, yet non zero, shear viscosity of water, all types of modes are expected to be significantly damped so that the substructures of the broad band remain hardly identifiable. In the absence of polarization selection rules in turbid samples, changing the shear and bulk viscosity of the solvent (through temperature change, or changing the nature of the solvent) might turn out as an efficient means of identification of the substructures. In the same time, it would be necessary to estimate how the liquid embedding medium affects the scattering intensities (as calculated for free spheres, Fig.4.30).

In the case of biological nanoparticles like viruses, accounting for the presence of water might turn out more complex as, in addition to its presence as bulk embedding medium, water has to be considered as a constituent of the biological assembly itself. This situation certainly reduces the acoustic mismatch that is essential for the detectability of the eigenmodes. In the following, we discuss how, in spite of the use of a reference system

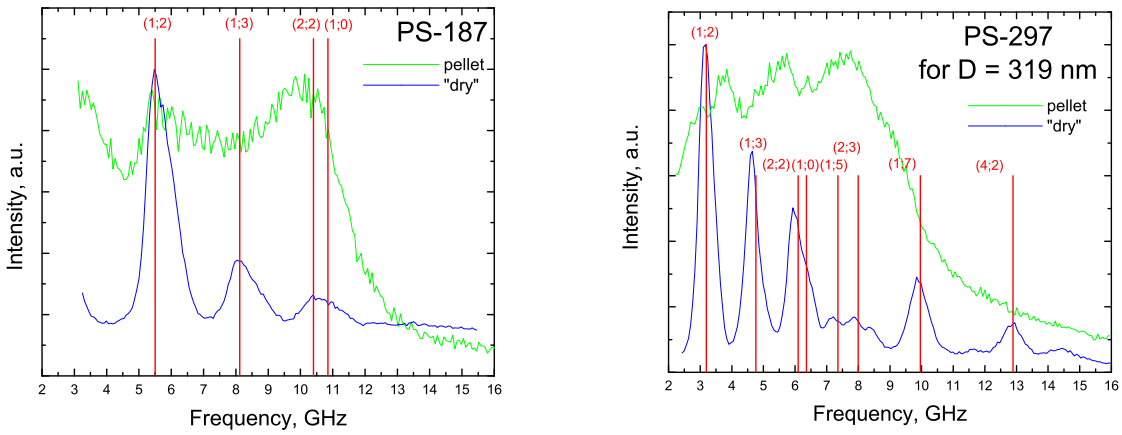

a b

Figure 4.33: Anti-Stokes sides of the inelastic spectra of PS-187 (**a**) and PS-297 (**b**) "dry" and wet colloids for exciting wavelength 532 nm ($q_{max}R = 3.51$ and 5.58 respectively). Red bars are the theoretically predicted SPH modes made by the FSM calculations. The heights of the bars do not correspond to intensities of the modes. According to the FSM calculations the real size of PS-297 is about 319 nm.

like PS colloids, the interpretation of the spectra from the viruses remains difficult.

From PS colloids to viruses

Overall scenario for PS colloids. Before trying to use the results obtained on PS colloids as a basis for the interpretation of those obtained from viruses, we first draw conclusions from the analyses of the former.

In the diluted state, the VV spectra of the turbid solutions are "regular" Brillouin spectra from liquids, featuring the usual inelastic doublet associated with the propagation of longitudinal acoustic modes in an aqueous solution. Unlike pure water Brillouin spectra, the VH spectra of the solutions evidence a broad band, whose frequency position is independent of the colloid size (Fig.4.23c). Moreover, this broad band shifts with q when using different excitation wavelenthgs (Fig.4.24a). One may therefore ascribe it to poorly defined transverse-like excitations (in comparison to plane transverse waves propagating in solids for instance), with a delocalized character. If related at all, the transverse character of most of the eigenmodes that appear in the low frequency spectra in the dry state might be a starting point for a possible interpretation of the VH broad

band in solutions.

Increasing the volume fraction of PS colloids up to $\sim 100\%$ "wet" pellets, the profile of the broad band progressively stretches to larger frequencies, forming a "continuum"-like band featuring substructures. At the stage of pellets, no more trace of propagating longitudinal modes from the solvent can be found, so that the VV and VH spectra are identical; it is therefore tempting to ascribe the substructures to eigenmodes of the colloids being affected by remaining interstitial water. However, from the study of the dried out pellets, where the eigenmodes of the PS colloids are clearly defined, the identification of the substructures in terms of quasi-eigenmodes is not straightforward. Further studies, with the help of theoretical developments concerning the effect of embedding water on scattering intensities, frequencies and dampings of nanosphere eigenmodes, may help clarify this situation. The poor definition of the substructures observed in the wet pellets should definitely be ascribed to a low acoustic mismtach between water and the PS colloids and to damping of the eigenmodes through the liquid viscosity. One should also notice that the wavelength dependence of the wet pellet spectra (Fig.4.24b) likely testifies a partial delocalization of the particle modes.

Virus spectra. The starting point of our compared analyses of large viruses and PS colloids (once morphological characterization proved they comparableness, section 4.3.2) has been the apparent similarity of their respective inelastic low frequency light scattering spectra. These similarities are obvious for both solutions and wet pellet spectra (Fig.4.22). The major advantage of PS colloids is that upon evaporation of the solvent, one can identify defined eigenmodes of the nanospheres. Such is definitely not possible with the large viruses: upon drying, the spectra of the pellets turned out to be unworkable.

Assuming the existence of eigenmodes for viruses, one would expect the intensity distribution of low frequency inelastic spectra to be comparable to those of the PS-187 spheres[4]. This can be derived from the estimated positions of the $q_{max}R$ values of the several viruses on Figure 4.29. Placing these same limits for the viruses require the knowledge of the corresponding refractive index. We may assume a common value of $n = 1.55$ which was experimentally determined for protein-based crystals [146], including virus crystals [64]. This latter value of n sets about the same limits of integration for PS-187 and PBCV-1 and CIV ($q_{max}R \simeq 3.5$) while for WIV $q_{max}R \simeq 2.6$ (see Figure 4.29).

[4]Assuming the icosahedral viruses as spheres is not expected to have consequences on the lowest frequency eigenmodes [148]. However, there surely is a problem assuming a full sphere instead of layers with the sphere.

The slightly lower position of $q_{max}R$ for WIV has minor consequences on the relative intensities of the spheroidal ($n = 1, \ell = 3$) and ($n = 1, \ell = 0$) modes, whose calculated intensities[5] are about 1/5 of that of the dominating ($n = 1, \ell = 2$) mode. It is worth emphasizing that Figure 4.29 was derived assuming a speed of sound ratio $v_L/v_T \approx 2$, as inferred from the parameters of PS. Although from the Brillouin study of hydrated virus crystals [64], a reliable value of the longitudinal speed of sound could be determined ($v_L = 1920$ m/s), the experimental determination of the transverse speed of sound (or of the Poisson ratio) in such biological assemblies is still lacking. This sets a definite difficulty in estimating absolute values of eigenmode frequencies from viruses, so that results of simulation works [9, 7, 147] can only be placed on a relative scale.

The removal of water from virus pellets leading to a dead end, one can discuss the apparent similarity of the spectra obtained from virus and PS colloid pellets since the latter potentially feature signatures of eigenmodes in the form of substructures. From the comparison between CIV (190 nm) and WIV (140 nm), but also from the comparison between two colloid sizes (Fig.4.23b), it occurs that the high "edge" frequency of the continuum-like profile of the wet pellet broad band signals cannot be interpreted as a pre-signature of eigenmode. An equally disappointing observation is that the broad band signals from virus pellets hardly evidence the presence of substructures, hence of possible eigenmodes. We review below several possible reasons for this situation.

1. **questioning the very existence of virus eigenmodes**: most theoretical works dedicated to virus particle modes refer in fact to the eigenmodes of the capisd, which identifies as the most solid-like structure in the viral assembly. Yet, in these works, two important aspects that may have important consequences on the existence of capsid eigenmodes are often neglected:

    - although compact, morphologically well defined, viral nanoparticles have complex inner structures (see for example Fig.4.3). Different elasticities and/or diffuse structures of the several constituents (genome core, lipid layer, etc) can preclude the development of motional coherence which is a basic ingredient of nanoparticle modes. A very complete simulation of an entire small plant virus (Satellite Tobacco Mosaic Virus, 15 nm) [149] did not indeed evidence coherent oscillations throughout the viral particle; instead "concerted oscillations" restricted to "belt"-like portions of the STMV could be identified.

[5] M. Montagna, private communication.

- as already mentioned, water is present throughout the structures of viruses, from the genome inner core to the oustide capsid. Due to this presence, the overall viral structure would not be stiff enough to sustain long lived eigenmodes but rather overdamped modes. In this respect, studies on the role of hydration water on the low frequency dynamics of proteins [150, 151] show how water strongly affects the vibrational collective dynamics in biological objects.

2. **observability of virus eigenmodes, if they exist**:

- if the entanglement of water throughout the viral edifice leads to strongly damped eigenmodes, the additional presence of water outside the virus certainly does not favor their detectability. A best case evaluation on the effect of water viscosity on the eigenmodes of an embedded virus-like full nanosphere [148] already captures the significant frequency downshifts and dampings induced by the presence of surrounding water. In the case of *large* viruses, these latter trends severely restrict a possible experimental reach.
- the absence of substructures in pellets of viruses such as CIV and WIV (Figure 4.22) may in fact be the result of a too strong interaction between the virions, which can lead to a reduction of the acoustic mismatch. This strong interaction would originate in the interdigitization of CIV and WIV fibrillar structures, which is not expected to occur in PBCV-1, as confirmed by the USAXS studies. In the presence of strong interaction, the delocalization of the eigenmodes (as testified by the shift of the broadband changing the wavelength excitation, Fig. 4.24) is indeed expected to smooth out the already poorly defined substructures observed in the case of least interacting PS colloids. From these considerations, it could be that the pellet spectra observed from PBCV-1 might be the most workable ones in the view of further studies.

Conclusions and perspectives

This thesis was dedicated to investigation of the acoustic properties of small metal NPs and large viruses by inelastic light Raman and Brillouin scattering. The results represented in this thesis are obtained due to high-resolution interferometer Tandem FP constructed by J. Sandercock. We showed that embedded in glass matrix Cu and AuAg NPs can be satisfactorily described by this technique in terms of their elastic and structure properties. Detailed inspection of recently discovered properties of LFRS to reflect a crystalline quality of metal NPs through a lift of degeneracy of the quadrupolar mode demonstrated the interesting results. Annealing the embedding glasses at corresponding glass transition temperatures leads to the formation of the NPs possess the monocrystal structure while the annealing at temperatures out of the T_g zone causes the formation of the non-crystal or polycrystal structure NPs. We also showed that the presence of a matrix dramatically influence the Raman profiles of the spectra but in this work we are not able to give a total analysis of this effect as we dealt with different metals in different matrices. That is why the future work would be interesting to dedicate to careful investigation of the matrix influence, i.e. to embed metal NPs in a matrix with acoustic impedance significantly different from that of the Si_2O glasses. In the case of Cu which easy oxidizes during the temperature treatment of Cu-doped glasses, it is worth to prepare NPs in oxygen-free conditions in order to investigate pure Cu formations. The additional experiments with Au NCs deposited on a surface showed that LFRS response reflects the inner structure of the studied NCs and the coexisting of mono- and polycrystalline NPs leads to overlap of the quadrupolar mode ($\ell = 2$) and E_g/T_{2g} modes.

Such knowledge about NP structure and the possibility to control the processes of its formation give an opportunity to apply the LFRS analysis in wide spectrum of areas due to the fact that metal NPs now are being exploited in material science, optics, chemistry, biology and medicine because the control of the size and shape of nanostructures is now one of the most challenging points for scientists. Due to the outstanding peculiarity of

metal NPs based on the excited SPR, LFRS allows to study the coupling of incident light with plasmon and so that to improve our understanding about the process inside the nanostructures. As NP plasmon response can be tuned by the choice of the metal and size/shape of the NP, the metal NPs are found to be attractive for many applications. For instance the role of the interparticle interaction and its influence on the properties of the self-assemblies of metal NPs is still relatively poor understood while such type of systems or similar ones (like co-assembly of metal and semiconductor NPs [152]) demonstrate interesting properties which easily find a scientific application [153]. The hybrid systems of metal NPs and biomaterials such as enzymes, antibodies, DNA, etc of comparable sizes are widely used in chemical and biochemical analyses [154], medicine and therapy [155], and also find a wide application as nano-antennas [156]. The development of LFRS detecting techniques nowadays permits to carry out the experiments hardly possible before. For example, the studies of the single-sphere (for instance a large sphere of the order of 100 nm) vibrations are of interest due to their difference from conventional inelastic light scattering [157]. In this case it would be possible to determinate accurately the real frequencies, non-widened with size/shape distribution, of acoustic modes.

The second part of the work was concerned of the study of vibrational Raman and Brillouin activity of the large icosahedral viruses of insects and plants. In order to understand the vibrational dynamics of these poorly known, in terms of inelastic light scattering, objects, we investigated also polystyrene colloids of different sizes. Making comparison of the different states of the colloids and drawing an analogy with investigated viruses we could conclude that the exact identification of the virus vibrational mode is impossible at this stage of progress but nevertheless we showed that in principle it is possible to get the elastic properties of viruses that can be very useful in applicative virology. Concerning our topic, the invisibility of the virus mode can be caused by weak acoustic impedance mismatching between viruses and embedding liquid which leads to strong damping of the active vibrations. This problem can be solved by embedding of the virus in a solid matrix. The freezing of the host liquid can be considered as the first step of realization of this idea. The results obtained for polystyrene colloids make us to continuer their investigation as the very recent theoretical works changed the well established conceptions of the vibrational dynamics of large polymeric colloids.

The results obtained by the LFRS investigations in combinations with other techniques, for example with nanoindentation measurements with an atomic force microscope [158, 159], may give an information about the elastic properties and vibrational modes

of viruses which is very needed in modern science. For example these data are also an important diagnostic tool to describe and analyze scientific applications involving viruses such as the synthesis of semiconductor NPs [160] and metals [161] or the constructing of various periodic 3D photonic crystals [132]. Another application can be the physical inactivation of viruses with ultrasonic energy absorption in viruses [162] and with resonance excitation of viruses by short light pulses which has been recently performed experimentally [163]. A wide application of viruses in nanotechnologies makes this area rapidly develop. Nowadays viruses are a valuable addition to the bionanotechnology tool for the construction of new materials, nanodevices and sensors [164, 165, 166]. Therefore the detailed investigations of the physical properties of viruses are very important.

References

[1] D.A. Weitz, T.J. Gramila, and A.Z. Genack *"Anomalous Low-Frequency Raman Scattering from Rough Metal Surfaces and the Origin of Surface-Enhanced Raman Scattering"*, Phys. Rev. Letters, vol. 45, 5, 1980

[2] E. Duval, A. Boukenter, and B. Champagnon *"Vibration Eigenmodes and Size of Microcrystallites in Glass: Observation by Very-Low-Frequency Raman Scattering"*, Phys. Rev. Lett., vol. 56, 2052-2055, 1986

[3] R.D. Hartschuh, S.P. Wargacki, H. Xiong, J. Neiswinger, A. Kisliuk, S. Sihn, V. Ward, R.A. Vaia, and A.P. Sokolov *"How rigid are viruses"*, Phys. Rev. E, vol. 78, 021907, 2008

[4] H. Lamb *"On the vibrations of an elastic sphere"*, Proc. Londo Math. Soc., vol. 13, 1882

[5] B. Stephanidis *"Modes de vibration de nano-objects: des nanoparticules métalliques aux virus biologiques"*, PhD thesis, University Claude Bernard — Lyon 1, 2008

[6] M.M. Gibbons and W.S. Klug *"Influence of Nonuniform Geometry on Nanoindentation of Viral Capsids"*, Biophysical Journal, vol. 95, 3640 – 3649, 2008

[7] L.H. Ford *"Estimate of the vibrational frequencies of spherical virus particles"*, Phys. Rev. E, vol. 67, 051924, 2003

[8] E.C. Dykeman and O.F. Sankey *"Atomic modeling of the low-frequency mechanical modes and Raman spectra of icosahedral virus capsids"*, Phys. Rev. E, vol. 81, 021918, 2010

[9] F. Tama and C.L. Brooks *"Diversity and Identity of Mechanical Properties of Icosahedral Viral Capsids Studied with Elastic Network Normal Mode Analysis"*, J. Mol. Biol., vol. 345, 299 – 314, 2005

[10] Z. Yang, I. Bahar, and M. Widom *"Vibrational Dynamics of Icosahedrally Symmetric Biomolecular Assemblies Compared with Predictions Based on Continuum Elasticity"*, Biophysical Journal, vol. 96, 4438 – 4448, 2009

[11] M. Talati and P.K. Jha *"Acoustic phonon quantization and low-frequency Raman spectra of spherical viruses"*, Phys. Rev. E, vol. 73, 011901, 2006

[12] P.G. de Gennes et M. Papoular *"Vibration de basse fréquence dans certaines structures biologiques"*, in the "Polarisation matière et rayonnement", vol. Jubilaire en l'honneur d'Alfred Kastler, Presses Universitaires de France, 1969

[13] H.W.T. van Vlijmen and M. Karplus *"Normal Mode Calculations of Icosahedral Viruses with Full Dihedral Flexibility by Use of Molecular Symmetry"*, J. Mol. Biol. vol. 350, 528 – 542, 2005

[14] R.J. Tseng, C. Tsai, L. Ma, J. Ouyang, C.S. Ozkan and Y. Yang *"Digital memory device based on tobacco mosaic virus conjugated with nanoparticles"*, Nature Nanotechnology, vol. 1, 2006

[15] W.L. Liu, K. Alim, and A.A. Balandin *"Assembly and characterization of hybrid virus-inorganic nanotubes"*, Appl. Phys. Lett., vol. 86, 253108, 2005

[16] T. Douglas and M. Young *"Host-guest encapsulation of materials by assembled virus protein cages"*, Nature, vol. 393, 1998

[17] K.T. Tsen, E.C. Dykeman, O.F. Sankey, S.-W.D. Tsen, N.-T. Lin and J.G. Kiang *"Raman scattering studies of the low-frequency vibrational modes of bacteriophage M13 in waterobservation of an axial torsion mode"*, Nanotechnology, vol. 17, 5474, 2006

[18] C. Kittel *"Introduction to Solid State Physics"*, Wiley, 7 edition, 1995

[19] N.W. Ashcroft, N.D. Mermin *"Solid State Physics"*, Thomson Learning, Inc., 1976

[20] M.M. Beg and S.M. Shapiro *"Study of phonon dispersion relations in cuprous oxide by inelastic neutron scattering"*, Phys. Rev. B, vol. 13, 4, 1976

[21] Benedek and Fritsch *"Brillouin Scattering in Cubic Crystals"*, Phys. Rev. vol. 149, 1966

[22] A.C. Eringen, E.S. Suhubi *"Elastodynamics (vol. 2) Linear theory"*, New York-London, Academic Press, 1975

[23] A.E.H. Love *"A treatise on the mathematical theory of elasticity. Forth edition"*, Dover Publications, Inc., USA, 1972

[24] L. Saviot and D. B. Murray *"Longitudinal versus transverse spheroidal vibrational modes of an elastic sphere*, Phys. Rev. B, vol. 72, 205433, 2005

[25] D. Murray and L. Saviot *"Phonons in an inhomogeneous continuum: Vibrations of an embedded nanoparticle"*, Phys. Rev. B, vol. 69, 094305, 2004

[26] L. Saviot, D. Murray, and M.Marco de Lucas *"Vibrations of free and embedded anisotropic elastic spheres: Application to low-frequency Raman scattering of silicon nanoparticles in silica"*, Phys. Rev. B, vol. 69, 113402, 2004

[27] V.A. Dubrovskiy and V. Morochnik, Izv., Acad. Sci., USSR, Phys. Solid Earth 17, 494, 1981

[28] L. Saviot, A. Mermet, E. Duval *"Handbook of Nanophysics: Nanoparticles and Quantum Dots. Chapter 11: Acoustic Vibrations in Nanoparticles"*, K.D. Sattler, Taylor and Francis group, 11.1 – 11.17, 2010

[29] D. Murray, L. Saviot *"Acoustic vibrations of embedded spherical nanoparticles"*, Physica E, vol. 26, 417-421, 2005

[30] H. Portales, N. Goubet, L. Saviot, S. Aditchev, D.B. Murray, A. Mermet, E. Duval, and M.-P. Pileni *"Probing atomic ordering and multiple twinning in metal nanocrystals trough their vibrations"*, PNAS, vol.105, 39, 2008

[31] L. Saviot and D.B. Murray, *"Acoustic vibrations of anisotropic nanoparticles"*, Phys. Rev. B, vol. 79, 214101, 2009

[32] D.B. Murray, A.S. Laarakker, and L. Saviot *"High precision numerical estimates of acoustic phonon frequencies of nonspherical nanoparticles"*, Phys. Stat. Sol. C, vol. 3, 11, 3935 – 3938, 2006

[33] J.Margueritat, J. Gonzalo, C.N. Afonso, A. Mlayah, D.B. Murray, L. Saviot *"Surface Plasmons and Vibrations of Self-Assembled Silver Nanocolumns"*, Nano Letters, vol. 6, 9, 2037 – 2042, 2006

[34] Derek A. Long *"The Raman Effect. A Unified Treatment of the Theory of Raman Scattering by Molecules"*, John Wiley and Sons, LTD, 2002

[35] L. Landau, E. Lifshitz *"Theoretical physics. T.8. Electrodynamics of continuous media"*, Moscow, Nayka, 1982

[36] M. Cardona, G. Guntherodt *"Topics in Applied Physics. Light Scattering in Solids II"*, vol. 50, Springer-Verlag, Berlin, Heidelberg, New York, 1982

[37] E. Duval *"Far-infrared and Raman vibrational transitions of a solid sphere: Selection rules"*, Phys. Rev. B, vol. 46, 9, 1992

[38] V. Heine, in *"Group Theory in Quantum Mechanics"*, Pergamon, New York, 1960

[39] M. Gyory *"A new proof of Wigner's theorem"*, Reports of mathematical physics, vol. 54, 2, 2004

[40] M. Kanehisa *"Infrared and Raman selection rules for elastic vibrations of spherical nanoparticles"*, Phys. Rev. B, vol. 72, 241405(R), 2005

[41] S. V. Goupalov, L. Saviot, E. Duval *"Comment on "Infrared and Raman selection rules for elastic vibrations of spherical nanoparticles"*, Phys. Rev. B, vol. 74, 197401, 2006

[42] M. Montagna *"Brillouin and Raman scattering from the acoustic vibrations of spherical particles with a size comparable to the wavelength of the light"*, Phys. Rev. B, vol. 77, 2008

[43] J.I. Gersten, R.L. Birke, J.R. Lombardi *"Theory of Enhanced Light Scattering from Molecules Absorbed at the Metal-Solution Interface"*, Phys. Rev. Lett., vol. 43, 2, 1979

[44] M. Moscovits *"Surface-enhanced Spectroscopy"*, Rev. Mod. Phys., vol. 57, 3, Part 1, 1985

[45] C.F. Bohren, D.R. Huffman *"Absorption and Scattering of Light by Small Particles"*, John Wiley and Sons, 1983

[46] E. Cottancin, M. Broyer, J. Lermé, M. Pellarin *"Handbook of Nanophysics: Nanoelectronics and Nanophotonics. Chapter 24: Optical Properties of Metal Clusters and Nanoparticles"*, K.D. Sattler, Taylor and Francis group, 24.1 – 24.25, 2010

[47] U. Kreibig, G. Bour, A. Higer, and M. Gartz *"Optical Properties of Cluster-Matter: Influence of Interfaces"*, Phys. Stat. Sol. (a), vol. 175, 351, 1999

[48] E. Cottancin, G. Celep, J. Lerme, M. Pellarin, J.R. Huntzinger, J.L. Vialle, M. Broyer *"Optical properties of noble metal clusters as a function of the size: comparison between experiments and a semi-quantal theory"*, Theor. Chem. Acc., vol. 116, 514 – 523, 2006

[49] G. Bachelier and A. Mlayah *"Surface plasmon mediated Raman scattering in metal nanoparticles"*, Phys. Rev. B, vol.69, 2004

[50] N. Del Fatti, C. Voisin, D. Christofilos, F. Vallée and C. Flytzanis *"Acoustic Vibration of Metal Films and Nanoparticles"*, J. Phys. Chem. A, vol. 104, 4321-4326, 2000

[51] B. Palpant, H. Portales, L. Saviot, J. Lermé, B. Prével, M. Pellarin, E. Duval, A. Perez, M. Broyer *"Quadrupolar vibrational mode of silver clusters from plasmon-assisted Raman scattering"*, Phys. Rev. B, vol. 60, 24, 1999

[52] H. Portales, L. Saviot, E. Duval, M. Gaudry, E. Cottancin, J. Lermé, M. Pellarin, M. Broyer, B. Prével, and M. Treilleux *"Resonance and composition effects on the Raman scattering from silver-gold alloy clusters"*, Eur. Phys. J., vol. 16, 197 – 200, 2001

[53] H. Portales, L. Saviot, E. Duval, M. Fujii, S. Hayash, N. Del Fatti, F. Vallée *"Resonant Raman scattering by breathing modes of metal nanoparticles"*, J. Chem. Phys., vol. 115, 3444, 2001

[54] A. Courty, I. Lisiecki, and M.P. Pileni *"Vibration of self-organized silver nanocrystals"*, J. Chem. Phys., vol. 116, 18, 2002

[55] A. Courty, A. Mermet, P.A. Albouy, E. Duval and M.P. Pileni *"Vibrational coherence of self-organized silver nanocrystals in f.c.c. supra-crystals"*, Nature Materials, vol. 4, 2005

[56] S. V. Gupalov and I. A. Merkulov *"Theory of Raman light scattering by nanocrystal acoustic vibrations"*, Phys. Solid State, vol. 41, 8, 1999

[57] M. Montagna, R. Dusi *"Raman scattering from small spherical particles"*, Phys. Rev. B, vol.52, 10080 - 10089, 1995

[58] W. Cheng, J. J. Wang, U. Jonas, W. Steffen, G. Fytas, R. S. Penciu, E. N. Economou *"The spectrum of vibration modes in soft opals"*, J. Chem. Phys., vol. 123, 121104, 2005

[59] B. Stephanidis, S. Adichtchev, S. Etienne, S. Migot, E. Duval, and A. Mermet *"Vibrations of nanoparticles: from nanospheres to fcc cuboctahedra"*, Phys. Rev. B, vol. 76, 121404(R), 2007

[60] R.S. Penciu, G. Fytas, E.N. Economou, W. Steffen, and S.N. Yannopoulos *"Acoustic Excitations in Suspensions of Soft Colloids"*, Phys. Rev. Lett., vol. 85, 21, 2000

[61] V.A. Fonoberov and A.A. Balandin *"Low-frequency vibrational modes of viruses used for nanoelectronic self-assemblies"*, Phys. Stat. Sol. (b), vol. 241, 12, 2004

[62] S.A. Overman and G.J. Thomas *"Novel Vibrational Assignments for Proteins from Raman Spectra of Viruses"*, J. Raman. Spectrosc, vol. 29, 23 – 29, 1998

[63] L. Saviot, D.B. Murray, A. Mermet, and E. Duval *"Comment on "Estimate of the vibrational frequencies of spherical virus particles"*, Phys. Rev. E, vol. 69, 023901, 2004

[64] B. Stephanidis, S. Adichtchev, P. Gouet, A. McPherson, and A. Mermet *"Elastic Properties of Viruses"*, Biophysical Journal, vol. 93, 2007

[65] B. Hillebrands *"Progress in multipass tandem Fabry-Perot interferometry: I. A fully automated, easy to use, self-aligning spectrometer with increased stability and flexibility"*, Rev. Sci. Instrum., vol. 70, 3, 1999

[66] S.M. Lindsay, M.W. Anderson and J.R. Sandercock *"Construction and aligment of a high performance multipass vernier tandem Fabry-Perot interferometer"*, Rev. Sci. Instrum., vol. 52, p. 1478 – 1486, oct. 1981

[67] R. Mock, B. Hillebrandst and R. Sandercock *"Construction and performance of a Brillouin scattering set-up using a triple-pass tandem Fabry-Perot interferometer"*, J. Phys. E: Sci. Instrum., vol. 20, 1987

[68] J.R. Sandercock *"Tandem Fabry-Perot Interferometer — Operator Manual"*, JRS Scientific Instruments, Lindenmoosstrasse 10 8910 Affoltern a.A. Suisse, 1999

[69] M. Born and E. Wolf *"Principles of optics, 6th edition"*, Pergamon Press, 1993

[70] A.N. Zajdel, G.V. Ostrovskaja, U.I. Ostrovskiy *"Technique and practice of spectroscopy"*, "Nayka", Moscow, 1976

[71] Y.Y. Huang, J.L. Hunt, and J.R. Stevens *"Determination of elastic constants in isotropic silicate glasses by Brillouin scattering"*, J. Appl. Phys., vol. 44, 8, 3589, 1973

[72] H. Portales *"Étude par diffusion Raman de nanoparticules métalliques en matrice diélectrique amorphe"*, PhD thesis, Uneversity Claude Bernard — Lyon 1, 2001

[73] S. Adichtchev, S. Sirotkin, G. Bachelier, L. Saviot, S. Etienne, B. Stephanidis, E. Duval, and A. Mermet *"High-order vibration modes of bimetallic Ag-Au nanoparticles embedded in glass"*, Phys. Rev. B, vol. 79, 201402(R), 2009

[74] H. Portales, N. Goubet, L. Saviot, P. Yang, S. Sirotkin, E. Duval, A. Mermet, and M.-P. Pileni *"Crystallinity Dependence of the Plasmon Resonant Raman Scattering by Anisotropic Gold Nanocrystals"*, ACS Nano, vol. 4, 6, 3489 - 3497, 2010

[75] F. E. Wagner, S. Haslbeck, L. Stievano, S. Calogero, Q. A. Pankhurst, K.-P. Martinek *"Before striking gold in gold-ruby glass"*, Nature, vol. 407, 12 October 2000

[76] J. J. Mock, M. Barbic, D. R. Smith, D. A. Schultz, and S. Schultz *"Shape effects in plasmon resonance of individual colloidal silver nanoparticles"*, J. Chem. Phys., vol. 116, 15, 2002

[77] S. Link, Z. L. Wang, and M. A. El-Sayed *"Alloy Formation of Gold-Silver Nanoparticles and the Dependence of the Plasmon Absorption on Their Composition"*, J. Phys. Chem. B, 1999, 103 (18), pp 3529-3533

[78] M. Gaudry, J. Lerme, E. Cottancin, M. Pellarin, J.-L. Vialle, M. Broyer, B. Prevel, M. Treilleux, and P. Melinon *"Optical properities of $(Au_xAg_{1-x})_n$ clusters embedded in alumina: Evolution with size and stoichiometry"*, Phys. Rev. B, vol. 64, 085407, 2001

[79] G. Battaglin, M. Catalano, E. Cattaruzza, F. D'Acapito, C. De Julian Fernandez, G. De Marchi, F. Gonella, G. Mattei, C. Maurizio, P. Mazzoldi, A. Miotello, C. Sada *"Influence of annealing atmosphere on metal and metal alloy nanoclusters produced by ion implantation in silica"*, Nuclear Instrument and methods in physics researh selection B, vol. 178, 176 – 179, 2001

[80] B. Rodrguez-Gonzalez, A. Sanchez-Iglesias, M. Giersig and L.M. Liz-Marzan *"AuAg bimetallic nanoparticles: formation, silica-coating and selective etching"*, Faraday Discuss., vol. 125, 133, 2004

[81] Y. Kim, R.C. Johnson, J. Li, J.T. Hupp, G.C. Schatz *"Synthesis, linear extinction, and preliminary resonant hyper-Rayleigh scattering studies of gold-core/silver-shell nanoparticles: comparisons of theory and experiment"*, Chem. Phys. Lett., vol. 352, 421 - 428, 2002

[82] M.M. Maye, L. Han, N.N. Kariuki, N.K. Ly, W. Chan, J. Luo, C. Zhong *"Gold and alloy nanoparticles in solution and thin film assembly: spectrophotometric determination of molar absorptivity"*, Analytica Chimica Acta, 496, 17 – 27, 2003

[83] M. Fujii, T. Nagareda, S. Hayashi, and K. Yamamoto *"Low-frequency Raman scattering from silver particles embedded in SiO_2 thim films"*, Phys. Rev. B, vol. 44, 6243 1991

[84] A. Tanaka, S. Onari, and T. Arai *"Low-frequency Raman scattering from CdS microcrystals embedded in a germanium dioxide glass matrix"*, Phys. Rev. B, vol. 47, 1237, 1993

[85] M.H. Kuok, H.S. Lim, S.C. Ng, N.N. Liu, and Z.K. Wang *"Brillouin Study of the Quantization of Acoustic Modes in Nanospheres"*, Phys. Rev. Lett., vol. 90, 255502, 2003

[86] L. Saviot, B. Champagnon, E. Duval, I.A. Kudriavtsev, and A.I. Ekimov *"Size dependence of acoustic and optical vibrational modes of CdSe nanocrystals in glasses"*, J. of Non-Cryst. Solids, vol. 197, 238 – 246, 1996

[87] L. Saviot and D.B. Murray *"Long Lived AcousticVibrational Modes of an Embedded Nanoparticle"*, Phys. Rev. Let., vol. 93, 5, 2004

[88] L. Saviot, Simulated vibrations of the sphere:

`http://noee.u-bourgogne.fr/~saviot/hdr/html/`

[89] G. Bachelier *"Propriétés optiques de nano-structures métalliques et semiconductrices"*, PhD thesis, University Paul Sabatier, Toulouse III, 2004

[90] N. Del Fatti, C. Voisin, F. Chevy, F. Vallée, and C. Flytzanis *"Coherent acoustic mode oscillation and damping in silver nanoparticles"*, J. Chem. Phys., vol. 110, 23, 1999

[91] C. Voisin, N. Del Fatti, D. Christofilos and F. Vallée *"Ultrafast Electron Dynamics and Optical Nonlinearities in Metal Nanoparticles"*, J. Phys. Chem. B, vol. 105, 12, 2264 – 2280, 2001

[92] L. Saviot, D.B. Murray, E. Duval, A. Mermet, S. Sirotkin, and M.C.M. Lucas *"Simple model for the vibrations of embedded elastically cubic nanocrystals"*, Phys. Rev. B, vol. 82, 115450, 2010

[93] N. Zheng, J. Fan, and G.D. Stucky *"One-Step One-Phase Synthesis of Monodisperse Noble-Metallic Nanoparticles and Their Colloidal Crystals"*, J. Am. Chem. Soc., vol. 128, 6550 – 6551, 2006

[94] Z.L. Wang *"Transmission Electron Microscopy of Shape-Controlled Nanocrystals and Their Assemblies"*, J. Phys. Chem. B, vol. 104 (6), pp 1153 – 1175, 2000

[95] S. Ogawaand, S. Ino *"Formation of Multiply-Twinned Particles in the Nucleation Stage of Film Growth"*, J. Vac. Sci. Technol., vol. 6, Issue 4, pp. 527 – 534, 1969

[96] E.M. Purcell, C.R. Pennypacker *"Scattering and Absorption of Light by Nonspherical Dielectric Grains"*, Astrophysical Journal 1973, 186, 705 – 714

[97] J. Rodríguez-Fernández, C. Novo, V. Myroshnychenko, A.M. Funston, A. Sánchez-Iglesias, I. Pastoriza-Santos, J. Pérez-Juste, F.J. García de Abajo, L.M. Liz-Marzán, and P. Mulvaney *"Spectroscopy, Imaging, and Modeling of Individual Gold Decahedra"*, J. Phys. Chem. C vol.113, 18623 – 18631, 2009

[98] E. Duval, H. Portales, L. Saviot, M. Fujii, K. Sumitomo, and S. Hayashi *"Spatial coherence effect on the low-frequency Raman scattering from metallic nanoclusters"*, Phys. Rev. B, vol.63, 075405, 2001

[99] N. Goubet, Y. Ding, M. Brust, Z.L. Wang and M.-P. Pileni *"A Way To Control the Gold Nanocrystals Size: Using Seeds with Different Sizes and Subjecting Them to Mild Annealing"*, ACS Nano, vol. 3, 11, 3622 – 3628, 2009

[100] http://www.saint-gobain-glass.com/saint-just/

[101] J. Marqusee and J. Ross *"Theory of Ostwald ripening: Competitive growth and its dependence on volume fraction"*, J. Chem. Phys., vol. 80, 1, 1984

[102] K. Sathiyamoorthy, C. Vijayan and M.P. Kothiyal *"Design of an M-line spectroscopy set-up for the characterization of polymeric waveguides"*, J. Instrum. Soc. India 37(4) 282 – 288, 2007

[103] O. Yeshchenko, I. Dmitruk, A. Alexeenko, A. Dmytruk *"Size-dependent melting of spherical copper nanoparticles embedded in a silica matrix"*, Phys. Rev. B, vol. 75, 085434, 2007

[104] S. Berthier *"Optique des milieux composites"*, Polytechnica, 1993

[105] P. Colomban and H.D. Schreiber *"Raman signature modification induced by copper nanoparticles in silicate glass"*, J. Raman Spectrosc., vol. 36, 884 – 890, 2005

[106] T. Bring *"Red Glass Coloration: A Colorimetric and Structural Study"*, PhD thesis, Stockholm, Sweden 2006

[107] N. Murase and T. Yazawa *"Partially Reduced Cuprous Oxide Nanoparticles Formed in Porous Glass Reaction Fields"*, J. Am. Ceram. Soc., 84 (10) 2269 – 2273, 2001

[108] O.A. Yeshchenko, I.M. Dmitruk, A. M. Dmytruk, A.A. Alexeenko *"Influence of annealing conditions on size and optical properties copper nanoparticles embedded in silica matrix"*, Materials Science and Engineering B vol. 137, 247 – 254, 2007

[109] G. Celep *"Propriétés optiques et processus dynamiques dans les nanoparticules mètalliques: agrégats de cuivre et systèmes mixtes cur-coquille Indium/Argent"*, PhD thesis of the University Claude Bernard Lyon 1, 2006

[110] G.De Marchi, G. Mattei, P. Mazzoldi, C. Sada, A. Miotello *"Two stages in kinetics of gold cluster growth in ion-implanted silica during isothermal annealing in oxidizing atmosphere"*, J. Appl. Phys., vol. 92, 8, 2002

[111] E. Duval, A. Mermet, A. Courty, P.A. Albouy, and M.P. Pileni *"Coherence effects on Raman scattering from self-organized Ag nanocrystals: Theory"*, Phys. Rev. B, vol. 72, 085439, 2005

[112] P.G. de Gennes et M. Papoular *"Vibration de basse frèquence dans certaines structures biologiques"*, in the "Polarisation matière et rayonnement", vol. Jubilaire en l'honneur d'Alfred Kastler, Presses Universitaires de France, 1969

[113] W. Cheng, J. Wabg, U. Jonasi, G. Fytas, and N. Stefanous *"Observation and tuning of hypersonic bandgaps in colloidal crystals"*, Nature Materials, vol. 5, october 2006

[114] T. Still, M. Mattarelli, D. Kiefer, G. Fytas, and M. Montagna *"Eigenvibrations of Submicrometer Colloidal Spheres"*, J. Phys. Chem. Lett., vol. 1, 2440 – 2444, 2010

[115] D.L.D. Caspar and A. Klug *"Physical principles in the construction of regular viruses"*, Cold Spring Harbor Symp. vol. 27, 1, 1962

[116] V.L. Lorman and S.B. Rochal1 *"Landau theory of crystallization and the capsid structures of small icosahedral viruses"*, Phys. Rev. B, vol. 77, 224109, 2008

[117] Yu. G. Kuznetsov, J.R. Gurnon, J.L. Van Etten, A. McPherson *"Atomic force microscopy investigation of a chlorella virus, PBCV-1"*, Journal of Structural Biology, 149 (2005) 256-263

[118] J.L. Van Etten, *"Encyclopedia of Virology. Volume 1. Algal Viruses"*, edited by A. Granoff, R.G. Webster, Second Edition, Academic Press, 1999

[119] M.V. Cherrier, V.A. Kostyuchenko, C. Xiao, V.D. Bowman, A.J. Battisti, X. Yan, P.R. Chipman, T.S. Baker, J.L. Van Etten, and M.G. Rossmann *"An icosahedral algal virus has a complex unique vertex decorated by a spike"*, PNAS, vol. 106, 27, 11085-11089, 2009

[120] X. Yan, N.H. Olson, J.L. Etten, M. Bergoin, M.G. Rossman and T.S. Baker *"Structure and assembly of large lipid-containing sDNA viruses"*, Natural Structural Biology, vol. 7, 2, 2000

[121] N. Nandhagopal, A. Simpsony, J. Gurnonz, X. Yan, T. Baker, M.V. Graves, L. Van Ettenx, M. Rossman *"The Structure and Evolution of the Major Capsid Protein of a Large, Lipid-Containing DNA Virus"*, Virology, Nebraska Center for Virology Papers, 2002

[122] X. Yan, V. Bowman, N. H. Olson, J. R. Gurnon, J. L. Van Etten, M. G. Rossmann, and T. S. Baker, *"The Structure of a T=169d Algal Virus, PBCV-1, at 15 Resolution"*, Microsc Microanal 11(Suppl 2), 2005

[123] R. Webby and J. Kalmakoff *"Encyclopedia of Virology. Volume 2. Iridoviridae - invertebrate"*, edited by A. Granoff, R.G. Webster, Second Edition, Academic Press, 1999

[124] M. Fukaya and S. Nasu *"A Chilo Iridescent Virus (CIV) from the Rice Stem Borer, Chilo suppressalis Walker"*, Appl. Ent. Zool. 1 (2) 69-72, 1966

[125] X. Yan, P.R. Chipman, A.J. Battisti, M. Bergoin, M.G. Rossmann, and T.S. Baker *"The Structure of the T=147 Iridovirus, CIV, at 13 Resolution"*, Microsc Microanal 11(Suppl 2), 2005

[126] X. Yan, P.R. Chipman, A.J. Battisti, M. Bergoin, M.G. Rossmann, and T.S. Baker *"The Structure of the T=147 Iridovirus, CIV, at 13 Resolution"*, Microsc Microanal 11(Suppl 2), 2005

[127] T. Williams *"The Insect Viruses"*, edited by L.K. Miller and L.A. Ball, Plenum Publishing Corporation, New York, 1998

[128] A. Granoff and R.G. Webster *"Encyclopedia of Virology"*, Second edition, vol. 2, Academic press, 1999

[129] X. Yan, Z. Yu, P. Zhang, A.J. Battisti, P.R. Chipman, C. Bajaj, M. Bergoin, M.G. Rossmann, and T.S. Baker *"The Capsid Proteins of a Large, Icosahedral dsDNA Virus"*, J Mol Biol., 385(4): 12871299, 2009

[130] A. Granoff and R.G. Webster *"Encyclopedia of Virology"*, Second edition, vol. 3, Academic press, 1999

[131] M. Fowler and J. S. Robertson *"Iridescent virus infection in field populations of Wiseana cervinata (lepidoptera: Hepialidae) and Witlesia sp. (lepidoptera: Pyralidae) in New Zealand"*, J. Invertebr. Pathol., vol. 19, 1, 154-155, 1972

[132] S.B. Juhl, E.P. Chan, Y.H. Ha, M. Maldovan, J. Brunton, V. Ward, T. Dokland, J. Kalmakoff, B. Farmer, E.L. Thomas, and R.A. Vaia *"Assembly of Wiseana Iridovirus: Viruses for Colloidal Photonic Crystals"*, Adv. Funct. Mater. , vol. 16, 1086 - 1094, 2006

[133] G. Oster and A.D. McLaren *"The Ultraviolet Light and Photosensitized Inactivation of Tobacco Mosaic Virus"*, JGP, vol. 33, 3, 215 – 228, 1950

[134] L.E. Bockstahler and P. Kaesberg *"The Molecular Weight and Other Biophysical Properties of Bromegrass Mosaic Virus"*, Biophysical Journal, vol. 2, 1962

[135] G. Holzwarth, D.G. Gordon, J.E. McGinness, B.P. Dorman, and M.F. Maestre *"Mie Scattering Contributions to the Optical Density and Circular Dichroism of T2 Bacteriophage"*, Biochemistry, vol. 13, 1, 1974

[136] F.-X. Jousset and M. Bergoin *"Characterization of the Drosophila C Virus"*, J. Gen. Virol., vol. 34, 269 – 285, 1977

[137] S. Scheuring, T. Boudier, J.N. Sturgis *"From high-resolution AFM topographs to atomic models of supramolecular assemblies"*, Journal of Structural Biology, vol.159, 268-276, 2007

[138] C.A.J. Putman, O. Werf van der Kees, G. Grooth de Bart, and F. Hulst van Niek and J. Greve *"Tapping mode atomic force microscopy in liquid"*, Appl. Phys. Lett., vol. 64, 18, 2454-2456, 1994

[139] H.-J. Butt, B. Cappella, M. Kappl *"Force measurements with the atomic force microscope: Technique, interpretation and applications"*, Surface Science Reports, vol. 59, 1 - 152, 2005

[140] T. Narayanan *"Synchrotron Small-Angle X-Ray Scattering"*, Springer-Verlag Berlin Heidelberg, 2008

[141] http://www.sztucki.de

[142] K.K. Lee, H. Tsuruta, R.W. Hendrix, R.L. Duda and J.E. Johnson *"Cooperative Reorganization of a 420 Subunit Virus Capsid"*, J. Mol. Biol., vol. 352, 723 – 735, 2005

[143] Z. Heiner and K. Osvay *"Refractive index of dark-adapted bacteriorhodopsin and tris(hydroxymethyl)aminomethane buffer between 390 and 880 nm"*, Applied Optics, vol. 48, 23, 2009

[144] D. Liu, J. Xu, R. Li, R. Dai, We. Gong *"Measurements of sound speed in the water by Brillouin scattering using pulsed Nd:YAG laser"*, Optics Communications, vol. 203, 335 – 340, 2002

[145] L. Saviot, C.H. Netting, D.B. Murray *"Damping by Bulk and Shear Viscosity of Confined Acoustic Phonons for Nanostructures in Aqueous Solution"*, J. Phys. Chem. B, vol. 111, 7457 – 7461, 2007

[146] S. Speziale, F. Jiang, C.L. Caylor, S. Kriminski, C.-S. Zha, R.E. Thorne, and T.S. Duffy *"Sound Velocity and Elasticity of Tetragonal Lysozyme Crystals by Brillouin Spectroscopy"*, Biophysical Journal, vol. 85, 3202 – 3213, 2003

[147] M. Widom, J. Lidmar, D.R. Nelson *"Soft modes near the buckling transition of icosahedral shells"*, Phys. Rev. E, vol. 76, 031911, 2007

[148] D.B. Murray, L. Saviot *"Damping by bulk and shear viscosity for confined acoustic phonons of a spherical virus in water"*, Journal of Physics: Conference Series, vol. 92, 1, 012036, 2007

[149] P.L. Freddolino, A.S. Arkhipov, S.B. Larson, A. McPherson and K. Schulten *"Molecular Dynamics Simulations of the Complete Satellite Tobacco Mosaic Virus"*, Structure, vol. 14, 3, 437 – 449, 2006

[150] G. Caliskan, D. Mechtani, J.H. Roh, A. Kisliuk, A.P. Sokolov, S. Azzam, M.T. Cicerone, S. Lin-Gibson, I. Peral *"Protein and solvent dynamics: How strongly are they coupled?"*, J. Chem. Phys., vol. 121, 4, 2004

[151] J.H. Roh, J.E. Curtis, S. Azzam, V.N. Novikov, I. Peral, Z. Chowdhuri, R.B. Gregory, and A.P. Sokolov *"Influence of Hydration on the Dynamics of Lysozyme"*, Biophysical Journal, vol. 91, 7, 2573 – 2588, 2006

[152] M. Adams, Z. Dogic, S.L. Keller, S. Fraden *"Entropically driven microphase transitions in mixtures of colloidal rods and spheres"*, Nature, vol. 393, 1998

[153] E.V. Shevchenko, D.V. Talapin, N.A. Kotov, S. OBrien, C.B. Murray *"Structural diversity in binary nanoparticle superlattices"*, Nature, vol 439, 2006

[154] C. Langhammer, V.P. Zhdanov, I. Zoric, and B. Kasemo *"Size-Dependent Kinetics of Hydriding and Dehydriding of Pd Nanoparticles"*, Phys. Rev. Lett, vol. 104, 135502, 2010

[155] A.C.S. Samia, X. Chen, and C. Burda *"Semiconductor Quantum Dots for Photodynamic Therapy"*, J. Aa. Chem. Soc. vol. 125, 15736 – 15737, 2003

[156] W. Zhang, A.O. Govorov, and G.W. Bryant *"Semiconductor-Metal Nanoparticle Molecules: Hybrid Excitons and the Nonlinear Fano Effect"*, Phys. Rev. Lett., vol. 97, 146804, 2006

[157] Y. Li, H.S. Lim, S.C. Ng, Z.K. Wang, M.H. Kuok, E. Vekris, V. Kitaev, F.C. Peiris, G.A. Ozin *"Micro-Brillouin scattering from a single isolated nanosphere"*, Appl. Phys. Lett., vol. 88, 023112, 2006

[158] J.P. Michel, I.L. Ivanovska, M.M. Gibbons, W.S. Klug, C.M. Knobler, G.J.L. Wuite, and C.F. Schmidt *"Nanoindentation studies of full and empty viral capsids and the effects of capsid protein mutations on elasticity and strength"*, PNAS, vol. 103, 16, 6184 – 6189, 2006

[159] W.H. Roos, R. Bruinsma and G.J.L. Wuite *"Physical virology"*, Nature Physics, vol. 6, 2010

[160] W. Shenton, T. Douglas, M. Young, G. Stubbs, S. Mann *"InorganicOrganic Nanotube Composites from Template Mineralization of Tobacco Mosaic Virus"*, Adv. Mater., vol. 11, 3, 253 – 256, 1999

[161] M. Knez, M. Sumser, A.M. Bittner, C. Wege, H Jeske, T.P. Martin, K. Kern *"Spatially Selective Nucleation of Metal Clusters on the Tobacco Mosaic Virus"*, Adv. Funct. Mater., vol. 14, 2, 116 – 124, 2004

[162] R. Cerf, B. Michels, J.-A. Schulz, J. Witz, P. Pfeiffer, and L. Hirth *"Ultrasonic absorption evidence of structural fluctuations in viral capsids"*, PNAS USA, vol. 76, 4, 1780 – 1782, 1979

[163] K.-T. Tsen, S.-W. Tsen, C.-L. Chang, C.-F. Hung, T.-C. Wu, and J. G. Kiang *"Inactivation of viruses by laser-driven coherent excitations via impulsive stimulated Raman scattering process"*, J. Biomed. Opt., vol. 12, 064030, 2007

[164] N.F. Steinmetz and D.J. Evans *"Utilisation of plant viruses in bionanotechnology"*, Org. Biomol. Chem., vol. 5, 2891 – 2902, 2007

[165] E. Dujardin, C. Peet, G. Stubbs, J.N. Culver, S. Mann *"Organization of Metallic Nanoparticles Using Tobacco Mosaic Virus Templates"*, Nano Lett., vol. 3, 3, 413 – 417, 2003

[166] E. Strable, J.E. Johnson, M.G. Finn *"Natural Nanochemical Building Blocks: Icosahedral Virus Particles Organized by Attached Oligonucleotides"*, Nano Lett., vol. 4, 8, 1385 – 1389, 2004

RESUME: The doctoral thesis **"Low frequency modes from small nanoparticles (metal nanocrystals) to large nanospheres (viruses): an inelastic light scattering study"** is dedicated to investigations of the acoustic properties of different nano-objects: small metal nanoparticles and nanocrystals ($D < 30$ nm) and large colloid/viral particles ($D \sim 200$ nm). Inelastic light Raman/Brillouin scattering is used as the main research tool to probe the nanoparticle vibrations and to determine their elastic and mechanical parameters. In the first chapter, the well developed theory of elasticity is used to perform a qualitative and nomenclatural analysis of solid sphere vibrations; several theoretical models allowing to describe the nanoparticle vibrational behavior within a surrounding medium and how the eigenvibrations are modified due to inner crystalline elastic anisotropy are discussed. The second chapter is dedicated to the description of the physics of inelastic light scattering which derives from the fluctuations of the polarizability induced by vibrations. Two types of inelastic light scattering are described: Brillouin scattering which results from the coupling of incident light (photon) with acoustic propagative waves (phonon) in a bulk substance and Raman scattering which is a result of the interaction between an incident photon and localized vibrations, hence nanoparticle vibrations in the present study. As essential in our study, the detailed description and principles of operation of the spectroscopic tools (tandem Fabry-Perot) used to perform these very low frequency inelastic light scattering spectroscopies (between 3 and 300 GHz typically) are given. The third chapter focuses on the study of low frequency modes from small metallic nanoparticles. Three systems are investigated: AuAg and Cu nanoparticles embedded in a vitreous matrix and Au nanocrystals deposited on a surface. The AuAg system allowed to study a notably rich Raman spectrum featuring contributions from fundamental modes and high order harmonics. The experimental data were found to compare rather well with theoretical predictions, thereby providing more insight into the essential ingredients of Raman scattering from nanoparticle modes. The study of deposited Au nanocrystals allowed characterizing the effect of nanocrystalline quality which results in a partial lifting of degeneracy of the nanoparticle modes due to elastic anisotropy. Investigating the wavelength dependence of the Raman spectrum allows a differentiation between single nanocrystals and multiply twinned nanoparticles. Both embedment effects and nanocrystallinity effects are integrated in the study of Cu nanoparticles grown in a glass matrix, where the influence of annealing conditions on the produced nanoparticles was investigated. It was shown that different annealing temperatures with respect to the glass transition of the matrix result in very different low frequency Raman profiles. While highly crystalline small nanoparticles are produced through annealing slightly above the glass transition, annealing well above Tg leads to larger nanoparticles with no signature of elastic anisotropy. The forth chapter reports on the exploration of the possible use of the low frequency inelastic light scattering probe in the characterization of large viruses, as illustrated in the third chapter for small nanoparticles. In order to address the change of the light selection rules as the wavelength of the exciting light becomes comparable to the size of the nanoparticles, the behaviors of the viruses are compared to those of polymer colloids. Ultra Small Angle X-ray Scattering and Atomic Force Microscopy are used to first ensure the comparableness of viruses and polystyrene colloids in terms morphologies. On the basis of the inelastic light scattering data obtained for PS colloids, in "wet" and "dry" states, we discuss the difficult interpretation in terms of eigenmodes of the virus counterparts.

RESUME en français: La thèse de doctorat **"Modes de basse fréquence de petites nanoparticules (nanocristaux métalliques) et de grosses nanosphères (virus) : une étude par diffusion inélastique de la lumière"** est dédiée à l'investigation des propriétés acoustiques de différents nano-objets: nanoparticules métalliques ($D < 30$ nm) d'une part et colloïdes/particules virales ($D \sim 200$ nm) d'autre part. La diffusion inélastique de la lumière (Raman/Brillouin) est utilisée comme instrument de recherche principal pour étudier les vibrations de nanoparticules et pour déterminer leurs paramètres élastiques et mécaniques. Dans le premier chapitre de ce travail, la théorie d'élasticité continue est utilisée afin de présenter une analyse qualitative et de nomenclature des vibrations de sphères solides; plusieurs modèles théoriques, permettant de décrire le comportement vibrationnel de nanoparticules dans un milieu environnant, et comment celui-ci dépend de l'anisotropie inhérente à une structure cristalline interne, sont discutés. Le deuxième chapitre est consacré à la description physique de la diffusion inélastique de la lumière provenant des fluctuations de polarisabilité induite par les vibrations. Deux types de diffusion inélastique de la lumière sont décrits: la diffusion Brillouin, associée au couplage de la lumière incidente (photon) avec les ondes acoustiques (phonon) dans un matériau massif, et la diffusion de Raman provenant de l'interaction entre un photon incident et des vibrations localisées, comme les vibrations de "petites" ($D < \lambda$) nanoparticules. La description détaillée et les principes d'opération des instruments spectroscopiques (tandem Fabry-Pérot) utilisés pour réaliser ces recherches (diffusion inélastique aux basses fréquences, entre 3 et 300 GHz) sont donnés. Le troisième chapitre se focalise sur l'étude des modes basse fréquence de petites nanoparticules métalliques. Trois systèmes sont étudiés : des nanoparticules d'alliage AuAg et de Cu insérées dans une matrice vitreuse et des nanocristaux d'Au déposés sur une surface. Le système AuAg permet d'étudier un spectre Raman remarquablement riche présentant des contributions des modes fondamentaux et des harmoniques d'ordre élevé. Les données expérimentales s'accordent relativement bien avec les calculs théoriques, étayant ainsi la compréhension des ingrédients essentiels de la diffusion Raman par les modes de nanoparticules. L'étude des nanocristaux d'Au déposés a permis de caractériser l'effet de la qualité nanocristalline à travers la levée de dégénérescence partielle des modes de nanoparticules du fait de l'anisotropie élastique. L'étude de la dépendance des spectres Raman en longueur d'onde permet de différencier mono-nanocristaux et nanoparticules polycristallines. Les effets de matrice et de nanocristallinité sont intégrés dans l'étude des nanoparticules de Cu formées dans une matrice vitreuse, o l'influence des conditions de recuit sur les nanoparticules produites a été étudiée. Différentes températures de recuit, par rapport à la température de transition vitreuse de la matrice, conduisent à des profils Raman basses fréquences très différents. Alors qu'un recuit proche de la température de transition vitreuse entraîne la formation de petites nanoparticules de haute cristallinité, un recuit opéré très au-dessus de Tg conduit à la formation de grosses nanoparticules, sans signature d'anisotropie élastique. Le quatrième chapitre rapporte l'exploration d'une éventuelle exploitation de la diffusion inélastique de la lumière pour la caractérisation de gros virus, comme illustré dans le troisième chapitre pour le cas des petites nanoparticules. Afin de mieux appréhender la relaxation des règles de sélection, puisque la longueur d'onde de la lumière devient comparable à la taille des nanoparticules, le comportement des virus a été comparé à celui de polymères colloïdaux. La Diffusion de Rayons X aux Très Petits Angles (USAXS) et la Microscopie à Force Atomique (AFM) sont utilisées pour garantir la bonne comparaison morphologique entre les virus et des colloïdes de polystyrène. La comparaison des spectres Raman/Brillouin de culots concentrés de virus et de colloïdes de polymère, ainsi que leur évolution en fonction de leur état d'hydratation, permet de discuter l'existence des modes de basse fréquence dans les nanoparticules virales.

DISCIPLINE: Physique

MOTS-CLES: Raman, Brillouin, virus, vibrations, diffusion inélastique de la lumière, nanoparticules métalliques.

INTITULE ET ADRESSE DU LABORATOIRE: LPCML - UMR CNRS 5620 - Université Claude Bernard, 10 rue Ada Byron, 69622 Villeurbanne Cedex (FRANCE)